Correlated phases in the vicinity of tunable van Hove singularities in Bernal bilayer graphene

Dissertation

for the award of the degree
"Doctor rerum naturalium" (Dr.rer.nat.)

of the Georg-August-Universität Göttingen

within the doctoral program Physics
of the Georg-August University School of Science (GAUSS)

submitted by

Anna Monika Seiler

from Bad Soden am Taunus

Göttingen, 2023

Thesis Committee

Prof. Dr. Thomas Weitz, I. Physikalisches Institut
Prof. Dr. Fabian Heidrich-Meisner, Institut für Theoretische Physik
Prof. Dr. Claus Ropers, Max-Planck-Institut für Multidisziplinäre Naturwissenschaften and IV. Physikalisches Institut

Members of the Examination Board

Reviewer:	Prof. Dr. Thomas Weitz, I. Physikalisches Institut
Second Reviewer:	Prof. Dr. Claus Ropers, Max-Planck-Institut für Multidisziplinäre Naturwissenschaften and IV. Physikalisches Institut
Third Reviewer:	ChunNing Lau, The Ohio State University

Further members of the Examination Board:

Prof. Dr. Fabian Heidrich-Meisner, Institut für Theoretische Physik
Prof. Dr. Stefan Mathias, I. Physikalisches Institut
Prof. Dr. Jasnamol Palakkal, Institut für Materialphysik
Prof. Dr. Martin Wenderoth, IV. Physikalisches Institut

Date of the oral examination: 13.06.2023

Abstract

The naturally occurring Bernal bilayer graphene exhibits a complex low-energy band structure hosting electric-field-controlled Lifshitz transitions and van Hove singularities. The diverging density of states is predicted to give rise to interaction-induced phenomena. However, signs of correlated phases mediated by these van Hove singularities in Bernal bilayer graphene have been elusive so far.

To find and explore correlated states, high-quality encapsulated Bernal bilayer graphene devices are fabricated and electrical transport measurements are performed at millikelvin temperatures. A dual-gate structure allows to tune the charge carrier density and the electric displacement field across the two layers simultaneously.

First, the trigonally warped low-energy Fermi surface topology of unbiased Bernal bilayer graphene is experimentally uncovered. By analyzing the Landau level spectrum, it is revealed that the band structure of Bernal bilayer graphene consists of four electron-hole asymmetric mini Dirac cones with a truly linear energy dispersion.

Applying a finite electric displacement field deforms the band structure: a band gap opens, the mini Dirac cones transform into parabolically-dispersed pockets, and the center cone is inverted. The latter results in the formation of an inner electron-like pocket in the valence band of Bernal bilayer graphene and produces multiple Lifshitz transitions and concomitant van Hove singularities. Near the Lifshitz transitions, correlated Stoner half and quarter metal phases are identified. More prominently, signatures consistent with a competing topologically non-trivial Wigner-Hall crystal, a topologically trivial Wigner crystal and two correlated metals whose behavior deviates from standard Fermi liquids are reported at zero magnetic field.

Lastly, interaction-driven phases of Stoner-type are revealed near the conduction band edge of strongly biased Bernal bilayer graphene where the energy bands are flatter, and the density of states is larger compared to hole-

doped Bernal bilayer graphene. Here, a transition of the Stoner metals into a spin- and valley-polarized correlated insulator and a spin-polarized insulator is revealed at low magnetic fields. These correlated phases are consistent with either charge density waves or Wigner crystals.

All in all, the measurements presented within this thesis reveal that the simple Bernal bilayer graphene hosts intriguing correlated phases in the vicinity of tunable van Hove singularities. These results open a new chapter for studying strongly interacting electrons using the platform of Bernal bilayer graphene.

Zusammenfassung

Das natürlich vorkommende Bilagen-Graphen mit Bernal-Lagenfolge besitzt bei niedrigen Energien eine komplexe Bandstruktur, die kontrollierbare Lifshitz-Übergänge und van-Hove-Singularitäten enthält. Es wird erwartet, dass die divergierende Zustandsdichte zu wechselwirkungsinduzierten Phänomenen führt, dennoch konnten bisher keine durch van-Hove-Singularitäten getriebenen korrelierten Phasen in Bernal-Bilagen-Graphen beobachtet werden.

Um korrelierte Zustände zu identifizieren und zu untersuchen, werden hochreine eingekapselte Bernal-Bilagen-Graphen Proben hergestellt und bei Temperaturen von wenigen Millikelvin elektrisch vermessen. Eine Feldeffekttransistorstruktur mit zwei Gate-Elektroden ermöglicht es gleichzeitig die Ladungsträgerdichte sowie das elektrische Verschiebungsfeld zwischen den beiden Graphenlagen zu verändern.

Zunächst wird die trigonal verformte niederenergetische Fermi-Oberflächentopologie von Bernal-Bilagen-Graphen experimentell beobachtet. Die Analyse der Landau-Niveaus zeigt, dass die Bandstruktur von Bernal-Bilagen-Graphen, falls kein elektrisches Verschiebungsfeld angelegt wird, aus vier kleinen, Elektron-Loch asymmetrischen Dirac-Kegeln mit linearer Energiedispersion besteht.

Das Anlegen von elektrischen Verschiebungsfeldern führt zu einer Veränderung der Bandstruktur: eine Bandlücke öffnet sich, die kleinen Dirac Kegel werden zu parabolisch-dispergierenden Ausbuchtungen und der innere Dirac Kegel wölbt sich nach innen. Letzteres führt zu einer lochartigen Einbuchtung im Valenzband von Bilagen Graphen und zu mehreren Lifshitz-Übergängen und van-Hove-Singularitäten in dessen Nähe korrelierte Stoner Halb- und Viertelmetalle identifiziert werden können. Darüber hinaus werden Signaturen von konkurrierenden wechselwirkungsgetriebenen Zuständen identifiziert, deren Verhalten mit dem eines topologisch trivialen Wigner Kristalls, eines topologisch nicht trivialen Wigner-Hall Kristalls und

zwei korrelierte Metallen, die andere Eigenschaften als normale Fermi-Flüssigkeiten aufweisen, übereinstimmt.

Zuletzt werden wechselwirkungsgetriebene Stoner Phasen auch bei hohen elektrischen Verschiebungsfeldern im Leitungsband von Bernal-Bilagen-Graphen beobachtet. Hier sind die Energiebänder flacher und die Zustandsdichte ist höher als in mit Löchern dotiertem Bernal-Bilagen-Graphen. Bei niedrigen Magnetfeldern wird hier ein Übergang der Stoner Metalle in einen spin- und valleypolarisierten korrelierten Isolator und einen spinpolarisierten korrelierten Isolator beobachtet. Diese korrelierten Phasen sind entweder mit Ladungsträgerdichtewellen oder mit Wigner-Kristallen vereinbar.

Zusammenfassend zeigen die in dieser Arbeit präsentierten Messungen, dass das einfache Bernal-Bilagen-Graphen faszinierende korrelierte Phasen in der Nähe von kontrollierbaren van-Hove-Singularitäten aufweist. Diese Ergebnisse öffnen ein neues Kapitel für die Erforschung von komplexer Wechselwirkungsphysik von Elektronen auf der Plattform von Bernal-Bilagen-Graphen.

Publications and Manuscripts

This cumulative dissertation is based on a peer-reviewed journal article and on two manuscripts that are currently prepared for publication. They are sorted in the order in which they are discussed in this thesis:

Mapping out the tunable multi-cone band structure in Bernal bilayer graphene

Anna M. Seiler, Nils Jacobsen, Martin Statz, Noelia Fernandez, Francesca Falorsi, Kenji Watanabe, Takashi Taniguchi, Zhiyu Dong, Leonid S. Levitov and R. Thomas Weitz

This work is currently prepared for publication. The current version of the manuscript is reprinted in Chapter 5. The supplementary material is reprinted in Appendix A.

Quantum cascade of correlated phases in trigonally warped bilayer graphene

Anna M. Seiler, Fabian Geisenhof, Felix Winterer, Kenji Watanabe, Takashi Taniguchi, Tianyi Xu, Fan Zhang and R. Thomas Weitz

Nature **608**, 298-302 (2022)

Reference [1], the full article including the Methods and Extended Data Figures is reprinted in Chapter 6.

Interaction-driven quasi-insulating ground states of gapped electron-doped bilayer graphene

Anna M. Seiler, Martin Statz, Isabell Weimer, Nils Jacobsen, Kenji Watanabe, Takashi Taniguchi, Zhiyu Dong, Leonid S. Levitov and R. Thomas Weitz

This work is currently prepared for publication. The current version of the manuscript including the Methods and Extended Data Figures is reprinted in Chapter 7.

Further peer-reviewed publications that originated over the course of this work and are not a direct part of this cumulative thesis are listed below in chronological order:

High-Performance Vertical Organic Transistors of Sub-5 nm Channel Length

> Jakob Lenz, Anna M. Seiler, Fabian R. Geisenhof, Felix Winterer, Kenji Watanabe, Takashi Taniguchi, R. Thomas Weitz.
>
> *Nano Lett.* 21, 4430–4436 (2021)

Quantum anomalous Hall octet driven by orbital magnetism in bilayer graphene

> Fabian R. Geisenhof, Felix Winterer, Anna M. Seiler, Jakob Lenz, Tianyi Xu, Fan Zhang, R. Thomas Weitz
>
> *Nature* 598, 53-58 (2021)

Spontaneous Gully-Polarized Quantum Hall States in ABA Trilayer Graphene

> Felix Winterer, Anna M. Seiler, Areg Ghazaryan, Fabian R. Geisenhof, Kenji Watanabe, Takashi Taniguchi, Maksym Serbyn, R. Thomas Weitz
>
> *Nano Lett.* 22, 3317–3322 (2022)

Interplay between topological valley and quantum Hall edge transport

> Fabian R. Geisenhof, Felix Winterer, Anna M. Seiler, Jakob Lenz, Ivar Martin, R. Thomas Weitz
>
> *Nat. Commun.* 13, 1-7 (2022)

Impact of Electric Field Disorder on Broken-Symmetry States in Ultraclean Bilayer Graphene

> Fabian R. Geisenhof, Felix Winterer, Anna M. Seiler, Jakob Lenz, Ivar Martin, R. Thomas Weitz
>
> *Nano Lett.* 22, 7378–7385 (2022)

Contents

1 Introduction

In condensed matter physics, the electronic properties of materials are described to a first approximation by a single-particle picture. Here, the kinetic energy of electrons at the Fermi energy is governed by the dispersion of electronic bands that contain the energy states that electrons can populate [2–5]. A system behaves insulating when the Fermi energy level lies in between two energy bands and the electrons cannot move from the highest occupied band (valence band) into the lowest unoccupied band (conduction band). On the contrary, a system exhibits metallic behavior when the Fermi energy level lies within a band, and electrons can move freely. However, since this simple picture does not take interaction between electrons into account, it often fails to describe the properties of many systems that exhibit a high density of states, such as those in which the energy bands are flat. In this case, the kinetic energy is significantly reduced and the Coulomb energy between electrons can dominate the system. Interactions between electrons can then lead to spontaneous symmetry breaking in the ground state, for example to a breaking of the spin degree of freedom [6]. Furthermore, they can induce correlated states of matter, such as correlated insulators that are insulating states not expected in the absence of correlations [2, 4, 5]. For decades, the investigation of the nature of correlated phases has been an active field of research, exciting both experimental and theoretical physicists [7–9].

A playground to study correlated phases are two-dimensional (2D) electronic systems, such as silicon or gallium arsenide metal-oxide-semiconductor field-effect transistors in which the electrons are confined in a plane and are thus more likely to interact. These systems are highly tunable as the charge carrier density can be controlled precisely by applying electrical gate voltages allowing the study of correlation effects in a variety of density regimes. Indeed, intensive investigations have led to the discovery of multiple interaction-induced effects, such as unexpected metal-insulator transitions observed as a function of the charge carrier density [9–11]. At low temperatures, the band dispersion in a 2D electronic system can be modified by applying a perpendicular magnetic field. Flat bands, known as Landau levels, are then formed in which the density of states diverges. Coulomb interactions between electrons can now dominate the system and various interaction-induced phenomena, such as fractional quantum Hall states in which the Hall conductance shows fractional values of e^2/h (where e is the electronic charge and h is Planck's constant), have been revealed [8, 12, 13].

With the first isolation of graphene, a single layer of carbon atoms arranged in a hexagonal lattice, a promising and much simpler 2D electronic system was found. Although pristine graphene exhibits a low density of states, broken symmetry and fractional quantum Hall states were seen in this system when applying magnetic fields [14, 15]. Following a landmark discovery in 2018, research in the graphene community has recently mainly focused on so-called 'magic-angle' twisted bilayer graphene where correlation effects were found even in the absence of magnetic fields [16–21]. In this system, two layers of graphene are stacked on top of another with an angle of precisely 1.1 degrees. Thereby, the energy bands of the two layers hybridize and become flat. Several correlating states, such as correlated insulators [16], ferromagnetism [19, 20] and even superconductivity - the complete disappearance of resistance - [17, 21] have been observed. The downside of twisted bilayer graphene, however, lies in the complicated sample fabrication and in the inhomogeneity and twist angle disorder that is always present in the system [22, 23]. Furthermore, the energy bands cannot be tuned from flat to non-flat after sample fabrication, limiting the extent to which the underlying correlation physics in these systems can be probed.

More recently, correlation-induced ferromagnetism and superconductivity were also observed in the naturally-occurring rhombohedral-stacked trilayer graphene when a high electric displacement field is applied [24, 25]. In this tunable system, the density of states does not diverge due to the presence of flat energy bands, but rather due to a van Hove singularity - a saddle point in the energy dispersion relation - that can be accessed by electrostatic gating.

The even simpler and more stable Bernal bilayer graphene exhibits a similar band structure to rhombohedral-stacked trilayer graphene [26, 27]. However, even though this system has been studied intensively in the past, signs of electron-electron interaction have been only seen at large out-of-plane magnetic fields [28–32] or when the bilayer graphene is freely suspended in vacuum [28, 29, 33, 34]. Another approach for the investigation of Bernal bilayer graphene is to encapsulate it in hexagonal boron nitride. Here, correlation effects are reduced compared to free-standing bilayer graphene samples. Encapsulated samples are in turn less fragile and allow for applying the large electric displacement fields needed to reach a regime in which the density of states diverges.

Exotic correlated states that emerge in encapsulated bilayer graphene samples when the Fermi energy level is tuned in the vicinity of the van Hove singularity have only recently been revealed during the course of this thesis[1]. The primary goal of this work was to observe and analyze the correlated states to elucidate the interacting phase diagram of natural bilayer graphene.

To observe electron-electron correlations, high-quality bilayer graphene samples are fabricated in which the bilayer graphene flakes are encapsulated in hexagonal boron nitride and equipped with top and bottom gates. Afterwards, charge transport measurements are performed at millikelvin temperatures. By analyzing the Landau level spectrum of bilayer graphene at zero and low electric displacement fields and comparing it to the theoretical expected spectrum, an understanding of the non-interacting band structure is obtained. Specifically, it is experimentally revealed for the first time that, due to trigonal warping - a deformation of the low-energy band structure near the K-points, the low-energy band structure of non-biased bilayer graphene consists of four linearly-dispersed cones which is consistent with theoretical predictions [37]. Furthermore, it is shown that the band structure is electron-hole asymmetric, which becomes relevant when analyzing the correlated phases that emerge at large electric displacement fields.

Following up on this work, the correlated phases appearing in hole-doped bilayer graphene, where the Fermi level sits in the valence band, are investigated. Here, a cascade of different correlated phases emerges when van Hove singularities are accessed via electrostatic gating. The correlated phase diagram includes Stoner phases - metallic phases showing spin and/or

---

[1] See also works by H. Zhou et al. [35] and S. C. de la Barrera et al. [36].

valley polarization even in the absence of magnetic fields, as well as correlated insulators and correlated metals of non-Stoner type. To distinguish between the different phases, low-temperature transport measurements are conducted and regions of similar conductance are traced as a function of the charge-carrier density (corresponding to the Fermi energy), the electric displacement fields, in-plane and out-of-plane magnetic fields, temperature and applied bias currents.

Finally, exotic correlated insulating states are also identified in the electron-doping regime (i.e. in the conduction band) where the density of states in the vicinity of the van Hove singularities is expected to be even larger than at hole doping, since the trigonal warping is less pronounced and the energy bands are flatter. The emerging states in electron-doped bilayer graphene are analyzed in a similar way as those appearing in hole-doped bilayer graphene. They are concluded to be consistent with ferromagnetic Stoner phases that transition either into insulating charge-density wave phases or Wigner crystal phases with different spin and valley polarization at low magnetic fields.

In summary, the investigations in this thesis reveal that due to its complex low-energy band structure, encapsulated Bernal bilayer graphene is suitable to study interaction effects when large electric displacement fields are applied. Since Bernal bilayer graphene is simpler, more stable, more tunable, and easier to fabricate than magic-angle twisted bilayer graphene, this system presents a versatile platform to study electron-electron interaction and is worth further experimental and theoretical effort.

The outline of this cumulative thesis is as follows:

- In Chapter 2, the theoretical background needed to understand the experimental results of this thesis is presented. After 2D materials and their heterostructures are introduced, the single-particle band structure model of bilayer graphene is discussed. Next, the theoretical foundations of the quantum Hall effect and electron-electron interaction induced quantum phenomena are given. In the last section of this chapter, the working principles of dual-gated bilayer graphene field-effect transistors are explained in detail.

- In Chapter 3, the essential techniques needed to fabricate high-quality bilayer graphene heterostructures are introduced. These include mechanical exfoliation, the identification and characterization of suitable flakes, the transfer of flakes via a stamping technique and the fabrication of electrical contacts. At the end of this chapter, an overview of all devices that have been measured in the course of this thesis is provided.
- In Chapter 4, the electrical transport measurements are discussed. Apart from introducing the working principle of the dilution refrigerator and the electrical measurement configuration, an overview of standard transport measurements that have also been conducted by other groups is given in order to provide comparative qualification of the samples presented in this work.
- The results part of this cumulative thesis (Chapters 5, 6, and 7) comprises one peer-reviewed article and two manuscripts in preparation for publication.
- In Chapter 8, the key messages presented in Chapters 5 - 7 are summarized. Furthermore, complementary works are discussed and future perspectives are provided.
- Finally, in Chapter 9, a conclusion that includes a summary of the thesis and a universal outlook is given.

2 Theoretical background

This chapter discusses the fundamental concepts and theories relevant to this thesis. It starts with a general introduction to 2D materials and continues with a detailed discussion of bilayer graphene's structural and electronic properties. Afterwards, an introduction to the quantum Hall effect is given. The theory discussed in these sections is based on single-particle physics, meaning no interaction between charge carriers is considered. In the following section, some of the emergent phenomena that can arise due to interaction of charge carriers, starting with broken symmetry quantum Hall states and followed by Stoner ferromagnetism and correlated insulators and metals, are introduced. In the end, an introduction to dual-gated bilayer graphene field-effect transistors is given.

2.1 Introduction to two-dimensional materials

The first isolation of graphene in 2004 [38] and the discovery of graphene’s exceptional mechanical [39], thermal [40], electrical [41, 42], and optical properties [43] stimulated an interest in crystalline materials consisting of single- or few-layer atoms. In the next few years, more so-called 2D materials such as hexagonal boron nitride, Tungsten Diselenide (WSe_2), and other dichalcogenides have been theoretically predicted and isolated [44–46]. Unlike their three-dimensional (3D) counterparts, 2D materials exhibit strong chemical bonds only within 2D layers, while different layers are held together by weak van der Waals forces [44, 47–49]. By applying external forces, individual layers can be isolated without leaving dangling bonds [47–49]. When more and more layers are removed, the material changes from being 3D to effectively 2D. This reduced dimensionality can result in a change of the material properties, which is also the case for graphene. [49, 50]

2.1.1. Monolayer graphene

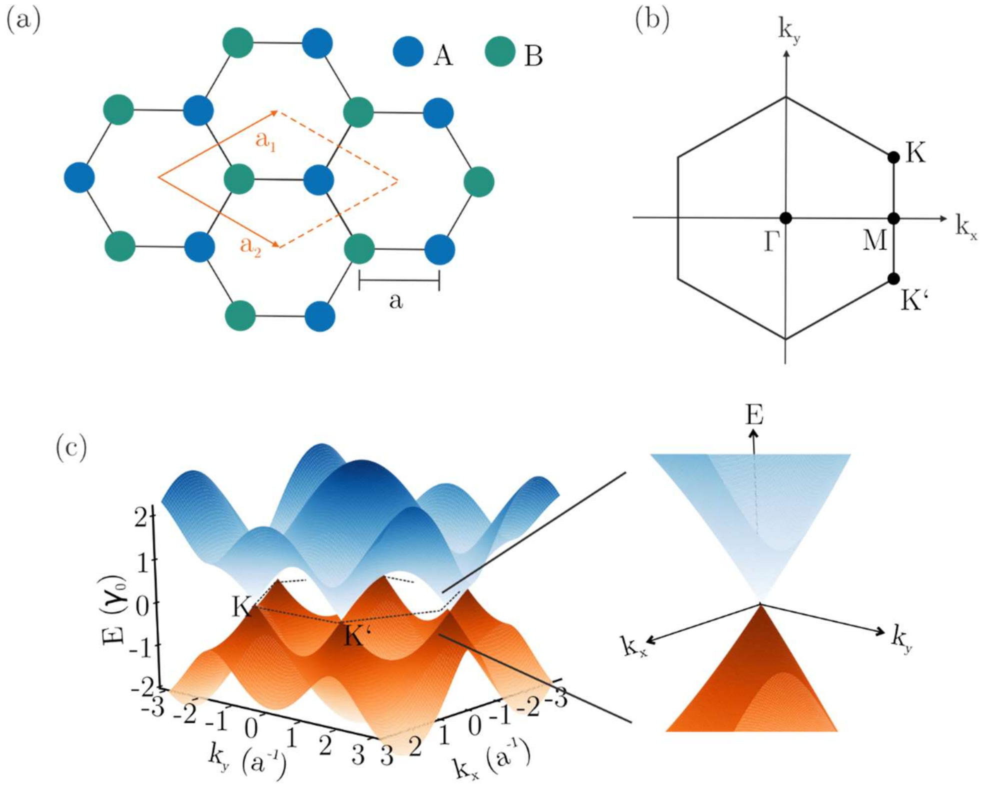

Figure 2.1 Lattice and band structure of monolayer graphene. (a) Hexagonal lattice structure of monolayer graphene with two atoms per unit cell. Atoms corresponding to sublattice A (B) are shown in blue (orange). The orange lines illustrate the unit cell that contains one atom of each sublattice. The unit cell vectors $\mathbf{a}_1$ and $\mathbf{a}_2$ are indicated by vectors. (b) First Brillouin zone of monolayer graphene. Points of high symmetry interest are labeled. (c) Band structure of monolayer graphene. The conduction band (blue) and valence band (green) touch at the K and K' points. A zoom-in of one of the K points is shown on the right. Near these points, the energy exhibits a linear dispersion.

Monolayer graphene consists of a single layer of carbon atoms arranged in a hexagonal lattice as shown in Figure 2.1a [49, 51]. Its triangular unit cell has two inequivalent atomic sites, A and B, that belong to different sublattices and are separated by $a = 0.142$ nm [49]. This arrangement results from the sp^2 hybridization of the carbon atoms and leads to the formation of strong planar covalent σ-bonds between nearest neighbor carbon atoms that are responsible for the exceptional mechanical robustness of graphene [39]. The remaining electrons lie within the p$_z$-orbital perpendicular to the carbon plane, forming $\boldsymbol{\pi}$-bonds. They are delocalized and can move through the lattice freely. [48, 49]

The reciprocal lattice of graphene is also hexagonal. Its primitive unit cell, that is known as the first Brillouin zone, exhibits multiple high-symmetry points that are labeled in Figure 2.1b. The high-symmetry points sitting at the corners of the hexagonal Brillouin zone are of particular importance. They are referred to as valleys, K and K' points, or Dirac points. Two of these points (one K and one K' point) are independent as they belong to different sublattices, the others are equivalent by symmetry.

Using a tight-binding approach and considering only nearest neighbor hopping (hopping between atoms A and B, black lines in Figure 2.1a) of electrons within the p$_z$-orbital yields the Hamiltonian

$$\mathcal{H}_{\mathrm{ML}} = -\gamma_0 \sum_{<\mathrm{i},\mathrm{j}>,\sigma} (\mathrm{a}^{\dagger}_{\sigma,\mathrm{i}}\, \mathrm{b}_{\sigma,\mathrm{j}} + \mathrm{h.\,c.}) \ , \tag{1}$$

where $\mathrm{a}_{\sigma,\mathrm{i}}$ $\left(\mathrm{a}^{\dagger}_{\sigma,\mathrm{i}}\right)$ is the annihilation (creation) operator for an electron with spin degree of freedom σ ($\sigma = \uparrow, \downarrow$; spin up or down) on site $\mathrm{r_i}$ on sublattice A and $\mathrm{b}_{\sigma,\mathrm{i}}$ $\left(\mathrm{b}^{\dagger}_{\sigma,\mathrm{i}}\right)$ is the annihilation (creation) operator for an electron with spin degree of freedom σ on site $\mathrm{r_i}$ on sublattice B. $\gamma_0 \approx 2.8$ eV is the hopping energy. [49]

The energy bands as a function of wavevector $\boldsymbol{k}$ can be derived from this Hamiltonian. They are given by

$$E_{\pm} = \pm\gamma_0\ |f(\boldsymbol{k})| \tag{2}$$

with

$$f(\boldsymbol{k}) = \sqrt{3 + 4\cos\left(\frac{3k_x a}{2}\right)\cos\left(\frac{3k_y a}{2}\right) + 2\ \cos\ (\sqrt{3}k_y \mathrm{a})} \tag{3}$$

and + (-) referring to the conduction (valence) band [49, 51].

The energy band structure (plotted in Figure 2.1c from Equation (2)) consists of two cosine-like energy bands that touch but not overlap at the K and K' points, resulting in a gapless energy dispersion and in the classification of monolayer graphene as a gapless semiconductor. Near these points, the energy bands mimic cones, and are also referred to as Dirac cones. They exhibit a linear energy dispersion given by

$$E_{\pm}\ (\boldsymbol{k}) \approx\ \pm v_F\ \hbar\ \boldsymbol{k} \tag{4}$$

with Fermi velocity $v_F = 3\gamma_0 a\ /\ 2\hbar\ \approx\ 10^6$ m/s. $\hbar$ is the reduced Planck constant (Planck constant h divided by 2π). [49–51] Remarkably, this linear band structure resembles the energy dispersion of massless relativistic (Dirac) particles whereas the Fermi velocity v_F replaces of the speed of light [52, 53]. As graphene's K and K' points are protected by inversion and time-reversal symmetry, the band touching without gap opening even persists when next-nearest neighbor and higher order couplings are considered [54, 55].

Because of its two sublattices A and B, graphene possesses an additional degree of freedom which is, in analogy with the spin degree of freedom, called pseudospin. Thus, charge carriers in graphene can be described by two-component spinors. Another degree of freedom arises from the degeneracy of electronic states associated with the two valleys and is called the valley degree of freedom. It can be shown that the valley and pseudospin degree of freedom are linked to the momentum. In fact, in the K valley, the pseudospin of an electron is always parallel to the momentum and the pseudospin of a hole is always antiparallel to the momentum while it is the opposite in the K' valley. This property of graphene is called chirality and gives rise to a valley contrasting Berry phase of $+\pi$ in the K-valley and of $-\pi$ in the K' valley. [49]

2.1.2. Multilayer graphene and graphite

The linear energy dispersion vanishes when another graphene sheet is stacked on top of the first one. Charge carriers can then not only hop in between atomic sites in one layer but also between neighboring layers resulting in a much more complex band structure [50, 56]. How this interlayer hopping effects the tight-binding Hamiltonian and the band structure will be discussed in detail for Bernal bilayer graphene in Section 2.2.

In multilayer graphene with more than two layers, the electronic properties depend on how different layers are stacked on top of each other [57, 58]. Naturally, two different stacking configurations, Bernal stacking and rhombohedral stacking, can occur [57, 59]. Since regions with rhombohedral stacking configuration usually transform into regions with Bernal stacking configuration during device fabrication [57], It is assumed that all multilayer graphene samples used for devices fabricated within this thesis exhibit a Bernal stacking configuration.

In case that Bernal-stacked multilayer graphene exhibits an odd layer number, the band dispersion can be viewed as a combination of the energy bands of monolayer graphene and of bilayer graphene [57]. In case of even layer numbers, a combination of the energy bands of multiple bilayers is formed [50, 58]. In addition, a small overlap of the conduction and valence band occurs due to interaction of next-nearest-neighboring layers.

Thus, from three layers on, Bernal-stacked multilayer graphene can be treated as a semimetal [50]. The overlap of the two bands increases with layer number until the number of layers reaches approximately ten. At ten layers, the band overlap reaches 40 meV [50, 60]. In this thesis, multilayer graphene consisting of ten or more layers is referred to as graphite. Due to its high electrical conductivity and its structural properties very similar to graphene, graphite can be used as a contact and gating material for graphene heterostructures (see Section 2.5 for more details).

2.1.3. Hexagonal boron nitride

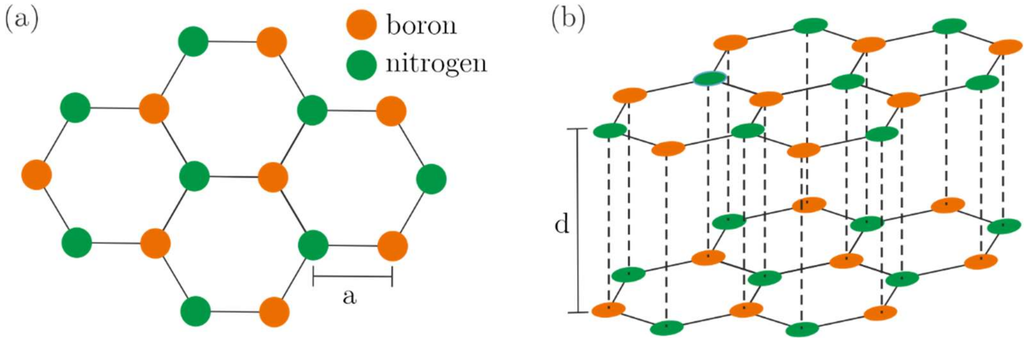

Figure 2.2 Lattice structure of hexagonal boron nitride. (a,b) Hexagonal lattice structure of hexagonal boron nitride with one boron (orange) and one nitrogen atom (green) per unit cell. (a) One layer and (b) two layers in an AA' stacking configuration are shown.

Shortly after the first isolation of graphene, also other 2D materials such as hexagonal boron nitride (hBN) were thinned down to crystalline monolayers [45]. Being an isomorph graphene, hBN exhibits a hexagonal lattice structure whereas alternating boron and nitrogen atoms are replacing the carbon atoms as shown in Figure 2.2a. The lattice constant of hBN is given by $a = 0.145$ nm [61]. Different layers are separated by $d = 0.35$ nm and are stacked in an AA' stacking configuration meaning that the boron (nitrogen) atoms lie on top of the nitrogen (boron) atoms in the consecutive layer (Figure 2.2b) [61–64].

Unlike in graphene, nearest-neighbor atoms in hBN are of different kind and exhibit a difference in electronegativity. Thus, they are not only hold together by covalent but also by ionic bonds and the electrons in the π-orbitals are localized closer to the nitrogen than to the boron atoms resulting in an insulating behavior and in a bandgap of 6 eV. [61, 65, 66]

2.1.4. Van der Waals heterostructures

One of the biggest advantages of 2D materials comes to light when different layers are stacked on top of each other and are combined to 2D heterostructures. They are then held together by van der Waals forces just like naturally occurring multilayers of one 2D material. Consequently, they are also referred to as van der Waals heterostructures. Building such heterostructures can fundamentally alter the material's characteristics. For example, bringing monolayers of WSe_2 on top of monolayer graphene, which intrinsically has weak spin-orbit coupling, induces strong spin-orbit coupling in monolayer graphene via proximity effects [67–69]. Apart from the choice and order of materials, their relative alignment can also change the material's properties [16, 17, 21, 25, 70, 71]. In particular, aligning two monolayer graphene sheets with an angle of 1.1° significantly modifies the band structure. The energy bands become strongly flattened and correlated insulators as well as superconductivity have been observed [16, 17].

Most importantly for this work, the rise of van der Waals heterostructures led to an enormous increase in the electronic quality of 2D materials [44, 72–74]. To protect graphene and its multilayer counterparts from surface impurities and strain on the typically used silicon (Si) and silicon dioxide (SiO_2) substrates, a widely adopted approach is to encapsulate graphene in hBN, that exhibits a very similar lattice structure with a lattice mismatch of only 1.7 % [73, 75, 76]. Being a 2D material with a precise number of layers, the surface of hBN is atomically flat, preventing graphene from forming wrinkles [73]. It is chemically and mechanically stable and an excellent thermal conductor, which helps to dissipate heat generated by graphene when currents flow through the sample [77]. Due to its insulating behavior, it does not interfere with the electronic properties of graphene unless the two lattices are closely aligned [71]. Furthermore, encapsulation in hBN keeps the graphene away from dirt and environmental influences [42, 74, 78]. By placing a sheet of graphite below the lower sheet of hBN, charge inhomogeneities coming from underlying substrates are screened [74].

Another major advantage of hBN/graphite heterostructures lies in their electrostatic tunability. With a relatively low dielectric constant ε_r ranging from $\varepsilon_r = 3 - 4$ [73], hBN can be used as a dielectric material for electrostatic gating [79]. The dielectric breakdown voltages in hBN range from 0.8 Vnm^{-1} [80] to 1.2 Vnm^{-1} [81].

Sheets of graphite or other metals can be added on both sides of the heterostructure and can be used as electrical gate electrodes [74, 76]. Furthermore, graphite can be used for contacting graphene and other 2D materials [82–84].

2.2 Structural and electronic properties of Bernal bilayer graphene

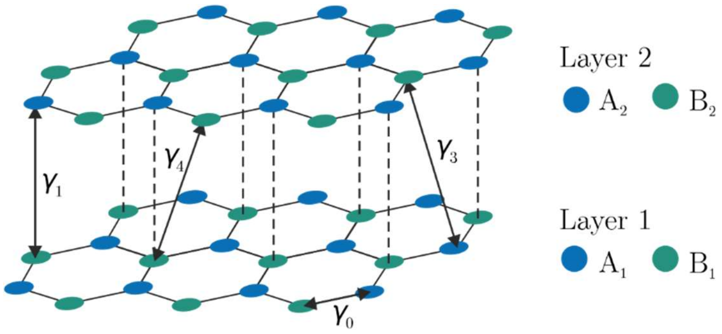

Figure 2.3. Lattice structure of Bernal bilayer graphene. Atoms A$_1$ and B$_1$ belong to different sublattices in one layer while atoms A$_2$ and B$_2$ belong to different sublattices in another layer. Electrons can hop within and between layers via hopping parameters γ_i.

The main focus of this work lies on Bernal bilayer graphene, that is also referred to as AB stacked bilayer graphene, and is the most energetically stable and naturally occurring form of bilayer graphene. The lattice structure of Bernal bilayer graphene is shown in Figure 2.3. In this stacking configuration, the upper carbon lattice (layer 2 in Figure 2.3) is shifted to the lower carbon lattice (layer 1 in Figure 2.3) in a way that atom A$_2$ in the upper lattice is located directly above atom B$_1$ in the lower lattice while atom A_1 in the lower lattice sits directly below the center of the upper lattice. The interlayer spacing between the two lattices is given by $d = 0.334$ nm.

In analogy to monolayer graphene, the band structure of bilayer graphene can be determined using a tight-binding approach for the π-electrons. Apart from an intralayer hopping energy γ_0 describing the hopping energy between atoms from different sublattices in one layer, also interlayer coupling energies referring to electron hopping between atoms from different layers must be considered. These interlayer coupling energies are γ_1, corresponding to nearest neighbor interlayer hopping between atoms of sublattice B_1 and A_2 that sit directly on top of each other and form dimers, γ_3, referring to hopping from atoms between non-dimer sites (i.e., hopping in between sublattice A_1 and B_2) and γ_4, referring to hopping from atoms between sublattices A_1 and A_2, and B_1 and B_2 (Figure 2.3). Their values were estimated in Reference [85] via a local-density approximation as

$$\begin{gathered}\gamma_0 = 2.61 \text{ eV},\\ \gamma_1 = 0.361 \text{ eV},\\ \gamma_3 = 0.283 \text{ eV},\\ \gamma_4 = 0.138 \text{ eV}\end{gathered}$$

and are in good agreement with experimental fits to Raman [86] and infrared spectroscopy data [87, 88]. Note that in principle also higher-order couplings, e.g. next nearest intralayer couplings, have to be included into this tight-binding model. However, their effects on the band structure are much smaller than the effects of $\gamma_0, \gamma_1, \gamma_3$ and γ_4 and they are consequently ignored in the following [26, 89].

Including hopping energies $\gamma_0, \gamma_1, \gamma_3$ and γ_4, the tight-binding Hamiltonian can be written as a 4 x 4 matrix considering p_z-electrons on the four atomic sides:

$$\mathcal{H}_{BLG} = \begin{pmatrix} \varepsilon_{A1} & -\gamma_0 f(\boldsymbol{k}) & \gamma_4 f(\boldsymbol{k}) & -\gamma_3 f^*(\boldsymbol{k}) \\ -\gamma_0 f^*(\boldsymbol{k}) & \varepsilon_{B1} & \gamma_1 & \gamma_4 f(\boldsymbol{k}) \\ \gamma_4 f^*(\boldsymbol{k}) & \gamma_1 & \varepsilon_{A2} & -\gamma_0 f(\boldsymbol{k}) \\ -\gamma_3 f(\boldsymbol{k}) & \gamma_4 f^*(\boldsymbol{k}) & -\gamma_0 f^*(\boldsymbol{k}) & \varepsilon_{B2} \end{pmatrix} \tag{5}$$

[26]. Here, ε_{A1}, ε_{B1}, ε_{A2} and ε_{B2} are the on-side energies that are not necessarily equal. In particular, there is an energy difference between dimer and non-dimer sites that is denoted as

$$\Delta' = \frac{1}{2}\ [(\varepsilon_{B1} + \varepsilon_{A2}) - (\varepsilon_{A1} + \varepsilon_{B2})]. \tag{6}$$

In bilayer graphene, Δ' was found to be 0.0015 eV [85]. f($\mathbf{k}$) describes nearest-neighbor hopping which was already introduced for monolayer graphene (see Equation (3)) and can be adapted to bilayer graphene. Near the K- and K'-points, $f(\boldsymbol{k})$ can be simplified by introducing momentum $\boldsymbol{p}$ with x- and y-components p_x and p_y which are measured from the center of the K-points. It can be approximated to

$$f(\boldsymbol{k}) \approx -\sqrt{3}a(\xi p_x - ip_y)/2\hbar, \tag{7}$$

whereas $\xi = \pm 1$ corresponds to the K and K' points and is denoted as the valley index [26]. $\mathcal{H}_{\text{BLG}}$ then becomes

$$\mathcal{H}_{\text{BLG}} = \begin{pmatrix} \varepsilon_{A1} & v\pi^+ & -v_4\pi^+ & v_3\pi \\ v\pi & \varepsilon_{B1} & \gamma_1 & -v_4\pi^+ \\ -v_4\pi & \gamma_1 & \varepsilon_{A2} & v\pi^+ \\ v_3\pi^+ & -\pi_4\pi & v\pi & \varepsilon_{B2} \end{pmatrix} \tag{8}$$

$$= \begin{pmatrix} 0 & v\pi^+ & -v_4\pi^+ & v_3\pi \\ v\pi & \Delta' & \gamma_1 & -v_4\pi^+ \\ -v_4\pi & \gamma_1 & \Delta' & v\pi^+ \\ v_3\pi^+ & -\pi_4\pi & v\pi & 0 \end{pmatrix} \tag{9}$$

with $\pi = \xi p_x + ip_y$, $\pi^+ = \xi p_x - ip_y$, $\varepsilon_{B1} = \varepsilon_{A2} = \Delta'$, $\varepsilon_{A1} = \varepsilon_{B2} = 0$ and effective velocities $v = \sqrt{3}a\gamma_0/2\hbar$, $v_3 = \sqrt{3}a\gamma_3/2\hbar$ and $v_4 = \sqrt{3}a\gamma_4/2\hbar$.

At low energies and for $\gamma_0, \gamma_1 \gg \gamma_3, \gamma_4$, it can be further simplified to a two-band model Hamiltonian describing the two lowest energy bands that approach each other at zero energy. It is reduced to the non-dimer sites, A_1 and B_2, and includes direct hopping via γ_3 and γ_4 as well as hoppings via dimer sites [26, 85]. The two-band model Hamiltonian can be expressed as

$$\mathcal{H}_{2-\text{band}} = \mathcal{H}_0 + \mathcal{H}_w + \mathcal{H}_{as} \tag{10}$$

whereas

$$\mathcal{H}_0 = -\frac{v^2}{\gamma_1}\begin{pmatrix} 0 & (\pi^+)^2 \\ \pi^2 & 0 \end{pmatrix} \tag{11}$$

dominates the band structure at large energies. $\mathcal{H}_0$ resembles the Hamiltonian of monolayer graphene (see Equation (1)) but with a quadratic-in-momentum term on the off-diagonals. It is responsible for the nearly parabolic energy bands of bilayer graphene that touch at zero energy as shown in Figure 2.4a.

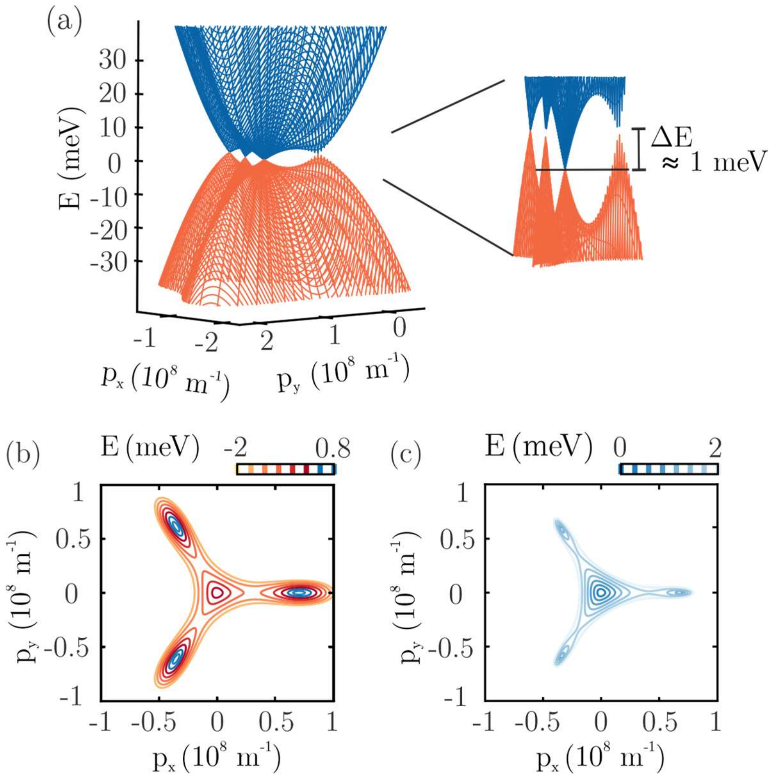

Figure 2.4. Band structure of bilayer graphene. (a) Band structure of bilayer graphene calculated from Hamiltonian $\mathcal{H}_{2-\text{band}}$ (Equation (10)). The valence band is colored in orange, the conduction band in blue. A zoom-in is shown in the right. (b,c) Fermi surface contour of the conduction band (b) and valence band (c) of bilayer graphene at different Fermi energies as a function of p_x and p_y calculated from Hamiltonian $\mathcal{H}_{2-\text{band}}$ (Equation (10)). The band structure calculations were performed by Nils Jacobsen.

At low energies below 2 meV, the second term

$$\mathcal{H}_w = v_3 \begin{pmatrix} 0 & \pi \\ \pi^+ & 0 \end{pmatrix} - \frac{v_3 a}{4\sqrt{3}\hbar} \begin{pmatrix} 0 & (\pi^+)^2 \\ \pi^2 & 0 \end{pmatrix} \tag{12}$$

and the third term

$$\mathcal{H}_{as} = \left(\frac{2vv_4}{\gamma_1} + \frac{\Delta' v^2}{\gamma_1^2} \right) \begin{pmatrix} \pi^+\pi & 0 \\ 0 & \pi\pi^+ \end{pmatrix} \tag{13}$$

become relevant and the band structure becomes more complex as displayed in the zoom-in which is shown on the right-hand side of Figure 2.4a. [26, 85]

$\mathcal{H}_w$ includes the interlayer coupling between non-dimer sites (γ_3) and consists of two terms. Like $\mathcal{H}_0$, the second term of $\mathcal{H}_w$ scales quadratically with momentum while the first term of $\mathcal{H}_w$ scales linearly with momentum. The linear term causes the band structure to undergo a trigonal deformation called trigonal warping. At energies < 1 meV, the contribution of the linear term becomes larger than the contribution of the quadratic terms resulting the conduction and valence bands to each break down into four separate pockets. While the central pocket is located around the K- or K'-point, the three so-called leg pockets exhibit small offsets in momentum. At low energies, all pockets exhibit a nearly linear energy dispersion. In analogy to the Dirac peak in monolayer graphene, they are referred to as mini Dirac cones [26, 90]. $\mathcal{H}_{as}$ includes both, the interlayer coupling energy γ_4 and an energy difference between dimer and non-dimer sites Δ' and produces an electron-hole asymmetry that becomes relevant in the regime in which the band structure consists of four different pockets. It results in an energetic shift of the central pocket compared to the three outer pockets that is also shown in Figure 2.4a. [26]

In order to visualize the electron-hole asymmetry better, it is useful to introduce the concept of a Fermi surface which is the surface in reciprocal space separating occupied from unoccupied electron states at zero temperature [91]. When the Fermi energy E of bilayer graphene is set to $E = 0$ meV where the valence and conduction band touch at the K and K' points, the area of the Fermi surface of the center pocket vanishes whereas the area of the Fermi surface of the three-leg pockets is finite. At -1 meV $< E < 0$ meV, the Fermi surface of the valence band consists of four disconnected pockets whereas the Fermi surface area of each of the three leg-pockets is larger than the Fermi surface area from the center pocket due to electron-hole asymmetry (see Figure 2.4b). At 0 meV $< E <$ 1 meV, only the center pocket contributes to the Fermi surface of the conduction band while the three leg pockets give a contribution to the Fermi surface of the valence band in the same energy range (see Figure 2.4b,c).

In Chapter 5, it is shown that the shape of the Fermi surface can be very relevant for bilayer graphene's electronic properties such as its quantum Hall effect.

Introducing an interlayer asymmetry:

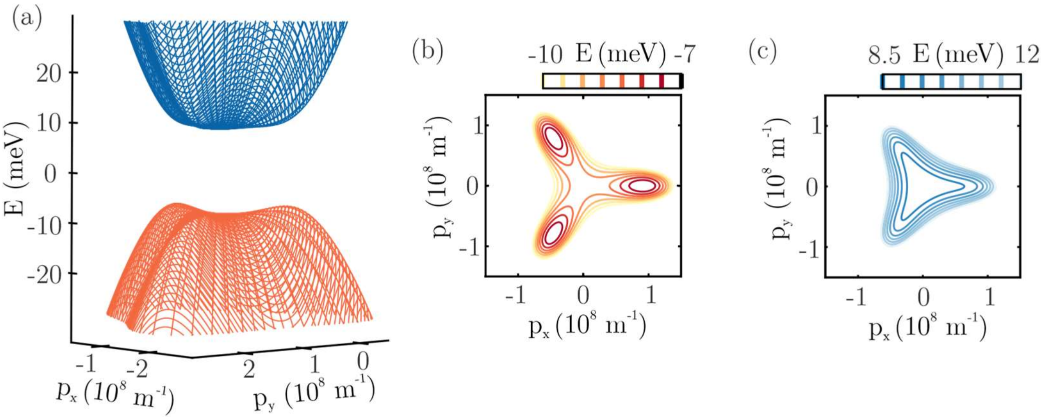

Figure 2.5. Band structure of gapped bilayer graphene. (a) Band structure of bilayer graphene at $U =$ 0.017 eV calculated from Hamiltonian $\mathcal{H}_{2-\text{band}}$ (Equation (10)). The valence band is colored in orange, the conduction band in blue. (b,c) Fermi surface contour of the valence band (b) and conduction band (c) of bilayer graphene at $U =$ 0.017 eV at different Fermi energy levels as a function of p_x and p_y calculated from Hamiltonian $\mathcal{H}_{2-\text{band}}$ (Equation (10)). U was set to 0.017 eV. The band structure calculations were performed by Nils Jacobsen.

An interesting characteristic of bilayer graphene appears when an energy difference between both layers is created. This can for example be realized by electrostatic gating [92] or doping [93]. The interlayer asymmetry U can be expressed as

$$U = \tfrac{1}{2}\ [(\varepsilon_{A1} + \varepsilon_{B1}) - (\varepsilon_{A2} + \varepsilon_{B2})] \tag{14}$$

and can be embedded into the two-band model Hamiltonian (Equation (10)) by adding an additional term [26]

$$\mathcal{H}_U = -\tfrac{U}{2}\left[\begin{pmatrix}1 & 0\\ 0 & -1\end{pmatrix} - \tfrac{2v^2}{\gamma_1^2}\begin{pmatrix}\pi^+\pi & 0\\ 0 & -\pi\pi^+\end{pmatrix}\right] \tag{15}$$

which results in the opening of a band gap at the K and K' points [37, 93, 94]. The size of the band gap increases with increasing U [94]. The possibility of creating a band gap via electrostatic gating allows to classify Bernal bilayer graphene as a semiconductor and makes it distinct from monolayer graphene where no tunable band gap can be opened.

Furthermore, a contribution of U results in a drastic change of the low-energy band structure: the center pocket then diminishes while the three leg pockets become more prominent and change their dispersion from being linear to being parabolic [26]. Due to electron-hole asymmetry, this happens at different energy scales for the valence and conduction band (see Figure 2.5) [26, 95]. In the valence band, the center cone vanishes at approximately $U \approx 10$ meV and is converted into an electron pocket at $U > 10$ meV. Thus, at $U > 10$ meV and small Fermi energies, the Fermi surface consists of three separated pockets. With increasing Fermi energy, these three pockets connect, and the Fermi surface becomes annular. When increasing the Fermi energy further, the Fermi surface is fully connected (Figure 2.5b). In the conduction band, where the center cone is very prominent at $U = 0$ meV (see Figure 2.4c), the center cone also becomes less prominent with increasing U. However, the center cone is still dominating at intermediate U and the band consequently becomes flatter until it is almost completely flat at approximately $U \approx 60$ meV. Only above this value, the low-energy Fermi surface consists of three pockets that transform into a single, annular Fermi surface and into a fully connected Fermi surface with increasing E.

In summary, the Fermi surface of bilayer graphene undergoes different topological transitions when the Fermi energy or the interlayer asymmetry is changed. Such topological transitions of the Fermi surface are called Lifshitz transitions [96]. They come along with a diverging density of states which is shown in the following.

Density of states:

The density of states (DOS) is defined as the number of available states at a particular energy level E

$$\mathrm{DOS}(E) = \frac{dn}{dE} = \frac{dn}{dk}\frac{dk}{dE}\,. \tag{16}$$

The DOS exhibits a singularity and diverges when $dk/dE \to \infty$, which is for example the case of flat bands or when the Fermi topology exhibits abrupt changes. The latter is called a *van Hove singularity* in the DOS.

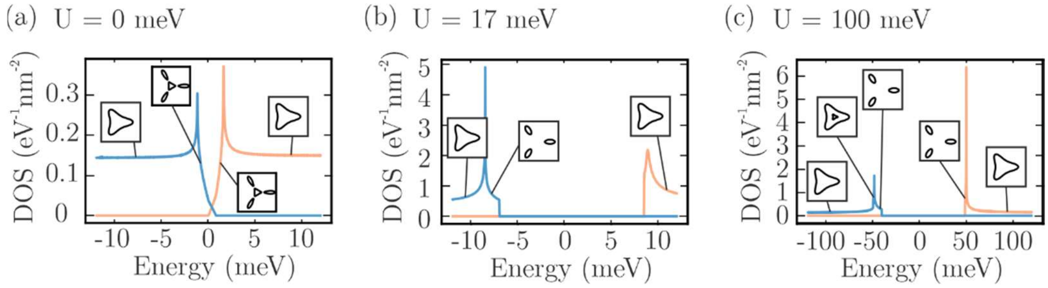

Figure 2.6. Density of states in bilayer graphene. Density of states plotted as a function of the Fermi energy for $U = 0$ meV (a), $U = 17$ meV (b) and $U = 100$ meV (c) in blue for the valence band and in orange for the conduction band. Insets show schematics of the corresponding Fermi surface. The calculations of the DOS were performed by Nils Jacobsen.

The evolution of the DOS as a function of the Fermi energy in Bernal bilayer graphene is shown in Figure 2.6 for different applied electric displacement fields. Note that due to the use of finite step sizes in the energy, the simulated DOS shown in Figure 2.6 does not actually diverge. Nevertheless, the DOS exhibits strong peaks when a Lifshitz transition occurs. At $U = 0$ (Figure 2.6a), the DOS near the Lifshitz transitions is relatively small compared to the DOS near the Lifshitz transition in lightly hole-doped bilayer graphene at $U = 17$ meV (Figure 2.6b). At $U = 100$ meV (Figure 2.6c), the DOS in electron-doped bilayer graphene becomes even larger at the band edge where the energy bands are almost flat (more details are given in Chapter 7).

Connection between the layer and valley degree of freedom:

In mono- and unbiased bilayer graphene ($U = 0$ meV), the valley and pseudospin degree of freedom are linked to the momentum which is known as chiral symmetry (see Section 2.1.1). In low-energy bilayer graphene, the pseudospin degree of freedom is also connected to the layer degree of freedom. In fact, electrons or holes in bilayer graphene are localized on the two non-dimer sites in opposite layers. It is worth noting that this result is used above for implementing the two-band model Hamiltonian (Equation (10)). It further leads to bilayer graphene's valley contrasting Berry phase of $\pm 2\pi$. [37]

When a band gap is electrostatically opened in bilayer graphene, an imbalance between the two graphene layers is created. Then, the inversion symmetry and thus also the chiral symmetry is broken. [26] In this case, low-energy electrons or holes are polarized into one of the two layers. Since the layer and pseudospin degree of freedom are still connected, the pseudospin degree of freedom is broken, too, and electrons "live" on one sublattice. When $U > 0$, electrons are polarized to the bottom layer and sublattice A and holes to the top layer and sublattice B. [26, 97, 98]

2.3 Landau level quantization and quantum Hall effect in a two-dimensional electron gas

At perpendicular applied magnetic fields, low temperatures and in a 2D electron gas (2DEG), the energy bands of conductors are reconstructed. Charge carriers moving through the conductor are then deflected by the Lorentz force perpendicular to their original direction of movement and are consequently forced into circular orbits. The Hamiltonian of such a system can be written as

$$\mathcal{H} = \frac{1}{2m}(\boldsymbol{p} + e\boldsymbol{A})^2 = \frac{1}{2m}\left(p_x^2 + (p_y + eBx)^2\right) \tag{17}$$

when charge carriers with momentum $\boldsymbol{p}$ and mass m are chosen to be confined in the x-y-plane and the magnetic field B is applied in the z-direction (the vector potential $\boldsymbol{A}$ describing the magnetic field can then be written as $\boldsymbol{A} = xB\hat{y}$). When using that this Hamiltonian is translationally invariant in the y-direction and choosing the right Ansatz for the energy eigenstates one can see that it resembles the Hamiltonian of a harmonic oscillator in x-direction. This leads to energy eigenvalues of

$$E_N = \left(N + \frac{1}{2}\right)\hbar\omega_c \tag{18}$$

with N = 0, 1, 2, …, cyclotron frequency $\omega_c = eB/m$. [99]

Thus, the energy of particles that are confined in 2D and move in a perpendicular applied magnetic field is quantized and independent of the momentum [99, 100]. The degeneracy of each energy level that is referred to as Landau level is given by

$$g = \frac{eB}{h} \tag{19}$$

when excluding spin and valley degeneracies of freedom [100, 101]. According to Equation (18) the Landau levels are equally spaced in energy whereas their spacing depends on the cyclotron frequency and thus on the applied magnetic field. Therefore, increasing the magnetic field leads to an increase of the degeneracy.

2.3.1. Quantum Hall effect

At large magnetic fields, the Landau level quantization gives rise to a quantized Hall resistance. This effect is known as the quantum Hall effect and was first measured by Klaus von Klitzing et al. in 1980 [101]. The following section is based on References [99–101].

The deflection of charge carriers moving perpendicular to an applied magnetic field due to Lorentz force leads to an accumulation of charge carriers at the sample boundary. A so-called Hall voltage perpendicular to the electrical current and to the magnetic field builds up. This voltage, $\mathrm{V_H}$, can be written as

$$V_H = \frac{IB}{ned} \tag{20}$$

where I is the applied current, n the charge carrier density and d the thickness of the sample. The Hall resistance R_{xy} that can be measured across the sample is then given by

$$R_{xy} = \frac{V_H}{I} = \frac{B}{ned}\,. \tag{21}$$

In a 2D limit and considering the Landau level quantization discussed above, it becomes

$$R_{xy} = \frac{B}{ned} = \frac{B}{gNe} = \frac{\hbar}{e^2}\frac{1}{gN} = \frac{h}{e^2}\frac{1}{\nu} \tag{22}$$

where in the last step the filling factor $\nu = gN$ is introduced. Thus, the Hall resistance becomes quantized and only depends on the filling factor and the two fundamental constants e and $\hbar$. The filling factor can be tuned as a function of the applied magnetic field B and the charge carrier density n and can be written as

$$\nu = \frac{hn}{eB}\,. \tag{23}$$

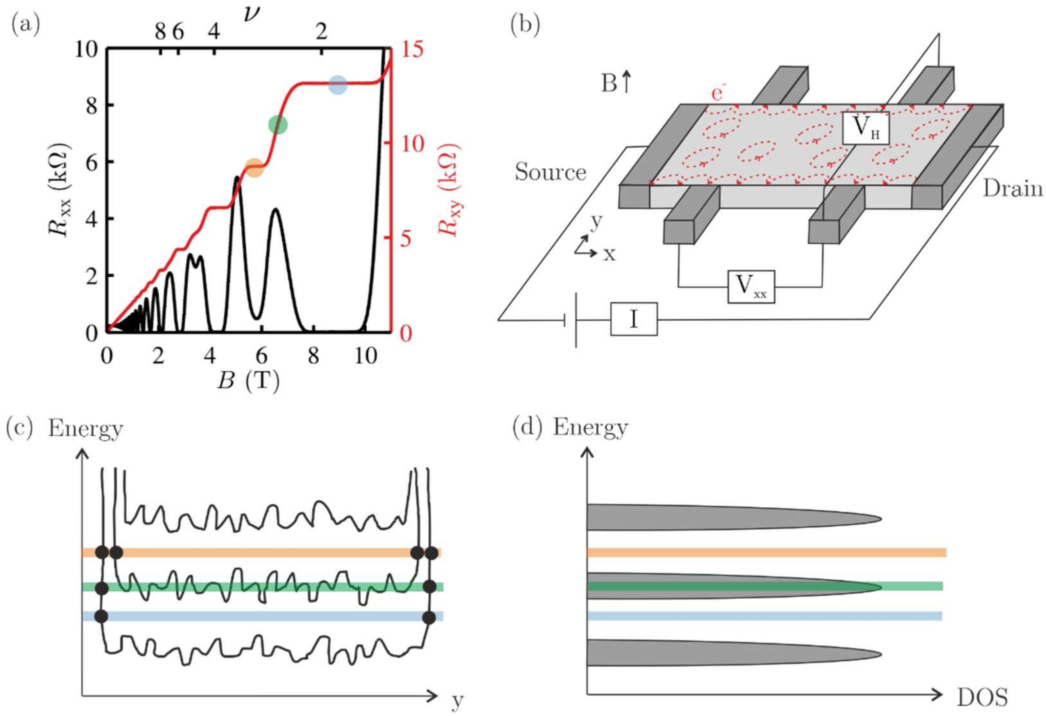

Figure 2.7. Quantum Hall effect. (a) Longitudinal resistance (R_{xx}, black) and Hall resistance (R_{xy}, red) as a function of the magnetic field in the quantum Hall regime. Image taken and adapted from Reference [102] under a Creative Commons Attribution-NonCommercial-ShareAlike 3.0 licence. (b) Schematic illustration of a Hall bar geometry and of the electron trajectories in the quantum Hall effect. In the center of the sample, charge carriers move in cyclotron orbits. Edge channels emerge at the sample boundary. The Hall voltage V_H can be measured across the sample while $V_{xx} = R_{xx}I$ can be measured in the longitudinal direction. (c) Energy spectrum of a 2DEG across the sample (in y-direction) at a finite magnetic field and low temperatures in the presence of disorder. At the edge of the sample, the spatial confinement leads to an increase in energy and to conducting edge channels (black dots). The position and number of edge channels depends on where the Fermi energy level lies. (d) Energy spectrum of a 2DEG as a function of the density of states (DOS) at a finite magnetic field and low temperatures in the presence of disorder. The Landau peaks are broadened. The blue, green and orange lines/ circles shown in (a), (c) and (d) correspond to different Fermi energy levels/ filling factors and should illustrate how they connect. For example, when the Fermi energy sits in between two Landau levels (blue line in (c), (d)), R_{xy} is quantized and $R_{xx} = 0$ (a).

To understand the formation of the famous quantum Hall plateaus shown in Figure 2.7a, it is necessary to include finite-sized samples and disorder into the model. In a semi-classical picture, charge carriers cannot perform closed cyclotron orbits at the sample edges. Instead, they get reflected as shown in Figure 2.7b and form conducting channels on both sides of the sample in which the charge carriers move in opposite directions. No current can flow in the bulk. The conducting channels are also referred to as edge states. Backscattering between the conducting channels is suppressed since charge carriers with opposite chirality are spatially separated.

The energy of the Landau levels then depends on the sample space: at the edge of the sample, the Landau levels bend upwards due to the confining potential imposed by the boundary of the sample. Disorder, that is always present in real samples due to finite sample sizes and finite temperature, can be accounted for by adding a random energy potential (Figure 2.7c) and leads to an energetic broadening of Landau levels (Figure 2.7d).

If the Fermi energy lies in between two Landau levels, edge channels at the sample boundary emerge. Current can flow ballistically along these channels and R_{xx}, the resistance measured in direction of the applied current flow that is constant in a classical limit, vanishes. As backscattering between the edges is suppressed, R_{xy} remains constant. The filling factor is given by the number of edge channels. If the Fermi energy level is increased and lies within a Landau level, transport between the sample edges can take place and R_{xy} jumps by 1 h/e^2. Since backscattering is now possible, R_{xx} becomes finite (see Figure 2.7a).

A Hall bar geometry, as shown in Figure 2.7b, allows to measure R_{xx} and R_{xx} independently. This is not the case if a device exhibits two terminal contacts that go across the entire sample, e.g., when it exhibits only one source and one drain contact. Then, the overall resistance is given by

$$R_{SD} = \frac{1}{\sqrt{R_{xx}^2 + R_{xy}^2}} \tag{24}$$

[103].

2.3.2. Landau level degeneracies and quantum Hall effect in bilayer graphene

Bilayer graphene exhibits a unique series of quantum Hall states due to its valley and spin degree of freedom and Berry phase of 2π that lead to a four-fold degeneracy of quantum Hall states [15, 37, 104]. In addition, the Fermi surface topology can alter the degeneracy of quantum Hall states. For example, it was shown that at large interlayer asymmetries, quantum Hall states in bilayer graphene exhibit an additional three-fold degeneracy due to the presence of three pockets [105, 106]. However, as discussed in Chapter 2.2, bilayer graphene exhibits a complex band structure close to its band edge even without applied interlayer asymmetry. A reordering of quantum Hall states in this regime was first seen during course of this thesis and is discussed in Chapter 5.

When large magnetic fields are applied (the magnitude of the magnetic fields needed depends on applied the interlayer asymmetry), the cyclotron orbits of electrons are too large to resolve the different pockets. In this regime, the band structure of bilayer graphene can be described by nearly parabolic bands that lead to the formation of Landau levels with energy

$$E = \hbar\omega_c\sqrt{N(N-1)} \tag{25}$$

with N = 0, 1, 2, … [37, 104]. As the energy of the Landau level with zero energy (N = 0) equals the energy of the first Landau level (N = 1), the lowest Landau level exhibits an additional two-fold degeneracy. This additional degeneracy is called orbital degeneracy. Thus, at sufficient high magnetic fields or when the Fermi energy level is set far enough away from the band edge, R_{xy} in bilayer graphene shows plateaus at filling factors $\nu = \pm 4, \pm 8, \pm 12, \ldots$ due to spin and valley degeneracy but no plateau at $\nu = 0$ as the lowest Landau Level exhibits an additional orbital degeneracy and is split between electron and holes [104].

2.4 Exchange interaction

The theory discussed in the previous sections is based on a single-particle picture, meaning that no interaction between charge carriers is introduced. However, under certain circumstances i.e., when the Coulomb energy, E_{C}, becomes much larger than the kinetic energy E_{kin}, the single-particle picture breaks down and several quantum phenomena can appear.

To quantify the importance of electron-electron interaction one can introduce the dimensionless Wigner-Seitz radius r_s as

$$r_s = \frac{E_C}{E_{\mathrm{kin}}} \tag{26}$$

with an estimated Coulomb energy E_{C} of

$$E_{\mathrm{C}} = \frac{e^2\sqrt{n}}{4\pi\varepsilon_0\varepsilon_r} \tag{27}$$

and a kinetic energy E_{kin} of

$$E_{\mathrm{kin}} = \frac{1}{n}\int\limits_{E<E_F} [E_{\mathrm{M}} - E_{\boldsymbol{k}}]\frac{d^2\boldsymbol{k}}{(2\pi)^2} \tag{28}$$

whereas ε_r is a material-specific dielectric constant that reduces the strength of Coulomb interactions, E_k is the band energy at momentum $\mathbf{k}$, and E_{M} is the valence band energy maximum/ the conduction band energy minimum [2, 5].

In a semi-classical picture, the influence of the kinetic energy and thus by the band dispersion can be accounted for by introducing the effective mass that is defined as

$$(m^*)^{-1} = \frac{1}{\hbar^2}\frac{\partial^2 E}{\partial k^2} \tag{29}$$

[5]. The kinetic energy (Equation (28)) then becomes

$$E_{kin} = \frac{\pi \hbar^2 n}{2m^*} \tag{30}$$

and r_s can be written as

$$r_s = \frac{e^2}{2\pi^2 \varepsilon_0 \hbar^2} \frac{m^*}{\varepsilon_r \sqrt{n}} \,. \tag{31}$$

Thus, when the energy band is homogenous, r_s is largest in vacuum where $\varepsilon_r = 1$ and when the charge carrier density is small, i.e. the Fermi energy level lies in the vicinity of the band edge [107].

Moreover, r_s diverges when the energy dispersion exhibits minima, maxima or saddle points and $\partial^2 E/\partial k^2$ goes down to zero. This is also case for Bernal bilayer graphene where several Lifshitz appear transitions that come along with saddle points in the energy dispersion (see Section 2.2). In this regime, the single-particle picture breaks down and electron-electron or hole-hole interactions can lead to intriguing quantum phenomena. In the following parts of this chapter, the theoretical foundations of some possible correlated phenomena are introduced.

2.4.1. Broken symmetry quantum Hall states

One way of creating a large DOS in bilayer graphene is by cooling it down and applying a large out-of-plane magnetic field. In this regime, the electrons are confined into strongly degenerate Landau level and bilayer graphene exhibits an intriguing quantum Hall effect with four-fold degenerate Landau level due to spin and valley degeneracies and an eight-fold degenerate lowest Landau level due to an additional orbital degeneracy (Section 2.3.2). To lower the energy of the system, spontaneous symmetry breaking can occur which is known as quantum Hall ferromagnetism [108]. Thereby, energy gaps between states with opposite spin and/ or valley quantum number are created and the charge carriers become spin and/ or valley polarized. These energy gaps are much more pronounced for opposite spins than for opposite valleys which is schematically shown by the size of the gaps between Landau level shown in Figure 2.8 [108, 109]. Furthermore, also the orbital degeneracy is weakly lifted [28, 29, 109]. When the disorder within a sample is lower than these energy gaps, broken-symmetry quantum Hall states with all integer filling factors can be observed [28, 29, 109–111].

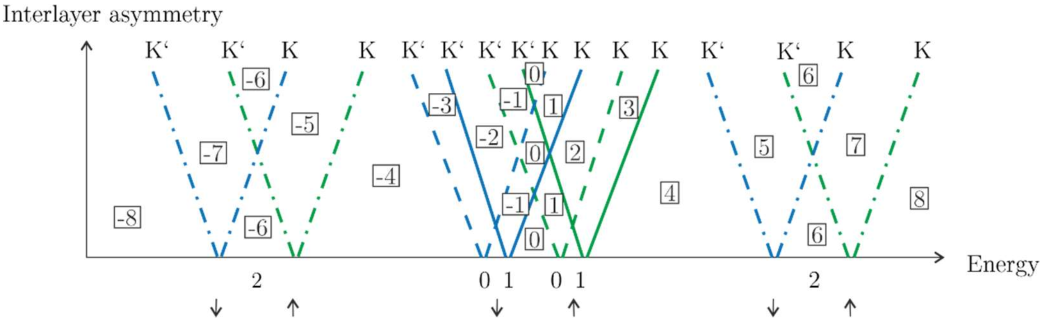

Figure 2.8 Schematic illustration of the evolution of Landau level with increasing interlayer asymmetry. Quantum Hall states are labeled by numerals in a box. Landau level of different spin are shown in green (spin up, arrow pointing up) and blue (spin down, arrow pointing down). Landau level with orbital index N=0 are shown by dashed lines, Landau level with orbital index N=1 are shown by solid lines and Landau level with orbital index N=2 are shown by dotted dashed lines. With increasing interlayer asymmetry, states with valley index K then are shifted up in energy while states with valley index K' are shifted down.

In bilayer graphene, charge carriers not only become valley polarized when the magnetic field is increased but also when an interlayer asymmetry is applied. Thereby, charge carrier are pushed into one of the two layers breaking the valley degree of freedom [28]. Also the orbital degeneracy of freedom is then slightly lifted [28].

The different dependences of the spin, valley, and orbital degeneracy of freedom on the magnetic field and the interlayer asymmetry result in many Landau level crossings. They are schematically shown in

Figure 2.8. In a regime where Landau levels cross, R_{xy} is not quantized anymore and R_{xx} does not vanish [29, 111].

2.4.2. Stoner ferromagnetism

According to the Stoner model of ferromagnetism that was proposed by Edmund Stoner in the 1930s, the interaction of charge carriers can also lead to spontaneous symmetry breaking and concomitant spin and valley polarization when no external magnetic field is applied. In case of a spin polarization, this leads to a change in energy of electrons with spin up and spin down compared to the energy of electrons defined in Equation (27) and Equation (28) where no electron spin is considered, i.e.

$$\Delta E_\uparrow = -\, c \cdot \frac{N_\uparrow - N_\downarrow}{N} \tag{32}$$

and

$$\Delta E_\downarrow = c \cdot \frac{N_\uparrow - N_\downarrow}{N} \tag{33}$$

with constant c and total number of electrons N of which $N_\uparrow$ have spin up and $N_\downarrow$ spin down. [3, 6] The overall energy is minimized and spontaneous spin polarization is possible when the so-called Stoner criterion

$$\frac{1}{2}\, U_E\ DOS(E_F) > 1 \tag{34}$$

is fulfilled (the derivation of the Stoner criterion can be found in References [3, 6]). When deriving the Stoner criterion, it is considered that the spin polarization leads to a magnetization

$$M_A \sim -\, \mu_0\ (N_\uparrow - N_\downarrow) \tag{35}$$

with μ_0 being the magnetic permeability. The energy density U_E, also known as Stoner exchange parameter, parameterizes the magnetic energy that is gained due to the exchange interaction of two electrons with parallel spins and is proportional to c. U_E can then be derived as

$$U_E = \frac{1}{2}\mu_0 \mu_B^2 \tag{36}$$

with μ_B being the Bohr magneton.

Since U_E is constant in bilayer graphene, the DOS needs to be large for the Stoner criterion to be fulfilled. This is for example the case in the vicinity of Lifshitz transitions that come along with van Hove singularities in the DOS. It is then more favorable for the system to create an imbalance of electrons with spin up and spin down whereby the system becomes magnetic. While the Stoner criterion was first derived by describing the energy difference between particles with opposite spin it also holds for other quantum numbers such as for particles in opposite valleys [25].

In experiment, one can detect Stoner magnetism by measuring the magnetic field, for example via a superconducting quantum interference device (SQUID) [112]. Furthermore, Stoner magnetism can be observed when tracing down quantum Hall oscillations. While at low magnetic fields quantum Hall states in bilayer or trilayer graphene would normally exhibit a four-fold degeneracy due to spin and valley degeneracies, quantum Hall states within a spin or valley polarized Stoner "half metal phase" are two-fold degenerate. Quantum Hall states within a spin and valley polarized Stoner "quarter metal phase" are fully polarized and non-degenerate. [25]

2.4.3. Strange metals

Apart from Stoner metals, there are other kinds of correlated metals such as strange metals that are metallic phases that do not obey Landau's Fermi liquid theory [113].

According to Landau's Fermi liquid theory, interacting electrons in a metal can be described by quasiparticles that behave like nearly free electrons and carry an effective mass m^* that incorporates all interaction effects. At low temperatures T, where electron-electron scattering dominates over electron-phonon scattering, the resistivity ρ of metals can then be described as

$$\rho(T) = \rho_0 + AT^2 \tag{37}$$

with A being a constant that is proportional to $(m^*)^2$ and ρ_0 accounting for a saturation of the resistance at low temperatures where quantized lattice vibrations freeze out. Thus, the resistivity scales quadratically with temperature. [114, 115]

In strange metals, such as in hole-doped cuprates [116] or in magic-angle twisted bilayer graphene [18], the resistivity, however, increases linearly with temperature T over a wide temperature range. This linear increase can be directly linked to the Planck constant h and the Boltzmann constant k_B via

$$\rho = \frac{m^*}{ne^2}\frac{1}{\tau} \tag{38}$$

with a universal scattering rate

$$\frac{1}{\tau} = \frac{k_B T}{h/2\pi} \tag{39}$$

[18, 113, 117]. Thermal vibrations of the underlying lattice that freeze out at low temperatures seem to be not relevant anymore indicating that the single-particle picture breaks down due to strong correlation effects [113].

Another interesting aspect of strange metals is that they often appear together with high-temperature superconductivity [113, 118]. However, a theoretical explanation for strange metal behavior is still under investigation and it is not yet proven that these two phenomena are fundamentally linked [113, 117].

2.4.4. Correlated insulators

Another kind of correlation effect that can occur when $r_s \gg 1$, is the formation of correlated insulators in which the hopping of electrons is suppressed and electrons start to localize whereby the energy bands split and an energy gap opens. At low temperatures and low disorder, the system then becomes insulating. There are various kinds of correlated insulators that each exhibit different electronic orderings. Some of them are briefly introduced below:

Mott insulators:

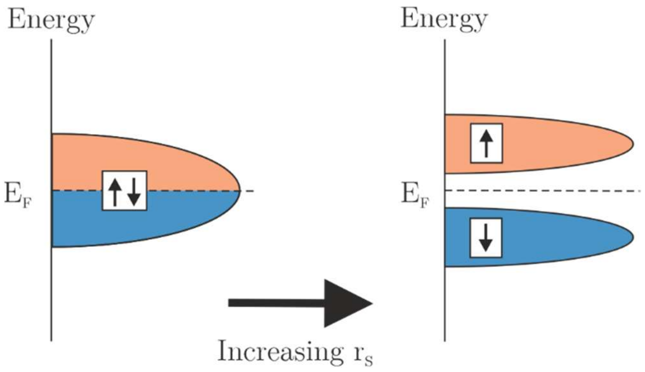

Figure 2.9 Schematic diagram of a Mott insulator. The energy band splits when r_s is increased. The dashed lines mark the position of the Fermi energy level E_F.

A Mott insulating state can occur in crystalline systems in which electrons hop between different lattice sites' whereas the lattice can be an atomic lattice [119], an optical lattice [120] or a superlattice potential [16]. According to the Pauli exclusion principle, each lattice site can be occupied by two electrons, for example by two electrons of different spin (it can be occupied by more than two electrons when the system exhibits additional degeneracies such as a valley degeneracy [16]). If the interactions are strong and the potential energy exceeds the kinetic energy of the system ($r_s > 1$), such double occupancy is forbidden due to Coulomb repulsion. At half filling, when there is one electron per lattice site, hopping of electrons is then not possible anymore. The electrons become localized, an energy gap opens up and the system becomes insulating when the Fermi energy level sits in the gap. [121–123] A schematic diagram of a Mott insulator is shown in Figure 2.9.

Charge density waves:

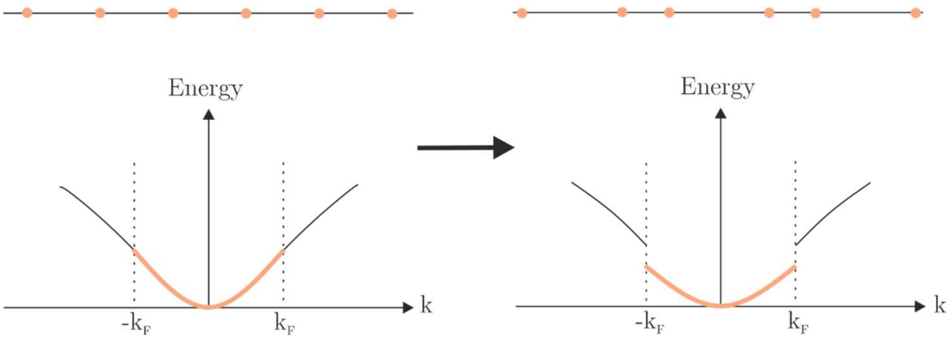

Figure 2.10 Schematic illustration of a charge density wave in one-dimension. The top panel shows electrons (orange) at their original position (left) and their new position corresponding to a periodic lattice distortion (right). The corresponding band structures are shown below. Filled bands are shown in orange, empty bands in black. Adapted from Reference [124].

A charge density wave is a periodic modulation of the charge density that arises due to electron-electron or electron-phonon interactions and is often accompanied by a periodic lattice distortion known as Peierls instability [125]. The periodicity can either be a multiple of the underlying lattice constant (commensurate charge density waves) or can be unrelated to it (incommensurate charge density waves) [125, 126]. The redistribution of the charge density leads to a shift in the electron's energy and to a reconstruction of the energy bands near the Fermi surface [125].

This can be visualized best in the one-dimensional (1D) case which is shown in Figure 2.10. Here, the top left panel shows a 1D chain of electrons that are equally spaced. Below, the corresponding half-filled energy band is sketched. When a periodic lattice distortion is created due to a Peierls instability (right panel of Figure 2.10), the charge density is modulated with a wavevector 2 k_F. The electrons exhibit a shift in their energy and an energy gap in the band is opened at ± k_F.

In 2D systems, the Fermi surface geometry is generally not favorable for Peierls instabilities, since it is often not planar, i.e. the Fermi surface contours do not coincide when they are shifted along a single wavevector. A single wavevector can then only displace certain sections of a Fermi surface which is known as Fermi surface nesting. Consequently, in 2D, a charge density wave usually only opens up a gap in small segments near specific points on the Fermi surface whereas the rest of the Fermi surface remains gapless [125].

In 2D, charge density waves cannot only occur due to Fermi surface nesting but also due to quantum fluctuations and excitonic insulator instabilities [125, 127]. Often it is not clear if the quantum phase transitions are driven by electron-phonon coupling or electron-electron interactions.

In analogion to charge density waves, there are also spin density waves which exhibit a real-space spin modulation.

Wigner crystals:

When the Coulomb energy much larger than the kinetic energy of a system ($r_s > 34$) electrons in 2D systems are predicted to spontaneously break translation symmetry and form an electronic crystal that is referred to as Wigner crystal [5, 9]. In this configuration, the electrons arrange themselves to minimize their energy and strongly localize [123, 128]. The exact structure of the Wigner crystal cannot be determined a priori [5].

This localization results in the opening of an energy band gap. Thus, Wigner crystals exhibit an insulating behavior that can be revealed by conductivity measurements [2, 129]. Recently, scanning tunneling microscopy was used to create the first real-space image of a Wigner crystal in a WSe_2/WS_2 moiré heterostructure [130].

When r_s is decreased, for example by decreasing the charge carrier density n (Equation (31)), the Wigner crystal melts, which means that the system then transitions into a different ground state. Similarly, melting of the Wigner crystal also takes place when the temperature is increased and the magnitude of thermal fluctuations exceeds the crystals lattice constant [131]. The crystal can then transition into a new correlated state such as a broken symmetry state (e.g. a spin-polarized liquid) or a CDW [5, 132, 133].

Correlated insulators with non-trivial band topology:

Every correlated insulator can in principle also exhibit a non-trivial band topology in which electrical current cannot flow in the bulk of the material (like in a topologically trivial insulator) but can flow on the sample edges [134]. The number of edge states is characterized by a finite Chern number $C \neq 0$ and manifests in a quantized resistance of

$$R_{xy} = \frac{1}{C}\frac{h}{e^2} \tag{40}$$

[3].

For example, topological Mott insulators [135, 136] as well as Wigner Hall crystals [137] have been theoretically predicted and a topological charge density wave was recently observed in twisted monolayer-bilayer graphene [138]. These states manifest in quantum anomalous Hall states, that are quantum Hall states that occur in the absence of externally applied magnetic fields due to spontaneously broken time-reversal symmetry [139].

Note that also quantum Hall states can be viewed as topological insulating states in which the Chern number C is given by the filling factor υ (see Section 2.3) [3].

2.5 Dual gated bilayer graphene field-effect transistors

In the previous sections, it is shown that the Fermi surface in bilayer graphene undergoes drastic changes when tuning the Fermi energy level. In experiment, the Fermi energy can be controlled via electrical gates [140, 141]. Applying a finite gate voltage creates an electrical field between the gate and one graphene layer and changes the charges carrier density n, the density of mobile electronic charges, in the bilayer graphene.

To probe the electronic properties of the bilayer graphene, one can utilize at least one source and one drain contact to the bilayer graphene flake and measure the current as a function of the gate voltage. Such configuration is called a graphene field-effect transistor and was first realized by Novoselov et al. in 2004 [140].

By applying a gate voltage, not only the charge carrier density is varied but also an electric displacement field across the two graphene sheets is created. To allow for an independent tuning of both, the electric displacement fields and the charge carrier density, dual-gated bilayer graphene heterostructures having a top as well as bottom gate electrode can be fabricated [28, 94]. While the electric displacement field allows to modify the band structure, tuning the charge carrier density allows to access the topologically different Fermi surfaces in the valence and conduction band and the band gap.

The total charge carrier density n is then given by the sum of the individual charge carrier density induced by the bottom gate n_B and by the top gate n_T and depends on the applied bottom gate and top gate voltages V_B and V_T and on the top and bottom gate capacitance per unite area C_B and C_T, respectively. It is defined as

$$n = n_B + n_T = \frac{C_B V_B + C_T V_T}{e}. \tag{41}$$

The gate capacitance per unit area depends on the dielectric constant in vacuum ε_0, the reduced dielectric constant of the dielectric material ε_r and the thickness of the dielectric d via

$$C_{B,T} = \frac{\varepsilon_0 \varepsilon_r}{d_{B,T}}. \tag{42}$$

B and T refer to the bottom (top) gate respectively. It is assumed that the same dielectric material is used as a top and bottom gate dielectric. The electric displacement field D is defined as

$$D = \frac{1}{2}(D_T + D_B) = \left(\frac{V_T \varepsilon_r}{d_T} - \frac{V_B \varepsilon_r}{d_B}\right) \tag{43}$$

whereby the factor of 1/2 results from the fact that the net displacement field is an average of the displacement field coming from the bottom gate/ top gate alone [94].

It is worth noting that these definitions of n and D are the standard definition used in the graphene community. n, as defined above, is not the real charge carrier density but the charge carrier density in case of a truly parabolic band structure and changes in the DOS are not considered [142]. D is often also called electric field E (for example in References [28, 33, 34] and also in Reference [1] that is reprinted in Chapter 6) or D/ε_0 (see for example Reference [98]) whereas the definition given in Equation (43) remains the same.

The equations for n (Equation (41)) and D (Equation (43)) are linearly independent, meaning that any choice of top and bottom gate voltages results in unique values for n and D. [28, 94]

Following the line of argumentation given in Section 2.1.4, hBN was used as a dielectric material for both layers. In all heterostructures, graphite was used as a bottom gate material and, in most heterostructures, also as a top gate material (for one heterostructure gold was used as a top gate). Source and drain contacts were fabricated out of graphite flakes or gold. Schematic illustrations of a typical 2D heterostructures are shown in the next chapter (Figure 3.1) where the methods needed to fabricate and characterize these devices are introduced.

3 Fabrication of bilayer graphene heterostructures

To observe low-energy band structure effects and interaction-driven phenomena in Bernal bilayer graphene, it is crucial to have high-quality devices. It is well known that the highest quality bilayer graphene flakes can be obtained by mechanical exfoliation [143] which was also used to obtain the graphene, hBN and graphite flakes used during the course of this thesis (Section 3.1). To build bilayer graphene field-effect transistors, the exfoliated flakes were then combined to delicate 2D heterostructures. Thereby, I spent much time on improving the fabrication process of these heterostructures as well as their quality. More specifically, I optimized the process of transferring exfoliated flakes by identifying selection criteria for choosing the right flakes to start with (Section 3.2) and by modifying the transfer setup as well as the stamping routines (Section 3.3). Furthermore, I implemented graphite flakes as an alternative contact material into some of my heterostructures that allow to contact the bilayer graphene flakes without etching into the insulating hBN layers, which is usually required for metal contacting (Section 3.4) and lowers the accessible electric displacement field range which are discussed in detail in Chapter 4.

Schematics of the bilayer graphene heterostructures before metal contacting are shown in Figure 3.1. An overview of all fabricated devices that are used for the results part of this thesis is given in Section 3.5.

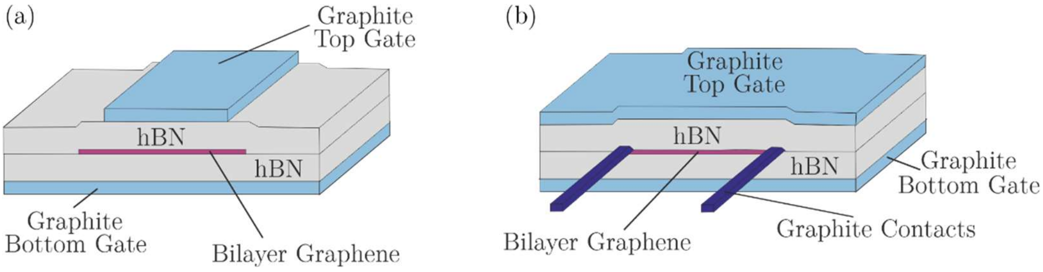

Figure 3.1. Bilayer graphene heterostructures. Schematic illustration of bilayer graphene heterostructures fabricated within this thesis without (a) and with graphite contacts (b). The heterostructures are shown without the metal contacts. The heterostructure without graphite contacts exhibit a local top gate while the other one exhibits a global top gate (see Section 4.5 for the corresponding discussion).

3.1 Mechanical exfoliation of two-dimensional materials

As mentioned in Section 2.1, layered 2D materials are typically held together by strong covalent in-plane bonds and weaker van der Waals forces between adjacent layers. Therefore, single or few layers can easily be peeled off from a bulk crystal. Mechanical exfoliation is used to cleave thin layers of graphene and hBN using commercially available adhesive tape. This method reliably gives flakes up to 100 × 100 μm^2 in size and is known to yield the highest quality flakes as it does not introduce dopants or residual chemicals [144].

Depending on the desired flakes, different tapes and crystals are used. To obtain thin layers of graphene, e.g., bilayer graphene flakes, a highly pyrolytic graphite crystal (Momentive Performance Materials Inc.) is first stuck onto a piece of tape (Magic Tape, Scotch) and is peeled off afterwards. A thin layer of the graphite crystal then remains on the tape. This piece of tape is repeatedly stuck onto and peeled off from a new piece of tape to further thin the graphite. After repeating this process three to four times, the tape is placed on a 130 °C preheated silicon wafer with a 300 nm thick layer of Silicon dioxide (SiO_2) on top. The tape is then slightly pressed onto the wafer and is retracted after approximately 20 s. Afterwards, the wafer is randomly covered by (multilayer) graphene and graphite flakes of different sizes.

On average, larger but thicker flakes are needed to fabricate graphite gates and contacts. Such flakes are obtained by using a natural graphite crystal (Natural graphite, HQ Graphene) instead of a highly pyrolytic graphite crystal. The rest of the exfoliation procedure then remains the same.

hBN bulk crystals are obtained by K. Watanabe and T. Taniguchi (National Institute for Materials Science) [145] and flakes are exfoliated using different tape (SWT20+, Nitto inc.). After placing an hBN crystal on a piece of tape, the tape is folded and unfolded 18 to 20 times to crush and thin down the crystal. It is placed on another preheated wafer (same wafer preparation as described above) and is pressed onto it for approximately 30 s. The wafer is then covered by multilayer hBN flakes of different thicknesses ranging from monolayers to 500 nm thickness.

3.2 Identification and characterization of suitable flakes

After exfoliating few-layer graphene and hBN flakes, components for bilayer graphene heterostructures are identified and selected using optical microscopy, Raman spectroscopy and atomic force microscopy. Suitable flakes are chosen regarding to their size, cleanliness, and homogeneity. All flakes should be free of dirt and wrinkles and should have not been in contact with chemicals to ensure that they are not contaminated. Furthermore, to allow for a successful pick-up during the transfer process (Section 3.3), care is taken that all flakes are located at least 100 µm away from other surrounding flakes, glue residuals stemming from exfoliation tape and the wafer edge.

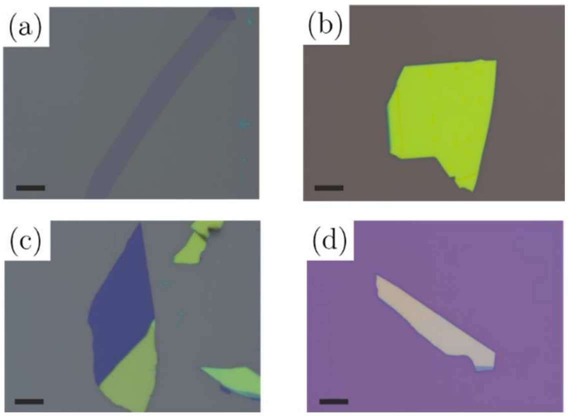

Figure 3.2 Optical microscopy images of preselected flakes. (a-d) Optical microscopy image of a preselected bilayer graphene flake (a), a preselcted hBN flake later serving as a bottom gate dielectric (b), a preselected graphite gate later serving as a bottom gate (c) and a preselected graphite gate later serving as a graphite contact (d). The scalebar is 10 µm in each image. The flakes shown in (a)-(c) were used to assemble Stack 70 (see Section 3.5), the graphite flake shown in (d) was embedded into the device measured in Reference [146].

First, bilayer graphene flakes are identified via optical microscopy and Raman spectroscopy (the corresponding methods are described below). To allow for successful alignment when building the heterostructures, flakes with lateral dimensions of at least 2 µm x 6 µm are chosen. Since the bilayer graphene flakes are the centerpiece of the heterostructures, it is always ensured that they are truly homogeneous, especially also at the edge of the flakes, which could be verified best by atomic force microscopy.

hBN flakes, later serving as dielectrics, are always chosen to be larger than the bilayer graphene flakes (at least in 1D) to achieve full encapsulation. Their thickness should be uniform within a flake (especially within the region that later covers the bilayer graphene flake) and is varied from 5 nm to 80 nm for different heterostructures. This range of thicknesses allows for an easy optical identification of the flakes and the flakes can be picked up safely during the subsequent transfer process. If the thickness of the hBN flakes determines the electronic properties of the heterostructure demands further investigation (see Chapter 8.2.1).

Graphite gates are chosen to be larger than the bilayer graphene flake to enable a full covering of the bilayer graphene. Moreover, the graphite gates are chosen to be smaller than the hBN flakes to electrically isolate the bilayer graphene flake and its contacts from the gates.

To ensure that the gates are conducting well, the graphite flakes are chosen to be thicker than ten layers but thinner than 40 nm (which corresponds to more than 100 layers) to allow for a successful pick-up during the transfer process. The last point also holds for graphite flakes serving as contacts that are embedded into some of the 2D heterostructures. Here, at least two long and narrow graphite flakes of at least 30 µm x 3 µm are chosen for each heterostructure. Flakes with these dimensions are easy to pick up and are usually sticking out of the hBN flakes allowing for an easy contacting procedure (see Section 3.4).

The properties discussed above are determined using the following set of techniques:

Optical microscopy:

Monolayer graphene, located on doped Si substrates coated with 300 nm of SiO_2, absorbs 3.7 % of incident white light whereas the absorbance linearly increases with the layer number [147]. Thus, even a single layer of graphene gives sufficient contrast to allow for optical detection of few-micrometer sized areas when using the magnification range of an optical microscope. Also hBN exhibits a thickness dependent contrast, although single layers, exhibiting an contrast of less than 1.5 % on Si substrates coated with 300 nm of SiO_2, are more difficult to detect [148, 149].

In this work, a reflected light microscope (Axio Scope.A1, Carl Zeiss Microscopy) is used in bright field mode. First, the substrates are quickly scanned using a 10x magnification (EC Epiplan 10x, Carl Zeiss Microscopy) to detect and preselect few-layer graphene, graphite and hBN flakes. Afterwards, a 100x magnification objective (LD EC Epiplan-Neofluar 100x, Carl Zeiss Microscopy) is used to determine the flakes' size, to identify dirt, winkles or large-scale inhomogeneities and to estimate the flakes' layer number from its optical contrast [147].

In Figure 3.2, optical microscopy images of a preselected bilayer graphene flake (Figure 3.2a), a preselected hBN (Figure 3.2b), a preselected graphite gate (Figure 3.2c) and a preselected Graphite contact (Figure 3.2d) are shown.

Raman spectroscopy:

To unambiguously distinguish bilayer graphene from monolayer or trilayer graphene which exhibit similar contrasts, Raman spectroscopy is used. Thereby, laser light is focused onto the sample where it interacts with phonons before it is inelastically scattered back to a detector. During this process, the energy of the incident photons changes whereas the change in energy can be detected. The difference between the incident and scattered photon energy is often referred to as Raman shift. [150]

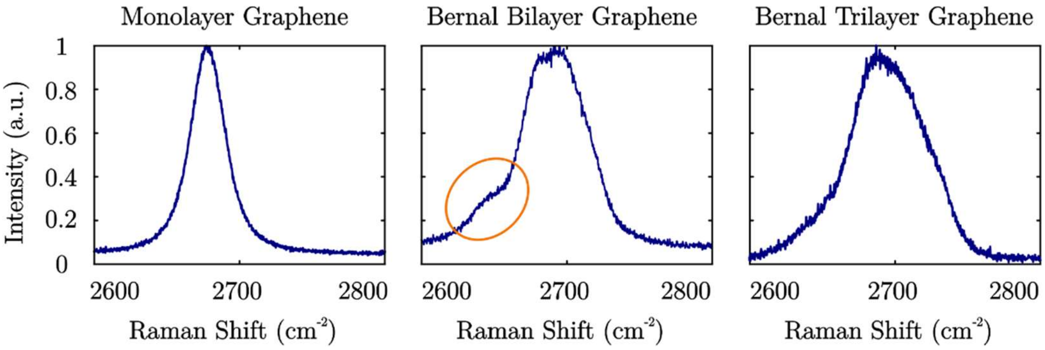

Figure 3.3. Normalized Raman spectra of the 2D peak of a monolayer, a Bernal bilayer and a Bernal trilayer graphene flake. The Raman spectrum shown in the middle is taken from the bilayer graphene flake shown in Figure 3.2a. On the left-hand side of this spectrum, the 2D peak exhibits a shoulder that is marked by an orange circle.

Monolayer graphene exhibits multiple peaks in its Raman spectrum including a prominent 2D peak at around 2700 cm^{-1} that is associated with a double-resonant process near the K-points and involves two phonons with opposite momentum in the highest optical branch. An example of a 2D peak of a monolayer graphene flake is shown in the left panel of Figure 3.3. For this and the other presented Raman spectra an excitation wavelength of

532 nm and an incident laser power of 0.5 mW was used. The spectrum was collected using a spectrometer (iHR550, Horiba Scientific) with 1800 lines per millimeter grating. In multilayer graphene, the 2D peak splits into several overlapping modes resulting in a distinct shape that varies for different numbers of layers. In bilayer graphene, the four components of the 2D peak result in a broadening of the peak and cause the peak to shift to higher wave numbers. Furthermore, the 2D peak of bilayer graphene exhibits a unique shoulder on the left-hand side of the primary peak that vanishes for higher layer numbers as shown in the middle and right panel of Figure 3.3, respectively. In the middle panel, showing the Raman spectrum of a bilayer graphene flake, the shoulder on the left-hand side of the primary peak is highlighted. [150–152]

Atomic force microscopy:

Atomic force microscopy (AFM) is used to determine the homogeneity of all flakes and the height of graphite and hBN flakes with sub-nanometer resolution. When the AFM is operated in the so-called tapping mode, an oscillating tip is brought close to the surface of a sample and performs a lateral line scan. Due to interactions with the surface, topographic changes in the sample lead to a change in the oscillation amplitude of the tip. A feedback loop then adjusts the height of the tip to keep the oscillation amplitude of the tip constant whereby a topographic map of the sample is obtained. [153]

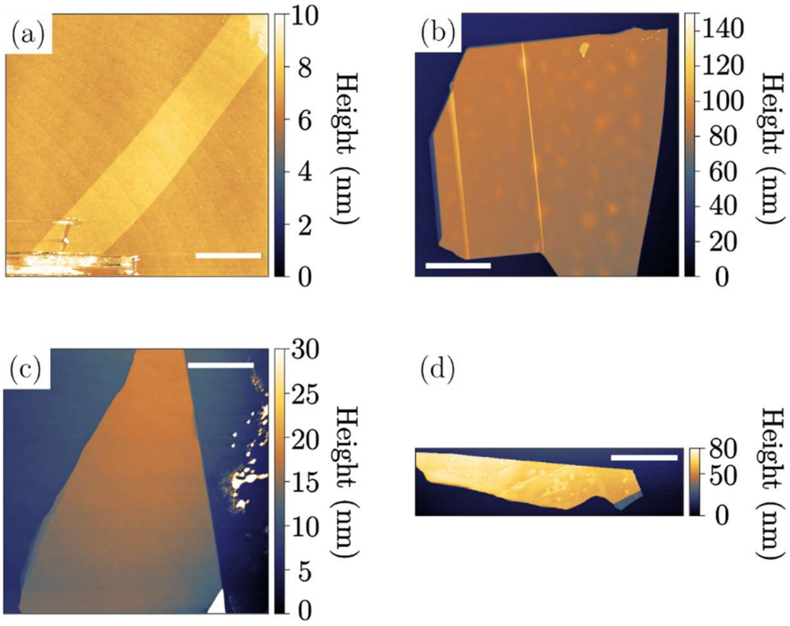

Figure 3.4. Atomic force microscopy images of preselected flakes. Atomic force Microscopy (AFM) images of the bilayer graphene flake (a), hBN flake serving as a bottom gate dielectric (b), graphite flake serving as a bottom gate (c) and graphite flake serving as a contact (d) shown in Figure 3.2. The scalebar is 10 µm in each image. The bilayer graphene flake shown in (a) broke while taking the AFM image (this can be seen in the bottom of the image). Since it was still large enough, the remaining part of the flake was still functional for building a bilayer graphene heterostructure. The hBN flake shown in (b) exhibits two wrinkles (vertical lines) that were not seen in the optical microscope image. While designing the bilayer graphene heterostructure Stack 70 (see Section 3.5), care was taken that the bilayer graphene flake was not placed directly on top of these wrinkles.

AFM is not only used to determine the height and homogeneity of exfoliated flakes on silicon/ silicon dioxide substrates (see for example Figure 3.4) but also to further characterize bilayer graphene heterostructures after fabrication. It is worth noting that AFM is not suitable to determine the layer number of graphene of few-layer hBN flakes as there is often water or air trapped between the flakes and wafer that increases the measured height of the flakes [154].

3.3 Transferring flakes and building van der Waals heterostructures

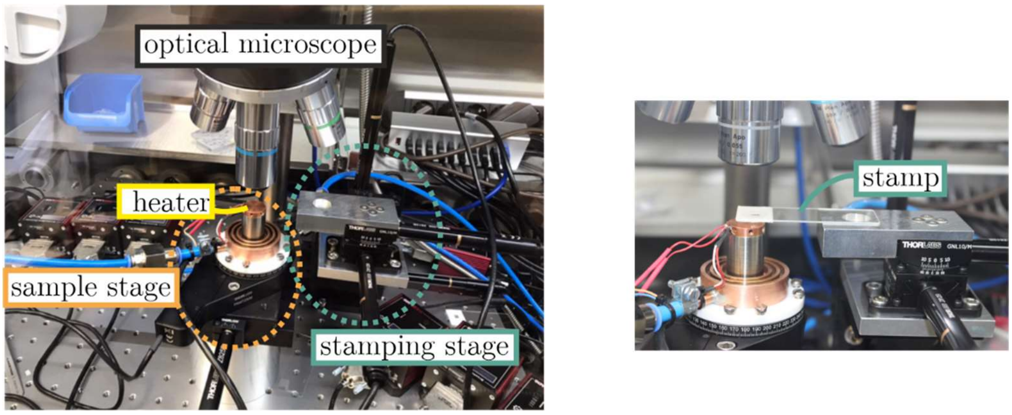

Figure 3.5. Stamping setup. Pictures of one of the stamping setups that is located in a glovebox. The stamping stage, the sample stage, the heater and the optical microscope are labeled. A zoom-in in the right panel shows a stamp that is located on the stamping stamp, this picture was taken by Christian Eckel.

A stamping technique [155–158] is employed to successively pick up the selected flakes using one out of two home-made "stamping setups". These setups contain an optical microscope (FS70Z, Mitutoyo) with attached camera and objectives that provide long working distances of more than 20 mm (M Plan Apo 5x, 10x, 20x and 50x), a heater that is attached to a sample stage, and a stamping stage. Both, the sample and the stamping stage exhibit vacuum chucks that allow holding the stamp and the wafer, respectively. Micromanipulators and actuators are used to move the sample stage in x- and y- direction and the stamping stage in x-, y- and z-direction. The sample stage can further be rotated while the stamping stage can be tilted. The setups are placed on optical tables whereby vibrations are minimized. One setup operates in ambient conditions while the other one is located in an argon-filled glove box. The two setups are built in a similar way but the one located in the glovebox is controlled by motorized micromanipulators while the other one is controlled by manual ones to move the sample and the stamp in x- and y-direction. Pictures of the stamping setup in the glovebox are shown in Figure 3.5. This setup was designed and assembled by myself during the course of this thesis. As hBN, graphene and graphite are all stable in air, both setups are used to fabricate the bilayer graphene heterostructures. No setup-dependent differences in the quality of the heterostructures is noticed.

The heterostructures are usually designed in advance by superimposing optical microscopy images. Care is taken that the bilayer graphene is fully covered by the hBN flakes and by the bottom graphite gate (constrains on the top gate are discussed below). In addition, the bottom graphite gate is designed to stick out on one side of the heterostructure to make sure that it can be easily contacted (see Section 3.4.). In case graphite contacts are used, they are chosen to stick out of the top hBN flake for the same reason. Furthermore, attention is given that the gates and the graphite contacts are separated by hBN flakes to prevent a gate leakage, and that the two graphite gates are always separated by both hBN flakes to decreases the chance of a dielectric breakthrough when large electric displacement fields are applied. In addition, straight edges of flakes lying on top of each other are intentionally misaligned to not create a moiré pattern that would change the electric properties of the bilayer graphene [71].

In the beginning of each stamping process, a stamp consisting of a block of polydimethylsiloxane (PDMS) used as a cushion layer, and a thin film of polycarbonate (PC) used as a transfer medium, is prepared.

The PDMS is prepared previously using commercially available kit (Sylgard 184, Dowsil) with a mass ratio of 1:10.5 between base and curing agent. After these two components are mixed, the emerging gel is cast into a petri dish at a height of 3 mm and is dried in vacuum for at least 72 h to remove bubbles. To prepare the PC film, PC (Poly(Bisphenol A carbonate), Sigma-Aldrich) is first dissolved in chloroform with a mass ratio of 1:12.5 and is stirred at room temperature for at least 24 h. Afterwards, a few drops of the PC solution are drop casted onto a film casting blade (ZUA 2000, Zehntner) with a set height of 1675 μm which is then moved across a glass slide with a speed of 6 mm/s leaving a thin and homogeneous film of PC on the glass slide. The film of PC on the glass slide is then dried in air for at least 1 h but for no more than one day.

The stamp is made by cutting out a window of 8 mm x 8 mm into a piece of double-sided adhesive tape which is glued onto a cleaned glass slide. Afterwards, a 5 mm x 5 mm large block of PDMS is cut and placed into the center of the window on the glass slide. A second piece of tape with a cut-out window of 8 mm x 8 mm is prepared and is used to pick up the previously prepared PC film. The PC film below the window is then placed on top of the PDMS block where it is hold by the surrounding tape. A picture of a stamp lying on the stamping stage of the stamping setup is shown in the right panel of Figure 3.5.

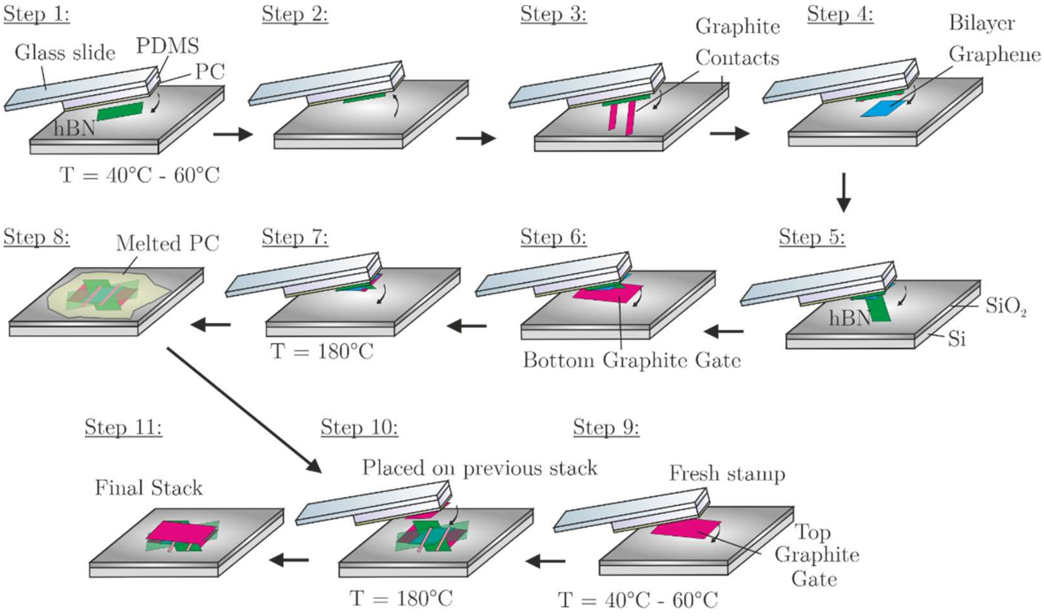

Figure 3.6 Stamping process. Schematic illustration of the stamping process. The third step only applies when graphite contacts are used. These contacts can either be picked up together from the same wafer as shown here or from different wafers. Adapted from Reference [157].

A schematic overview of the stamping technique that also includes a schematic illustration of a stamp is shown in Figure 3.6. A detailed step-by-step description is given at the end of this section and is based on optical images taken during the process of assembling Stack 70 that exhibits no graphite contacts and Stack 99 that exhibits two-terminal graphite contacts (see Figure 3.7 and Figure 3.8).

The flake on top of the 2D heterostructure are picked up first and the bottom flake last. As flakes lying below a graphite flake are only weakly visible, the upper hBN flake is usually picked up first (Step 1 and 2 in Figure 3.6), followed by the successive pick up of the two graphite contacts (if needed, Step 3 in Figure 3.6), a bilayer graphene flake (Step 4 in Figure 3.6), the lower hBN flake (Step 5 in Figure 3.6) and the lower graphite gate (Step 6 in Figure 3.6). The two graphite contacts are either picked up from different wafers in two steps or, if two parallel graphite flakes separated by approximately 5 µm - 10 µm are found on the same wafer, in one step. The top graphite gate is stamped on top of this heterostructure in a second stamping step using another stamp (Step 9-11 in Figure 3.6).

Before each transfer step, the wafer with the selected flake, e.g., the top hBN flake, is placed on the sample stage, heated to 40 °C, and the prepared stamp is placed on the stamping stage and tilted by approximately 1°. The stamp is then moved down until it touches the surface of the wafer. By moving the stamp further down, the contact area between stamp and wafer expands. When the contact line is approximately 50 µm away from the desired flake, the temperature of the hotplate is further increased to 60 °C within 2 min. Thereby, the stickiness of the PC increases, and the contact area expands further due to thermal expansion. When the hotplate reached 60 °C, the stamp is usually in touch with the desired flake. After waiting for one to two more minutes, the stamp is slightly moved upwards until the contact area between stamp and wafer starts to decrease. Then, the temperature of the hotplate is decreased back to 40 °C. The desired flake (and other flakes nearby) then stays on the stamp and detaches from the wafer. The optical transparency of the glass slide, the PDMS and the PC allows to monitor the entire process via the optical microscope and to locate the flake on the stamp. In a next step, the wafer is removed and a new wafer, e.g., a wafer with a desired graphite contact, is placed on the sample stage. The entire procedure is repeated whereas the new flake is picked up using the previously picked up flake. The flakes are aligned according the design made previously. If a flake does not stick to the stamp or to the previously picked up flakes, the process is repeated with higher temperatures of up 100 °C. While elevating the temperature increases the chance of picking up a flake, it also increases the chance for the stamp to break. For example, a common problem is that the PC film comes off from the block of PDMS.

Once all flakes are picked up, the PC film and the stack, can be melted onto an empty, precleaned wafer. To increase the stickiness of the wafer, the wafer is additionally exposed to an oxygen plasma which makes its surface more hydrophilic. For the melting process, the cleaned wafer is first placed on the sample stage which is heated to 160 °C. Then, the stamp is brought close to the wafer and is slowly moved further down until it first touches the surface of the wafer. By setting the temperature of the heater to 180 °C, the contact area slowly increases until the entire stamp is in contact with the wafer. Thereby, interlayer contaminants, that usually get trapped between layers, became mobile and are squeezed out [155, 157]. As the temperature of the wafer is above 150 °C, the glass transition temperature of PC [155, 159], the PC melts onto the surface on the wafer and is released from the stamp. After waiting for approximately 10 min, the stamp was then retracted and the wafer can be removed from the sample stage. By letting the wafer sit in chloroform for at least one hour, the PC dissolves and only the heterostructure as well as other picked-up flakes nearby are left on the wafer.

An additional annealing step is performed at 200 °C in vacuum for eight hours to increase the adhesion of the heterostructure to the wafer and to remove PC residues on the sample surface. At the end, optical microscopy and AFM images are taken of each heterostructure to ensure that all flakes are located at their desired location and that the stack is clean and mostly free of interlayer contaminants.

In the following, the process of assembling Stack 70 and Stack 99 (Section 3.5) is shown on the basis of optical microscopy images taken during the transfer process:

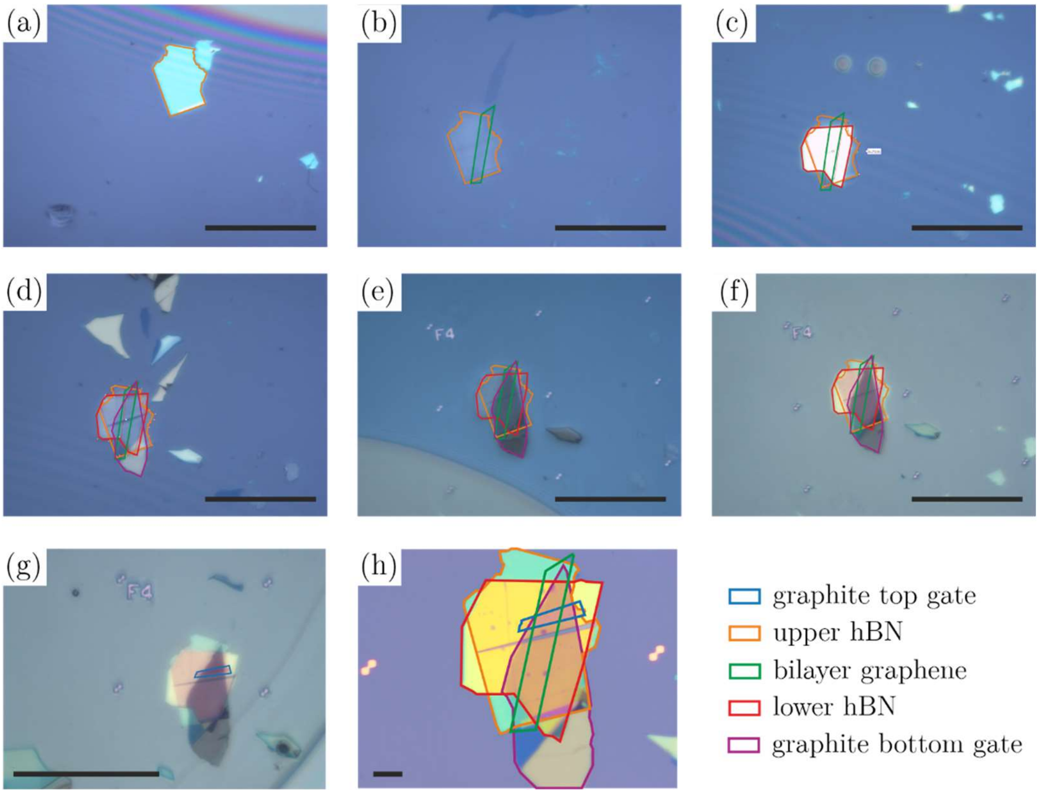

Figure 3.7 Step-by-step assembling of Stack 70. Sequential optical microscopy images taken during the process of assembling Stack 70 that does not have graphite contacts. The scalebar is 80 µm in (a) - (g) and 8 µm in (h). (a) The stamp is approaching an hBN flake that is outlined in orange and is located on a wafer. It is in contact with the wafer in the upper right part of the image (yellow background) but not yet in contact with the rest of the wafer (purple background). Interference fringes appear in between these two regions. (b) The upper hBN shown in (a) as well as parts of the bilayer graphene flake have been picked up (outlined in green). The bilayer graphene flake was ripped in two part while taking an AFM image (see Figure 3.4) and only the outlined part of the bilayer graphene flake was picked up. The hBN and the bilayer graphene flake are both located on the stamp. (c) The stamp is approaching a wafer with another hBN flake on top (bottom hBN flake, outlined in red). (d) The bottom hBN flake was picked up and the stamp with the upper hBN flake, the bilayer graphene flake and the lower hBN flake on top is approaching a wafer with a graphite flake (outlined in purple). (e) The graphite flake was picked up and is now placed on the stamp, too. The stamp is

approaching a clean wafer that exhibits gold markers (used for later contacting the stack via electron-beam lithography) and is heated to 180 °C. (f) The stack as well as the PC film of the stamp are melted onto the wafer. (g) Another graphite flake that was picked up using a fresh stamp that is then melted on top of the previously cleaned stack. (h) Optical microscope image of the completed heterostructure. All flakes are outlined. As the bilayer graphene was in touch with the graphite bottom gate after the stamping process which would produce a gate leakage, the touching parts were edged away in later step. The finished device is shown in Figure 3.10.

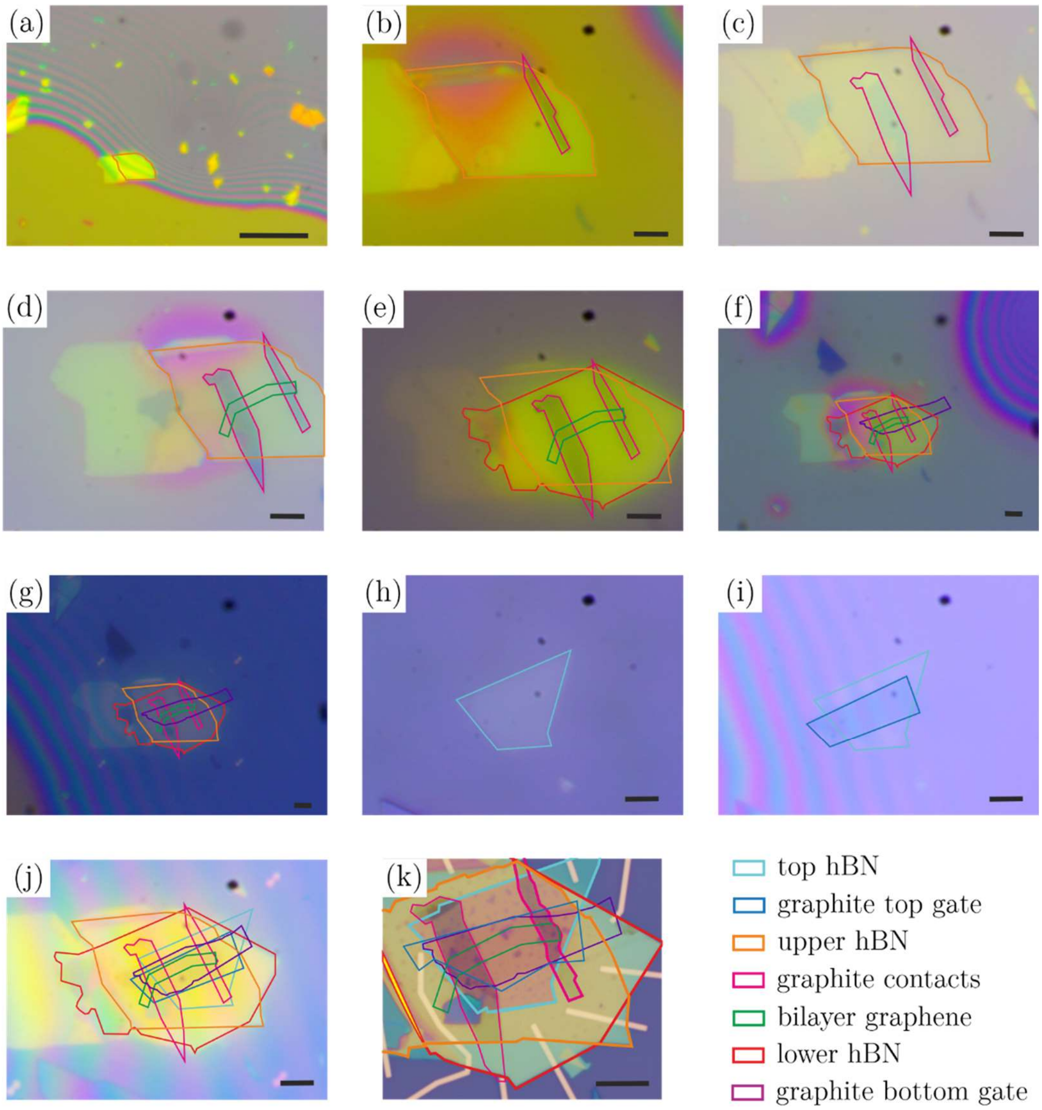

Figure 3.8 Step-by-step assembling of Stack 99. Sequential optical microscopy images taken during the process of assembling Stack 99 that has graphite contacts. The scalebar is 100 µm in (a) and 10 µm in (b) - (k). (a) The stamp is approaching an hBN flake that is outlined in orange and is located on a wafer. It is in contact with the wafer in the lower left part of the image (yellow background) but not yet in contact with the rest of the wafer (grey background). Interference fringes appear in between these two regions. Half of the hBN flake is in contact with the stamp, the other half of the hBN flake is not yet in contact. (b) The hBN flake on the stamp is approaching one of the graphite contacts (outlined in pink). (c) The upper hBN flake and one graphite contact are located on the stamp, the other graphite contact

is located on a wafer. The stamp is approaching the wafer. (d) The upper hBN flake and both graphite contacts have been picked up and are located on the stamp. The stamp is in contact with a new wafer that has a bilayer graphene flake on top (outlined in green). (e) The bilayer graphene flake was picked up and is now located on the stamp (below the upper hBN flake and the two graphite contacts). The stamp is approaching the lower hBN flake that is outlined in red. (f) The lower hBN flake was picked up, too and the stamp is now in contact with the graphite bottom gate (outlined in purple). (g) After picking up the graphite bottom gate, the stack is melted onto an empty wafer that exhibits markers and is heated to 180 °C. The stack as well as the PC film are melted onto the wafer. (h) To make it easier to pick up the graphite top gate, a top hBN (outlined in turquoise) is picked up using a fresh stamp. (i) The top hBN is used to pick up the graphite top gate that is outlined in blue. (j) The top hBN flake and the graphite top gate are both stamped on top of the previously cleaned stack. (h) Optical microscope image of the finished stack after it had been further contacted with gold contacts (see next section). All flakes are outlined.

3.4 Fabrication of electrical contacts

Before measuring the electronic properties of the 2D heterostructures, electrical contacts have to be applied to the conducting layers. In the absence of graphite contacts in heterostructures, edge contacts are fabricated in a Hall bar configuration (Section 3.4.1). In a second step, contact lines and contact pads are applied to the edge or graphite contacts (Section 3.4.2) allowing to make electrical connections from the sample to a universal chip carrier (Section 3.4.3).

3.4.1. Fabrication of edge contacts

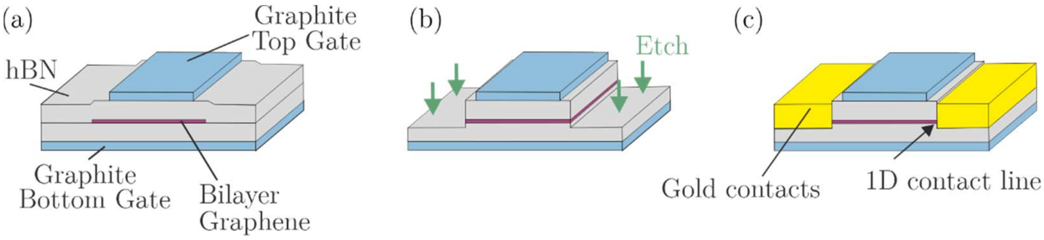

Figure 3.9 Schematic representation edge contact fabrication process. (a) Illustration of a bilayer graphene heterostructure consisting of a bottom graphite flake, a bottom hBN flake, a bilayer graphene flake, a top hBN flake and a top graphite flake. (b) Illustration of the etching process. (c) Illustration of a contacted bilayer graphene heterostructure. Only a one-dimensional edge of the bilayer graphene flake touches the gold contact.

In the first devices that were fabricated during the course of this thesis, the bilayer graphene flakes were fully encapsulated in hBN and no graphite contacts were utilized. To electrically contact the bilayer graphene flakes in these samples, edge contacts are fabricated in which only the (almost) 1D edge of a bilayer graphene flake is contacted [156]. The process of fabricating edge contacts is schematically shown in Figure 3.9 and is described below.

The contacts are designed to be in a Hall bar geometry (see Section 2.3) and are patterned using a standard electron-beam lithography process. For this, the sample is first spin-coated with the positive resist polymethylmethacrylate (PMMA) 950 k dissolved in anisole (AR-P 672.045, Allresist) in a 4.5 wt.% solution at 800 rpm for 1 s and subsequently at 4000 rpm for 30 s. Afterwards, a soft bake is performed at 150 °C for at least 3 min. Contact lines going to the sample are then exposed with an electron beam at 10 kV with a dose of 110 µCcm^{-2} and an aperture of 7.5 µm. In a second step, the sample is developed in a 1:3 solution of methylisobutylketon (MIBK) and isopropanol for 2 min and is then rinsed in isopropanol whereby the exposed PMMA resist is removed. Afterwards, inductive coupled plasma reactive ion etching (ICP-RIE) is used to etch into the heterostructure and to expose the edges of the bilayer graphene flake whereby the PMMA resists serves as a mask for the rest of the sample (Figure 3.9b). The etch rate of hBN flakes is determined to be 7 nm min^{-1} when using a gas mixture of sulfur hexafluoride (SF_6) and argon (Ar) with flow rates of 10 sccm and 5 sccm, respectively, an ICP power of 70 W and an RF power of 50 W. After removing the upper hBN flake, an oxygen plasma with a flow rate of 10 sccm, an ICP power of 40 W and an RF power of 150 W is generated to also etch through the bilayer graphene flake which takes approximately 20 s. Directly after the etching process, metals are deposited using electron-beam physical vapor deposition at 3×10^{-7} mbar. A 5 nm adhesion layer of chromium (Cr) at a rate of 0.2 Å/s and a 30 nm to 80 nm layer of gold (Au) at a rate of 1.0 Å/s are evaporated. The thickness of the gold is chosen to be always larger than the thickness of the thickest flake to ensure electrical contact when the contact lines cross this flake. In a last step, the sample is placed in acetone to lift-off the remaining resist. After rinsing it in isopropanol and blow-drying it with dry-air, only the contact lines are covered with gold (Figure 3.9c).

3.4.2. Fabrication of contact lines and contact pads

In order to fabricate the contact pads and to extend contact lines, another step of e-beam lithography is performed. To speed up the patterning, an aperture of 60 µm and a dose of 170 µCcm^{-2} is used to expose pads and large contact lines (wider than 5 µm). After development, the samples are cleaned in an UV/Ozone cleaner (UV Ozone Cleaner, Ossila) for 30 s to improve the adhesion of the pads. The deposition rates of Cr and Au are the same as described in the previous section although only 1 nm of Cr and 40 nm of Au are used.

After evaporation and lift-off, the devices are in principle completed. All lines and pads are tested for connection at a point probe station by bringing two conductive needles that are connected with a source-measure unit (Keithley 2450, Tektronix), in contact with two pads.

3.4.3. Wire bonding

To be able to measure the samples in cryogenic setups, they are glued onto universal chip carriers using conductive silver paint. The contact pads are then connected to pins on the sample holder with gold wires using a wedge bonder (MEI 1204W, Marpet Enterprises or K&S 4500 Series, Kulicke & Soffa Ltd.). The samples are grounded during the entire procedure to prevent electrostatic discharging.

3.5 Summary of all devices

In this section, an overview of the four devices used for measurements discussed in Chapters 4 - 8 is given. Their labels match the labels given in my laboratory notebook. Pictures of all devices are shown in Figure 3.10.

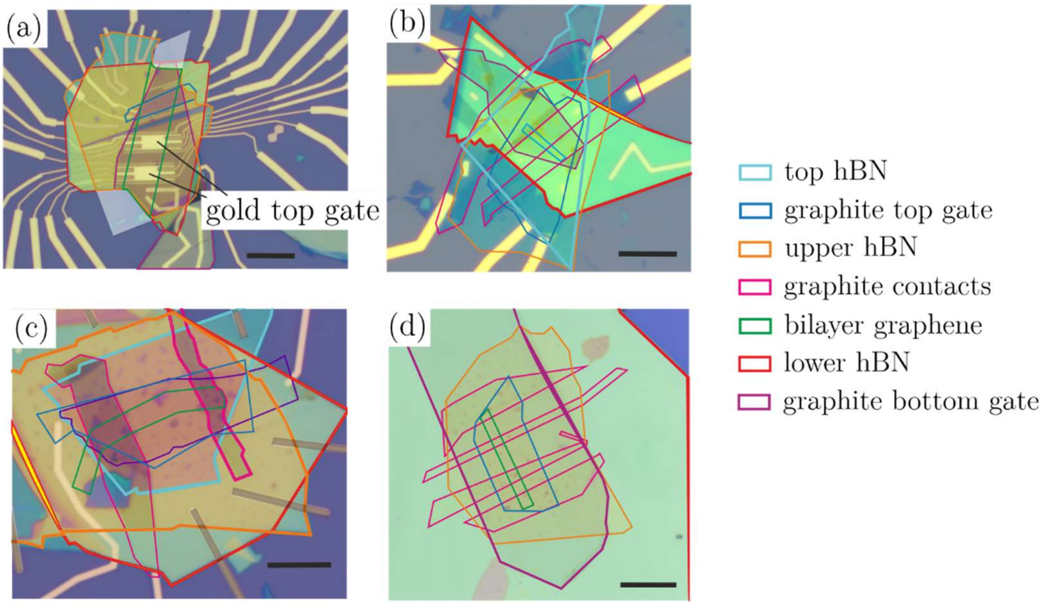

Figure 3.10 Overview of all devices. Pictures of the devices measured during the course of this thesis. Stack 70 (a), Stack 82 (b), Stack 99 (c) and StackMartinAnna (d). All flakes are outlined. The grey shaded regions in (a) mark the region that were edged to prevent electrical shorts between the bilayer graphene flake and the gates. The black

shaded regions in (c) mark gold lines that were designed to hold the stack in place to make sure that it is not washed away while removing the PMMA layer after evaporation. All scalebars are 10 µm.

- Stack 70

  Stack 70 was already introduced in Sections 3.2 and 3.3 and is shown in Figure 3.10a. It was assembled without graphite contacts and has edge contacts made out of gold. As Stack 70 is very large (the encapsulated part of the bilayer graphene flake has lateral dimensions of about 30 µm x 8 µm), three separate devices were fabricated out of it that each have six contacts patterned in a Hall bar geometry. The top device has a local graphite top gate, i.e., the graphite top gate does not cover the entire bilayer graphene flake but only parts which made it easier to fabricate edge contact. The middle and bottom devices have gold top gates that were patterned using electron beam lithography (the fabrication process was the same as for the edge contacts but without etching into the hBN). After stamping Stack 70, the bilayer graphene flake was partially in touch with the graphite bottom gate. These regions where etched away using ICP-RIE. The lower hBN flake of Stack 70 has a thickness of 69.3 nm and the upper hBN flakes a thickness of 29.6 nm (verified by AFM). The top device of Stack 70 was used to measure the results discussed in Chapter 7.

- Stack 82

  Stack 82 has two-terminal graphite contacts and was fabricated the same way as Stack 99 that was already introduced in Section 3.3. It is shown in Figure 3.10b. The lower hBN flake of Stack 82 has a thickness of 32 nm and the upper hBN flakes a thickness of 13 nm (verified by AFM). Stack 82 was used to measure the results discussed in Chapter 6.

- Stack 99

  Stack 99 has two-terminal graphite contacts. The process of assembling Stack 99 is shown in detail in Figure 3.8, the completed device is shown in Figure 3.10c. The lower hBN flake of Stack 99 has a thickness of 42 nm and the upper hBN flakes a thickness of 34 nm (verified by AFM). Stack 99 was used to measure the results discussed in Chapter 5, 6 and 7.

- StackMartinAnna

  StackMartinAnna was fabricated in collaboration with Dr. Martin Statz. The measurements conducted with this device are discussed in Appendix A. The data shown within this thesis were taken by both of us. StackMartinAnna has four graphite contacts instead of two that go across the bilayer graphene flake as shown in Figure 3.10d. Since stamping a device with four graphite contacts is more complex and requires additional stamping steps compared to stamping a device with two graphite contacts, the bottom part, consisting of the lower hBN flake and the bottom graphite flake, was stamped first and was then melted onto a clean wafer. Using a new stamp, the upper hBN flake, four graphite flakes serving as contacts and the bilayer graphene flake were then successively picked up. Two of the graphite flakes serving as contacts were located next to each other on the same wafer so that the graphite contacts could be picked up within three steps. The stamp was then melted onto the previously cleaned bottom part. The graphite top gate was stamped in a last step. The thicknesses of the hBN flakes were determined as 58 nm (bottom hBN flake) and 15 nm (top hBN flake) via AFM. Despite having four terminals, StackMartinAnna still exhibits a finite contact resistance. Likely, this contact resistance stems from the fact that different graphite flakes that exhibit different conductivities were used as contacts. More investigation is needed to further elucidate this aspect.

4 Introduction to electrical transport measurements

All measurements discussed within the results part of this thesis were conducted in a cryogen-free dilution refrigerator at a base temperature of below 7 mK (Dilution Refrigerator BF-LD250, Bluefors). In the first two sections of this chapter, the working principle of this dilution refrigerator as well as the corresponding electrical setup is described. In the following sections, an introduction into the sample calibration is given. Moreover, standard transport measurements in bilayer graphene are introduced. Lastly, samples with and without graphite contacts are compared.

4.1 Dilution refrigerator

Cryogen-free dilution refrigerators allow to continuously cool down samples to millikelvin temperatures and do not require an external supply of liquid nitrogen and helium. A pulse tube is used to frequently compress and expand helium gas within a closed volume whereby heat is removed from one end of the tube and generated on the other end. By heat exchangers, the heat of compression is removed while the cold end is thermally coupled to the cryostat and cools down the system to approximately 3 K, the boiling temperature of low-pressure helium gas. [160, 161] To achieve temperatures below 3 K, a ^{3}He/^{4}He dilution unit is used, whereby ^{3}He and ^{4}He correspond to the two isotopes of helium. When the mixture of ^{3}He and ^{4}He is let into the cycle, it is first condensed into the system and precooled to 3 K using heat exchangers to the compressor line. By pumping the mixture of ^{3}He and ^{4}He away from the still and letting it back in through the compressor line the temperature is decreased further to below 800 mK due to evaporative cooling. At this temperature, a phase separation occurs in the mixing chamber and the mixture separates into a ^{3}He concentrated phase with a ^{3}He concentration of almost 100 % and a diluted phase with a ^{3}He concentration of about 6.4 %. By pumping on the diluted phase, ^{3}He atoms evaporate due to their lower vapor pressure and ^{3}He from the concentrated phase move into the dilute phase. This process dissipates energy and results in cooling of the system down to millikelvin temperatures. [162, 163]

To conduct temperature dependent measurements, a heater is implemented at the mixing chamber. Since the mixture evaporates at temperatures above 1 K, measuring at temperatures between 1 K and 3 K is possible only within a very short time frame. Measurements above 3 K can be conducted when the mixture is collected from the dilution unit and heat switches are activated to thermally link the still and the mixing chamber to the pulse tube line. [163]

The system is further equipped with a superconducting magnet that can generate magnetic fields of up to 14 T. By changing the orientation of the sample, the magnetic field can be applied perpendicular or in-plane with the sample.

Even though the base temperature of our cryostat, which is measured at the mixing chamber, is below 7 mK, the actual sample temperature is likely larger than this as the sample is connected to the ambient environment by its electric wiring. To reduce the heat transfer coming from the wires and to cool down the sample thereby effectively, the wires are thermally linked to gold plated copper bobbins at every temperature stage. In addition, the wires are twisted in pairs and filtering circuits were added just before the wires enter the cryostat and at the mixing chamber to reduce noise.

From the cryostat and the room-temperature filter box, the wires are directed to a breakout box where they are connected to measurement units.

4.2 Electrical measurement configuration

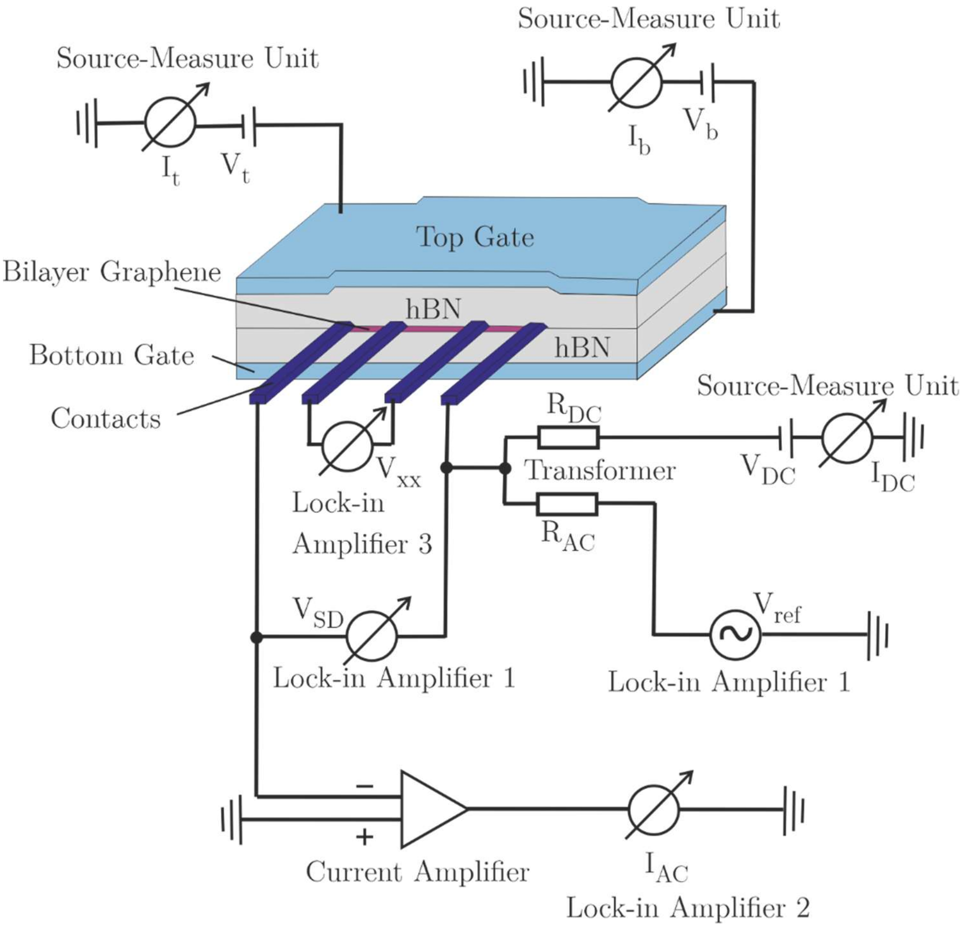

Figure 4.1 Electrical measurement configuration of a four-terminal device with top and bottom gates. The details are discussed in the main text.

During the course of this thesis, all electrical measurements were conducted in a (quasi-)four-point configuration using a standard lock-in technique. In case the sample is connected with two graphite contacts, a quasi-four-point measurement configuration is used to avoid in-series resistances stemming from the filters. In this configuration, the two bonding pins that are connected with the graphite contacts, are each interconnected with a second bonding pin on the sample holder. The electrical measurement setup is shown in

Figure 4.1. An AC reference signal V_{ref} with a frequency of 78 Hz is generated from a lock-in amplifier (Lock-in amplifier 1; SR865, Stanford Research Systems) and is transformed into a small AC current-signal of 1 nA using a high resistance R_{AC}. This exact frequency is chosen randomly but it is ensured that any 50 Hz noise coming from the power lines is suppressed and that the noise spectrum is minimized. The current signal is then sent through the device. To measure the actual current flow I_{AC}, a current amplifier (Model 1211, DL Instruments) is connected to the source contact. The amplified current is measured using a second lock-in amplifier (Lock-in amplifier 2; SR865, Stanford Research Systems). The voltage drops between the probe contacts V_{xx} (referring to the voltage drop in direction of the applied current), V_{H} (referring to the voltage drop perpendicular to the direction of the applied current) and V_{SD} (referring to the voltage drop between the source and the drain contact) are measured using the Lock-in amplifiers 1, 3 and 4 (Lock-in amplifier 4 is used to measured V_{H} and is not shown in

Figure 4.1) that are all linked to Lock-in amplifier 1 via V_{ref} (this link is shown in

Figure 4.1). For some measurements, an additional DC bias signal is generated using a DC source-measure unit (SourceMeter 2450, Keithley) and a resistance R_{DC}, and is modulated onto the AC reference signal using a transformer. After the overall current signal is amplified, the DC component is measured using a multimeter (Multimeter 34461A, Keysight).

The resistances in the sample can then be calculated as

$$R_{\mathrm{xx}} = \frac{V_{\mathrm{xx}}}{I_{\mathrm{AC}}}\ , \quad R_{\mathrm{xy}} = \frac{V_{\mathrm{H}}}{I_{\mathrm{AC}}}\ , \quad R_{\mathrm{SD}} = \frac{V_{\mathrm{SD}}}{I_{\mathrm{AC}}} - R_{\mathrm{C}} \tag{44}$$

whereas R_{C} is the contact resistance that includes the resistance coming from the graphite and gold contacts. When measuring R_{xx} or R_{xy} in four-terminal devices, the contact resistance is eliminated from the measurement and no contact resistance has to be subtracted.

Two source-measure units (SourceMeter 2450, Keithley) are used to apply the top and bottom gate voltages and to simultaneously measure the gate leakage currents I_t and I_b.

To avoid grounding loops, all measurement units, except for the current amplifier, are decoupled from the standard power lines using an isolating transformer. Only one electrical ground is used.

4.3 Device calibration

Before starting with the actual measurements, a set of calibration measurements is conducted in order to convert the top and bottom gate voltages into the charge carrier density *n* and the electric displacement field *D*. While this section shows in detail how these calibration measurements are conducted and reads rather technical, an introduction to magnetotransport measurements in bilayer graphene is given in Section 4.4.

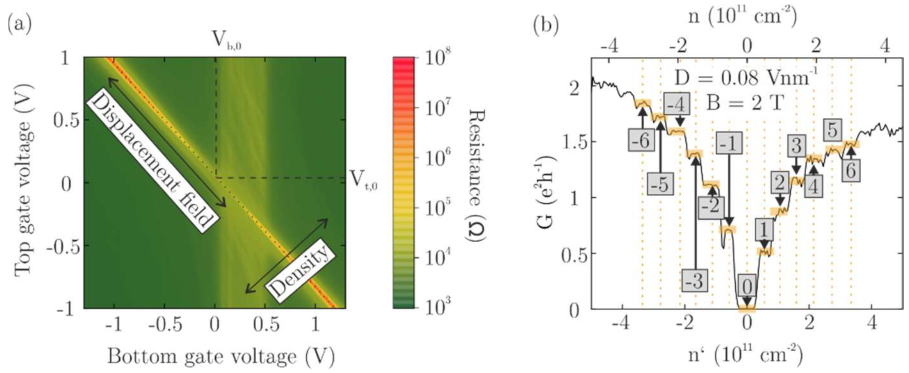

Figure 4.2 Device calibration. (a) Measured resistance ($R_{SD}+R_C$ (see Equation (44)) as a function of the bottom and top gate voltage without applied magnetic field. (b) Measured conductance as a function of the preliminary charge carrier density *n'* and the actual charge carrier density *n* at an out-of-plane magnetic field $B = 2$ T and electric displacement field $D = 0.08$ Vnm^{-1}. Quantum Hall states are highlighted in orange and are labeled by numerals. These data set were conducted at a temperature of 10 mK using Stack 99 that exhibits two-terminal graphite contacts.

After a sample is loaded into the cryostat and all connections are checked, a sweep of the top and bottom gate voltages at zero magnetic field is usually performed first. A bottom gate voltage range of approximately (-0.03 to +0.03) nVm/d_b and a top gate voltage range of approximately (-0.03 to +0.03) nVm/d_t is mostly sufficient to align the sample. d_b, the thickness of the bottom hBN flake, and d_t, the thickness of the top hBN flake, were determined previously via AFM. While sweeping the gate voltages, V_{SD} and I_{AC} are measured allowing to calculate $R_{\mathrm{SD}}+R_{\mathrm{C}}$ (see Equation (44)). In case a device with four-terminal contacts is measured, V_{xx} and V_{H} are measured as well.

In the following, the device calibration is exemplary discussed for Stack 99, a device with two-terminal graphite contacts. This data set is shown in Figure 4.2a. By sweeping the top and the bottom gate voltages, the charge carrier density n and the electric displacement field D are both varied at the same time. The corresponding axes of n and D are indicated by arrows. The opening of a band gap at finite D is apparent from the increasing resistance with increasing D at $n = 0$ and will be discussed in more detail in the next section.

The ratio between the height of the top and bottom hBN flake α can be determined by taking the slope of the $n = 0$ line in the V_b vs V_t plot (Figure 4.2a).

In Stack 99, α was determined as

$$\alpha = \frac{\Delta V_b}{\Delta V_t} = \frac{1.175\ V - (-1.065\ V)}{1\ V - (-1\ V)} = 1.12\ . \tag{45}$$

It is worth mentioning that α cannot be determined precisely by dividing d_b by d_t since the heights measured via AFM are usually not precise enough. In fact, there is often water or residuals underneath the flakes that falsify the height measurements. For example, the quotient of the measured heights of the two flakes in Stack 99 would give $\alpha = 1.23$.

Using the *SuperFunAnalyzer*, a measurement software that was written by Felix Winterer and was further advanced by Jonas Pöhls, Christian Eckel and Philipp Kaiser, the subsequent data sets are acquired as a function of n

and D. Applying Equations (41), (43) and (45), the top and bottom gate voltages can be set in the software as

$$V_b = \frac{d_b}{2\varepsilon_r} \left(\frac{e}{\varepsilon_0} n - 2D\right) + V_{b,0} \tag{46}$$

and

$$V_t = \frac{d_b}{2\alpha\varepsilon_r} \left(\frac{e}{\varepsilon_0} n + 2D\right) + V_{t,0} \ . \tag{47}$$

Offsets in the applied gate voltages, $V_{b,0}$ and $V_{t,0}$, are introduced to correct for charge traps screening the gate field.

Even though $V_{b,0}$, $V_{t,0}$ and ε_r, the reduced dielectric constant of hBN, are still unknown at this point, a n' vs D' sweep (n' and D' are the preliminary values for n and D) is performed at a magnetic field of 2 T. Therefore, $V_{b,0}$ and $V_{t,0}$ are both set to zero and $\varepsilon_{\mathrm{hBN}}$, that can in principle vary from 3 to 4 [73], is set to 3.5. At $B = 2$ T, Landau level are usually well resolved and all integer quantum Hall states can be observed.

By comparing n' with the expected density at certain filling factors ($n = \nu\, eB/h$, Figure 4.2b), the exact value for ε_{hBN} is determined. This is illustrated in Figure 4.2b, where the measured conductance

$$G = \frac{1}{R} = \frac{I_{\mathrm{AC}}}{V_{\mathrm{SD}}} \tag{48}$$

is shown as a function of $n'(n)$ and D at $B = 2$ T before (after) the sample has been aligned. Furthermore, it is checked whether the observed Landau level crossings agree with those theoretically predicted and observed previously (see Section 2.4.1). As many quantum Hall states, e.g., quantum Hall states with $\nu = \pm 2, \pm 5$ and ± 7 exhibit crossings at $D = 0$, it is possible to extract the $D = 0$ line and $V_{b,0}$ and $V_{t,0}$ can be determined by extracting the top and bottom gate voltages at $n = D = 0$ (see Extended Data Fig. 3c of Ref. [1] that is reprinted in Chapter 6 for the corresponding data).

In a last step, R_{C} is estimated in case two-terminal graphite contacts are used. In general, it is possible to estimate R_{C} by comparing the measured resistance with the expected Hall resistance R_{xy} since $R_{xx} \approx 0$ when R_{xy} is quantized [33, 105, 156, 164]. However, when using graphite contacts this is more challenging since the contact resistance changes as a function of the applied top gate voltage (and therefore also as a function of n and D, see Section 4.4.1), the magnetic field, the applied current and temperature. How the contact resistance can still be approximated for constant values of I and T and in a small range of n and D is shown in detail in the Methods of Reference [1] that are reprinted in Chapter 6. In the following, the measured conductance G of two-terminal devices is shown in arbitrary units (a.u.) and R_C is not subtracted.

4.4 Magnetotransport in bilayer graphene

In the following, some of the standard magnetotransport measurements conducted in bilayer graphene samples are discussed. Reproducing these results allows to determine the quality of the samples and ensures that they do not show unwanted features coming from graphite contacts or gates or from a alignment of different flakes.

4.4.1. Tuning the Fermi energy level and bandgap opening in bilayer graphene

In pristine bilayer graphene, the Fermi energy level lies directly at the touching point of the valence and conduction band. Here, the charge carrier density n is zero. By applying a top and/or bottom gate voltage, n can be tuned whereby the Fermi energy level is moved. At a negative n, corresponding to hole doping, it is shifted into the valence band. Analogously, it is shifted into the conduction band when a positive n is applied. The latter corresponds to electron doping, respectively.

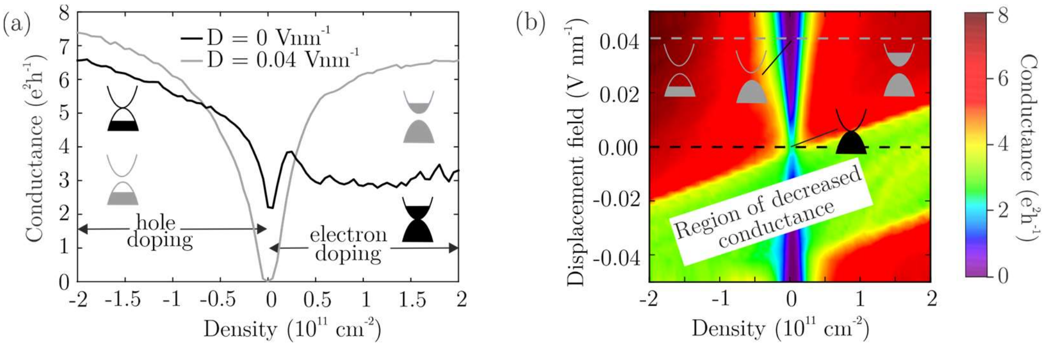

Figure 4.3 Tuning the charge carrier density and the electric displacement field. (a) Measured conductance as a function of charge carrier density n at $D = 0$ Vnm^{-1} and $D = 0.04$ Vnm^{-1}. The dip in the conductance corresponds to the charge neutrality point. At this point, the conductance decreases with increasing electric displacement field D. The insets schematically show the band structure at the corresponding value of n and D. The Fermi energy level sits at the interface of the filled/ non-filled bands. (b) Measured conductance as a function of n and D. The region of low conductance (green line) corresponds to a region that only depends on the bottom but not on the top gate voltage (see Section 4.5). These data set were conducted at a temperature of 10 mK using Stack 99 that exhibits two-terminal graphite contacts.

Changing n and thereby the Fermi energy level has direct consequences on the resistance R measured along the bilayer graphene sheet. At charge neutrality ($n = 0$), the number of available states is low and charge transport is hindered. Thus, R is large and the conductance G is minimal. At finite n, the Fermi energy level is moved into one of the bands and the bilayer graphene sample becomes more conducting. Therefore, G increases (Figure 4.3a) [140].

Apart from n, also the electric displacement field D can be varied. When D is increased, a band gap opens up and charge transport is hindered when the Fermi energy level lies within the gap. Thus, the conductance at charge neutrality is decreasing with increasing D [28, 94, 165]. At $D \approx 0.04$ Vnm^{-1}, the minimal measured conductance is about 0.003 e^2/h corresponding to a resistance of approximately 8.6 MΩ which is the highest resistance value that can be measured in our setup.

A common representation of these results is to use three-dimensional color plots, as shown in Figure 4.3b, where the conductance is shown as a function of both, n and D [28, 33, 92]. The opening of the bandgap is apparent from the decreased conductance at the charge neutrality point and the broadening of this region in n with increasing D. The line of decreased conductance (green line across $D = 0$) and also the electron-hole asymmetry that can be seen in Figure 4.3a comes from the contact resistance of graphite contacts and is discussed in more detail in Section 4.5.

4.4.2. Observation of an integer quantum Hall effect in bilayer graphene

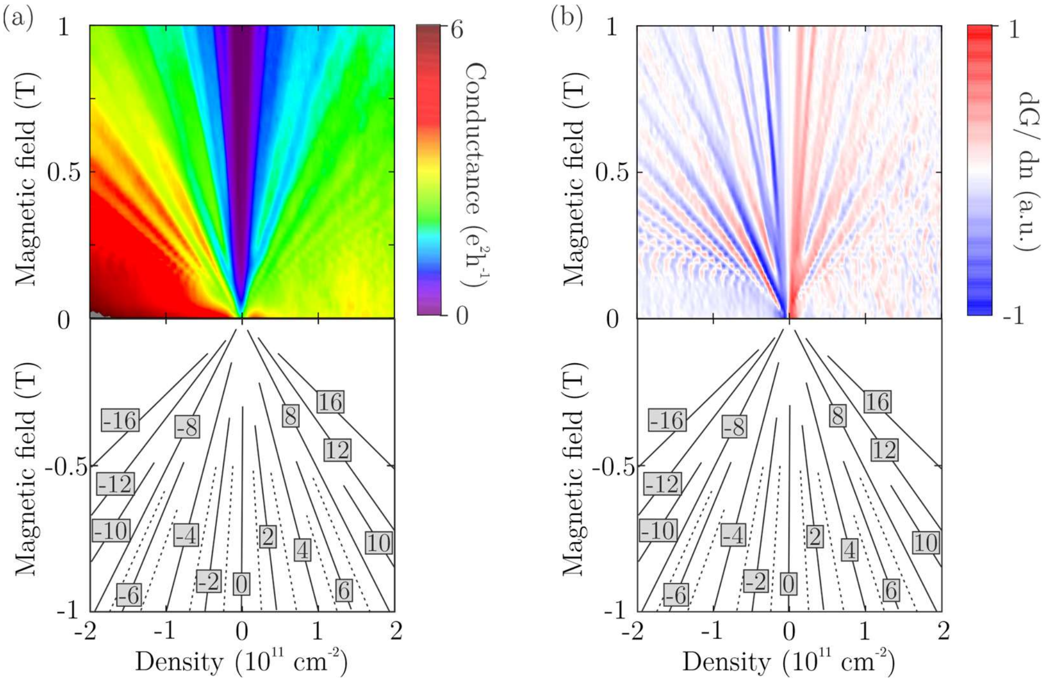

Figure 4.4 Landau Fan diagrams. Conductance (a) and derivative of the conductance ($\mathrm{d}G/\mathrm{d}n$) (b) plotted as function of n and B at $D = 0$ measured in a two-terminal device with graphite contacts. Quantum Hall states exhibit a constant conductance over a finite regime in n and a vanishing derivative of the conductance. The conductance values are not consistent with the expected conductance since the sample exhibits a finite contact resistance. The slopes of the lowest quantum Hall states are traced by lines in the mirror image. Quantum Hall states with odd $\boldsymbol{\nu}$ are traced by dotted lines, quantum Hall states with even ν are traced by solid lines. The corresponding quantum

Hall states are labeled by numerals. These data set were conducted at a temperature of 10 mK using Stack 99 that exhibits two-terminal graphite contacts.

In Chapter 2, it is shown that quantum Hall states in bilayer graphene are four-fold degenerate due to spin and valley degeneracies and eight-fold degenerate in the lowest Landau level due to spin, valley and orbital degeneracies at large B above the magnetic breakdown (Section 2.3.2). In very clean samples, at low temperatures and large B, these degeneracies can be lifted due to exchange interaction (Section 2.4.1). As the exchange energy increases with magnetic field, probing the quantum Hall states as a function of B allows to observe a continuous splitting of quantum Hall states [28, 29]. An example is shown in Figure 4.4 where the conductance (a) as well as the derivative of the conductance (b) is plotted as a function of n and B. This graphical representation of quantum Hall states is known as a Landau fan diagram as the quantum Hall states move to larger densities with increasing B forming a pattern that resembles a fan.

Notably, quantum Hall states measured in the presented device (Stack 99) can be traced down to remarkably low magnetic fields of approximately $B_{\mathrm{crit}} = 50$ mT which is about one order of magnitude lower than in other devices shown in literature [28, 29]. At this magnetic field, the cyclotron orbits electrons travel are largest in real space. B_{crit} can thus be used to calculated the minimal mean free path of electrons (l_{MFP}) that describes the minimal average distance that an electron travels before it is scattered or adsorbed by other particles or obstacles in its path. Following References [24, 156], l_{MFP} can be calculated as

$$l_{\mathrm{MFP}} = 2\pi k_{\mathrm{F}} l_{\mathrm{B}}^2 \tag{49}$$

with Fermi wavevector

$$k_{\mathrm{F}} = \sqrt{\pi |n|} \tag{50}$$

and magnetic length

$$l_{\mathrm{B}} \geq \sqrt{\hbar/(eB_{\mathrm{crit}})}. \tag{51}$$

In Stack 99, l_{MFP} was found to be $\geq 1 \mu m$ using $n = 4 \times 10^9\ cm^{-2}$ and $B_{\mathrm{crit}} = 50$ mT. This value is about one magnitude smaller than the lateral device dimension (≈10 μm, Figure 3.10c) and comparable with values reported in literature hinting towards a high sample quality [24, 156, 166].

While a zoom-in of the low-B regime of the fan diagram shown in Figure 4.4 is discussed in more detail in Chapter 5, the regime in which $B > 100$ mT is discussed in this section. At 100 mT $< B <$ 300 mT (here, the inverse magnetic length is larger than the distance between two adjacent mini Dirac cones), the lowest Landau level is eight-fold degenerate due to valley, spin and orbital degeneracies and only quantum Hall states with $\nu = \pm 4$ are well resolved, i.e., these states exhibit a constant conductance and a vanishing derivative of the conductance. At B ≈ 300 mT, also quantum Hall states with $\nu = \pm 2$ and $\nu = 0$ appear due to spin, valley or orbital splitting while a full splitting of the lowest Landau level can be observed at B > 500 mT. This splitting of quantum Hall states in the lowest Landau level is consistent with literature [28, 29, 109, 111].

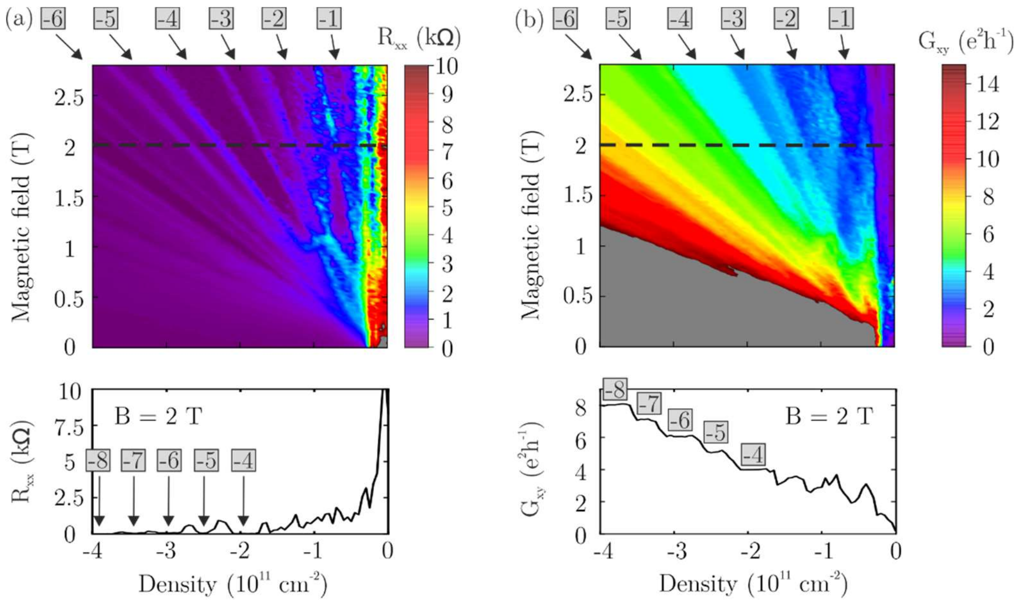

Figure 4.5 Quantum Hall effect measured in a four-terminal device. (a) R_{xx} plotted as a function of n and B at $D = 0.1$ Vnm^{-1}, a linecut at $B = 2$ T is shown below. (b) G_{xy} plotted as a function of n and B at $D = 0.1$ Vnm^{-1}. A linecut at $B = 2$ T is shown below. These data sets were conducted at a

temperature of 10 mK using the middle Hall bar of Stack 70 that exhibits four-terminal edge contacts and a gold top gate.

When using four-terminal contacts in a Hall bar configuration, e.g. Stack 70, R_{xx} and R_{xy} can both be measured. Such a measurement is shown in Figure 4.5. As derived in Chapter 2.3, R_{xx} is vanishes when the Fermi energy level lies in between two Landau levels and ν is an integer. It is finite when the Fermi energy level lies within a Landau level. When R_{xx} vanishes, R_{xy} (and therefore also the Hall conductance G_{xy}) is constant and G_{xy} matches exactly $\nu e^2 h^{-1}$ since the contact resistance is eliminated from the four-terminal measurement. The middle Hall bar of Stack 70 exhibits a gold top gate which is why this device is expected to be less clean compared to Stack 99 [74]. Indeed, quantum Hall states only appear at larger magnetic fields of $B > 500$ mT in Stack 70 (corresponding to $l_{\mathrm{MFP}} \approx 320\ nm$) and quantum Hall states at $B = 2$ T and low n are not well resolved, i.e. G_{xy} is not fully quantized and $R_{xx} \neq 0$.

4.5 Comparison of samples with edge and graphite contacts

In Section 3.5, different devices are introduced that have been fabricated during the course of this thesis. Most of these devices exhibit graphite contacts while Stack 70 exhibit commonly used edge contacts. In the following, the different contacts are compared and their effects on magnetotransport measurements are discussed.

As using graphite contacts involves an extra transfer step for each contact it is technically demanding to use four-probe contacts here. Thus, a two-terminal device configuration is mostly used when using graphite contacts. In such devices, R_{xx} and R_{xy} cannot be measured independently and consequently, some features such as a vanishing R_{xx} cannot be resolved. Another disadvantage of using graphite contacts is that their contact resistance depends on the applied current, temperature and the magnetic field as graphite exhibits a Hall effect. Furthermore, the location of the graphite contacts leads to a region of decreased conductance that only depends on the applied bottom gate voltage but not on the applied top gate voltage (e.g. Figure 4.2). Since the bilayer graphene flakes are located below the graphite contacts, the contacts screen the field from the top gate. The latter does not happen when etched gold contacts are used where only the (almost) 1D edge of a bilayer graphene flake is contacted.

Despite these disadvantages, graphite contacts also offer many advantages that are discussed below. Graphite contacts can be used to avoid the process of reactive ion etching (Chapter 3.4) that requires a precise calibration of etching rates since, on the one hand, the upper hBN flake has to be etched away to provide good electrical contact with the bilayer graphene flake and, on the other hand, the lower hBN should be etched away as little as possible to not significantly lower the electric breakdown voltages (see Chapter 2.1.4). When using graphite contacts, no etching is needed and larger electric displacement fields can be applied. Another advantage of using graphite contacts comes with the fact that they are completely embedded into the heterostructures. The bilayer graphene then remains intact and does not come in contact with polymers which lowers the sample quality. Furthermore, a global top gate can easily be applied when using graphite contacts since it can be simply placed on top of the upper hBN flake that is serving as a dielectric. For Stack 70, where etched contacts were used, only local top gates could be applied resulting in a device region that only depends on the bottom gate but not on the top gate voltage. Last, graphite contacts are already widely used in the TMDC and recently also in the graphene community as they offer good electrical contact [82–84]. Different groups have now started to fabricate devices with multi-terminal graphite contacts that sit on one side of the bilayer graphene sheet and that allow to also measure R_{xx} but not R_{xy} [35, 98]. However, fabricating such devices was beyond the scope of this thesis.

5 Manuscript: Mapping out the tunable band structure in bilayer graphene

The results presented in this Chapter are currently prepared for publications. The current version of the manuscript is reprinted below. The supplementary material is reprinted in Appendix A.

Contributions:

I fabricated and measured the device which is discussed in the main text (Stack 99, introduced in Chapter 3.5). The device shown in the supplementary materials (StackMartinAnna, introduced in Chapter 3.5) was fabricated and measured together with Dr. Martin Statz. Furthermore, I performed the data analysis, prepared the first version of the manuscript, except from some theoretical sections in the supplemental material, and designed all figures. The band structure and Landau level calculations were performed by Nils Jacobsen. Lastly, I produced the current version of this manuscript.

Mapping out the tunable multi-cone band structure in Bernal bilayer graphene

Anna M. Seiler[1], Nils Jacobsen[1], Martin Statz[1], Noelia Fernandez[1], Francesca Falorsi[1], Kenji Watanabe[2], Takashi Taniguchi[3], Zhiyu Dong[4], Leonid S. Levitov[4], R. Thomas Weitz[1]*

[1]1st Physical Institute, Faculty of Physics, University of Göttingen, Friedrich-Hund-Platz 1, Göttingen 37077, Germany

[2]Research Center for Functional Materials, National Institute for Materials Science, 1-1 Namiki, Tsukuba 305-0044, Japan

[3]International Center for Materials Nanoarchitectonics, National Institute for Materials Science, Tsukuba, Japan

[4]Department of Physics, Massachusetts Institute of Technology, Cambridge, Massachusetts 02139, USA

*Corresponding author. Email: thomas.weitz@uni-goettingen.de

Early band structure calculations of Bernal bilayer graphene (BLG) predict a complex low-energy band structure consisting of four mini Dirac cones with different chiralities in the vicinity of each valley. Even though BLG was subject to many experimental studies in the last two decades, experimental evidence of this exotic band structure is still elusive, likely due to constrictions in the energy resolution. Rather than probing the band structure using spectroscopy, we use Landau levels as a marker of the energy dispersion and carefully analyze the Landau level spectrum in a regime where the cyclotron orbits of electrons or holes in momentum space are small enough to resolve the distinct mini Dirac cones. We thereby cannot only identify the presence of four distinct Dirac cones but also complex electric displacement field induced topological transitions and bandgap openings. These findings make BLG the first massless Dirac material with truly linear energy dispersion that can be tuned electrostatically.

Graphene, a single layer of carbon atoms arranged in a hexagonal lattice, exhibits intriguing electronic properties due to its linear dispersed bands forming Dirac cones at the K and K' points. Yet, one of the key limitations of graphene is its zero-bandgap, which makes it e.g. not-well suited for digital electronic applications. Several attempts have been made to artificially open up a bandgap in monolayer graphene including chemical doping [167–169] and strain engineering [170–173]. However, while these methods allow to create a gap in the otherwise gapless dispersion, they also create disorder in the system. Opening a tunable band gap in pristine monolayer graphene by electrostatic gating, as it can been done in Bernal bilayer graphene (BLG) [28, 94, 165], remains challenging since one would require electric field control with atomic precision to induce a potential difference between the two sublattices.

Bernal-stacked bilayer graphene (BLG) on the other hand allows electrostatic tunability of the high-energy parabolic dispersion – as shown by experimental spectroscopy and transport measurements [38, 93, 94] as well as theoretical calculations [26, 174]. Surprisingly, there is no consensus between experiment and theory regarding its low-energy bandstructure. For example, quantum Hall measurements identified an eightfold degeneracy of the lowest Landau level (LLL), facilitated by a two-fold spin, valley and orbital degeneracy, consistent with a low-energy parabolic dispersion [28, 34, 104]. When including higher-order hopping terms one would however expect four Dirac cones at each valley, inconsistent with experimental findings of quantum oscillations. While such quantum Hall measurements provide an elegant means to identify band symmetries, also the presence of strong exchange-driven phases in suspended bilayer graphene [28, 33, 34, 175] is inconsistent with low-energy a linear dispersion of BLG. On the other hand, signatures of changes in Fermi surface topology due to trigonal warping have been identified in the case strong displacement fields are applied and sizable bandgaps are opened. Specifically, in strongly biased BLG [1, 35, 105, 106], Bernal trilayer graphene [146, 176], rhombohedral trilayer graphene [24, 25] and Bernal tetralayer graphene [177] it was shown that a trigonally warped low-energy Fermi surface topology is consistent with the unusual ordering of quantum Hall states.

The goal of the present work is to resolve the puzzle why at zero and low electric displacement field the linear dispersion and electric-field controlled changes of topology (Fig. 1a-c) have not been observed experimentally in BLG. Signs of topological changes in the bandstructure should be detectable e.g. in quantizing magnetic field in which the presence of four Dirac cones would lead to a clearly distinct sequence of LL compared to the known sequence arising from a parabolic dispersion.

To reveal the detailed low-energy bandstructure and detect electric-field controllable linear dispersing bands, we prefer here the hexagonal Boron Nitride (hBN) encapsulated Bernal-stacked bilayer graphene sample system over suspended BLG – even though in both samples quality is similar. In the latter however, due to the low-dielectric constant of the dielectric (vacuum), the exchange energy scale seems to dominate the low-energy physics leading to a variety of nontrivial groundstates [28, 33, 34, 175]. Our encapsulated BLG is equipped with graphite top-and bottom gates and two terminal contacts (see Supplemental Material). All measurements were recorded in a cryostat at a temperature of 10 mK employing standard lock-in techniques at 78 Hz and an ac bias current of 1 nA. By varying both gate voltages, we were able to tune n and D independently. Since we on the one side use two-terminal measurements (i.e. contact resistance cannot be easily determined), and on the other side show measurements down to B=0 the respective LL are not fully developed (quantized) yet, and we hence show $\mathrm{d}G/\mathrm{d}n$ values. We complement our measurements with tight binding single particle bandstructure calculations of expected quantum Hall states in BLG at zero and low D-fields, in which we include also the weaker inter-layer coupling parameters γ_3 and γ_4 as well as an energy difference between dimer and non-dimer atomic sites Δ' [26, 85] (Fig. 1a) (see Supplemental Material for technical details of the calculations).

We first discuss the tight binding calculations of LL that are used as a tool to later experimentally identify the transition from Dirac bands to a gapped parabolic dispersion. Without the presence of an interlayer potential difference U and in the case trigonal warping is ignored or irrelevant due to disorder, the bandstructure of BLG exhibits a nearly low-energy parabolic dispersion (Fig 1b (left)) [26, 28, 37]. Consistent with previous experiments conducted in quantizing magnetic fields $B > 0.5$ T [28, 33, 104], this leads to an eight-fold degeneracy of the lowest Landau level (LLL) due to spin, valley and orbital degrees of freedom, and to a four-fold degeneracy of all higher Landau levels due to spin and valley degrees of freedom (see

Supplemental Material). In case that the low-energy bandstructure at the charge neutrality point can be resolved below a Fermi energy $E \sim \pm 1$ meV, the bandstructure dramatically changes when including trigonal warping, and three off-center and one center cones emerge in each valley (also referred to as mini Dirac cones), resulting from the weaker skew interlayer hopping term γ_3. The four cones with a Dirac-like spectrum resemble a four-fold copy of the spectrum of monolayer graphene, for which the LLL is shared equally by electrons and holes, overall leading to a 16-fold degeneracy (2 spins, 2 valleys, 4 mini Dirac cones). This would result in the appearance of quantum Hall states with filling factors $\nu = \frac{hn}{eB} = \pm 8$ [15, 37, 104]. In addition, the second skew interlayer hopping term γ_4 and on-site parameter Δ', describing the energy difference between atoms A and A' or B and B', create an energetic asymmetry between these cones [26]. While the center cone of the conduction and valence band meet at zero energy, the off-center cones meet at higher energies (Fig. 1b, c; more information on the impact of γ_3, γ_4, *and* Δ' is given in Fig. S1 in the Supplemental Material). In quantum Hall measurements, these changes in the bandstructure can be discerned only at $B < 0.2$ T since here, the inverse of the magnetic length $l_B = \sqrt{\hbar/(eB)}$ with $\hbar = h/2\pi$ and Planck's constant h is smaller than the distance in momentum space between two adjacent mini Dirac cones (i.e. below the fields at which magnetic breakdown appears) [105, 106].

Fig. 1e shows the calculated inverse compressibility ($\partial\mu/\partial n$ with chemical potential μ, n charge carrier density) as function of n and B at $D = 0$ V/nm (Landau fan diagram). Here, larger energy gaps in the Landau level spectrum (Fig. 1f) manifest as prominent peaks corresponding to quantum Hall states that are labeled by numerals (the calculations include γ_0, γ_1, γ_3, γ_4 and Δ', spin splitting is included manually in the LL for the figures, both valleys are included in the calculation and are fully degenerate; see Supplemental Material for further details). While quantum Hall states with $\nu = \pm 8$ indeed exhibit the largest compressibility and go down to the lowest B in the valence/ conduction band also the quantum Hall state with $\nu = -4$ (but not $\nu = +4$) is very robust, i.e., it can be resolved until very low B (Fig. 1e), which is a manifestation of the electron-hole asymmetry. Neglecting the spin and valley degrees of freedom, the three off-center cones exhibit a three-fold degenerate LLL and are shifted to higher energies. Thus, the center cone LLL is non-degenerate with the LLL that belong to the off-center cones (Fig 1f). Since the LLL is shared between electrons and holes, the non-degenerate center cone as well as one of three LL originating from the three off-center cones contribute to hole transport and give rise to quantum Hall states with ν = -8 and ν = -4 respectively. The other two LL stemming from the three off-center cones contribute to electron transport and give rise to a quantum Hall state with $\nu = +8$. The quantum Hall state with $\nu = +4$ only emerges at larger B where the degenerate LL diverge. With increasing n, the conventional sequence quantum Hall states with filling factors $\nu = \pm12, \pm16, \pm20$ is recovered the Fermi level lies above the Lifshitz transition where the Fermi surface is fully connected.

The theory thus shows in great detail how the presence of four Dirac cones can unambiguously be identified in experiment. Figure 1g shows now the normalized derivative of the measured two-terminal conductance |dG/dn| as a function of n and B at $D = 0$ V/nm. Quantum Hall states appear as plateaus in the conductance and thus as dips in |dG/dn| and can be assigned by their corresponding slopes in the Landau fan diagram (see Supplemental Material). Consistent with our theoretical simulations, quantum Hall states with $\nu = \pm8$ are the most robust and can be observed at the smallest B, down to $B \approx 0.05$ T which reveals the presence of four mini Dirac cones. Additionally, due to electron-hole asymmetry, the quantum Hall state with ν = -4 appears at slightly larger magnetic fields (B ≈ 0.15 T), while the $\nu = +4$ quantum Hall state only appears above 0.2 T when the magnetic breakdown occurs (indicated by dashed lines in Fig 1e and g). At magnetic fields above 0.3 T, a sequence of even integer quantum Hall states appears which is consistent with previous measurements in freestanding BLG [28, 29, 33, 34] and which reveals the high quality of our sample. Here, the spin degeneracy is likely lifted due to Coulomb interactions resulting in a two-fold degeneracy (valley) instead of the predicted four-fold degeneracy (spin and valley) [37, 109, 111]. Notably, some of the non-four-fold degenerate quantum Hall states including the quantum Hall states with $\nu = \pm6$ also go down to below 0.3 T and then merge with the quantum Hall states with $\nu = \pm4$ and demand further investigation. Since spin and valley splitting are both neglected in our theoretical simulations, this two-fold degeneracy is only observed in our experimental data but not visible in the calculated inverse compressibility.

While the measurements at zero displacement fields show the existence of four Dirac cones near charge neutrality, we now show the tunability of the

Dirac cones with concomitant bandgap opening controlled by D. We first discuss our calculations and corresponding charge transport measurements at constant small D, where already a bandgap has opened up in the previously linear Dirac spectrum of BLG. This goes along with drastic changes of the bandstructure: the center cone diminishes whereas the three off-center cones (Fig. 2a,b) with however a parabolic dispersion remain, which we consequently refer to as pockets.

In the valence band, where the three off-center cones already dominate at $D = 0$ due to electron-hole asymmetry, the number of pockets changes from four to three at finite D (Fig. 2b) resulting in a reordering of expected quantum Hall states (Fig. 2c-e) [85, 178]. We expect the LLL to be six-fold degenerate at low B due to the remaining three leg pockets (3 pockets, 2 spins, the 2 valleys are degenerate, Fig. 2d,e)[105, 106] and the $\nu = -6$ quantum Hall state is expected to be the most robust for hole doping (Fig. 2c). These theoretical considerations are confirmed by our measurements. As shown in Fig. 2e, for $D = 50$ mV/nm the $\nu = -6$ quantum Hall state can be resolved down to very low magnetic fields of $B = 100$ mT. Surprisingly, this also holds for the $\nu = -3$ quantum Hall state which could result from spin or valley polarization at low B and low n due to Stoner ferromagnetism that can occur in the vicinity of the Lifshitz transition [1, 35, 36]. At $B = 600$ mT, a sudden change in the degeneracy of Landau level takes place for $n < 0$ which can be attributed to the magnetic breakdown. Here the effects of the trigonal warping are no longer relevant and we can observe all integer quantum Hall states. It is worth noting that at larger densities, quantum Hall states with $\nu = -7$ and $\nu = -9$ appear below $B = 500$ mT. In this regime, the Fermi energy level lies above the Lifshitz transition and quantum Hall states start to become valley and spin polarized with increasing magnetic field.

The effects of band flattening and disappearing of the low-energy Dirac spectrum can be also seen in the conduction band (Fig. 2a) where the center pocket also becomes less prominent with increasing D. However, due to electron-hole asymmetry the center cone is still dominating at $U = 17$ meV and the band becomes flatter with increasing U until $U \approx 60$ meV. At $U = 17$ meV, the degeneracy of quantum Hall states is not as much affected by trigonal warping as in the valence band and quantum Hall states with even ν appear first in the magnetic field in our conductance measurements (Fig.

2e). Remarkably, the quantum Hall states with $\nu = +3$ and $\nu = +4$ disappear at a magnetic field of 0.5 T and then reemerge at about 0.6 T (Fig. 2c,e) resulting from a crossing of two bands that correspond to different valleys (Fig. 2d).

The active control and lifting of the four-fold Dirac spectrum can be also traced by controlling the displacement field at constant B (Fig. 3a,b). For example, at $B = 0.25$ T (Fig. 3a) the magnetic breakdown has already occurred for low D resulting in the appearance of eight-fold degenerate quantum Hall states at $D = 0$ mV/nm (2 valleys, 2 spins, 2 orbits). At 3 mV/nm < |D|< 25 mV/nm the quantum Hall state with $\nu = \pm 2$ appears due to valley polarization [33] while at $|D| > 20$ mV/nm the three pockets can be resolved individually and a crossover from a two-fold (two spins) to a three-fold degenerate Landau level spectrum (three pockets) appears at hole doping (yellow circle in Fig. 3a). Higher LL are four-fold degenerate (2 valleys, 2 spins) above a Lifshitz transition since their corresponding Fermi surface is fully connected. For larger *B,* e.g. at $B = 0.4$ T (Fig. 3b), the crossover to the parabolic shifts to larger D where the three pockets are more pronounced. Here also the crossings of LL stemming from different valleys in the conduction band can be discerned in the n vs. B plot.

In conclusion, we show that bilayer graphene exhibits a highly tunable low-energy bandstructure where four distinct Dirac cones merge into a parabolic band or into three pockets with a gapped parabolic dispersion. Here, topological transitions result in a complex series of Landau levels that we extract by virtue of numerical diagonalization methods based on a realistic tight binding model and measure for the first time in high quality hBN-encapsulated samples. These results show that the simple and seemingly well understood Bernal bilayer graphene is a true example of a long sought tunable Dirac material with linear dispersion at low energies[179]. It remains to be investigated, how trigonal warping affects the renormalized many-body band structure in high quality freestanding BLG samples where interaction effects dominate even at low electric fields [28, 33].

Acknowledgements

R.T.W. and A.M.S. acknowledge funding from the Deutsche Forschungsgemeinschaft (DFG, German Research Foundation) under the SFB 1073 project B10. K.W. and T.T. acknowledge support from JSPS KAKENHI (Grant Numbers 19H05790, 20H00354 and 21H05233).

Author contributions

A.M.S. and M.S. fabricated the devices and conducted the measurements. A.M.S. conducted the data analysis. N.J. performed the theoretical simulations supervised by L.S.L.. K.W. and T.T. grew the hexagonal boron nitride crystals. All authors discussed and interpreted the data. R.T.W. supervised the experiments and the analysis. The manuscript was prepared by A.M.S., N.J., L.S.L. and R.T.W. with input from all authors.

Corresponding authors

R. Thomas Weitz (thomas.weitz@uni-goettingen.de)

Competing interests

Authors declare no competing interests.

Data availability

The datasets generated during and/or analyzed during the current study are available from the corresponding author on reasonable request.

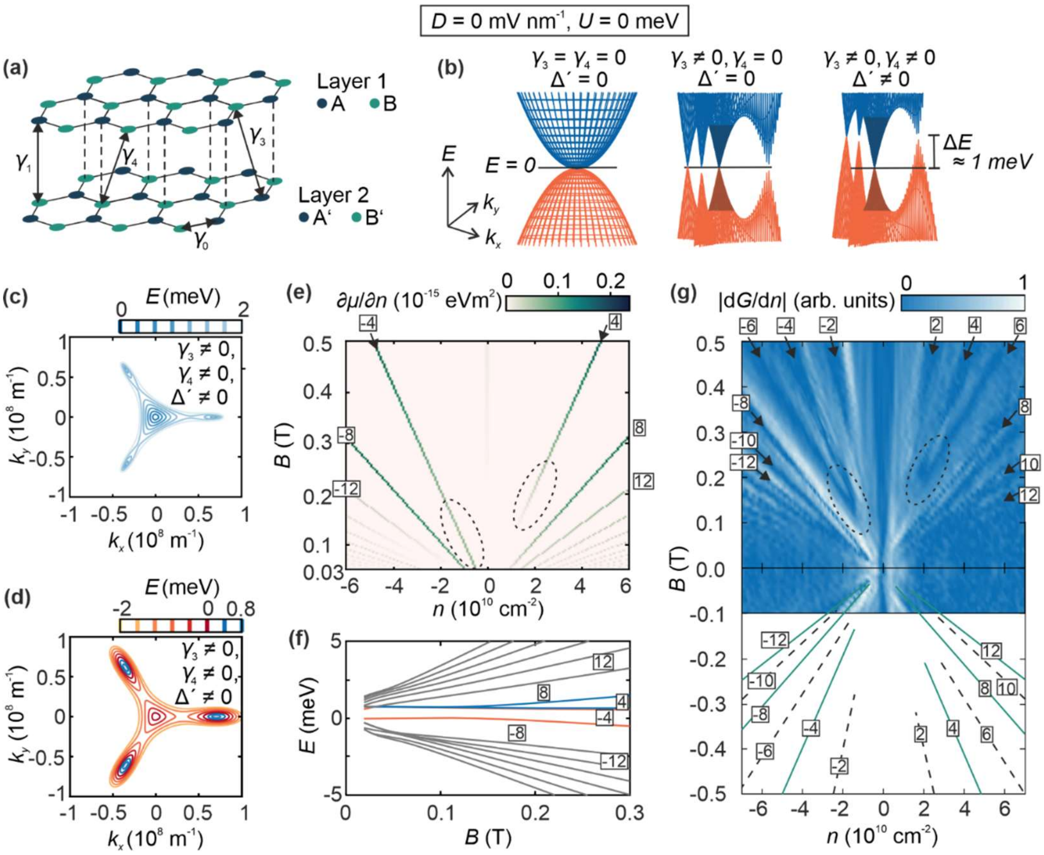

FIG. 1. Lattice, bandstructure and quantum Hall states of Bernal bilayer graphene at $D = 0$ mV/nm. (a) Lattice structure and hopping parameters of Bernal bilayer graphene. (b) Bandstructure of bilayer graphene in an energy range of -2 mV to +2 mV at $D = 0$ mV/nm calculated with a tight binding model including various subsets of coupling parameters. The center cones are shaded darker. (c,d) Fermi surface contour of the conduction band (c) and valence band (d) of bilayer graphene at different Fermi energy levels. (e) Calculated inverse compressibility ($\partial\mu/\partial n$) as a function of charge carrier density and magnetic field at $D = 0$ mV/nm and temperature $T = 0.1$ K. The corresponding quantum Hall states are labeled by numerals. The regions in which quantum Hall states with filling factors $\nu = \pm 4$ end are highlighted by dashed circles. (f) Evolution of Landau levels as a function of magnetic field at $D = 0$ mV/nm. The four lowest Landau levels are colored whereas Landau levels contributing to hole transport are colored in red and Landau levels contributing to electron transport are colored in blue. The lowest red colored Landau level is coming from the center mini Dirac cone, the other three lowest Landau levels are coming from the three off-center mini Dirac cones. Filling factors are indicated by numerals. A larger version of this plot is shown in Fig. S1. (g) Derivative of the normalized conductance measured

as a function of the charge carrier density and the magnetic field at $D = 0$ mV/nm. Blue regions correspond to vanishing differential conductance (i.e. a conductance plateau). The slopes of the lowest quantum Hall states are traced by lines in the mirror image. Every fourth quantum Hall state is colored in green to make comparison with theory (Fig. 1e) easier. The regions in which quantum Hall states with filling factors $\nu = \pm 4$ are highlighted by dashed circles.

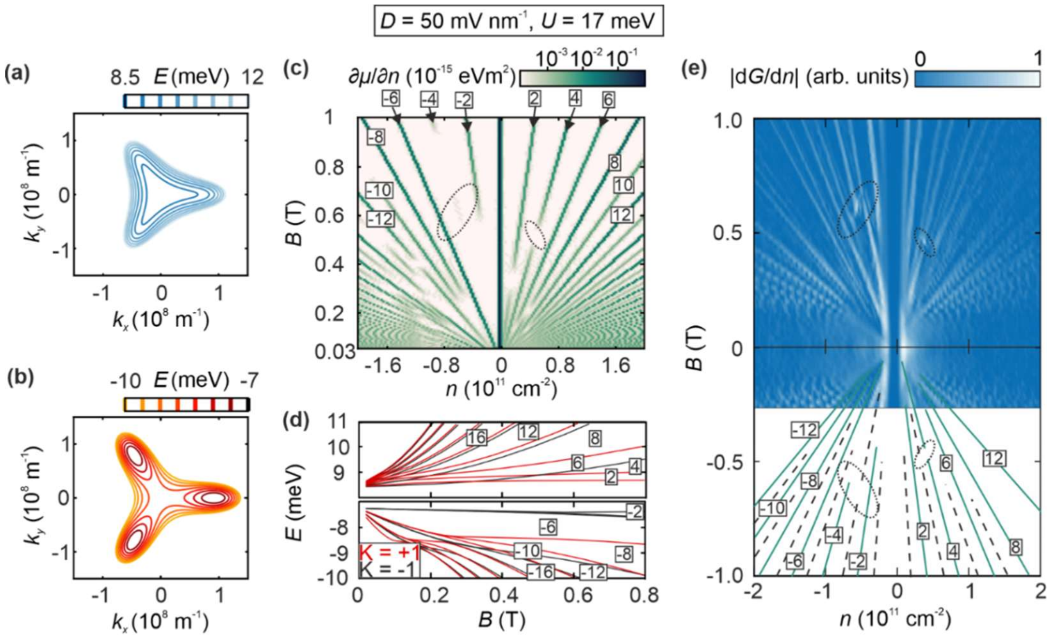

FIG. 2. **Bandstructure and quantum Hall states of bilayer graphene at finite D.** (a,b) Fermi surface contour of the conduction band (a) and valence band (b) of bilayer graphene at different Fermi energy levels at $\mathrm{U} = 17$ meV. (c) Calculated inverse compressibility ($\partial \mu / \partial \mathrm{n}$) as a function of charge carrier density and magnetic field at $U = 17$ meV and temperature $T = 0.1$ K. The corresponding quantum Hall states are labeled by numerals. Regions corresponding to Landau level crossings are marked by dotted circles. (d) Evolution of Landau levels as a function of the magnetic field. (e) Derivative of the normalized conductance measured as a function of the charge carrier density and the magnetic field at $D = 50$ mV/nm. The slopes of the lowest even quantum Hall states are traced by green lines, the slopes of the lowest odd quantum Hall states are traced by dashed lines. The corresponding quantum Hall states are labeled by numerals. The regions corresponding to Landau level crossings are marked by dotted circles.

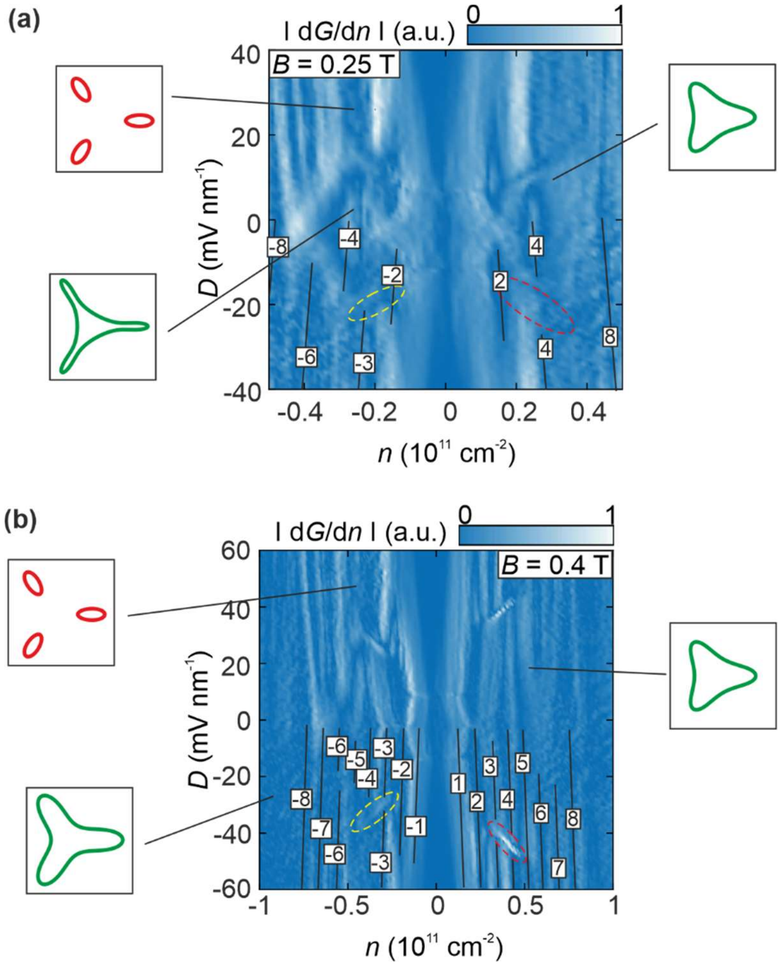

FIG 3. Controlling the magnetic breakdown by applying an electric displacement field. (a, b) Derivative of the normalized conductance measured as a function of the charge carrier density and electric displacement field at $B = 0.25$ T (a) and $B = 0.4$ T (b). Quantum Hall states are labeled by numerals and traced by lines. Note, that the quantum Hall states are symmetric for positive and negative values of D but the labelling was restricted to $D < 0$ for better visibility. Transitions between quantum Hall states due to trigonal warping and electron-hole asymmetry are highlighted by yellow dotted lines, crossings between Landau levels of different K valleys are highlighted by red dotted circles. Schematics of Fermi contours corresponding to regions in which the magnetic breakdown has already occurred and to regions in which the magnetic breakdown has not yet occurred are shown in red and green, respectively.

6 Manuscript: Quantum cascade of correlated Phases in trigonally warped bilayer graphene

The results presented in this Chapter have been published in Reference [1]. The full article is reprinted below with permission from Springer Nature. Material from Anna M. Seiler et al., Quantum cascade of correlated phases in trigonally warped bilayer graphene, *Nature*, published 2022, Springer Nature.

Nature 608, 298-302 (2022)
DOI: 10.1038/s41586-022-04937-1

Contributions:

I fabricated the devices (device A in the article corresponds to Stack 99 that is introduced in Chapter 3.5 and device B in the article corresponds to Stack 82), conducted all measurements, and performed the data analysis. I further prepared the first version of the manuscript except from some theoretical sections and I designed all figures. In addition, I produced the final version of the publication.

Article

Quantum cascade of correlated phases in trigonally warped bilayer graphene

https://doi.org/10.1038/s41586-022-04937-1

Received: 6 November 2021

Accepted: 7 June 2022

Anna M. Seiler[1,2], Fabian R. Geisenhof[2], Felix Winterer[2], Kenji Watanabe[3], Takashi Taniguchi[4], Tianyi Xu[5], Fan Zhang[5]✉ & R. Thomas Weitz[1,2,6]✉

Divergent density of states offers an opportunity to explore a wide variety of correlated electron physics. In the thinnest limit, this has been predicted and verified in the ultraflat bands of magic-angle twisted bilayer graphene[1–5], the band touching points of few-layer rhombohedral graphite[6–8] and the lightly doped rhombohedral trilayer graphene[9–11]. The simpler and seemingly better understood Bernal bilayer graphene is also susceptible to orbital magnetism at charge neutrality[7] leading to layer antiferromagnetic states[12] or quantum anomalous Hall states[13]. Here we report the observation of a cascade of correlated phases in the vicinity of electric-field-controlled Lifshitz transitions[14,15] and van Hove singularities[16] in Bernal bilayer graphene. We provide evidence for the observation of Stoner ferromagnets in the form of half and quarter metals[10,11]. Furthermore, we identify signatures consistent with a topologically non-trivial Wigner–Hall crystal[17] at zero magnetic field and its transition to a trivial Wigner crystal, as well as two correlated metals whose behaviour deviates from that of standard Fermi liquids. Our results in this reproducible, tunable, simple system open up new horizons for studying strongly correlated electrons.

Electron–electron interactions can give rise to macroscopic quantum phenomena such as magnetism, superconductivity and quantum Hall (QH) effects. It is well known that interaction effects can be boosted near where the density of states (DOS) of electrons diverges. One remarkable example is twisted bilayer graphene, in which the Dirac minibands become flattest when the twist angle is near the so-called magic angle[1]. Indeed, orbital ferromagnetism[18], the quantum anomalous Hall (QAH) effect[19] and nematic superconductivity[20] have been observed in this delicately designed system[5]. In fact, strongly interacting behaviour has also been discovered in the simpler, naturally occurring, Bernal bilayer graphene (BLG) at charge neutrality. Under a high magnetic field, its bands quantize into Landau levels (LL) that are exactly flat, and both the fractional QH effect and QH ferromagnetism have been reported[6,13,21,22]. Near zero magnetic field, its quadratic band touching points that each has a non-trivial winding number of ±2 are susceptible to spontaneous gaps driven by topological orbital magnetism[7], as evidenced by a QAH octet observed in free-standing BLG[13]. Interestingly, when lightly doped, the trigonal warping of the Fermi surface of BLG (and its rhombohedral cousins) attributed to the interlayer next-nearest-neighbour coupling[23] becomes pronounced. The winding number and the C_{3z} symmetry dictate a deformation of each quadratic cone into one central Dirac cone and three surrounding ones. An electric field can gap these cones and even invert the central one[14,15]. These produce multiple Lifshitz transitions and van Hove singularities (vHSs) tunable by the electric field and the charge density. However, so far, correlated phases mediated by this trigonal warping effect have escaped experimental observation in BLG, although ferromagnetism and superconductivity have been recently reported in lightly doped rhombohedral trilayer graphene (RTG)[10,11].

Here we show that, at large electric fields, gate-tunable correlated insulating and metallic phases emerge in lightly doped high-quality BLG, without the presence of a moiré potential. The two insulating phases are consistent with a Wigner crystal and an unprecedented Wigner–Hall crystal, respectively, and the novel metallic phases are most likely fractional metals that develop LLs and correlated metals that show no signs of Landau quantization.

The investigated BLG flakes are encapsulated in hexagonal boron nitride (hBN) and equipped with graphite top and bottom gates as well as graphite contacts in a two-terminal configuration (Extended Data Fig. 1 and Methods). By varying both gate voltages, the charge carrier density n and the perpendicular electric field E can be tuned. Figure 1a shows the two-terminal conductance G in arbitrary units (a.u.) measured at zero magnetic field B and a temperature T of 10 mK. A crystallographic alignment between the BLG, hBN and graphite contacts that would produce a moiré pattern can be excluded, given the clear absence of additional conductance minima at higher density[24,25].

Magnetotransport in bilayer graphene

We focus our discussions on the hole side at large electric fields where the most distinctive features are observed; an onset of similar physics is observed on the electron side, and the features at low electric fields[6,14,15,24,25] exemplify the ultrahigh quality of our devices (Methods and Extended Data Figs. 2 and 3). At larger electric fields, the trigonal warping becomes more visible as the central hole pocket is inverted into an electron pocket at lower energies (Fig. 1b,f). At very low doping, the Fermi surface is consequently composed of three disconnected

---

[1]1st Physical Institute, Faculty of Physics, University of Göttingen, Göttingen, Germany. [2]Physics of Nanosystems, Department of Physics, Ludwig-Maximilians-Universität München, Munich, Germany. [3]Research Center for Functional Materials, National Institute for Materials Science, Tsukuba, Japan. [4]International Center for Materials Nanoarchitectonics, National Institute for Materials Science, Tsukuba, Japan. [5]Department of Physics, University of Texas at Dallas, Richardson, TX, USA. [6]Center for Nanoscience (CeNS), Munich, Germany. ✉e-mail: zhang@utdallas.edu; thomas.weitz@uni-goettingen.de

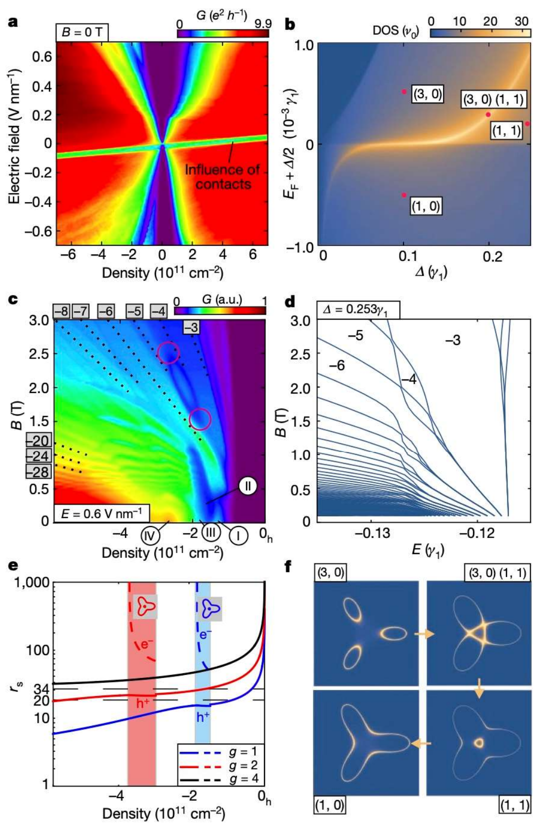

Fig. 1 | Magnetotransport in bilayer graphene. a, Conductance map as a function of E and n measured at $B = 0$ T and $T = 10$ mK. **b**, Calculated DOS as a function of the interlayer potential difference Δ and the Fermi energy E_F (in units of the constant DOS ν_0 of the BLG without trigonal warping). The red dots correspond to the calculated Fermi surfaces shown in **f**. The Fermi surface topology is classified by two invariants (i, j), where i and j are the numbers of hole and electron pockets, respectively. The brightest line manifests the vHS at the Lifshitz transition between the (3, 0) and the (1, 0) Fermi surfaces for $\Delta < 0.1\gamma_1$ or the (3, 0) and the (1, 1) Fermi surfaces for $\Delta > 0.1\gamma_1$. The $E_F = -\Delta/2$ line at $\Delta > 0.1\gamma_1$ shows the (dis)appearance of the central electron pocket at the Lifshitz transition between the (1, 1) and the (1, 0) Fermi surfaces. **c**, Fan diagram of the conductance at $E = 0.6$ V nm^{-1}. QH states are traced by black dotted lines and corresponding filling factors (ν) are indicated by arabic numerals. The two crossings between the $\nu = -4$ and $\nu = -5$ QH states are highlighted by red circles. New correlated phases are indicated by roman numerals. **d**, Calculated LL spectrum at $\Delta = 0.253\gamma_1$ for a non-degenerate Fermi surface. Δ is the interlayer potential difference induced by E. $\gamma_1 \approx 400$ meV is the interlayer nearest-neighbour coupling. The filling factors of QH states are indicated by arabic numerals. **e**, The calculated Wigner–Seitz radius r_s as a function of n (see Methods for details) for the quadruply ($g = 4$, black line), doubly ($g = 2$, red lines) and singly ($g = 1$, blue lines) degenerate Fermi surfaces, respectively. The solid lines are for the outer hole (h$^+$) pockets and the dashed lines are for the inner electron (e$^-$) pockets. The shaded regions are where the Fermi surface is annular between the two Lifshitz transitions. $r_s = 20$ and $r_s = 34$ are the thresholds for the ferromagnetic instability and the Wigner crystallization of 2D electron gases, respectively. **f**, Calculated trigonally warped Fermi surfaces under a large E field. The classifying invariants (i, j) are defined in **b** above. The arrows indicate the two Lifshitz transitions with increasing $|n|$.

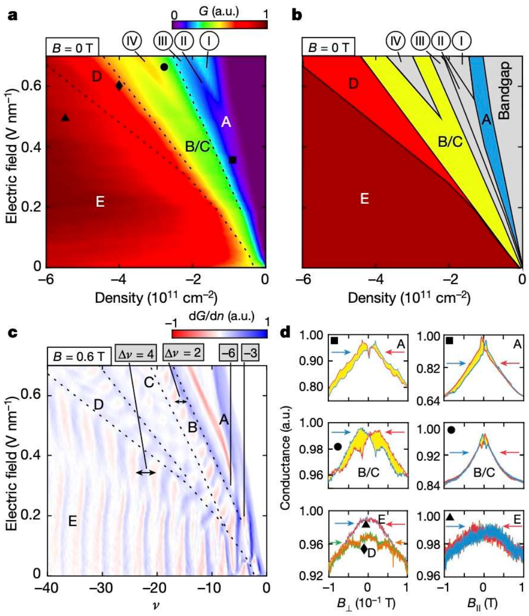

Fig. 2 | Stoner ferromagnetism in bilayer graphene. a, Conductance map as a function of E and n measured at $B = 0$ T for the valence band and positive electric fields. Stoner phases are labelled with the letters A–E and separated by dashed lines. New correlated phases are labelled by the roman numerals I–IV. **b**, Schematic of the phase diagram shown in **a**. **c**, Density derivative of conductance as a function of E and ν at $B = 0.6$ T. **d**, Hysteresis of the conductance as a function of the out-of-plane and in-plane magnetic fields in phase A ($n = -8.5 \times 10^{10}$ cm^{-2}, $E = 0.36$ V nm^{-1}), phase B/C ($n = -2.6 \times 10^{11}$ cm^{-2}, $E = 0.65$ V nm^{-1}), phase D ($n = -4.0 \times 10^{11}$ cm^{-2}, $E = 0.6$ V nm^{-1}) and phase E ($n = -5.5 \times 10^{11}$ cm^{-2}, $E = 0.5$ V nm^{-1}). The forward sweeps in **d** are shown in blue (green for phase D) and the backwards ones in red (orange for phase D). The hysteresis loop areas are shaded in yellow.

hole pockets ((3, 0) panel in Fig. 1f) that move apart with increasing E. At slightly higher doping, these three pockets connect, and the Fermi surface undergoes the first Lifshitz transition featuring a vHS and then becomes an annulus, that is, an inner electron pocket and an outer hole pocket ((1, 1) panel in Fig. 1f). As the doping increases further, the hole pocket enlarges whereas the electron pocket contracts and disappears in the second Lifshitz transition ((1, 0) panel in Fig. 1f). Figure 1c shows the Landau fan diagram at $E = 0.6$ V nm^{-1}. At very low doping, the three disconnected hole pockets result in a three-fold LL degeneracy per spin–valley, and only the filling factor $\nu = -3$ and $\nu = -6$ QH ferromagnetic states emerge at $B < 1.2$ T (Fig. 1c and Extended Data Fig. 3g), whereas at $B > 2.5$ T all the integer QH ferromagnetic states are resolved. Between 1.5 T and 2.5 T there are two crossings between the $\nu = -4$ and $\nu = -5$ QH states, originating from the emergence and contraction of the inner electron pocket (Fig. 1f) whose LLs do not mix with the hole LLs[14,15]. The magnetic fields and densities associated with the observed LL crossings match well with the calculated LL spectrum (Fig. 1d) and density range with an annular Fermi surface (Fig. 1e) for the non-degenerate case.

Moreover, at $B < 1.3$ T, the conductance pattern strongly deviates from any conventional LL sequence (Fig. 1c). For example, in sharp contrast to the established single-particle picture[6,26], a complex non-monotonous E- and n-dependent variation of the conductance emerges for $E > 0.1$ V nm^{-1} even at $B = 0$ (Fig. 1a). Below we identify

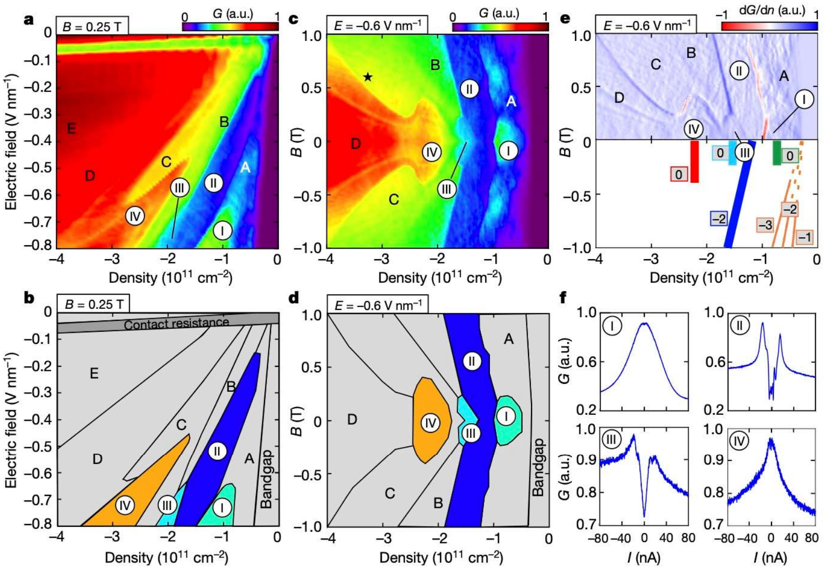

Fig. 3 | New correlated phases at large electric fields. **a**, Conductance map as a function of E and n measured at $B = 0.25$ T for the valence band and negative electric fields. Stoner phases are labelled with the letters A–E. New correlated phases are labelled by the roman numerals I–IV. **b**, Schematic of the phase diagram shown in **a**. **c**, Conductance map as a function of B and n measured at $E = -0.6$ V nm^{-1}. Indication of the onset of insulating phase V is marked by a star (Extended Data Fig. 12). **d**, Schematic of the phase diagram shown in **c**. **e**, Top: density derivative of the conductance in **c**. Bottom: schematic of the slopes of the lowest integer QH states and the phases I–IV. The corresponding slopes are indicated by arabic numerals. The lines are solid if the states are present and dashed otherwise. **f**, Conductance as a function of d.c. current bias for the phases I–IV at $E = -0.6$ V nm^{-1} and $B = 0$ T. The corresponding densities are $n = 0.8 \times 10^{11}$ cm^{-2} for phase I, $n = 1.1 \times 10^{11}$ cm^{-2} for phase II, $n = 1.4 \times 10^{11}$ cm^{-2} for phase III and $n = 2.2 \times 10^{11}$ cm^{-2} for phase IV.

various phases (A–E and I–V) by their conductance and evolution in the space of temperature, density, magnetic and electric fields, and bias current. This unexpected phase diagram of BLG stems from the intricate interplay between electron–electron interaction and trigonal warping.

Stoner spin–valley ferromagnetism

The prominent steps in the conductance that already start to appear at low electric fields above 0.1 V nm^{-1} in Fig. 1a are highlighted in Fig. 2a,b for positive electric fields. We label regions of different constant conductance with the letters A–E. Their E and n dependence is reminiscent of those of half and quarter metals with spontaneous spin–valley polarization or coherence observed recently in RTG[10], analogous to the textbook Stoner ferromagnets. Indeed, the experimental signatures observed in our BLG agree well with the exchange-interaction-driven ferromagnetic phases that can be well resolved at $B = 0.6$ T (Fig. 2c).

Phase A is close to the valence-band edge, and the $\nu = -3$ and $\nu = -6$ QH states emerge owing to the three-fold degeneracy of the trigonally warped Fermi surface ((3, 0) panel in Fig. 1f). This phase shows slight out-of-plane magnetic hysteresis but a large in-plane one (Fig. 2d), and is most consistent with a quarter metal with in-plane spin polarization and inter-valley coherence. At higher densities, phase B/C emerges at $B = 0$. At finite magnetic fields, this phase splits up into two distinct phases B and C. Phase B exhibits two-fold LL degeneracy consistent with a half metal[10] (Fig. 2c). Its strong hysteresis that is of the same order in in-plane and out-of-plane magnetic fields (Fig. 2d) is indicative of spin polarization. Unlike phases A and B, phase C exhibits conductance oscillations versus E instead of n, possibly owing to a partial polarization or a more complex order. Phase D shows similar LL degeneracy and conductance oscillations to phase C (Fig. 2c) but no magnetic hysteresis (Fig. 2d), which may indicate inter-valley coherence. Phase E emerges at higher densities, exhibits four-fold LL degeneracy (Fig. 2c) and an absence of magnetic hysteresis (Fig. 2d), and is most consistent with a full metal without spin–valley polarization.

Consistently, our calculation for $E = 0.6$ V nm^{-1} and the measured densities reveals that with four-fold or two-fold degeneracy, the Wigner–Seitz radius r_s exceeds 20 (Fig. 1e and Methods), a threshold for the ferromagnetic instability of two-dimensional (2D) electron gases[27]. Moreover, phases A, B and E are below the first Lifshitz transitions and the vHS of the non-, two-fold- and four-fold-degenerate Fermi surfaces, respectively, whereas phases C and D are on the two sides of the second Lifshitz transition of the doubly degenerate Fermi surface (Figs. 1e and 2c). As the DOS of BLG is smaller than that of RTG, phases A–E emerge in narrower density ranges.

New correlated metallic and insulating phases

Besides the Stoner phases, we can also identify several phases that compete with them yet have not been previously reported in graphene systems. We focus hereafter on these new phases in the large-negative-electric-field range, and there are at least four distinct phases at $B = 0$ (I–IV, Fig. 3a–d) that can be identified by steps in the conductance and stabilities in the space of T, n, B, E and bias current I. All four phases were also identified in a second device (Methods and Extended Data Fig. 4). For low doping, the conductance increases with increasing density until it reaches a plateau (phase I). The conductance then drops significantly (phase II) with further increasing density until it increases again (phase III). In addition, another plateau of higher conductance can be observed at still higher densities (phase IV). Although these phases are all unstable against the Stoner phases at large magnetic fields ($B > 0.5$–1.5 T), their mutual phase boundaries

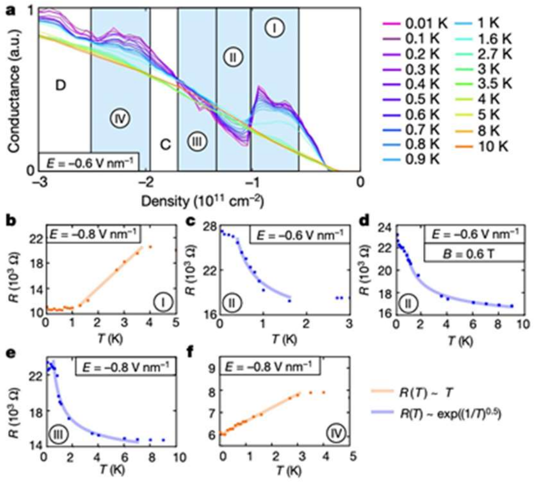

Fig. 4 | Temperature stability of new correlated phases. a, Conductance as a function of n at $E = -0.6$ V nm^{-1} and different temperatures. The new correlated phases I–IV are highlighted in light blue. **b**–**f**, Temperature dependence of the resistance in phase I at $n = -1.3 \times 10^{11}$ cm^{-2}, $E = -0.8$ V nm^{-1} and $B = 0$ T (**b**), phase II at $n = -1.2 \times 10^{11}$ cm^{-2}, $E = -0.6$ V nm^{-1} and $B = 0$ T (**c**), phase II at $n = -1.4 \times 10^{11}$ cm^{-2}, $E = -0.6$ V nm^{-1} and $B = 0.6$ T (**d**), phase III at $n = -2.0 \times 10^{11}$ cm^{-2}, $E = -0.8$ V nm^{-1} and $B = 0$ T (**e**), and phase IV at $n = -3.2 \times 10^{11}$ cm^{-2}, $E = -0.8$ V nm^{-1} and $B = 0$ T (**f**). The linear temperature dependence in phases I and IV is highlighted by orange lines. For phases II and III $R(T) = R_0 e^{\sqrt{T_0/T}}$ (blue lines) is fitted by using $R_0 = 12{,}932.36\ \Omega$ and $T_0 = 0.1978$ K in **c**, $R_0 = 13{,}581.63\ \Omega$ and $T_0 = 0.1199$ K in **d**, and $R_0 = 12{,}142.09\ \Omega$ and $T_0 = 0.2189$ K in **e**.

and those with the Stoner phases exhibit sharp conductance changes at small magnetic fields (Fig. 3a–e).

Phase I is an island of relatively high conductance at very low densities close to the valence-band edge. It occurs in the density range below the first Lifshitz transition with a concomitant vHS of the non-degenerate Fermi surface (Fig. 1e) and exhibits an E-dependent phase boundary in the space of n and B against phase A (Fig. 3c–e and Extended Data Figs. 5 and 6). Its intimate connection to the trigonal warping and the layer polarization is also evidenced by the observation that its centre and extent in density increase with increasing electric field (Fig. 3a,b and Extended Data Fig. 6). Phase I exhibits intrinsic magnetism, as revealed by its magnetic hysteresis (Extended Data Figs. 5 and 7) that is, however, smaller than that of phase A. The in-plane magnetic hysteresis is larger than the out-of-plane one, indicating its in-plane spin order and inter-valley coherence. Moreover, large out-of-plane magnetic fields (Fig. 3c–e and Extended Data Fig. 8a) or applied bias currents (Fig. 3f and Extended Data Fig. 9) suppress phase I, which suggests that it is a correlated metal. This is further confirmed by the strong linear temperature dependence $dR/dT = 5{,}000\ \Omega\,K^{-1}$ with resistance $R = 1/G$ in phase I, compared with the 'normal' metallic phase at $E = 0$ and the Stoner phases (Fig. 4d and Extended Data Fig. 10); this linear behaviour is similar to that of strange metals observed in twisted bilayer graphene[28]. Surprisingly, although at low electric fields LLs are visible down to 0.2 T (Extended Data Fig. 3b), phase I shows no signs of Landau quantization, which could result from the possible large effective masses, open Fermi surfaces or strange-metal properties of this phase that require future inspection.

At slightly higher densities, an abrupt transition from phase I to phase II of lower conductance is visible (Fig. 3a–d and Extended Data Fig. 5). Remarkably, phase II shows an increasing resistance with decreasing temperature (Fig. 4c,d), which is indicative of an energy gap, and its low-temperature conductance not only matches that of the $\nu = -2$ QH state but also features a slope of −2 in the fan diagram (Fig. 3c–e and Extended Data Fig. 3g). The presence of an energy gap is also supported by a sudden increase in conductance at large increasing bias currents (Fig. 3f). These together provide strong evidence for a QAH phase with a Chern number of −2. In sharp contrast to the QAH octet reported in free-standing BLG[13], this QAH phase II is stabilized at finite densities that increase with increasing electric field (Fig. 3a,b and Extended Data Fig. 8e), which implies an intimate connection to the trigonal warping. Indeed, our calculation shows that phase II emerges between the two Lifshitz transitions of the non-degenerate annular Fermi surface (Fig. 1e) in which $r_s > 34$, a threshold for the Wigner crystallization of 2D electron gases[27], for the electron pocket. It can be suppressed by the magnetic field (Extended Data Fig. 8b), bias currents (Fig. 3f) and temperature (Fig. 4), but this QAH phase II is present at $B = 0$ T for 0.3 V nm$^{-1} < E < 0.8$ V nm^{-1} (Extended Data Fig. 6). While for $E < 0.6$ V nm^{-1} a larger electric field stabilizes it against the magnetic field, for $E > 0.8$ V nm^{-1} phase II becomes less stable to the magnetic field (Extended Data Figs. 6 and 8b).

The observation of a QAH phase emerging at $B = 0$ yet $n \neq 0$ is extraordinary. This indicates a topological gap opening at densities where the non-interacting phase and even the Stoner phases would not be gapped. Given that phase II with a large r_s in theory is topologically insulating, compressible in extremely low density and incommensurate with the BLG lattice, most consistent is a Wigner–Hall crystal phase, that is, an electron crystal with a quantized Hall conductance. Indeed, the temperature-dependent resistance scales as $R(T) \sim e^{\sqrt{T_0/T}}$ with a scaling parameter T_0, consistent with the anticipated Efros–Shklovskii hopping transport for electron crystals[29] (Fig. 4c,d). Such a Wigner–Hall crystal at a finite magnetic field was originally proposed by ref. [17], and here phase II may be viewed as its anomalous counterpart at $B = 0$. Elegantly, Wigner–Hall crystals can be described by the Diophantine equation (Methods).

Phase II is unstable to another gapped phase III at slightly higher densities. The two phases compete in nearly the same density space (Fig. 3a–e), and phase III dominates for $E > 0.8$ V nm^{-1} at $B = 0$ (Extended Data Fig. 6). Phase III shows a similar resistance and temperature scaling to phase II (Fig. 4e) but shows neither a slope nor a sign of any LL in the fan diagram, and in fact it can be suppressed by the magnetic field (Fig. 3c–e). Along a similar line of arguments, a potential candidate for phase III is a Wigner crystal. Phases II and III exhibit magnetic hysteresis of similar magnitudes, with stronger in-plane ones (Extended Data Fig. 7). Their phase boundary does not shift with increasing in-plane magnetic field (Extended Data Fig. 11). This suggests that phases II and III probably carry similar in-plane spin order and inter-valley coherence. Compared with phase I, both phases probably have larger magnitudes of spin polarization as they are more stable against large in-plane magnetic fields.

At higher densities the system enters a metallic phase IV of high conductance but unstable at the magnetic fields that favour the Stoner phases. In the fan diagram (Fig. 3c–e), phase IV has a similar shape to phase I but a larger critical magnetic field that increases with increasing E (Extended Data Fig. 8d). Phase IV competes with the half metals B/C and appears close to but below the vHS of the doubly degenerate Fermi surface (Fig. 1e). Compared with phase I, phase IV shows stronger and more isotropic magnetic hysteresis (Extended Data Fig. 7). Its linear temperature-dependent resistance (Fig. 4f) and stability in density, electric and magnetic fields, and bias current (Fig. 3f) are very similar to phase I. These together suggest phase IV to be a spin polarized correlated metal.

Discussion and outlook

Our results reveal a cascade of density- and field-dependent correlated phases in BLG. Transport evidence is provided for Stoner phases including the half and quarter metals, electron crystals including the Wigner crystal and the unprecedented Wigner–Hall crystal (topologically non-trivial), and two correlated metals whose behaviour deviates from that of standard Fermi liquids. Indicated by the tunable vHS and the large r_s (Fig. 1e), these new phases are driven by the complex interplay between electron–electron interaction, Fermi surface trigonal warping with vHS and the interlayer electric field. However, deciphering the origin of each phase and deeper understanding of this strongly correlated electron system call for further experiments and more theoretical works. Likely there exist finer and weaker phases such as the Stoner phase E and another gapped phase V (Methods and Extended Data Fig. 12).

Note added in proof: During the submission of our work, we became aware of two related experimental works by Zhou et al.[30] and de la Barrena et al.[31] on trigonally warped Bernal bilayer graphene. They both reported the metallic Stoner phases but not the new correlated phases (I–V) with metallic and insulating behaviour.

Online content

Any methods, additional references, Nature Research reporting summaries, source data, extended data, supplementary information, acknowledgements, peer review information; details of author contributions and competing interests; and statements of data and code availability are available at https://doi.org/10.1038/s41586-022-04937-1.

1. Bistritzer, R. & MacDonald, A. H. Moiré bands in twisted double-layer graphene. *Proc. Natl Acad. Sci. USA* **108**, 12233–12237 (2011).
2. Cao, Y. et al. Correlated insulator behaviour at half-filling in magic-angle graphene superlattices. *Nature* **556**, 80–84 (2018).
3. Cao, Y. et al. Unconventional superconductivity in magic-angle graphene superlattices. *Nature* **556**, 43–50 (2018).
4. Shen, C. et al. Correlated states in twisted double bilayer graphene. *Nat. Phys.* **16**, 520–525 (2020).
5. Lau, C. N., Bockrath, M. W., Mak, K. F. & Zhang, F. Reproducibility in the fabrication and physics of moiré materials. *Nature* **602**, 41–50 (2022).
6. Weitz, R. T., Allen, M. T., Feldman, B. E., Martin, J. & Yacoby, A. Broken-symmetry states in doubly gated suspended bilayer graphene. *Science* **330**, 812–816 (2010).
7. Zhang, F., Jung, J., Fiete, G. A., Niu, Q. & MacDonald, A. H. Spontaneous quantum Hall states in chirally stacked few-layer graphene systems. *Phys. Rev. Lett.* **106**, 156801 (2011).
8. Shi, Y. et al. Electronic phase separation in multilayer rhombohedral graphite. *Nature* **584**, 210–214 (2020).
9. Zhang, F., Sahu, B., Min, H. & MacDonald, A. H. Band structure of ABC-stacked graphene trilayers. *Phys. Rev. B* **82**, 35409 (2010).
10. Zhou, H. et al. Half and quarter metals in rhombohedral trilayer graphene. *Nature* **598**, 429–433 (2021).
11. Zhou, H., Xie, T., Taniguchi, T., Watanabe, K. & Young, A. F. Superconductivity in rhombohedral trilayer graphene. *Nature* **598**, 434–438 (2021).
12. Velasco, J. et al. Transport spectroscopy of symmetry-broken insulating states in bilayer graphene. *Nat. Nanotechnol.* **7**, 156–160 (2012).
13. Geisenhof, F. R. et al. Quantum anomalous Hall octet driven by orbital magnetism in bilayer graphene. *Nature* **598**, 53–58 (2021).
14. Varlet, A. et al. Anomalous sequence of quantum Hall liquids revealing a tunable Lifshitz transition in bilayer graphene. *Phys. Rev. Lett.* **113**, 116602 (2014).
15. Varlet, A. et al. Tunable Fermi surface topology and Lifshitz transition in bilayer graphene. *Synth. Met.* **210**, 19–31 (2015).
16. Shtyk, A., Goldstein, G. & Chamon, C. Electrons at the monkey saddle: a multicritical Lifshitz point. *Phys. Rev. B* **95**, 35137 (2017).
17. Tešanović, Z., Axel, F. & Halperin, B. I. "Hall crystal" versus Wigner crystal. *Phys. Rev. B* **39**, 8525–8551 (1989).
18. Sharpe Aaron, L. et al. Emergent ferromagnetism near three-quarters filling in twisted bilayer graphene. *Science* **365**, 605–608 (2019).
19. Serlin, M. et al. Intrinsic quantized anomalous Hall effect in a moiré heterostructure. *Science* **367**, 900–903 (2020).
20. Cao Yuan, et al. Nematicity and competing orders in superconducting magic-angle graphene. *Science* **372**, 264–271 (2021).
21. Kou, A. et al. Electron–hole asymmetric integer and fractional quantum Hall effect in bilayer graphene. *Science* **345**, 55–57 (2014).
22. Ki, D.-K., Fal'ko, V. I., Abanin, D. A. & Morpurgo, A. F. Observation of even denominator fractional quantum Hall effect in suspended bilayer graphene. *Nano Lett.* **14**, 2135–2139 (2014).
23. McCann, E. & Fal'ko, V. I. Landau-level degeneracy and quantum Hall effect in a graphite bilayer. *Phys. Rev. Lett.* **96**, 86805 (2006).
24. Yankowitz, M. et al. Emergence of superlattice Dirac points in graphene on hexagonal boron nitride. *Nat. Phys.* **8**, 382–386 (2012).
25. Dean, C. R. et al. Hofstadter's butterfly and the fractal quantum Hall effect in moiré superlattices. *Nature* **497**, 598–602 (2013).
26. Zhang, Y. et al. Direct observation of a widely tunable bandgap in bilayer graphene. *Nature* **459**, 820–823 (2009).
27. Giuliani, G. & Vignale, G. *Quantum Theory of the Electron Liquid* (Cambridge Univ. Press, 2005).
28. Jaoui, A. et al. Quantum critical behaviour in magic-angle twisted bilayer graphene. *Nat. Phys.* **18**, 633–638 (2022).
29. Abrahams, E., Kravchenko, S. V. & Sarachik, M. P. Metallic behavior and related phenomena in two dimensions. *Rev. Mod. Phys.* **73**, 251–266 (2001).
30. Zhou, H. et al. Isospin magnetism and spin-polarized superconductivity in Bernal bilayer graphene. *Science* **375**, 774–778 (2022).
31. de la Barrera, S. C. et al. Cascade of isospin phase transitions in Bernal-stacked bilayer graphene at zero magnetic field. *Nat. Phys.* https://doi.org/10.1038/s41567-022-01616-w (2022).

Methods

Device fabrication

Bilayer graphene flakes, graphite flakes and hBN flakes, synthesized as described previously[32], were exfoliated on silicon (Si)/silicon dioxide (SiO_2) substrates and subsequently identified with optical microscopy. Raman spectroscopy was used to confirm the number of layers of the bilayer graphene flakes. The encapsulated bilayer graphene devices were fabricated using the same dry transfer method as described in ref. [33]. An hBN flake, two few-layer graphite flakes serving as contacts, a bilayer graphene flake, a lower hBN flake and a graphite flake serving as a bottom gate were picked up and then placed onto a highly doped Si/SiO_2 substrate. Afterwards, the samples were annealed in a vacuum chamber at 200 °C for 12 h. In a second step, a top hBN flake and, subsequently, a graphite flake serving as a top gate were picked up and released onto the annealed heterostructures. The thicknesses of the hBN flakes serving as dielectrics were determined to be 34 nm (top dielectric of device A), 42 nm (bottom dielectric of device A), 13 nm (top dielectric of device B) and 32 nm (bottom dielectric of device B) by using atomic force microscopy. Metal contacts (chromium/gold, 5 nm/60 nm for device A and 2 nm/45 nm for device B) that connect the graphite contacts and gates with larger pads were then structured using electron-beam lithography and were evaporated onto the sample. Optical images and a schematic of our devices are shown in the Extended Data Fig. 1.

Electrical measurements

All quantum transport measurements were conducted in a dilution refrigerator equipped with a superconducting magnet. Unless stated otherwise, the sample temperature was 10–20 mK. Two-terminal conductance measurements were performed using an a.c. bias current of 1–10 nA at 78 Hz using Stanford Research Systems SR865A and SR830 lock-in amplifiers. Home-built low-pass filters were used to reduce high-frequency noises. Gate voltages were applied using Keithley 2450 SourceMeters.

Device characterization

The charge carrier density (n) and the electric field (E) can be tuned independently by varying the top-gate and bottom-gate voltages (V_t and V_b, respectively) and are defined as follows:

$$n = \frac{1}{e}(C_t V_t + C_b V_b)$$

and

$$E = \frac{1}{2\varepsilon_0}(C_t V_t - C_b V_b)\ ,$$

where ε_0 is the vacuum permittivity, and C_t and C_b are the top-gate and bottom-gate capacitances. C_t and C_b were extracted at low electric fields by aligning the integer QH plateaus at finite magnetic fields with their corresponding slopes in a fan diagram (Extended Data Fig. 3a,b). The observed LL crossings at different filling factors (Extended Data Fig. 3c,d) show excellent agreement with those observed previously[6,34,35]. Owing to the screening of Coulomb interaction by hBN, the interaction induced spontaneously gapped phase at $E = 0$ and $n = 0$ is absent, unlike in free-standing BLG[6,12,13,36].

Comment on graphite contacts

Using graphite contacts allows us to avoid etching into the insulating hBN layers, which is usually required for metal contacting but would lower the accessible electric-field range. However, using graphite contacts makes it technically demanding to use four-probe contacts, and thus two-point measurements were used here.

At $B = 0$, we see a line of decreased conductance across $E = 0$ that depends only on the applied bottom-gate voltage but is independent of the top-gate voltage (Extended Data Fig. 3f). We assume that this effect comes from the region of the BLG that is located below the graphite contacts. Here the contacts screen the field of the top gate, which is why we observe only a dependence of the bottom gate. It is worth noting that all the correlated phases that we observe depend on both the top gate and the bottom gate (Extended Data Fig. 3f) and can therefore not be related to the line of decreased conductance that depends on only the bottom-gate voltage. Apart from this line, we see no sudden changes in conductance as a function of density and electric field at small electric fields where the physics is known (Extended Data Fig. 3).

The contact resistance is also visible in the presence of a magnetic field. By tracing the measured conductance along one QH state as a function of the magnetic field, one can observe a linearly decreasing conductance with increasing magnetic field (without any steps in the conductance, right panel in Extended Data Fig. 3a), which we attribute to a magnetic-field-dependent contact resistance of our graphite contacts. This makes it difficult to extract contact resistances for entire fan diagrams. Thus, the measured conduction is given in arbitrary units in most of the figures. Nevertheless, the contact resistance can be determined and subtracted for constant magnetic fields by recording density versus conductance sweeps and by assigning the resistance plateaus to the assigned fillings factors. An exemplary density versus conductance sweep is shown for $B = 2$ T and $E = 0.08$ V nm^{-1} in Extended Data Fig. 3e. Here, the contact resistance was determined to be 7,800 Ω.

At large electric fields, we can also subtract a linearly magnetic-field-dependent contact resistance and find constant conductances in filling factors, and can further determine the conductance of phase II to be approximately $2\,e^2 h^{-1}$, where e is the charge of a bare electron, and h is Planck's constant (Extended Data Fig. 3g). Owing to the dependence of the bottom-gate voltage, the contact resistance varies slightly for different electric fields and charge carrier densities.

Apart from a bottom-gate and magnetic-field dependence, the contact resistance of graphite contacts can also depend on temperature. To exclude distortion of our temperature-dependent measurements at high electric fields, we further investigated the resistance as a function of temperature without electric field where the temperature dependence in bilayer graphene is well known. Consistent with previous results[37], we find that the measured resistance only slightly increases with increasing temperature (approximately 750 Ω from 10 mK to 10 K), whereas we see much larger changes in resistance in all the correlated phases in the same temperature range (Extended Data Fig. 10). Thus, we do not expect large changes in our contact resistance with varying temperature.

In Fig. 1a and in the temperature-dependent measurements shown in Fig. 4 and Extended Data Figs. 10 and 12c, we show the measured conductance or resistance (that includes contact resistance) to provide the readers with the original values.

Model Hamiltonian

The following four-band Hamiltonian[23] was used to describe the non-interacting physics near the valley K of BLG

$$H = \begin{bmatrix} \Delta/2 & v_0\pi^\dagger & 0 & v_3\pi \\ v_0\pi & \Delta/2 & \gamma_1 & 0 \\ 0 & \gamma_1 & -\Delta/2 & v_0\pi^\dagger \\ v_3\pi^\dagger & 0 & v_0\pi & -\Delta/2 \end{bmatrix}$$

in the sublattice basis (A_1, B_1, A_2, B_2). Here Δ is the interlayer potential difference, $\pi = p_x + ip_y$ is the complex momentum operator with p_x and p_y the x and y components of the momentum vector, $a = 0.246$ nm is the graphene lattice constant, $v_i = \frac{\sqrt{3}}{2}\frac{a\gamma_i}{\hbar}$ with $\hbar$ the reduced Planck's constant, and γ_i ($i = 0, 1, 3$) depict the nearest-neighbour intralayer hopping and the vertical and skew interlayer hopping processes. Other remote hopping processes in the Slonczewski–Weiss–McClure parametrization can be added into the model conveniently but have little effect on any of the calculated results and were thus ignored for simplicity. In the calculations, $\gamma_1 = 400$ meV and $\upsilon_3 = 0.1\upsilon_0$ were used.

When a perpendicular magnetic field is applied, the momentum operator $\mathbf{p}$ becomes $\mathbf{p} = -\mathrm{i}\hbar\nabla + e\mathbf{A}$, where e is the charge of a bare electron, and $\mathbf{A} = (0, Bx)$ is the magnetic vector potential in the Landau gauge. $\pi^{\dagger}$ and π act as raising and lowering operators of the LLs of a simple quadratic band, that is, $|n\rangle$ ($n = 0, 1, 2\ldots$) with the following identities

$$\pi^{\dagger}|n\rangle = \frac{\mathrm{i}\hbar}{\ell_{\mathrm{B}}}\sqrt{2(n+1)}\,|n+1\rangle,\ \pi|n\rangle = -\frac{\mathrm{i}\hbar}{\ell_{\mathrm{B}}}\sqrt{2n}\,|n-1\rangle,\ \pi|0\rangle = 0,$$

where ℓ_{B} is the magnetic length. To obtain the LLs of trigonally warped BLG, the following eigenstates

$$\left(\sum_n A_n\ |n\rangle,\ \ \sum_n B_n\ |n\rangle,\ \ \sum_n C_n\ |n\rangle,\ \ \sum_n D_n\ |n\rangle\right)^{\mathrm{T}}$$

with a cut-off $N_{\mathrm{c}} = 100$ were constructed to diagonalize the Hamiltonian. Diagonalizing the coefficient matrix in the basis ($A_0, B_0, C_0, D_0, A_1, B_1, C_1, D_1, \ldots$) produced the LL structure in Fig. 1d.

Generalized Wigner–Seitz radius

To evaluate the important roles of electron–electron interactions in a low-density electron gas system, it is suggested to examine the dimensionless Wigner–Seitz radius[27] $r_{\mathrm{s}} = U/W$, where $U = e^2\sqrt{\pi n}/\epsilon$ is the estimated Coulomb potential, W is the average kinetic (band) energy of electrons/holes with respect to the band bottom/top, n is the charge carrier density and ϵ is the dielectric constant. The r_{s} calculation is extremely neat for a perfect quadratic band with a constant isotropic effective mass, and W turns out to be exactly half of the Fermi energy E_{F} in two dimensions. However, the r_{s} calculation is complex for the current case, because the Fermi surface is trigonally warped, because the effective mass varies strongly with momentum and electric field, and because the electron and hole pockets can coexist in between the two Lifshitz transitions. Nevertheless, the net charge density n and the average kinetic energy W were naturally defined as follows

$$n = \int_{E>E_{\mathrm{F}}} \frac{\mathrm{d}^2\mathbf{k}}{(2\pi)^2},\ W = \frac{1}{n}\int_{E>E_{\mathrm{F}}} [E_{\mathrm{M}} - E_{\mathbf{k}}]\frac{\mathrm{d}^2\mathbf{k}}{(2\pi)^2},$$

where $E_{\mathbf{k}}$ is the band energy at momentum $\mathbf{k}$, and E_{M} is the valence-band energy maximum. When the electron and hole pockets coexist, the charge density n_{e}, the average kinetic energy W_{e} and the estimated Coulomb potential U_{e} for the electrons in the inner (in) pocket were naturally defined as follows

$$n_{\mathrm{e}} = \int_{E<E_{\mathrm{F}},\,\mathbf{k}\in\mathrm{in}} \frac{\mathrm{d}^2\mathbf{k}}{(2\pi)^2},\ W_{\mathrm{e}} = \frac{1}{n_{\mathrm{e}}}\int_{E<E_{\mathrm{F}},\,\mathbf{k}\in\mathrm{in}} [E_{\mathbf{k}} - E_0]\frac{\mathrm{d}^2\mathbf{k}}{(2\pi)^2},\ U_{\mathrm{e}} = \frac{e^2\sqrt{\pi n_{\mathrm{e}}}}{\epsilon},$$

where E_0 is the band energy at $\mathbf{k} = 0$. It follows that the charge density n_{h}, the average kinetic energy W_{h} and the estimated Coulomb potential U_{h} for the holes in the outer pocket(s) read

$$n_{\mathrm{h}} = n + n_{\mathrm{e}},\ W_{\mathrm{h}} = W + W_{\mathrm{e}},\ U_{\mathrm{h}} = \frac{e^2\sqrt{\pi n_{\mathrm{h}}}}{\epsilon}.$$

Thus, for the electrons $r_{\mathrm{s}} = U_{\mathrm{e}}/W_{\mathrm{e}}$, whereas for the holes $r_{\mathrm{s}} = U_{\mathrm{h}}/W_{\mathrm{h}}$. When the inner electron pocket is absent, $r_{\mathrm{s}} = U_{\mathrm{h}}/W_{\mathrm{h}} = U/W$. In the estimations, the experimentally extracted $\epsilon = 3$ was used.

Calculations of LLs and r_{s} values

In Fig. 1, the experimental fan diagram at $E = 0.6$ V nm^{-1} and two types of theoretical calculation are compared. First, by using experimental relevant parameter values, we can estimate the interlayer potential difference Δ to be around $0.25\gamma_1$, and then calculate the LL structure for the non-degenerate valence band. The LL crossings between the $\nu = -4$ and $\nu = -5$ QH states are well matched between the experiment (Fig. 1c) and the calculation (Fig. 1d). Next, we use the same set of parameters to calculate the Wigner–Seitz radius r_{s} as a function of the charge carrier density n.

First, assuming a four-fold (spin and valley) degeneracy for all the states, we find that no Lifshitz transition can be reached in the density range of the experimental fan diagram, and that the corresponding r_{s} (black curve in Fig. 1e) is always larger than 34, a threshold for the Wigner crystallization of 2D electron gases[27], not to mention 20, a threshold for the ferromagnetic instability of 2D electron gases[27]. Following this result, next, we assume all the states to be ferromagnetic and two-fold (either spin or valley) degenerate, and find that both Lifshitz transitions can be reached, and that the r_{s} values (red curves in Fig. 1e) of the outer hole (h^+) and inner electron (e^-) pockets are generally larger than 20. Following this result, lastly, we assume all the ferromagnetic states to be non-degenerate, and find that both Lifshitz transitions can be reached, and that the r_{s} (blue curves in Fig. 1e) of the outer hole (inner electron) pocket is smaller (larger) than 20 (34).

Relation between critical densities and correlated phases

When compared with our experimental findings, these theoretical calculations at least suggest the following five facts. (1) The observed LL crossing can be attributed to the annular Fermi surface in between the two Lifshitz transitions of the quarter metal (Fig. 1d). Consistently, a similar crossing can be seen at $B = 2.4$ T and $n = -4 \times 10^{11}$ cm^{-2} (Fig. 1c), near which the half metal has an annular Fermi surface. (2) The result $r_{\mathrm{s}} < 20$ for the non-degenerate case is consistent with that phase A is a non-degenerate quarter metal at low densities where there is no inner electron pocket. (3) The result $r_{\mathrm{s}} > 34$ for the non-degenerate electron pocket is consistent with that phases II and III are non-degenerate Wigner crystals. In addition, we observe indications of another insulating phase similar to phase II (phase V, only at finite B; Extended Data Fig. 12) near the density in which the doubly degenerate inner electron pocket is present, consistent with the result $r_{\mathrm{s}} > 34$ for the doubly degenerate electron pocket. (4) Phases I and IV are metallic, with very similar behaviour in temperature (Fig. 4), bias current (Fig. 3f), and both in-plane and out-of-plane magnetic fields (Extended Data Figs. 6 and 7). This is consistent with that they both occur in a density range close to but below the Lifshitz transition associated with the vHS. (5) The phase boundary between D and C and that between C and B at $E = 0.6$ V nm^{-1} (Fig. 2c) are almost coincident with the two calculated Lifshitz transition densities for the states being doubly degenerate (half metal), that is, the boundaries of the light red shaded region in Fig. 1e.

Diophantine equation and Wigner–Hall crystals

Wigner–Hall physics can be captured by the Diophantine equation $n = \nu n_{\phi} + \eta A_0^{-1}$, where ν is the total Chern number, $n_{\phi} = eBh^{-1}$ is the density of magnetic flux quanta, η is the band filling and A_0 is the unit cell area of electron crystal[17]. A Wigner crystal has $\nu = 0$ and $\eta \neq 0$ (for example, phase III), whereas a Hall crystal or a QH state has $\nu \neq 0$ and $\eta = 0$. The more unusual case for $\nu \neq 0$ and $\eta \neq 0$ is the Wigner–Hall crystal. For phase II, one possible scenario is $\nu = -2$ and $\eta \neq 0$: the doped holes spontaneously crystallize with the formation of Chern bands[7,38], or they form a Wigner crystal on top of the undoped system that is in one state of the QAH octet[7,13].

Device quality

Extended Data Fig. 3a shows the conductance plotted as a function of the density and the magnetic field at $E = 0.0\ \mathrm{V\ nm^{-1}}$. It is clear that the lowest QH states start to emerge at very low magnetic fields of 0.2 T, demonstrating the high quality of our device[13]. At higher magnetic fields, all integer filling factors appear owing to spontaneous symmetry breaking[6]. Extended Data Fig. 3c shows the conductance as a function of the density and the electric field at $B = 2$ T. All integer QH states are clearly visible. In addition, one can see several transitions in the electric field that mark the collapse of different LLs owing to the interplay of spin and valley splitting[34]. We further investigated the $\nu = 0$ QH state as a function of the electric field and the magnetic field (Extended Data Fig. 3d). We observed unusual sharp conductance peaks marking the transition between the canted antiferromagnetic phase and the fully layer polarized phase. This underlines the high quality of our device[39].

The conductance map shows slight asymmetry in electric field, probably owing to the different cleanliness levels of the two sides of BLG. Nevertheless, the main signatures described are the same for both the negative and positive electric fields.

Additional magnetotransport data

In the main text, we have focused on the hole side where the most distinct features were observed. Although we did not find signatures of phases I–IV on the electron side (Fig. 1a), there could be Stoner phases in the conduction band. In Extended Data Fig. 2, we show the derivative of the conductance as a function of the filling factor ν ($\nu > 0$) and the electric field and highlight regions with two-fold and four-fold degeneracies that potentially correspond to half and full metal phases. For completeness, the conductance as well as its derivative as functions of the charge carrier density and the magnetic field are shown in Extended Data Fig. 6 for different electric fields not shown in the main text. Furthermore, the derivative of the conductance as a function of the charge carrier density and the magnetic field at an electric field of $-0.8\ \mathrm{V\ nm^{-1}}$ is shown for a second device (device B) in Extended Data Fig. 4. Even though device B is not as clean as device A, we still identified all the phases discussed in the main text. The four phases I–IV show approximately the same density, electric field and magnetic field behaviour in both devices (Extended Data Fig. 8).

Data availability

The data that support the findings of this study are available from the corresponding authors upon reasonable request.

32. Taniguchi, T. & Watanabe, K. Synthesis of high-purity boron nitride single crystals under high pressure by using Ba–BN solvent. *J. Cryst. Growth* **303**, 525–529 (2007).
33. Winterer, F. et al. Spontaneous gully-polarized quantum Hall states in ABA trilayer graphene. *Nano Lett.* **22**, 3317–3322 (2022).
34. Lee, K. et al. Chemical potential and quantum Hall ferromagnetism in bilayer graphene. *Science* **345**, 58–61 (2014).
35. Li, J., Tupikov, Y., Watanabe, K., Taniguchi, T. & Zhu, J. Effective Landau level diagram of bilayer graphene. *Phys. Rev. Lett.* **120**, 47701 (2018).
36. Freitag, F., Trbovic, J., Weiss, M. & Schönenberger, C. Spontaneously gapped ground state in suspended bilayer graphene. *Phys. Rev. Lett.* **108**, 76602 (2012).
37. Das Sarma, S., Hwang, E. H. & Rossi, E. Theory of carrier transport in bilayer graphene. *Phys. Rev. B* **81**, 161407 (2010).
38. Haldane, F. D. M. Model for a quantum Hall effect without Landau levels: condensed-matter realization of the "parity anomaly". *Phys. Rev. Lett.* **61**, 2015–2018 (1988).
39. Maher, P. et al. Evidence for a spin phase transition at charge neutrality in bilayer graphene. *Nat. Phys.* **9**, 154–158 (2013).

Acknowledgements We thank V. I. Fal'ko, L. Levitov, A. H. MacDonald and Di Xiao for discussions. R.T.W. and A.M.S. acknowledge funding from the Center for Nanoscience (CeNS) and by the Deutsche Forschungsgemeinschaft (DFG, German Research Foundation) under the SFB 1073 project B10 and under Germany's Excellence Strategy-EXC-2111-390814868 (MCQST). T.X. and F.Z. acknowledge support from the Army Research Office under grant number W911NF-18-1-0416 and the National Science Foundation under grant numbers DMR-1945351 through the CAREER programme, DMR-2105139 through the CMP programme, and DMR-1921581 through the DMREF programme. K.W. and T.T. acknowledge support from the Elemental Strategy Initiative conducted by the MEXT, Japan (grant number JPMXP0112101001) and JSPS KAKENHI (grant numbers 19H05790, 20H00354 and 21H05233).

Author contributions A.M.S. fabricated the devices and conducted the measurements and data analysis. K.W. and T.T. grew the hexagonal nitride crystals. T.X. performed the calculations and contributed to the theories. F.Z. supervised the computational and theoretical parts. All authors discussed and interpreted the data. R.T.W. supervised the experiments and the analysis. The manuscript was prepared by A.M.S., F.Z. and R.T.W. with input from all authors.

Competing interests The authors declare no competing interests.

Additional information
Supplementary information The online version contains supplementary material available at https://doi.org/10.1038/s41586-022-04937-1.
Correspondence and requests for materials should be addressed to Fan Zhang or R. Thomas Weitz.
Peer review information *Nature* thanks Dong-Keun Ki, Folkert de Vries and the other, anonymous, reviewer(s) for their contribution to the peer review of this work. Peer reviewer reports are available.
Reprints and permissions information is available at http://www.nature.com/reprints.

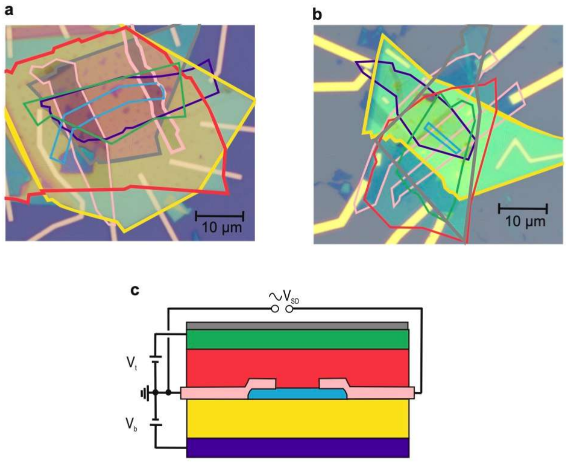

Extended Data Fig. 1 | Bilayer graphene devices studied here. a, **b**, Optical images of device A (presented in the main manuscript) (**a**) and device B (**b**). The top hBN is encircled in grey, the upper graphite flake in green, the upper hBN flake in red, the graphite contacts in pink, the bilayer graphene flake in blue, the lower hBN flake in yellow, and the lower graphite flake in purple. **c**, Schematic of the bilayer graphene devices. The colours of different flakes match those in **a**, **b**.

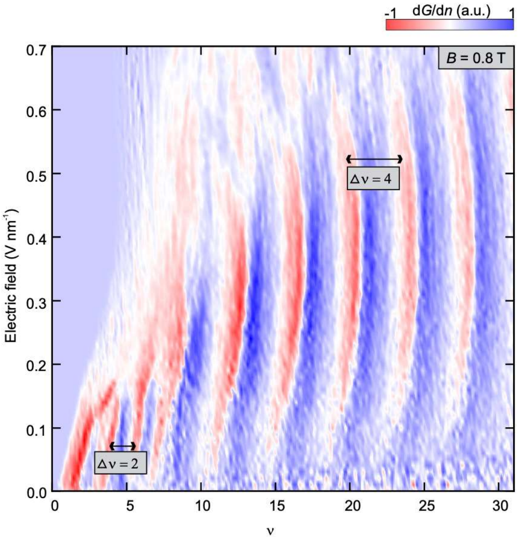

Extended Data Fig. 2 | Stoner physics in the conduction band. Density derivative of the conductance as a function of the filling factor ν and the electric field at $B = 0.8$ T for positive filling factors. Two-fold and four-fold LL degeneracies are marked.

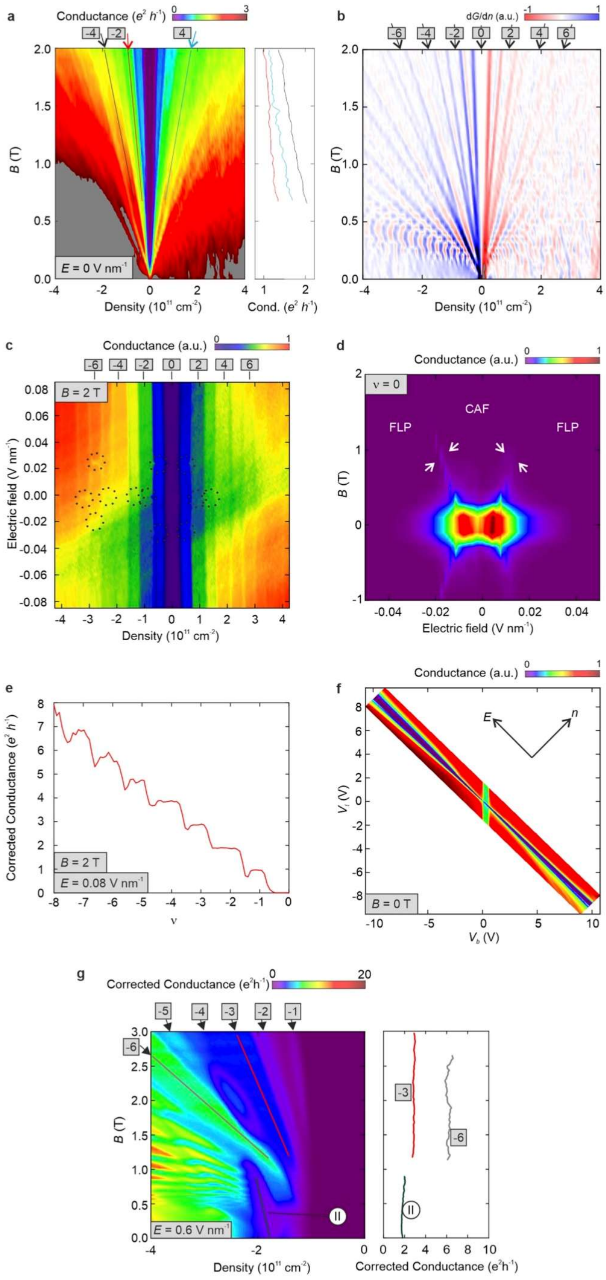

Extended Data Fig. 3 | See next page for caption.

Extended Data Fig. 3 | Device Characterizations. **a**, Fan diagram at $E = 0$ V/nm. The QH states $\nu = -4, -2$, and 2 are traced as function of the magnetic field and the charge carrier density. **b**, Derivative of the conductance in **a**.
c, Conductance as a function of the charge carrier density and the electric field at $B = 2$ T. Transitions induced by the electric field are marked by dashed circles. (In **a**–**c**, Integer QH states are labelled by numerals.) **d**, Conductance as a function of the electric field and the magnetic field at $\nu = 0$. The phase transitions between the canted antiferromagnetic (CAF) and fully layer polarized (FLP) phases are indicated by arrows. **e**, Conductance as a function of the charge carrier density at $E = 0.08$ V/nm and $B = 2$ T (extracted from data in **c**). Here a contact resistance of 7800 Ω was subtracted. **f**, Conductance as a function of the top and bottom-gate voltages at $B = 0$ T in the space of -7×10^{11} cm$^{-2} < n < 7 \times 10^{11}$ cm^{-2} and -0.7 V/nm $< E < 0.7$ V/nm. **g**, Conductance as a function of charge carrier density and magnetic field at $E = 0.6$ V/nm. A contact resistance of $R_c = 2000\,\Omega + 3000\,\Omega/\mathrm{T} \times B$ (T) was subtracted from the measured values. The data are the same measurements presented in Fig 1c of the main manuscript.

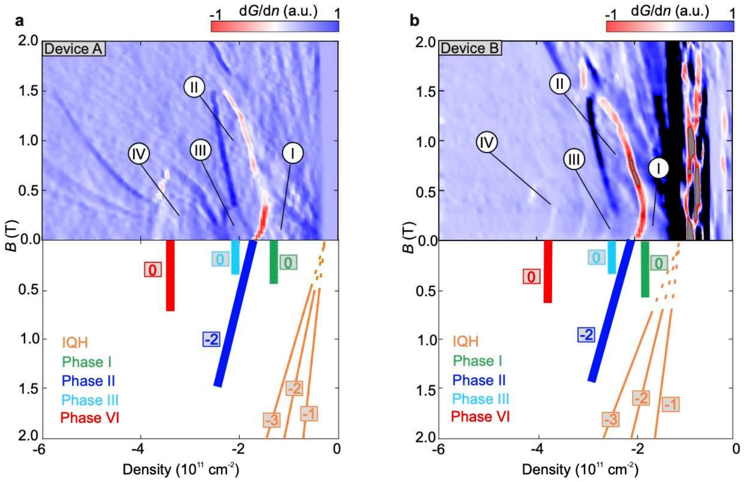

Extended Data Fig. 4 | Magnetotransport data of a second device. Density derivative of the conductance plotted as a function of the charge carrier density and the magnetic field at $E = -0.8$ V/nm for device A (shown in the main manuscript) (**a**) and device B (**b**). The slopes of the lowest integer QH states and of the phases I–IV discussed in the main text are traced by lines in the mirror schematics of the fan diagrams. The corresponding slopes are indicated by arabic numerals. The lines are solid if the states are present and dashed otherwise.

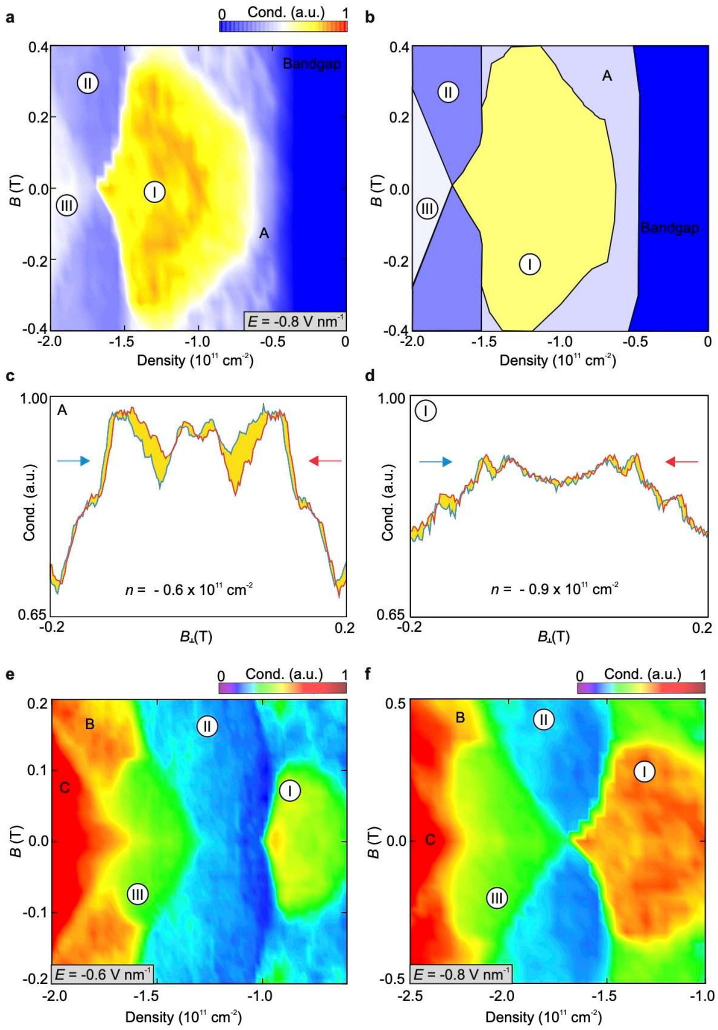

Extended Data Fig. 5 | Zoom-in of phases I–III and A. a, Conductance as a function of charge carrier density and magnetic field at $E = -0.8$ V/nm showing the clear distinction between phases I and A. **b**, Schematic of phases A and I-III at $E = -0.8$ V/nm. **c,d**, Magnetic hysteresis of phase A (**c**)and phase I (**d**). The forward sweeps are shown in blue while the backward ones in red. The hysteresis loop areas are shaded in yellow. **e**, **f**, Conductance as a function of charge carrier density and magnetic field at $E = -0.6$ V/nm (**e**) and $E = -0.8$ V/nm (**f**) showing the clear distinction between phases I, II and III and B and C that show distinct values in conductance and clear steps of conductance at the phase boundaries.

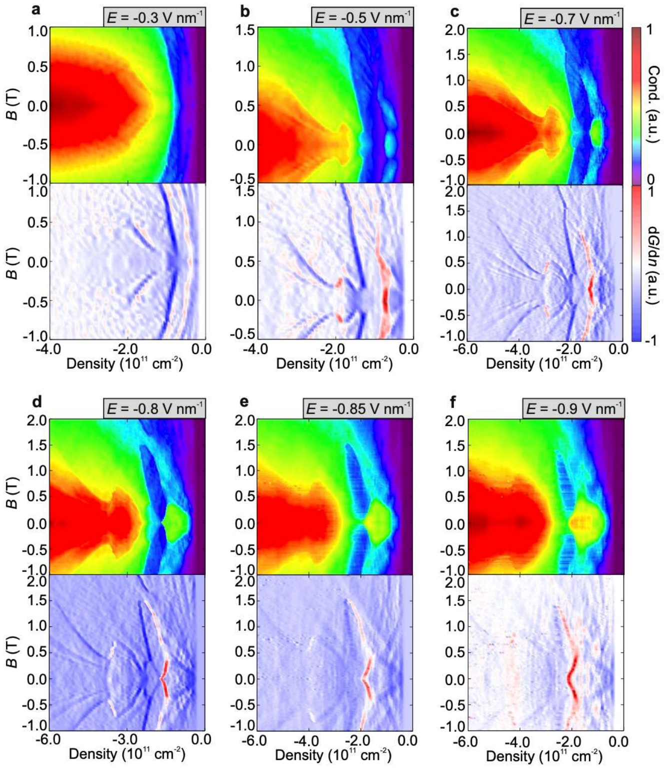

Extended Data Fig. 6 | Additional magnetotransport data at various electric fields. Conductance and its density derivative plotted as functions of the charge carrier density and the magnetic field at different electric fields.

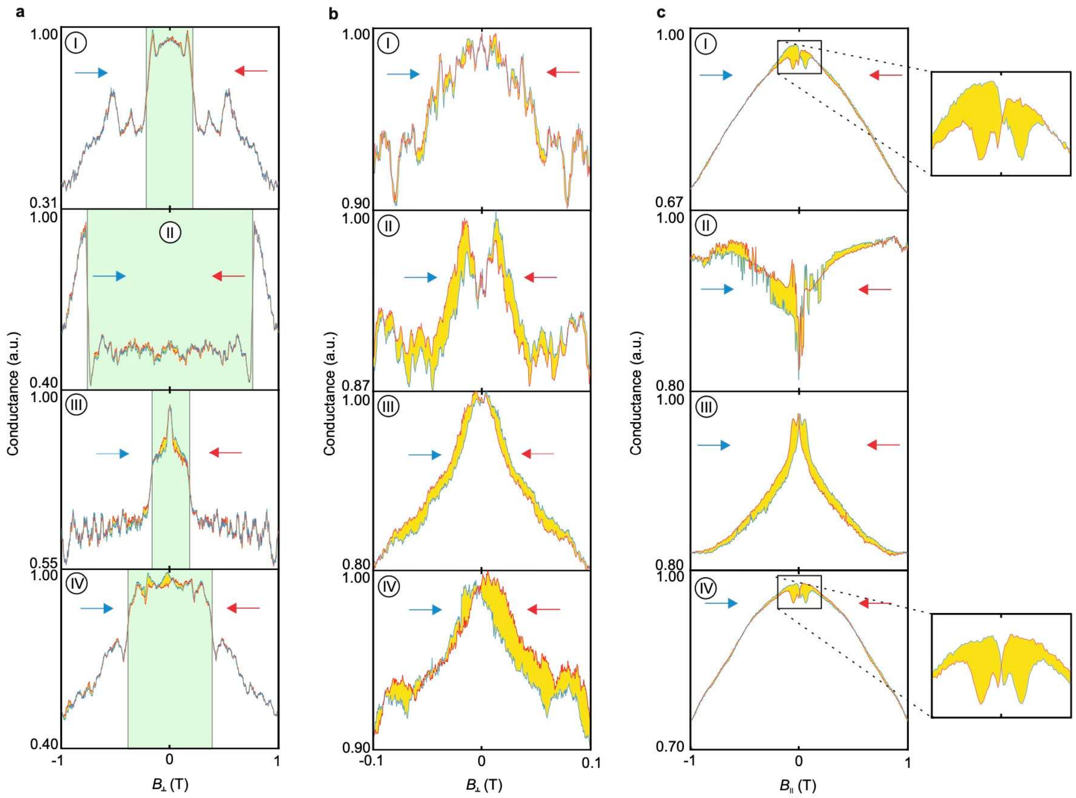

Extended Data Fig. 7 | Magnetic field hysteresis of phases I–IV. Hysteresis of the conductance as a function of the out-of-plane magnetic field $B_\perp$ (**a**, **b**) and the in-plane magnetic field $B_{||}$ (**c**) at $E = -0.6$ V/nm and charge carrier densities corresponding to phase I ($n = -0.85 \times 10^{11}$ cm^{-2}), phase II ($n = -1.2 \times 10^{11}$ cm^{-2}), phase III ($n = -1.5 \times 10^{11}$ cm^{-2}), and phase IV ($n = -2.2 \times 10^{11}$ cm^{-2}), respectively. The forward sweeps are shown in blue while the backward ones in red. The hysteresis loop areas are shaded in yellow. The data shown in **a**, **b** stem from two different sets of measurement. The magnetic field sweeps were started at −1 T and −0.1 T respectively. In (a) the $B_\perp$ ranges in which phases I–IV are stable are highlighted in green.

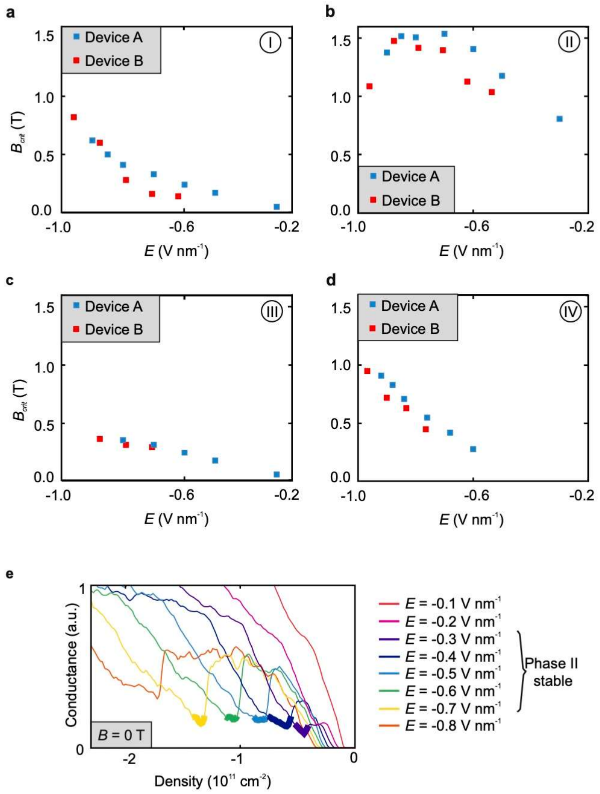

Extended Data Fig. 8 | Critical magnetic fields and conductance of phase II at various different electric fields. **a–d**, Critical magnetic fields for devices A and B of phase I (**a**), phase II (**b**), phase III (**c**), and phase IV (**d**) at different electric fields. **e**, Conductance as a function of charge carrier density at different electric fields and $B = 0$. Density regions of stable phase II are highlighted.

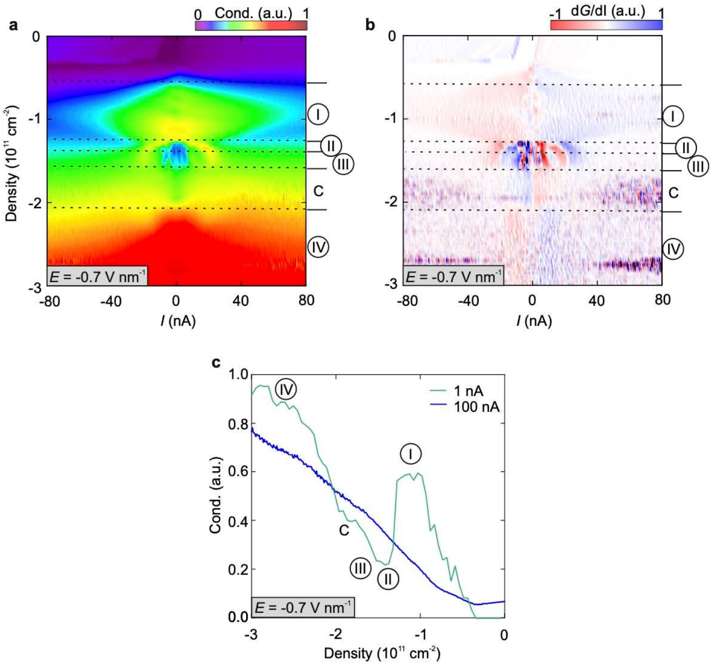

Extended Data Fig. 9 | Current dependent measurements. a, b, Conductance (**a**) and bias current derivative of conductance (**b**) as a function of bias current I and charge carrier density n at $E = -0.7$ V/nm and $B = 0$ showing a gap in phases II and III at small currents. **c**, Conductance as a function of n at $E = -0.7$ V/nm and $B = 0$ for $I = 100$ nA (blue) and $I = 1$ nA (green). The phases I – IV can not be seen at large currents, indicative of the many-body nature of the phases.

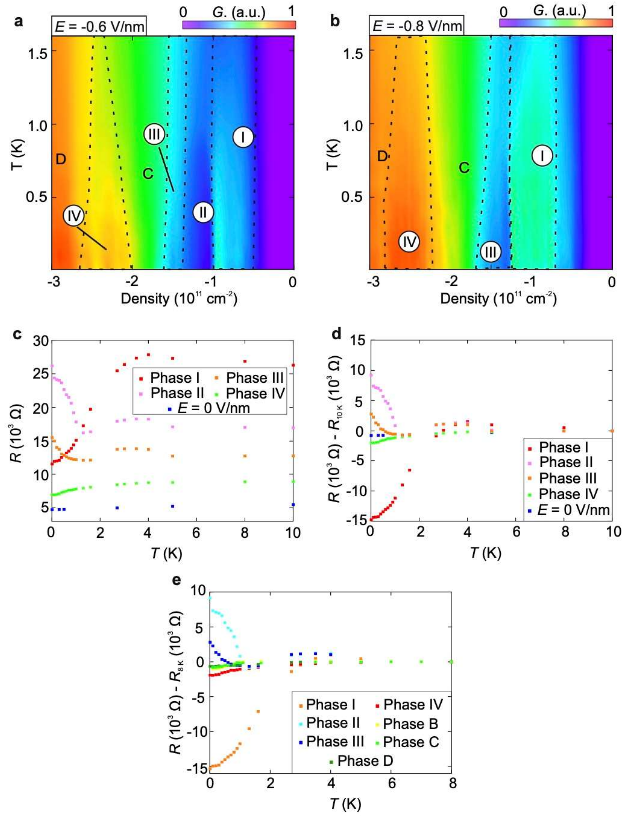

Extended Data Fig. 10 | Temperature dependence of phases I–IV and B–D. **a**, **b**, Conductance as a function of charge carrier density and temperature T at $B = 0$ and $E = -0.6$ V/nm (**a**) and $B = 0$ and $E = -0.8$ V/nm (**b**).**c**, **d**,R(**c**) and $R - R$ (10K) (**d**) as a function of temperature T for phase I ($n = -0.9 \times 10^{11}$ cm^{-2}), phase II ($n = -1.2 \times 10^{11}$ cm^{-2}), phase III ($n = -1.5 \times 10^{11}$ cm^{-2}), and phase IV ($n = -2.2 \times 10^{11}$ cm^{-2}) at $E = 0.6$ V/nm and for the normal state at $E = 0$ V/nm ($n = -1.0 \times 10^{11}$ cm^{-2}). **e**, $R - R$ (8K) as a function of temperature T for phase I ($n = -0.9 \times 10^{11}$ cm^{-2}), phase II ($n = -1.2 \times 10^{11}$ cm^{-2}), phase III ($n = -1.5 \times 10^{11}$ cm^{-2}), and phase IV ($n = -2.2 \times 10^{11}$ cm^{-2}) at $E = -0.6$ V/nm and $B = 0$ T and for the phase B ($n = -2.2 \times 10^{11}$ cm^{-2}), phase C ($n = -2.5 \times 10^{11}$ cm^{-2}), and phase D ($n = -4.0 \times 10^{11}$ cm^{-2}) at $E = -0.6$ V/nm and $B = 0.6$ T.

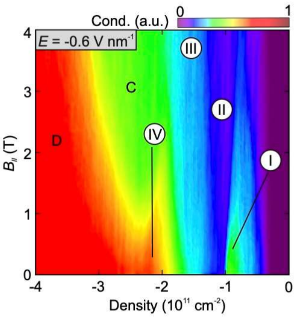

Extended Data Fig. 11 | In-plane magnetic field dependence of phases I–IV. Conductance as a function of charge carrier density and in-plane magnetic field $B_{||}$ at $B_{\perp} = 0$ and $E = -0.6$ V/nm. The phase boundary between phase II and III does not shift with increasing the in-plane magnetic field suggesting that both phases likely carry similar in-plane spin order and inter-valley coherence. Compared with phase I, both phases likely have larger magnitudes of spin polarization since they are more stable against large in-plane magnetic fields.

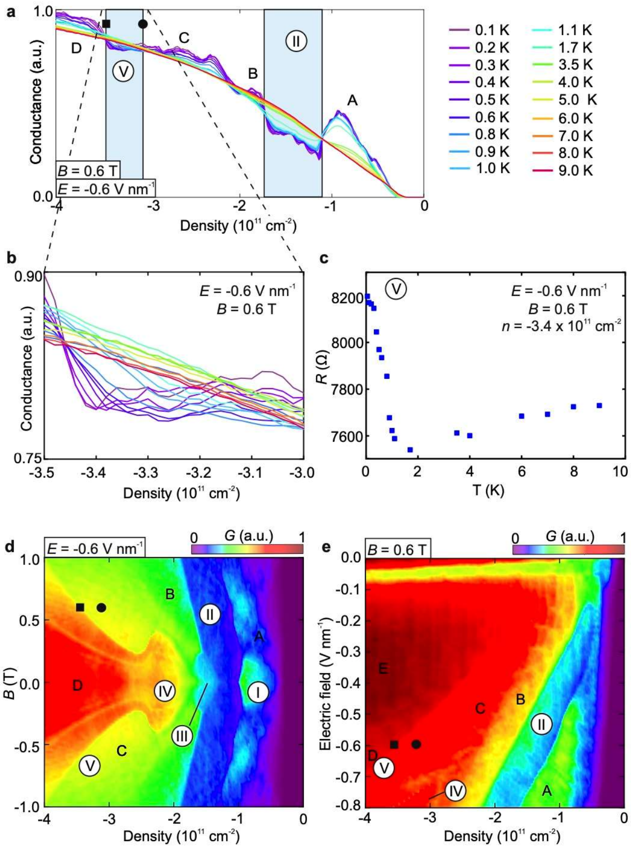

Extended Data Fig. 12 | Experimental indications of a further novel phase close to the Lifshitz transition of the half metal, termed phase V. We find this additional phase near the density in which the doubly degenerate inner electron pocket is present, consistent with the result $r_s > 34$ (dashed red) for the electron pocket in Fig 1e of the main manuscript. Potentially this phase resembles phase II and/or III but for the doubly degenerate case.
a, Conductance as a function of charge carrier density for different temperatures at $E = -0.6$ V/nm and $B = 0.6$ T. The insulating correlated phases are highlighted in blue. The maximum/minimum charge carrier density at which phase V is stable is marked by a black square/circle. **b**, Zoom-in of **a** around phase V. **c**, Resistance as a function of temperature T for phase V at $E = -0.6$ V/nm, $B = 0.6$ T, and $n = -3.4 \times 10^{11}$ cm^{-2}. **d**, Conductance as a function of charge carrier density and magnetic field at $E = -0.6$ V/nm. The maximum/minimum charge carrier density at which phase V is stable at $B = 0.6$ T is marked by a black square/circle. **e**, Conductance as a function of charge carrier density and electric field at $B = 0.6$ T. The maximum/minimum charge carrier density at which phase V is stable at $E = -0.6$ V/nm is marked by a black square/circle.

7 Manuscript: Interacting ground states of electron-doped bilayer graphene at large electric displacement fields

The results presented in this Chapter are currently prepared for publication. The current version of the manuscript is reprinted below.

Contributions:

I fabricated the devices (device 1 in the article corresponds to Stack 99 in this thesis and device 2 in the article corresponds to Stack 70), conducted all measurements, and performed the data analysis. I further prepared the first version of the manuscript except from some theoretical sections and I designed all figures. In addition, I produced the current version of the manuscript.

Interaction-driven quasi-insulating ground states of gapped electron-doped bilayer graphene

Anna M. Seiler[1], Martin Statz[1], Isabell Weimer[1], Nils Jacobsen[1], Kenji Watanabe[2], Takashi Taniguchi[3], Zhiyu Dong[4], Leonid S. Levitov[4], R. Thomas Weitz[1]*

[1]1st Physical Institute, Faculty of Physics, University of Göttingen, Friedrich-Hund-Platz 1, Göttingen 37077, Germany

[2]Research Center for Functional Materials, National Institute for Materials Science, 1-1 Namiki, Tsukuba 305-0044, Japan

[3]International Center for Materials Nanoarchitectonics, National Institute for Materials Science, Tsukuba, Japan

[4]Department of Physics, Massachusetts Institute of Technology, Cambridge, Massachusetts 02139, USA

*Corresponding author. Email: thomas.weitz@uni-goettingen.de

Bernal bilayer graphene has recently been discovered to exhibit a wide range of unique ordered phases resulting from interaction-driven effects and encompassing spin and valley magnetism [1, 35, 36], correlated insulators [1], correlated metals [1], and superconductivity [35, 98]. This letter reports on a novel family of correlated phases characterized by spin and valley ordering, observed in electron-doped bilayer graphene. The novel correlated phases demonstrate an intriguing non-linear current-bias behavior at ultralow currents that is sensitive to the onset of the phases and is accompanied by an insulating temperature dependence, providing strong evidence for the presence of unconventional charge carrying degrees of freedom originating from ordering. These characteristics cannot be solely attributed to any of the previously reported phases, and are qualitatively different from the

behavior seen previously on the hole-doped side. Instead, our observations align with the presence of a charge- or spin-density-wave state that opens a gap on a portion of the Fermi surface. The resulting new phases, quasi-insulators in which part of the Fermi surface remains intact or valley-polarized and valley-unpolarized Wigner crystals, coexist with previously known Stoner phases, resulting in an exceptionally intricate phase diagram.

Graphene flat-band systems, moiré and non-moiré, provide a rich platform in which a wide variety of correlated electronic states can be realized and explored [1, 16, 17, 19, 24, 25, 28, 33–36, 98, 180]. After initial observations of exchange driven phases in suspended Bernal bilayer graphene at charge neutrality [28, 34, 175], a family of exotic interaction-driven orders has been found in magic-angle twisted bilayer graphene (TBG), where flat electronic bands are created by superposing two layers of graphene with a relative twist angle. In TBG, Mott insulating and superconducting phases have been found to compete at half filling of either electron or hole Moiré bands [16, 17]. However, it quickly became evident that TBG does not possess an exclusive monopoly on hosting interesting correlated states in the vicinity of van-Hove-singularities. These states have also been found in the naturally occurring Bernal bilayer graphene (BLG), where strongly correlated behavior arises at large electric displacement fields (D), assisted by field-induced flat bands and a divergence in the density of states (DOS) [1, 35, 36, 98, 181] at Lifshitz transitions. Close to the band edge interactions between charge carriers are large enough to satisfy the Stoner criterion [6] and carriers become spin or valley polarized, as can be deduced from varying Landau level (LL) spacings at finite magnetic fields B [1, 35, 36]. Previous studies on BLG focused on the hole-doped regime where several exotic orders beyond Stoner magnetism such as correlated and superconducting[1, 35, 98] phases have been observed. These states have often been attributed to the presence of annular Fermi surfaces or pocket physics, as found on the hole side in BLG [1, 35] and in ABC trilayer graphene [24, 25]. Yet, at this point it is far from clear whether the correlated phases are driven primarily by the band dispersion or by some exotic interaction effects [9].

To shed light on this question, here we report on the previously unexplored electron-doped regime of BLG. The low-energy dispersion on the electron side is markedly different compared to the hole side. For example, the trigonal warping induced rotational symmetry breaking is significantly less pronounced at the conduction band minimum (Fig 1a,b). In fact, at large D, the bands are flatter and the DOS-peak due to the still remaining Lifshitz transition is significantly stronger than in the valence band (Fig. 1c, Extended Data Fig. 1). Nevertheless, so far, only metallic Stoner phases have been observed in electron-doped Bernal-stacked bilayer graphene[1, 36]. Surprisingly, we find a new interaction-driven behavior that is clearly beyond Stoner physics. Specifically, complex correlated phases appear close to the band edge at large D and low magnetic fields (B) that cannot be explained solely by Stoner ferromagnetism. As discussed below, the isospin polarized orders in this doping regime show an insulating temperature dependence and a striking nonlinear current-bias dependence. These behaviors are distinct from the previously reported results [36], indicating an unexplored ground state of the electron-doped bilayer graphene. There are several theoretical pictures in recent literature that account for these observations, such as formation of a spin or charge density wave order that gaps out part of the Fermi surface [182] or a Wigner crystal, potentially coexisting with mobile carriers [1].

The bilayer graphene flakes investigated for this study are encapsulated in hexagonal boron nitride (hBN) and equipped with graphite top and bottom gates, which allows to continuously tune the displacement field D as well as the charge carrier density n (see methods). Measurements shown in the main text were conducted in a device with two-terminal graphite contacts (Fig. 1d), which is why all conductance data except the data presented in Extended Data Fig. 2 is given in arbitrary units (a.u., see methods for details). Measurements conducted in a second device with four-terminal edge contacts, which shows qualitatively similar behaviour to the device discussed in the main manuscript, are shown in Extended Data Fig. 3. All measurements, unless stated otherwise, were conducted in a dilution refrigerator at a base temperature T of 10 mK.

Figure 1e shows the measured two-terminal conductance G as a function of n and D for electron doping and negative D. At charge neutrality, an electric-field induced band gap opens up resulting in a well-known conductance minimum [28]. Outside the gap, G increases monotonically as a function of n. At large D, where interactions are expected to be strong due to a peak in the DOS (Fig. 1c), two steps emerge, separating regions of similar conductance that we tentatively label with **svi** (spin and valley polarized insulator), **si** (spin polarized insulator), and **m** (metal). In the following we will discuss in further detail why we chose these labels. The regions of similar conductance can be differentiated best in the normalized derivative of G with respect to n ($|\mathrm{d}G/\mathrm{d}n|$), where the steps in between them appear as peaks (Fig. 1f, see Extended Fig. 3 for a corresponding 4-terminal measurement). Parts of these features have been observed previously in capacitance measurements without magnetic fields ($B = 0$ T) and at finite out-of-plane magnetic fields $B_\perp > 0.6$ T [36]. In Ref. [36], one of the peaks is suggested to mark the transition between a Stoner quarter and a full metal, corresponding to a region with one-fold and another region with four-fold degenerate LL. We can reproduce these results (both the results at $B = 0$ T and at $B_\perp > 0.6$ T) and find regions with one-fold and four-fold degenerate quantum Hall states at $B_\perp > 0.3$ T (Extended Data Fig. 4, 5).

At present, however, the nature of the phases at $B = 0$ T is unclear since their nature had previously only been extrapolated from the high-magnetic field behavior (at $B_\perp > 0.6$ T) [36]. This means, while previous studies focused on Stoner ferromagnetism in bilayer [1, 35, 36] and trilayer graphene [25] at finite magnetic fields, the true $B = 0$ T ground state of the system remains unknown. In fact, at magnetic fields $B_\perp < 0.3$ T, we were not able to observe quantum Hall states in the density regime of the svi and si phases (Fig. 2a-c), while quantum Hall states are well visible even below 200 mT in the m phase (Fig. 2c, Extended Data Fig. 5). This observation clearly indicates that the phases studied at elevated magnetic field likely are distinct in nature from the truly interacting $B = 0$ T ground state.

To analyze the nature of these phases, we first study the system around $B = 0$ T as function of D. At constant $D = -0.6$ V nm^{-1}, all three phases are well resolved at $B_\perp = 0$ T . Wit0h slightly increasing $B_\perp$ (Fig. 2a), the mutual phase boundary of the **svi** phase and the **si** phase shifts towards larger densities i.e., the **svi** phase becomes stable in a larger density region. Above $B_\perp \approx 200 - 300$ mT, the phase boundary between the **svi** and **si** phases becomes less pronounced or vanishes. Remarkably, the **si** phase is even less stable against $B_\perp$ at large D-fields (Fig. 2b,c) while at D-fields below |D| = 0.5 V nm^{-1}, small $B_\perp$ can even stabilize this phase (Fig. 1f, Fig. 2c). Since in BLG the energy scale given by the coupling between the out-of-plane magnetic field and the valley degree of freedom via the orbital momentum is larger compared to other magnetic field induced splittings (e.g. Zeeman) [33], we conclude that the **svi** and the **si** phases must have different valley orderings. In the simplest case, the **svi** phase is then valley polarized due to exchange-driven Stoner physics, while the **si** and **m** phases are valley unpolarized [25, 36]. Notably, the phase boundary of the **si** phase and the **m** phase shifts also slightly with $B_\perp$, likely resulting from different spin orderings in these phases that are discussed below.

Next, we investigate the phase transitions as a function of the in-plane magnetic field $B_{||}$ that primarily couples to the spin degree of freedom via the Zeeman effect (Fig. 2d). Whereas increasing $B_{||}$ does not change the phase boundary between the **svi** and the **si** phase (Fig. 2d), the phase boundary between the **si** and the **m** phase moves towards higher densities marking a phase transition with different spin polarization [25]. Since the **si** phase becomes broader with increasing $B_{||}$, we assume the si phase to be spin polarized, while we suggest the **m** phase to be spin degenerate. The **svi** phase is likely spin polarized as well since the phase boundary between the **si** and **svi** phase does not move in density with increasing $B_{||}$. At $|D| < 0.6$ V/nm, where the **svi** and **si** phases do not exist at zero magnetic field, $B_{||}$ stabilizes the spin polarized **si** phase (Fig. 2e,f).

The assignment of spin and valley polarization is consistent with the LL degeneracies discussed above [25, 36] and also with magnetic hysteresis measurements shown in Extended Data Fig. 5. While the spin polarized **svi** and **si** phases show an in-plane magnetic field hysteresis due to spin polarization (Extended Data Fig. 5a), the spin and valley polarized **svi** phase exhibits also an out-of-plane magnetic field hysteresis resulting likely from orbital magnetism as there is no out-of-plane magnetic field hysteresis in the **si** phase (Extended Data Fig. 5b). Interestingly, in the **svi** phase, the in-plane magnetic field hysteresis induced by spin magnetism is despite weak spin-orbit coupling in graphene much larger than the out-of-plane magnetic hysteresis induced by orbital magnetism, which might be explained by an inter-valley coherent component of this phase [183]. For example, at $D = -\ 0.6$ Vnm^{-1}, the hysteretic behavior in the in-plane magnetic field ends at $B_{||} = \pm 0.6$ T while in an out-of-plane magnetic field it is only present until $B_{\perp} = \pm 0.03$ T.

To conclude our initial observation, three phases with spin and valley ordering have been identified in electron-doped BLG close to the band edge were electron-electron interactions are strong: the **svi** phase is likely spin and valley polarized, the **si** phase is likely spin polarized and the **m** phase is spin and valley unpolarized.

While we revealed different regions of spin and valley polarization, our measurements up to now cannot identify if the observed phases are conventional Stoner phases in which e.g., the absence of LL at low magnetic fields stem from flat electronic bands with concomitant large effective masses and small LL spacings, or if the ground state of the system is of a more exotic nature. This is why we have performed detailed temperature and bias-dependent measurements (Fig. 3 and 4). Remarkably, close to the base temperature of our cryostat of 10 mK, we observe an increasing conductance with increasing temperature (insulating temperature dependence) in the **svi** and **si** phases which suggests these phases to be different from normal Stoner metals, where a metallic temperature dependence would be expected. This insulating temperature dependence is likely not connected to contact effects since it is only present within the **svi** and **si** phases but not at the phase boundaries which can be seen best in Fig. 3b (see also below).

The **svi** phase displays an insulating temperature dependence until T ≥ 4 K (Fig. 3, Extended Data Fig. 6). Since it is closest to the band edge where the DOS diverges (Fig. 1c), correlation effects are expected to be the most prominent in this phase. The **si** phase displays an insulating temperature dependence in a comparably lower temperature range (critical temperature $T_{\mathrm{crit}} < 100$ mK at $D = -0.6$ V nm^{-1}, Fig. 3a), but T_{crit} can be increased by applying a finite $B_{||}$ (e.g. $T_{\mathrm{crit}} \approx 2.5$ K at $B_{||} = 2$ T, Fig. 3b, Extended Data Fig. 7). The **m** phase only shows insulating behavior at $T_{\mathrm{crit}} < 100$ mK in the vicinity of the phase boundary to the si phase but acts weakly metallic at large densities (even at the lowest T) as expected in the non-interacting regime of bilayer graphene (Fig. 4, Extended Data Fig. 8). The observation of insulating temperature dependence in the **svi** and **si** phases aligns well with the measured bias current (I) dependence that shows strong nonlinearities and is indicative of a comparably larger gap in the **svi** phase and a smaller one in the **si** phase where it vanishes at small applied bias currents of approximately 10 nA at $D = -0.8$ V nm^{-1} (Fig. 4a,b, Extended Data Fig. 9,10). It resembles the bias current dependence of correlated phases in hole-doped bilayer graphene where similar behavior was suggested to be consistent with the formation of charge or spin density waves (CDW or SDW) [35] or Wigner crystals (WC) [1] in which Coulomb interaction breaks translation symmetry and strong electron-electron interactions lead to a collective ordering of electrons in a periodic standing wave or crystal.

Indeed, for a 2D system in a Stoner regime that is introduced above, theory predicts a CDW or SDW instability, arising because the momentum dependence of particle-hole susceptibility for 2D systems is in general non-monotonic - the susceptibility at a finite momentum q can exceed that at $q = 0$. The resulting CDW or SDW instability with a wavelength corresponding to the most unstable harmonic q, will modulate the Stoner-polarized Fermi sea in electron density or spin density [182].

The hallmark of this state is a highly nonlinear transport arising due to CDW or SDW sliding in the presence of an applied bias current. Indeed, we observe a conductance in the **svi** and **si** phase that peaks at a finite current (see Figure 4a). One possible explanation for this intriguing behavior involves the pinning of CDW/SDW sliding at low currents and its subsequent depinning at higher currents [184]. Essentially, the conductivity experiences a sharp increase beyond a critical current that induces the depinning of the CDW/SDW and initiates the sliding motion. However, as the current continues to rise, the conductivity begins to decline. This can be potentially attributed to the Doppler shift of the particle-hole excitation dispersion caused by the sliding CDW/SDW, eventually leading to the closure of the CDW/SDW gap at high currents [185, 186]. Consequently, the conductivity at high currents remains slightly above that at low currents.

This interpretation is consistent when studying the evolution of nonlinear conductance under varying carrier density (Fig. 4a and b, Extended Data Fig. 9, 10). The peak current decreases continuously to zero when approaching the phase transition into **svi** phase and **m** phase. Following our interpretation above that the peak corresponds to the CDW/SDW gap, this observation implies a gap closing at the phase boundary (Extended Data Fig. 11).

Next, we discuss how the 2D CDW or SDW picture explains the measured conductance temperature dependence described above. A CDW/SDW in 2D opens up gaps in small segments near the Fermi surface regions where nesting occurs, whereas the rest of Fermi surface remains gapless. The coexistence of gapped and gapless segments leads to two effects:

(i) As temperature rises, the CDW/SDW gap decreases. In that, the length of the gapped segments also decreases, whereas the gapless segments increase. As a result, the effective carrier density in this system increases. This effect leads to conductivity monotonically increasing with temperature.

(ii) However, as in ordinary metals, the conductivity at a fixed carrier density should decrease as temperature increases. This effect tends to give a conductivity monotonically decreasing with temperature.

These two effects compete with each other, leading to two possible outcomes. If the effect (i) is stronger, the system will mimic an insulator's behavior where a conductivity monotonically increases with temperature. Yet, unlike a true insulator, this increase of conductivity will be weak. We call such a system a quasi-insulator. This prediction is indeed in line with our measurement in **svi** and **si** phases (Fig. 4a,b, resistance values in these phases are shown in Extended Data Fig. 2).

Surprisingly, also the **m** phase exhibits an insulating temperature dependence and a non-linear bias current dependence in the vicinity of the phase boundary between the **si** and **m** phase (but not deep within the metallic phase, Extended Data Fig. 8, 11) which we explain by fluctuations of the collected electronic mode near the second order phase transition.

While our experimental data is in line with the picture of CDWs/SDWs that are coexisting with the Stoner phases and gap out parts of the Fermi surface there are in principle also other possible theories explaining the insulating temperature dependence and strong non-linearities with applied dc currents. For example, the Stoner phases could transition into weak Wigner crystal states that have different spin and valley orderings. To unambiguously determine the kind of ordering, further measurements, e.g. using scanning tunneling microscopy [130], would be needed.

In summary, electron-doped bilayer graphene exhibits an intriguing phase diagram at small magnetic fields characterized by three phases that exhibit different spin and valley ordering (a summary of the experimental findings is given in Extended Data Table 1). We find a quasi-insulating temperature dependence (conductance growing with temperature) and a nonlinear current bias dependence in two phases and consequently name them as spin and valley polarized insulators (**svi**) and spin polarized insulators (**si**). The high-density metal phase (**m**), on the other hand, is consistent with a non-interacting phase. In contrast to previously studied hole-doped bilayer graphene, the phases are only stable at very low n and do not seem to be related to changes in the Fermi surface topology within the band but rather to flat electronic bands and divergent DOS at the band edge. Here, the DOS seems to be large enough to facilitate the formation of an exotic ordering of electrons such as in a CDW/SDW or WC. Similar orderings might also appear in electron-doped rhombohedral trilayer graphene where Stoner phases were investigated at finite magnetic fields using compressibility measurements[25]. Possibly, also these phases show an insulating temperature and intriguing bias current dependence at $B = 0$ T.

Methods

Sample fabrication and transport measurements

Bilayer graphene, graphite and hexagonal boron nitride (hBN) flakes were prepared by mechanical exfoliation of bulk crystals and identified via optical microscopy. The bilayer graphene flakes were then encapsulated in hBN and equipped with graphite top and bottom gates using a stamping technique with a polycarbonate (PC) film on top of a polydimethylsiloxane (PDMS) stamp[146, 155]. In a first step, the heterostructures were assembled without top gate which was then added in a second stamping step. The device described in the main text was additionally equipped with graphite contacts and also used for measurements shown in Ref.[1] were this device is noted as device A and is described in detail. The sample shown in Extended Data Fig. 1 was fabricated in the same way but without graphite contacts. For this device, contacts were defined using electron-beam lithography and etched using an SF_6 plasma. The one-dimensional electrical contacts were then deposited by electron-beam evaporation of Cr/Au.

All electrical measurements (unless stated otherwise) were conducted in a dilution refrigerator equipped with home-made low-pass filters at a base temperature of 10 mK. The conductance was measured in a configuration shown in Fig. 1b/ Extended Data Fig. 1a using an a.c. bias current of 1 nA and an additional d.c. current where noted. Applying top gate voltages (V_t) and bottom gate voltages (V_b) allowed us to tune n and D as follows:

$$n = \frac{\varepsilon_0 \varepsilon_r}{d_b e} \ (\alpha V_t + V_b)$$

$$D = \frac{\varepsilon_r}{d_b e} \ (\alpha V_t - V_b)$$

where ε_0 is the permittivity in vacuum, ε_r is the dielectric constant of hBN, d_b is the thickness of the bottom hBN flake, e is the charge of an electron and α is the ratio of d_b and the thickness of the top hBN flake. As contact resistance in graphite contacts depends on T, I, n, D and $B_\perp$[1] we did not subtract contact resistance but mostly plotted G in a.u.. Measured resistances $R = 1/G$ (with no subtracted contact resistances) are shown in Extended Data Fig. 1.

Acknowledgements

R.T.W. and A.M.S. acknowledge funding from the Deutsche Forschungsgemeinschaft (DFG, German Research Foundation) under the SFB 1073 project B10. R.T.W. acknowledges partial funding from the SPP2244 from the Deutsche Forschungsgemeinschaft (DFG, German Research Foundataion). K.W. and T.T. acknowledge support from the JSPS KAKENHI (Grant Numbers 20H00354, 21H05233 and 23H02052) and World Premier International Research Center Initiative (WPI), MEXT, Japan.

Author contributions

A.M.S. fabricated the devices and conducted the measurements and data analysis. K.W. and T.T. grew the hexagonal boron nitride crystals. N.J, Z.D and L.S.L contributed the theoretical part. All authors discussed and interpreted the data. R.T.W. supervised the experiments and the analysis. The manuscript was prepared by A.M.S., Z.D, L.S.L. and R.T.W. with input from all authors.

Corresponding authors

R. Thomas Weitz (thomas.weitz@uni-goettingen.de)

Competing interests

Authors declare no competing interests.

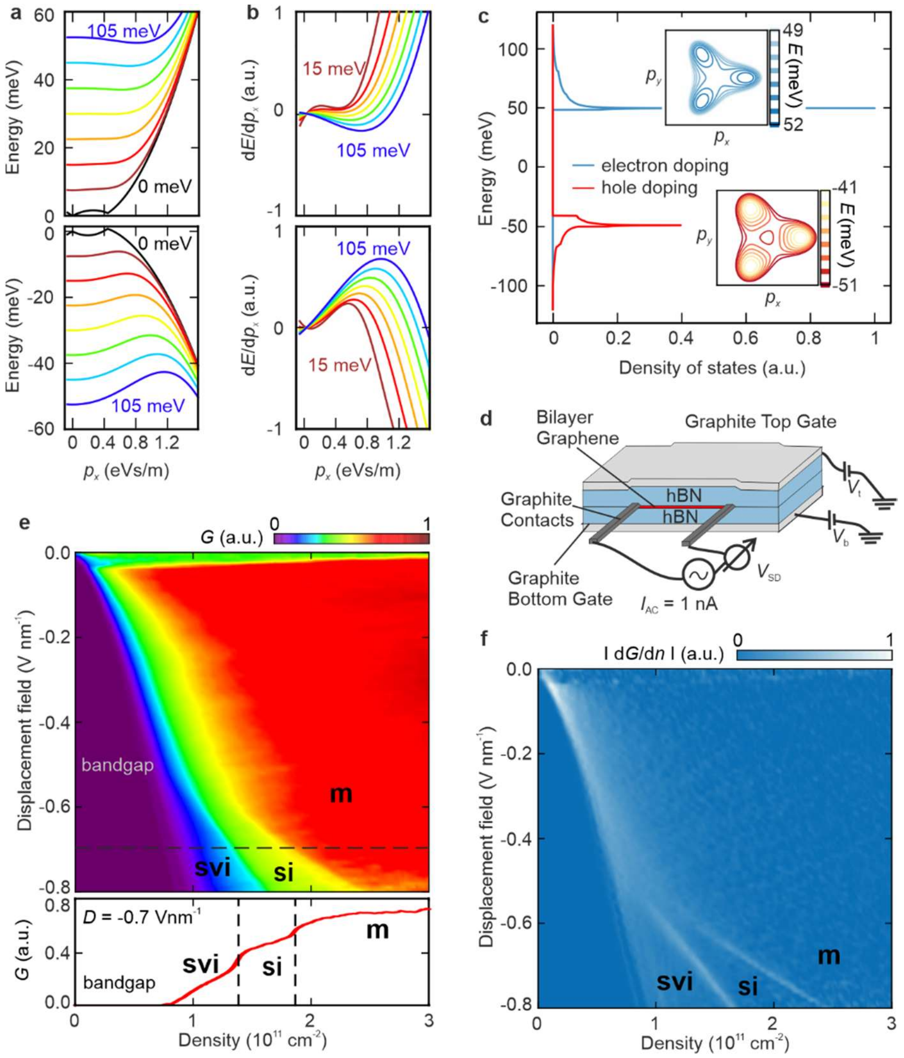

Fig. 1. Density of states and phase transitions in electron-doped Bernal bilayer graphene without magnetic field. **(a)** Calculated band structure of bilayer graphene at interlayer potential differences U ranging from 0 meV to 105 meV. Coupling parameters were taken from Ref. [85]. **(b)** Derivative of the energy bands with respect to the momentum in x-direction p_x. At large U, trigonal warping leads to a large $|dE/dp_x|$ in the valence band while the conduction band are relatively flat ($|dE/dp_x| \approx 0$). **(c)** Calculated density of states (DOS) as a function of the Fermi energy level at an interlayer potential difference $U = 100$ meV. Insets: Fermi surface contour at different Fermi energy levels at an interlayer potential difference $U = 100$ meV (please note the different energy scales in the valence and conduction band). At electron doping, trigonal warping is less pronounced and bands are flatter, i.e. changes in the Fermi surface topology appear in a smaller energy regime, resulting in

a larger density of states at the band edge. (d) Schematic of the device as well as its electrical wiring used to conduct the transport measurement shown in the main text. (e,f) Conductance (e) and normalized derivative of the conductance (f) as a function of n and D with $B_{\perp} = B_{II} = 0$. Steps in the conductance appear as peaks in the normalized derivative of the conductance. The svi, si and m phases are labeled.

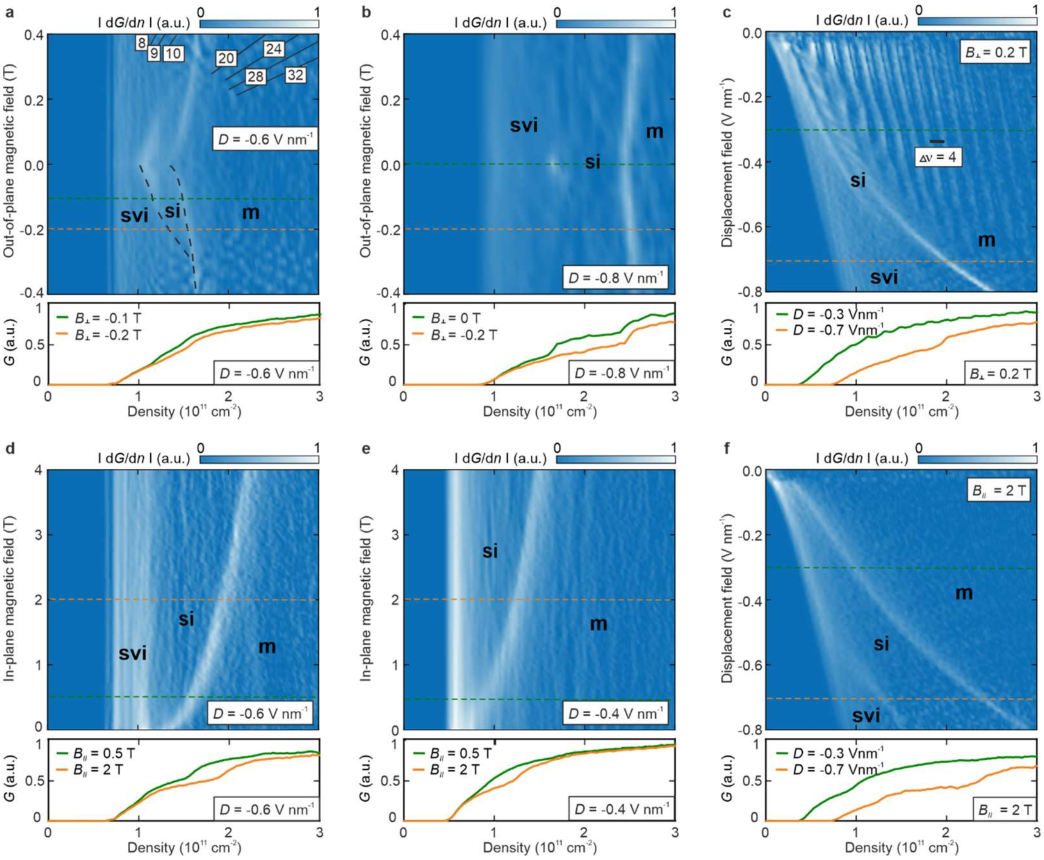

Fig. 2. Magnetic field dependence of spin and valley ordered phases. (a,b) Normalized derivative of the conductance as a function of n and $B_\perp$ for $D =$ -0.6 V nm^{-1} (a) and $D =$ -0.8 V nm^{-1} (b). Quantum Hall states are traced by lines and labeled by numerals for $B_\perp > 0$. At $D =$ -0.6 V nm^{-1} they are one-fold degenerate in the density regime of the **svi** phase that becomes a spin and valley polarized Stoner metal at $B_\perp > 0.3$ T and four-fold degenerate in the density regime of the **m** phase. No quantum Hall states appear at $D =$ -0.8 V nm^{-1}. (c) Normalized derivative of the conductance as a function of n and D for $B_\perp = 0.2$ T. Four-fold degenerate quantum Hall states appear in the density regime of the **m** phase. (d,e) Normalized derivative of the conductance as a function of n and B_{II} for $D =$ -0.6 V nm^{-1} (d) and $D =$ -0.4 V nm^{-1} (e). (f) Normalized derivative of the conductance as a function of n and D for $B_{II} = 2$ T. Line traces of the conductance G as a function of n are shown below each plot for different values of D and B.

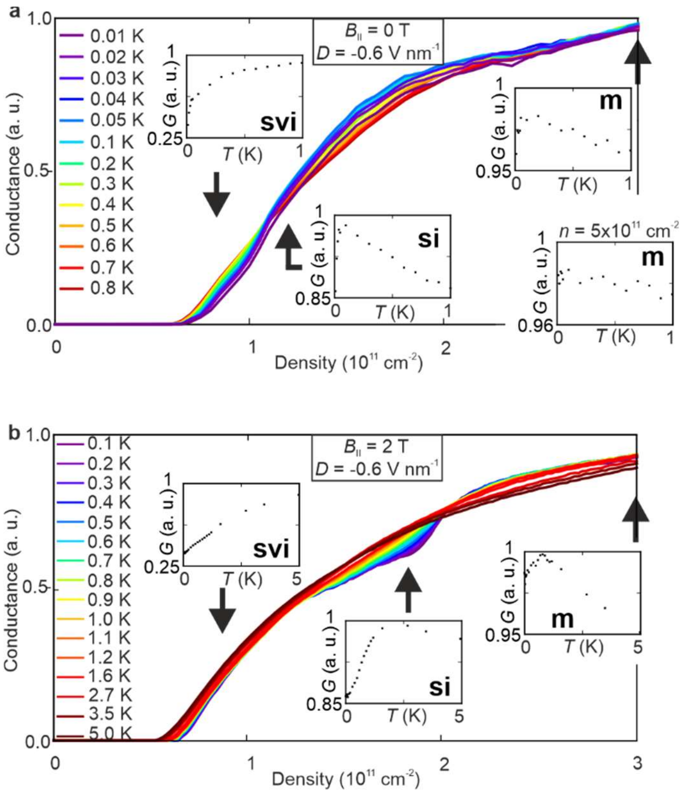

Fig. 3. Temperature dependence of spin and valley ordered phases. (a,b) Conductance G as a function of the charge carrier density for D = -0. 6 V nm^{-1} and $B_{||}$ = 0 T (a) and $B_{||}$ = 2 T (b) for different temperatures. (insets) G as a function of temperature T. Please note the different temperature scales in the insets of (a) and (b). The corresponding densities are marked by an arrow ((a) **svi** phase: n = 0.8 x 10^{11} cm^{-2}, **si** phase: n = 1.2 x 10^{11} cm^{-2}, **m** phase: n = 3 x 10^{11} cm^{-2} and n = 5 x 10^{11} cm^{-2}; (b) **svi** phase: n = 0.8 x 10^{11} cm^{-2}, **si** phase: n = 1.8 x 10^{11} cm^{-2}, **m** phase: n = 3 x 10^{11} cm^{-2}).

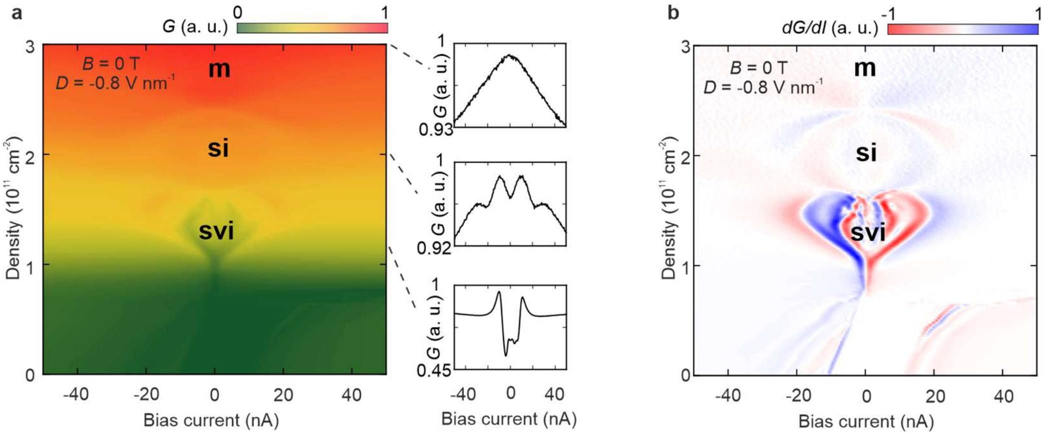

Fig. 4. Bias current dependence of spin and valley ordered phases. (a) Conductance in arbitrary units (a.u.) as a function of the bias current and the charge carrier density at $D =$ -0. 8 V nm^{-1} and $B = 0$ T. Line traces of the conductance as a function of the bias current are shown in the right panel for the **svi** phase ($n =$ 1.2 x 10^{11} cm^{-2}), the **si** phase ($n =$ 2.0 x 10^{11} cm^{-2}) and the **m** phase ($n =$ 3.0 x 10^{11} cm^{-2}). (b) Derivative of the conductance as a function of the bias current and the charge carrier density at $D =$ -0. 8 V nm^{-1} and $B = 0$ T.

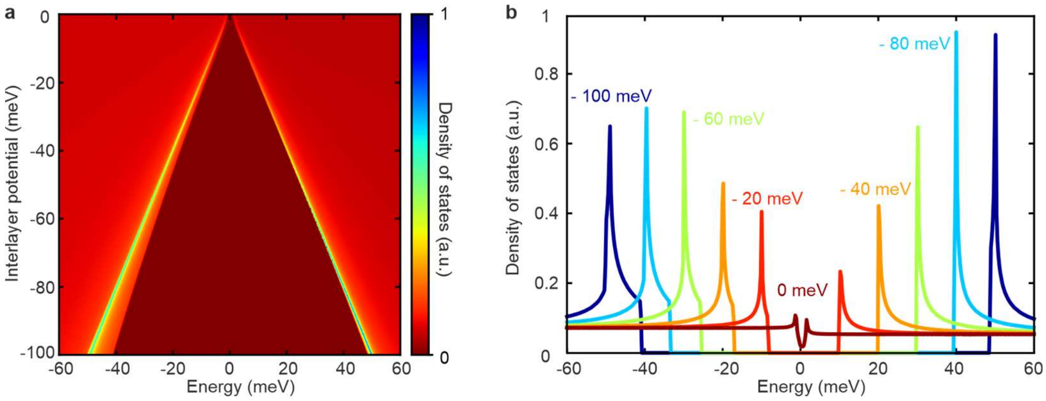

Extended Data Fig. 1. Density of states in bilayer graphene. (a) Calculated density of states as a function of the Fermi energy and the interlayer potential difference. Coupling parameters were taken from Ref.[85]. (b) Calculated density of states as a function of the Fermi energy for different interlayer potential differences. Due to electron-hole asymmetry, the peak in the density of states in electron doped bilayer graphene is located closer to the band edge than the peak in hole doped bilayer graphene and is more pronounced at large interlayer potential differences.

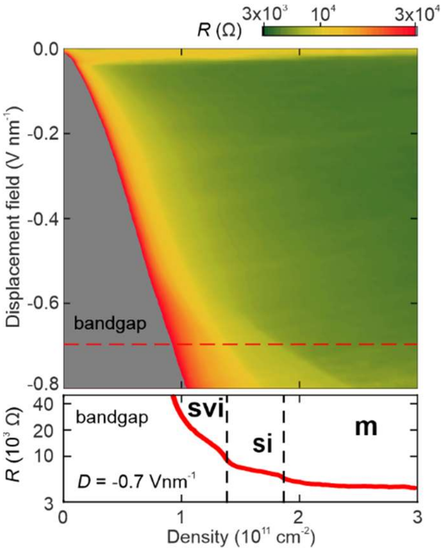

Extended Data Fig. 2. Measured resistance in the svi, si and m phases. Resistance as a function of n and D with $B_\perp = B_{II} = 0$ and linecut showing the resistance as a function of n at $D =$ -0.7 Vnm^{-1}. The **svi**, **si** and **m** phases are labeled.

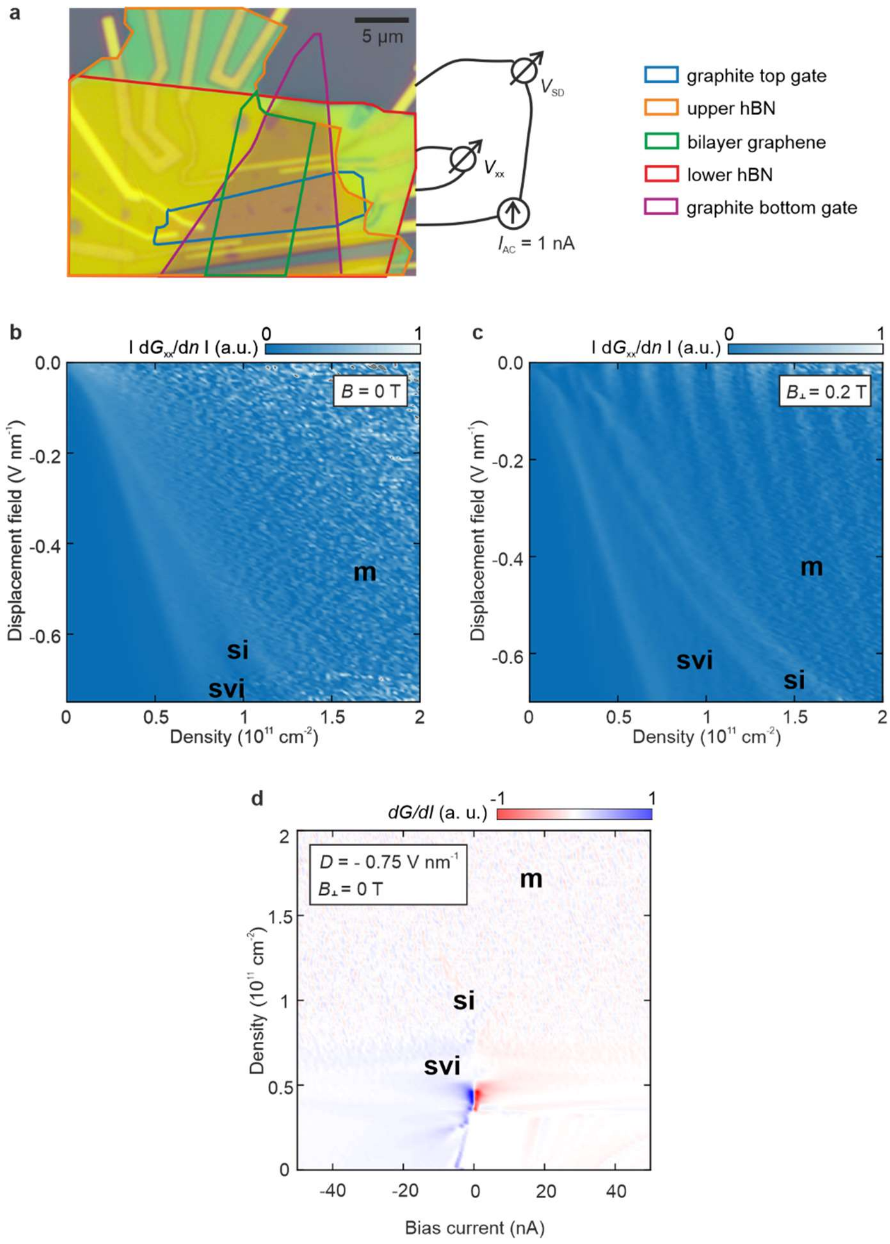

Extended Data Fig. 3. Measurements conducted in a second device. (a) Optical image of a second device. The corresponding hBN thicknesses were 69 nm (bottom hBN) and 30 nm (top hBN). **(b,c)** Normalized derivative of the conductance as a function of n and D with $B_\perp = B_{II} = 0$ T (b) and $B_\perp =$ 0.2 T, $B_{II} = 0$ T (c) measured in the device shown in (a). The three different phases are labeled and show similar behavior as the device analyzed in the main text . **(d)** Derivative of the conductance as a function of I and n at $B_\perp = B_{II} = 0$ T and $D =$ -0.75 V nm^{-1} measured in the same device. While a gap is clearly present in the **svi** phase, a gap in the **si** phase is only weakly visible.

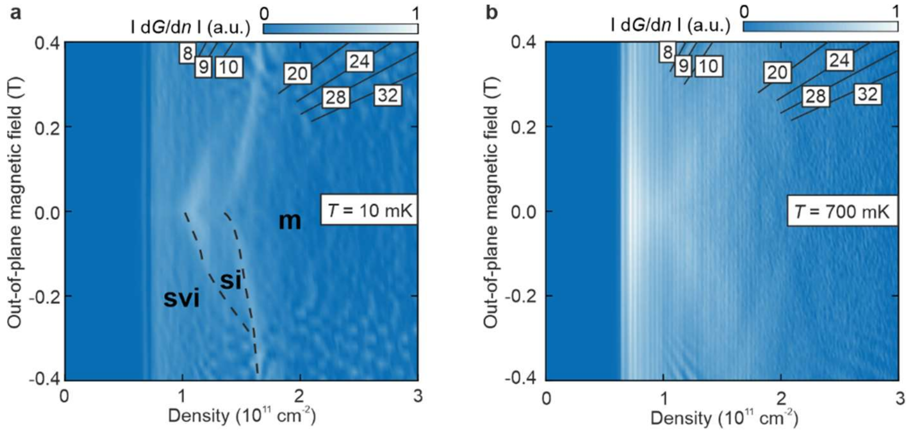

Extended Data Fig. 4. Quantum Hall states at $D = 0.6$ V nm^{-1}. (a,b) Normalized derivative of the conductance plotted as a function of charge carrier density and out-of-plane magnetic field at a temperature of 10 mK (a) and 700 mK (b). Quantum Hall states are traced by lines for positive out-of-plane magnetic fields. Corresponding filling factors are labeled by numerals. In the density regime of the **svi** phase, Landau levels are one-fold degenerate due to spin and valley polarization, in the density regime of the **m** phase they are four-fold degenerate due to spin and valley degeneracy. The one-fold degenerate quantum Hall states are even present at 700 mK when the **svi** and **si** phases at low B are not stable anymore.

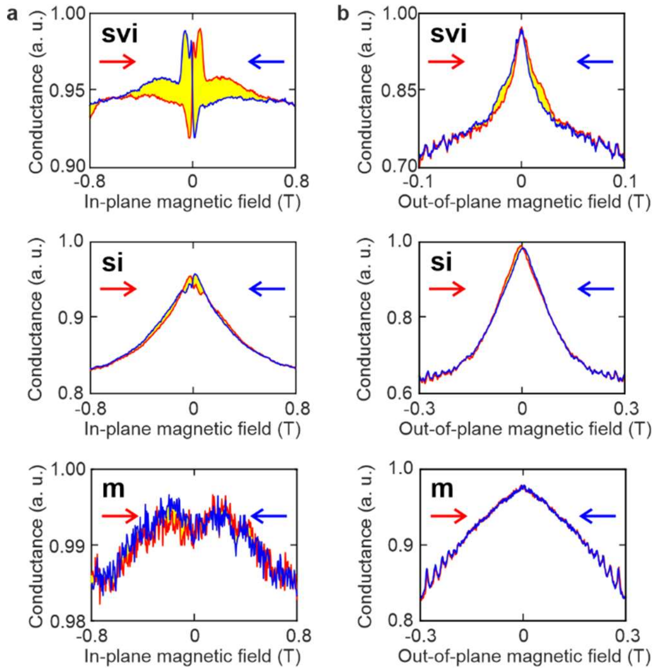

Extended Data Fig. 5. Magnetic hysteresis of spin and valley ordered phases. **(a,b)** In-plane magnetic hysteresis **(a)** and out-of-plane magnetic hysteresis **(b)** of the **svi**, **si** and **m** phases at D = -0.6 V nm^{-1}. The corresponding charge carrier densities are n = 1.0 x 10^{11} cm^{-2} (svi phase), n = 1.2 x 10^{11} cm^{-2} (**si** phase) and n = 3.0 x 10^{11} cm^{-2} (**m** phase). The forward sweeps are shown in red and the backward sweeps in blue. The hysteresis loop areas are shaded in yellow. Quantum oscillations appear at finite out-of-plane magnetic fields in the m phase.

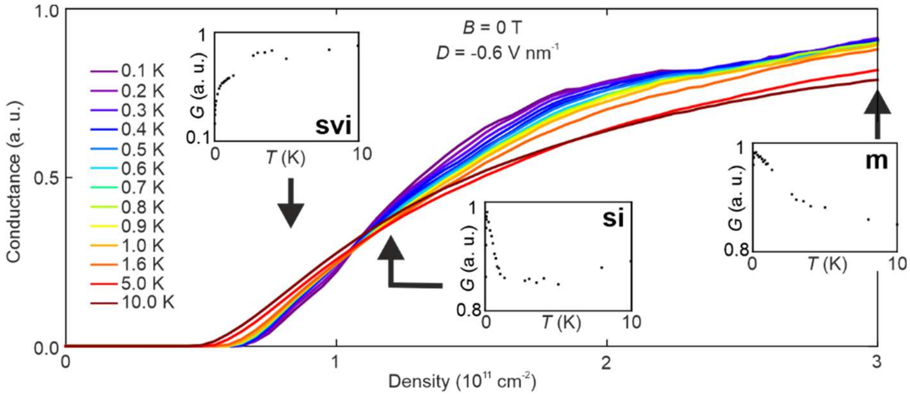

Extended Data Fig. 6. Large temperature regime. Conductance as a function of n at different temperatures at $B = 0$ T and $D =$ -0.6 Vnm^{-1}. The insets show linecuts of the conductance as a function of temperature for the different phases (si phase: $n = 0.8$ x 10^{11} cm^{-2}, svi phase: $n = 1.2$ x 10^{11} cm^{-2}, m phase: $n = 3$ x 10^{11} cm^{-2}). The **svi** phase is insulating until T ≥ 10 K.

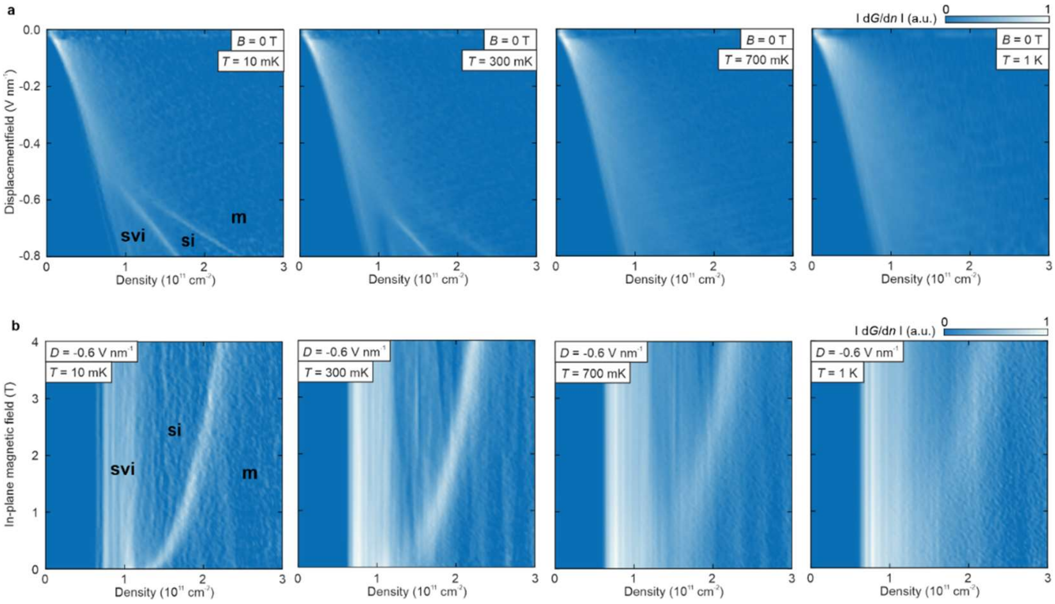

Extended Data Fig. 7. Magnetic and electric field dependence of spin and valley ordered phases at large temperatures. (a) Normalized derivative of the conductance as a function of charge carrier density and displacement field at zero magnetic field and at temperatures of 10 mK, 300 mK, 700 mK and 1 K. (b) Normalized derivative of the conductance as a function of charge carrier density and in-plane magnetic field at a displacement field of -0.6 V nm^{-1} and at temperatures of 10 mK, 300 mK, 700 mK and 1 K.

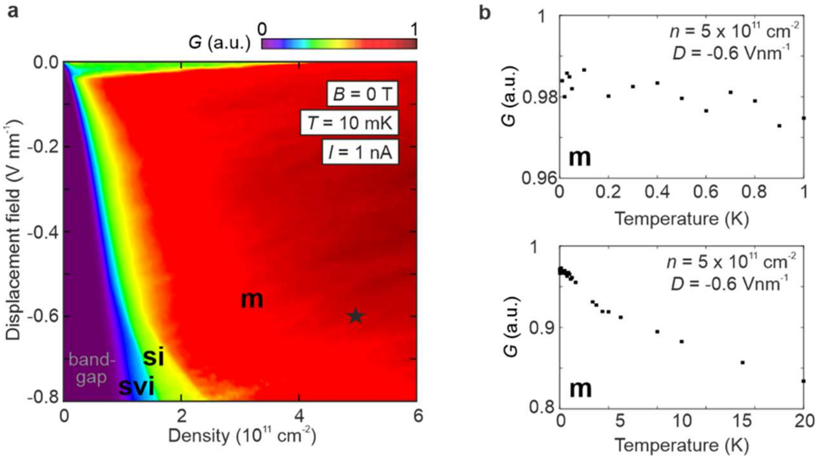

Extended Data Fig. 8. Large density regime of the m phase. (a) Conductance as a function of n and D with $B_{\perp} = B_{II} = 0$. **(b)** Line traces of the conductance as a function of temperature at D = -0.6 Vnm^{-1} and n = 5 x 10^{11}cm^{-2} (metallic phase, marked with a star in (a)).

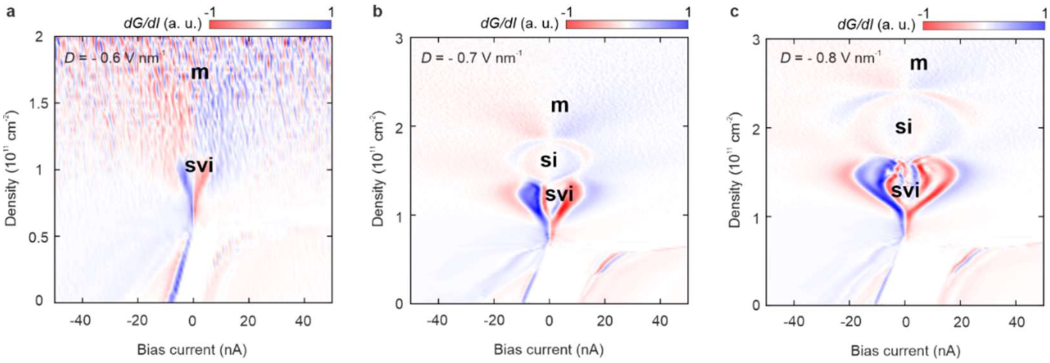

Extended Data Fig. 9. Bias current dependence for different displacement fields. (a-c) Derivative of the conductance as a function of bias current and charge carrier density at $B = 0$ T, $T = 10$ mK and $D = -0.6$ V nm^{-1} (a), $D = -0.7$ V nm^{-1} (b) and $D = -0.8$ V nm^{-1} (c). The different phases are labeled.

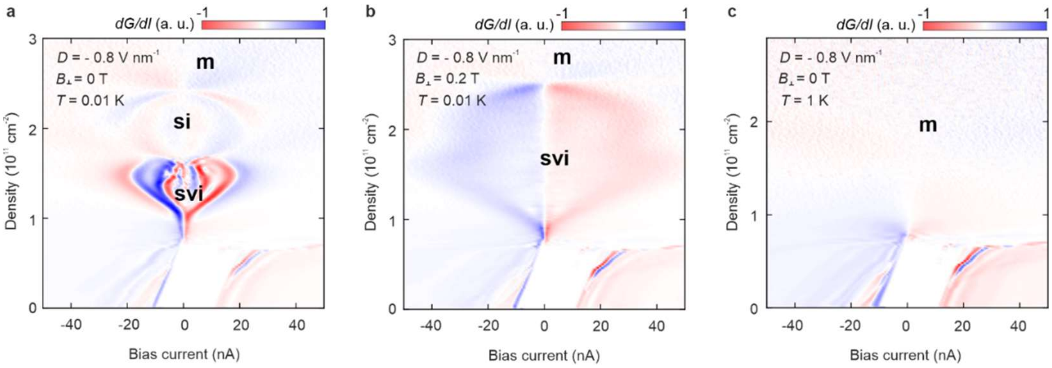

Extended Data Fig. 10. Bias current dependence at $D =$ -0.8 V nm^{-1}. (a-c) Derivative of the conductance as a function of bias current and charge carrier density at $D =$ -0.8 V nm^{-1} and $B = 0$ T and $T = 10$ mK (a), $B_\perp = 0.2$ T and $T = 10$ mK (b) and $B = 0$ T and $T = 1$ K (c).

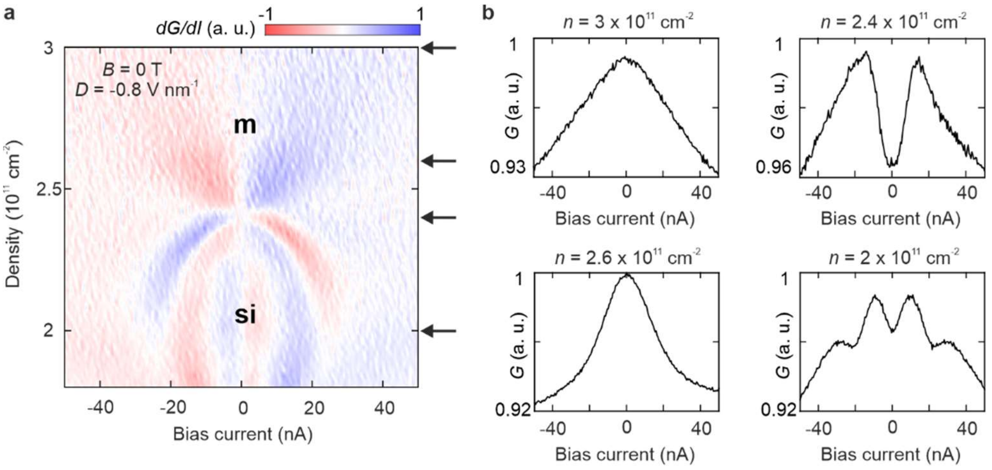

Extended Data Fig. 11. Bias current dependence near the phase boundary between the si and m phases. **(a)** Derivative of the conductance with respect to bias current (I) as a function of I and the charge carrier density at $D = -0.8$ V nm^{-1} and $B = 0$ T. **(b)** Line traces of the conductance as a function of I at different charge carrier densities that are marked with arrows in **(a)**. The **m** phase exhibits a non-linear bias current dependence in the vicinity of the phase boundary between the **si** and **m** phase that becomes weaker with increasing charge carrier density, i.e. the peak becomes less pronounced and $|dG/dI|$ becomes smaller. At the phase boundary (n ≈ 2.4 x 10^{11} cm^{-2}) the dependence on the applied bias current is weak. Please note the different scales in the conductance.

	svi phase	**si** phase	**m** phase
Valley polarization	yes	no	no
Spin polarization	yes	yes	no
Hysteresis in B_{II}	yes	yes	no
Hysteresis in $B_{\perp}$	yes	no	no
Onset of quantum Hall oscillations	$B_{\perp}$~ 300 mT	$B_{\perp}$>300 mT	$B_{\perp}$< 200 mT
Insulating T-dependence?	yes	yes	no (only near phase boundary to **si** phase)
T_{crit} at D = -0.6 Vnm^{-1} and $B_{II} = 0$ T	$\geq$ 10 K	< 100 mK	-
T_{crit} at D = -0.6 Vnm^{-1} and $B_{II} = 2$ T	$\geq$ 5 K	≈ 2.5 K	-
Non-linear bias-dependence?	yes	yes	no (only near phase boundary to **si** phase)

Extended Data Table 1. Summary of our main findings. The table summarizes the behavior of the **svi**, **si** and **m** phases that is most consistent with experimental measurements shown and discussed in the main text.

8 Discussions and outlook

In this chapter, the key results presented in Chapters 5 - 7 are summarized. Furthermore, the impact of the different works is discussed, comments on complementary works are given, and an outlook on the developments of correlated phases in Bernal bilayer graphene is presented.

8.1 Mapping out the tunable band structure in bilayer graphene

Theoretical calculations show that Bernal bilayer graphene exhibits a complex low-energy band structure. For example, trigonal warping is expected to result in the formation of four mini Dirac cones in each valley when no electric displacement field is applied. Furthermore, electron-hole asymmetry is anticipated to cause an energetic shift of the center cone compared to the three off-center cones. When a small electric displacement field is applied, a band gap opens in bilayer graphene, and the number of pockets is expected to reduce from four to three in the valence band and from four to one in the conduction band. In addition, the energy dispersion of the pockets is predicted to change from being linear to being parabolic (see Chapter 2.2 for more details).

While theoretical band structure calculations are well established, experimental evidence of the formation of four mini Dirac cones is still elusive. Moreover, several previous experiments are consistent with a simpler, truly parabolic energy dispersion. This includes previous measurements of the quantum Hall effect in bilayer graphene down to magnetic fields of 500 mT [28, 29, 34, 109, 111, 187] and the presence of a quantum anomalous Hall octet even below 20 mT [33].

In our manuscript that is reprinted in Chapter 5, the low-energy quantum Hall spectrum of Stack 99 and StackMartinAnna is analyzed in detail. In these high-quality devices, quantum Hall states can be traced down to magnetic fields below 50 mT where the inverse magnetic length and thus the cyclotron orbit of an electron in momentum space is smaller than the distance between adjacent pockets. In this regime, quantum Hall states are used as markers for the low-energy dispersion. By comparing the experimentally revealed ordering of quantum Hall states with the theoretically predicted ordering of Landau levels, it is revealed that the low-energy band structure of bilayer graphene indeed consists of four mini Dirac cones with a truly linear low-energy dispersion. Furthermore, the Landau level spectrum is shown to be consistent with electron-hole asymmetry and an energetic shift of the center cone compared to the off-center cones.

By applying small electric displacement fields, the opening of a band gap and a reordering of quantum Hall states are observed. The Landau level spectrum is then consistent with the formation of three pockets in the valence band and one pocket in the conduction band.

All in all, we find evidence for electron-hole asymmetry in Bernal bilayer graphene at zero and finite electric displacement fields and reveal an electric displacement field induced transition from a Dirac spectrum to a parabolic energy dispersion. These results not only help to unravel the low-energy band structure of a seemingly well-understood material but also classify Bernal bilayer graphene as a true example of a long sought tunable Dirac material with linear energy dispersion at zero electric displacement field.

8.1.1. Towards applications of the linearly dispersed energy bands in bilayer graphene

Monolayer graphene is well known for its linear energy dispersion that gives rise to intriguing optical and electronic properties [42, 188]. However, these properties cannot be used in applications such as in high-performance integrated logic circuits since monolayer graphene does not have a band gap, and the on/ off ratios are too low [188, 189]. To gain higher on/ off ratios, a controllable band gap needs to be induced. This would, however, imply a controlled breaking of the sublattice symmetry which is challenging.

In Bernal bilayer graphene, the sublattice degree of freedom is coupled to the layer degree of freedom (see Chapter 2.2) and previous works showed that a band gap can be electrostatically opened [94, 165]. However, signs of linear dispersed low-energy bands that give rise to intriguing electronic properties were never observed in experiment. Moreover, the mobility of bilayer graphene was always measured to be lower than the mobility of monolayer graphene which was explained by bilayer graphene's parabolic band structure [190].

Yet, in our work that is reprinted in Chapter 5, it is experimentally revealed that the low-energy band structure of high-quality Bernal bilayer graphene samples is indeed linear and compromises four mini Dirac cones. Only when electric displacement fields are applied, a band gap opens up and the low-energy band dispersion changes from being linear to parabolic. These findings offer new possibilities for high-quality bilayer graphene field-effect transistors that can be turned off effectively but should still incorporate the advantages of materials with linear dispersed energy bands such as a high mobility [191].

In a next step, future experiments will need to confirm that the intriguing electronic properties of monolayer graphene survive in high-quality unbiased bilayer graphene. For example, the mobility of bilayer graphene needs to be determined in high-quality four-terminal devices in which the mini Dirac cones can be resolved. In these samples, the mobility is likely comparable or even larger than the mobility of monolayer graphene due to the presence of four Dirac cones instead of just one Dirac cone [191].

Lastly, it is worth highlighting that the energy scale at which the dispersion is linear in bilayer graphene is very small. Thus, the measurements suggested above would need to be conducted in samples with a disorder of < 1 meV which is the energy scale at which the mini Dirac cones are present at $D = 0$ Vnm^{-1} (the corresponding band structure calculations are shown in Chapter 5). Presumably, sample disorder is why previously measured bilayer graphene samples exhibit a lower mobility compared to monolayer graphene samples which have linear dispersed bands also at higher energies.

8.1.2. Suggestions for future experiments using freestanding bilayer graphene

A lot of the research on Bernal bilayer graphene performed in the last few years has been conducted using freestanding bilayer graphene devices [28, 29, 33, 34, 164, 175, 192]. In these systems, electron-electron interaction is stronger than in encapsulated bilayer graphene devices which results from the reduced dielectric constant of the vacuum ($\varepsilon_r = 1$) compared to hBN ($\varepsilon_r > 3$, see also Chapter 2.4).

In a recent work by F. R. Geisenhof et al. [33], it is revealed that at $D = 0$ Vnm^{-1}, quantum Hall states with filling factors $\nu = \pm 4$ (instead of $\nu = \pm 8$ in this work) appear at the lowest magnetic fields in freestanding bilayer graphene (even below $B = 100$ mT where the cyclotron orbits are expected to be small enough to resolve the mini Dirac cones). At $D = \pm 15$ mVnm^{-1}, quantum Hall states with filling factors $\nu = \pm 2$ appear at the lowest magnetic fields and can be traced down to < 20 mT. These states are consistent with competing ordered ground states with quantum anomalous Hall effects in bilayer graphene [33, 193].

At first glance, these results seem to be consistent with a truly parabolic band structure and inconsistent with the results discussed in Chapter 5. A potential explanation for this inconsistency is that the mini Dirac cones are renormalized in freestanding bilayer graphene due to stronger interaction effects [142, 194]. It would be interesting to find a regime, e.g., when the freestanding samples are measured in a medium with a dielectric constant $1 < \varepsilon_r < 3$ or when the metallic gates are brought closer to the bilayer graphene, in which electron-electron interactions are suppressed but quantum Hall states can still be resolved to very low magnetic fields. The interplay between band structure and correlation effects could then be analyzed in detail.

8.1.3. Resistive features near Landau level crossings

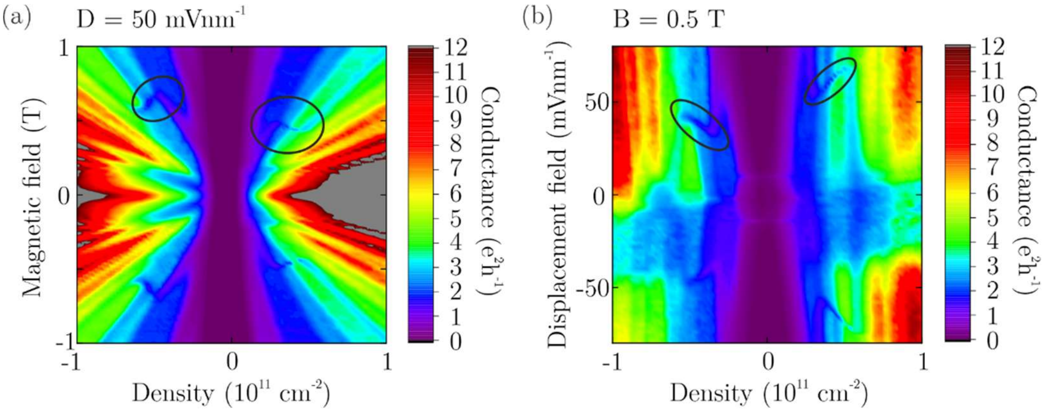

Figure 8.1 Resistive features near Landau level crossings. Conductance as a function of the charge carrier density and the out-of-plane magnetic field at an electric displacement field of 50 mVnm^{-1} (a) and as a function of the charge carrier density and the electric displacement field at an out-of-plane magnetic field of 500 mT (b). Resistive features near Landau level crossings are encircled. A magnetic-field dependent contact resistance was subtracted (see Appendix A for more information).

In our work, Landau levels are used as markers of the low-energy dispersion and Lifshitz transitions manifest as changes in the ordering of quantum Hall states. In addition, at finite electric displacement fields and finite magnetic fields, resistive features in the conductance appear when the degeneracy of the Landau levels changes and Landau levels cross. These features are encircled in Figure 8.1 for positive values of B and D.

It is not clear why the Landau level crossings result in such resistive features. Potentially, these features are first signs of correlated insulating states that appear due to the increased DOS near the Lifshitz transitions.

While correlated behavior in the vicinity of Lifshitz transitions was not studied in detail for zero or low electric displacement fields during the course of this thesis, interaction effects were indeed observed at large electric displacement fields where the DOS is larger (see Chapter 2.2). Correlated phases in the vicinity of Lifshitz transitions are discussed in Chapters 6 and 7, and in the following sections.

8.2 Quantum cascade of correlated phases in trigonally warped bilayer graphene

Bernal bilayer graphene exhibits a complex and exotic band structure consisting of four pockets in each valley that merge at finite Fermi energies. Applying an electric displacement field across the two layers not only leads to the opening of a bandgap but further results in an inversion of the center pocket and in a 'mexican hat' energy dispersion [26]. Close to the valence band edge, the Fermi surface is then composed of three disconnected pockets. When the Fermi energy is slightly shifted into the valence band, these three pockets connect: the Fermi surface becomes annular, and an inner electron-like pocket appears. When the Fermi energy is tuned far into the valence band, the Fermi surface is fully connected. Concomitant with these Lifshitz transitions, changes in the Fermi surface topology, in bilayer graphene, are van Hove singularities and a diverging DOS. Near the Lifshitz transitions, electron-electron interactions are expected to be strong and correlated behavior is possible.

In Chapter 6 (Reference [1]), transport measurements are presented that were conducted in Stack 99 and Stack 82 at millikelvin temperatures and elevated electric displacement fields. A strong deviation of the single-particle picture is observed in the vicinity of Lifshitz transitions and van Hove singularities. New phases emerge at zero and low out-of-plane magnetic fields and are revealed to be different from the well-known quantum Hall states discussed in Chapter 4.4.

These experimental findings are consistent with the formation of various interaction-driven states close to the valence band edge of hole-doped bilayer graphene where the DOS is large enough to fulfill the Stoner criterion. More specifically, we find evidence of spin and/ or valley polarized half and quarter Stoner metals with varying Landau level degeneracy and hysteresis in the in-plane and out-of-plane magnetic field. In the direct vicinity of Lifshitz transitions, correlated phases that cannot be explained by Stoner physics are revealed. These phases include two exotic metals (phase I and phase IV) that exhibit a strong linear temperature dependence, do not show signs of Landau level quantization and are consistent with strange metals.

Furthermore, three insulating phases that show an activated temperature behavior (resistance decreases with increasing temperature) and a non-linear current bias dependence that is consistent with an energy gap are revealed. One of the insulating phases that we call ‘phase II’ exhibits a slope in the out-of-plane magnetic field and is consistent with a quantum anomalous Hall phase and a Chern number of -2 while the second one (phase III) does not have a slope in the out-of-plane magnetic field and seems to be topologically trivial. The third insulating phase, phase V, appears at larger densities near the Lifshitz transition in the Stoner half metal regime and demands further investigation.

Finding gapped phases in Bernal bilayer graphene that even emerge at zero magnetic field and at finite charge carrier densities is surprising since no energy gap is expected in the non-interacting phase diagram or in the Stoner phases. Most consistent with our results is the formation of a Chern-insulating Wigner-Hall crystalline state (phase II) and a topologically trivial Wigner crystalline state (phase III) in the vicinity of the Lifshitz transitions due to strong Coulomb interactions. The formation of Mott insulating states or commensurate charge density waves can be excluded since the phases appear at very low charge carrier densities that are incommensurate with any fractional filling of the energy bands of bilayer graphene.

Overall, the results show that at large electric displacement fields, hole-doped bilayer graphene hosts a cascade of different correlated phases and offers an ideal platform for studying electron-electron interactions and exploring intricating many-body phases.

8.2.1. Comments on complementary works

Two complementary articles by H. Zhou et al. (group of Andrea Young, Reference [35]) and by S. C. de la Barrera et al. (group of Raymond Ashoori, Reference [36]) have been published at around the same time as our work that is reprinted in Chapter 6 (Reference [1]). These works show and analyze the experimental findings of interaction induced quantum phases in hole-doped bilayer graphene, too, but have different focuses. [195]

One common finding in all three works is the existence of spin and valley polarized Stoner phases that were identified by determining the degeneracy of quantum oscillations at finite out-of-plane magnetic fields. While we performed two-terminal electrical transport measurements [1], S. C. de la Barrera et al. [36] conduct compressibility measurements, and H. Zhou et al. [35] inspect both, the compressibility as well as the longitudinal resistance. In addition, we uniquely analyze the magnetic hysteresis in the Stoner phases to determine whether they are spin or valley polarized [1] while S. C. de la Barrera et al. [36] study the in-plane magnetic field dependence of all Stoner phases in detail. [195]

While all experiments report the observation of Stoner ferromagnetic states, our work uniquely reports on insulating phases and metallic phases of non-Stoner type (phases I-IV). The phase boundaries of these phases, can also be extracted from the experimental data shown in Reference [35], see for example Figure 1E and Figure 2A in Reference [35]. For example, our phases II and III are located in the same density and electric displacement field regime as the first isospin ferromagnet (IF_1) and the first partially isospin polarized phase (PIP_1) reported in Reference [35], where these phases are suggested to be metallic Stoner phases. This classification, however, is not in agreement with the temperature and current bias dependent measurements that are only shown in our work and reveal the insulating behavior of these phases.

In the density regime of the correlated metals of non-Stoner type (phases I and IV) [1], Reference [35] reports a twelve-fold degenerate phase which is neither valley nor spin polarized and in which the Fermi surface consist of three disconnected pockets. This observation is in contrast to our findings due to the observed magnetic hysteresis and the absence of Landau levels in these phases.

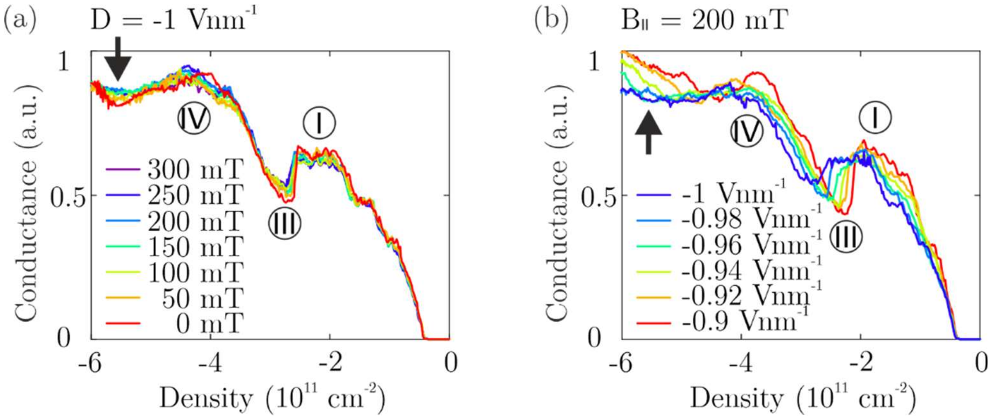

Figure 8.2 Attempt to measure superconductivity. Conductance measured as a function of density at an electric displacement field D of -1 Vnm^{-1} and different in-plane magnetic fields $B_{||}$ (a) and at $B_{||}$ = 200 mT and different D (b) at T = 10 mK using Stack 99. Phases I, III and IV are labeled. Phase II is not stable at $|D| \geq 0.9$ Vnm^{-1} when no out-of-plane magnetic field is applied. According to Reference [35], superconductivity is expected in the density regime marked by an arrow.

Remarkably, Reference [35] observes superconductivity when applying an in-plane magnetic field of 0.1 T to 1 T. The superconducting phase is located near the symmetry breaking transition between a partially isospin polarized phase and a non-polarized phase at electric displacement fields of $|D| \geq$ 0.92 Vnm^{-1}. Its density regime matches the density regime of the insulating phase V that appears at finite out-of-plane magnetic fields and is also reported in Reference [35] where it even appears without out-of-plane magnetic field. In fact, H. Zhou et al. [35] observe a transition from the insulating phase to the superconducting phase when increasing the in-plane magnetic field [35].

Measurements in the D- and $B_{||}$-field regime in which superconductivity was reported in Ref. [35] were also conducted using Stack 99, which exhibits two-terminal contacts. These measurements are shown in Figure 8.2. In a two-terminal device, the first sign of superconductivity would be the emergence of a region with increased conductance that appears when increasing D or $B_{||}$. However, no such region emerged. A possible reason why there are no signs of superconductivity in this device could be that the superconducting phase is competing with other correlated phases that are stronger in some devices than in others due to differences in the sample quality, possible alignment with one of the hBN flakes or due to different thicknesses of the hBN flakes (the thickness of the dielectric medium has an influence on r_s, see Equation(31)). As the critical temperature dependence of the superconducting phase is about 25 mK, it could also be that the effective electron temperature of our cryostat is too high to observe superconductivity (a short discussion on the effective electron temperature in our cryostat is given in Chapter 4.1).

Superconductivity in pure Bernal bilayer graphene is has not been reproduced by any other group. However, recently different groups reported the observation of an enhanced region of superconductivity when placing a sheet of WSe_2 on top of a bilayer graphene flake whereby spin-orbit coupling is enhanced [69, 98, 196]. Superconductivity then appears in the same density regime and can even be seen without applying an in-plane magnetic field. Why spin-orbit coupling enhances superconductivity in bilayer graphene is still under investigation [98, 196–199].

Several pairing mechanisms for superconductivity and different hypotheses why superconductivity competes with purely interacting correlated insulator states were suggested [198, 200–205]. For example, M. Xie and S. Das Sarma [201] suggest that the superconducting phase in bilayer graphene is phonon-driven and is competing with an intervalley coherent state that is suppressed by in-plane magnetic fields, spin-orbit coupling or the screening of Coulomb interactions due to nearby metallic gates. A. Jimeno-Pozo et al. [198] suggest that screened long-range Coulomb interaction alone gives rise to superconductivity in bilayer graphene and suppresses other exchange driven phases and Z. Dong et al. [203] suggest that spin triplet superconductivity arises from quantum-critical fluctuations whereas without in-plane magnetic fields strong repulsive interaction leads to the formation of a correlated insulator state.

Future experiments such as a systematic study on the influence of gate screening via controlling the dielectric thickness and testing different dielectric mediums are needed to experimentally assess these theoretical considerations and to further disentangle the interplay between correlated insulators and superconductivity.

8.2.2. Towards a characterization of the quantum cascade of correlated phases using four-terminal devices

The correlated insulator phases II, III and V and correlated metals of non-Stoner type (phase I and IV) are not yet fully understood and demand further investigation. In fact, possible correlated states that are consistent with our measurements can only be suggested but cannot be surely assigned.

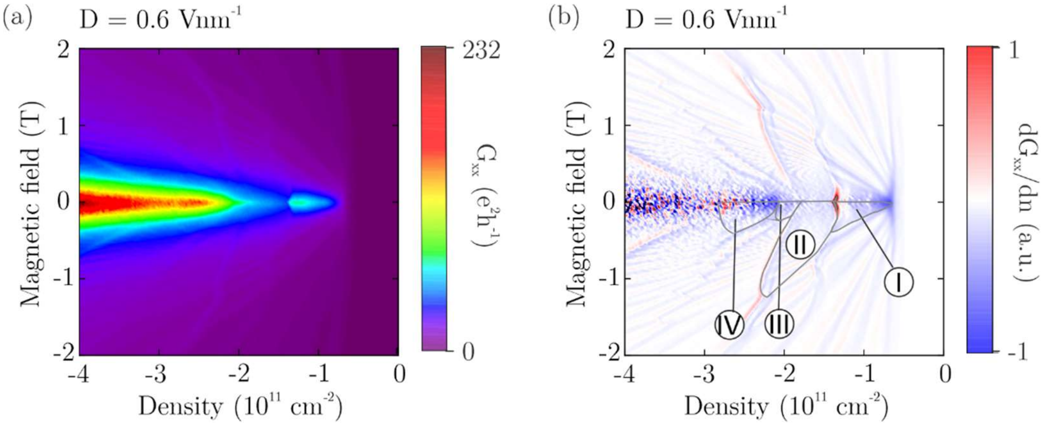

Figure 8.3 Correlated phases measured in Stack 70. (a, b) Measured longitudinal conductance G_{xx} (a) and derivative of the longitudinal conductance $\mathrm{d}G_{\mathrm{xx}}/\mathrm{d}n$ as a function of the charge carrier density and the out-of-plane magnetic field at an electric displacement field of $D = 0.6$ Vnm^{-1}. The correlated phases I-IV are labeled and highlighted in grey for $B_{\perp} < 0$. The measurement was conducted at a temperature of $T = 10$ mK.

Measuring devices with contacts shaped in a Hall bar geometry will allow to make more accurate statements on the temperature dependence of these phases. For example, it needs to be confirmed that the resistance in phase I and IV indeed increases linearly with increasing temperature. Furthermore, it would be very interesting to see whether the Hall conductance G_{xy} of phase II is indeed $2e^2h^{-1}$ which would support or current understanding of this phase.

First four-terminal measurements of the correlated phases have been conducted using the upper device of Stack 70 that exhibits edge contacts shaped in a Hall bar geometry and a local graphite top gate. So far, only G_{xx} and G_{SD} but not G_{xy} were measured in this device. G_{xx} plotted as a function of n and $B_\perp$ is shown in Figure 8.3a. While in general the phase diagram of correlated phases is reproduced, the phases are not as well pronounced as in other devices which is likely due to disorder in the sample. However, all phase boundaries can be clearly resolved in the derivative of the conductance that is shown in Figure 8.3b. If the disorder in this device comes from the use of gold contacts, from the use of a local top gate or from other factors cannot be revealed at this point.

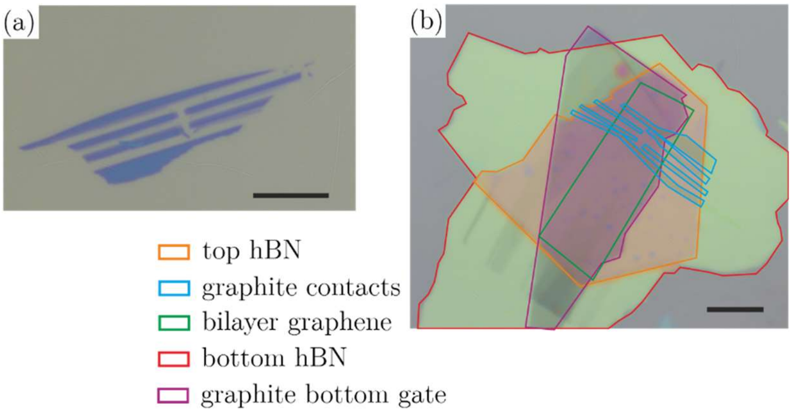

Figure 8.4 Implementation of graphite contacts shaped in a Hall bar geometry. (a) Optical microscope image of a graphite flake that is patterend into contacts shaped in a Hall bar geometry. (b) Optical microscope image of a bilayer graphene heterostructure that has patterned graphite contacts. The graphite contacts moved during the sample assembly and are now deformed. The scalebar is 10 μm in both images.

Lastly, to better understand phases I - V, high-quality four-terminal devices that allow to measure G_{xx} and G_{xy} are needed. Since devices with graphite contacts gave the highest quality so far, it would be very useful to fabricate devices that exhibit graphite contacts shaped in a Hall bar geometry. In cooperation with Dr. Lisa Walter, David Urbaniak, Monica Kolek Martinez de Azagra, Jonas Pöhls and Isabell Weimer, I have been working on a technique to employ patterned graphite contacts in bilayer graphene heterostructures. Therefore, few-layer graphite flakes are patterned using electrode-free anodic oxidation nanolithography that is described in detail in Reference [206]. This technique allows to pattern the graphite contacts without bringing them in contact with polymers such as a PMMA resist which would leave behind residuals and would introduce disorder in the sample. A picture of such a patterned contact is shown in Figure 8.4a. In a next step, we will need to embed the contacts into our devices using the stamping technique described in Chapter 3.3 which is, however, challenging since the contacts tend to break and move during this process. This is for example illustrated in the optical microscope image presented in Figure 8.4b. Here, a heterostructure is shown in which patterned graphite flakes have been embedded. The contacts moved during the assembly of the heterostructure and are now deformed.

8.2.3. Suggestions for a characterization beyond electrical transport measurements

When performing electrical transport measurements, it is only possible to probe the conductance or resistance in bilayer graphene and to then conclude on possible correlation effects. However, to elucidate the correlated phases further, a set of different measurement techniques is needed. For example, scanning tunneling microscopy could be used to locally map the DOS which might reveal ordered states such as Wigner crystals [130] or charge density waves [207]. Angle-resolved photoemission spectroscopy would allow to determine the effective band structure [93]. In this regard, a graphene sensing layer could be used as a top gate to still be able to gate the bilayer graphene samples from both sides [130]. Also these measurements would need to be conducted at millikelvin temperatures.

8.3 Interacting ground states of electron-doped bilayer graphene at large electric displacement fields

In the previous section, it is shown that hole-doped Bernal bilayer graphene exhibits a complex phase diagram at large electric displacement fields where multiple Lifshitz transitions give rise to van Hove singularities and a divergent density of states. In this regime, we and other groups found Stoner ferromagnets [1, 35, 36] as well as other correlated phases such as correlated insulators [1, 35], correlated metals of non-Stoner type [1] and even a superconducting state [35].

The electron-doped regime of Bernal bilayer graphene is expected to host similar interaction effects. Compared to the valence band, trigonal warping in the conduction band is less pronounced and changes in the Fermi surface topology only appear at large electric displacement fields and at very low electric displacement field where the three-off-center cones disappear (the latter electric displacement field regime is ignored for now). However, at large electric displacement fields, the energy bands of electron-doped bilayer graphene are flatter, and close to the conduction band edge, the DOS becomes even larger than the DOS in hole-doped bilayer graphene (see Extended Data Fig. 1 in Chapter 7). Nevertheless, only Stoner ferromagnetism was reported in electron-doped bilayer graphene in a previous work [36].

In our manuscript that is reprinted in Chapter 7, electrical transport measurements in electron-doped bilayer graphene at large electric displacement fields are presented. Two interaction induced phases at zero and low out-of-plane magnetic fields that cannot be explained by just Stoner ferromagnetism are revealed and analyzed. We label these phases with **svi** (spin and valley polarized insulator) and **si** (spin polarized insulator) and find that they have different spin and valley orderings by investigating their in-plane and out-of-plane magnetic field dependence and their hysteresis in the magnetic field.

Furthermore, an insulating temperature dependence (conductance increases with increasing temperature) and an intriguing current-bias dependence that is consistent with a gap in both phases are revealed. These results hint towards an exotic ground state of the spin and valley polarized phases. We conclude that interaction effects in electron-doped bilayer graphene not only result in a breaking of the spin and valley degrees of freedom but also in a reconstruction of the energy bands. At small Fermi energies, the Fermi surface seems to become (partially) gapped and the **svi** and **si** phases are then consistent with either incommensurate charge density waves or Wigner crystals with different spin and valley polarizations.

8.3.1. Comparing the correlated phases in electron-doped and hole-doped bilayer graphene

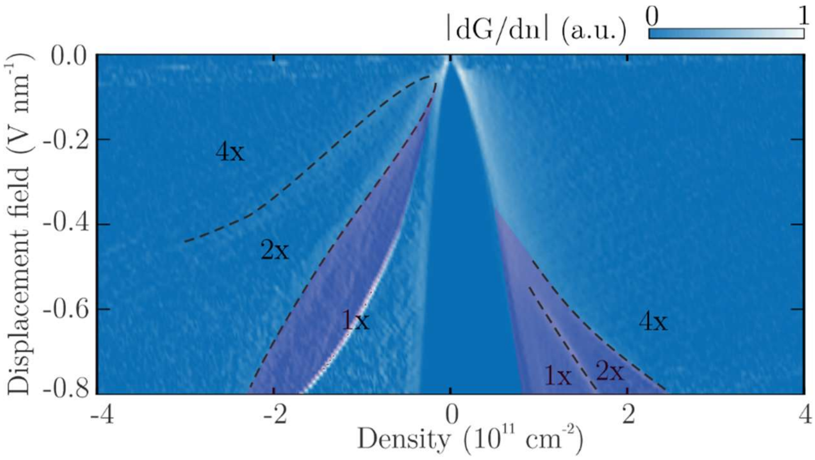

Figure 8.5 Phase transitions in hole- and electron-doped bilayer graphene. Normalized derivative of the conductance as a function of n and D with $B_{\perp} = B_{II} = 0$ T. Steps in the conductance appear as peaks in the normalized derivative of the conductance. Regions in which the bilayer graphene is spin and valley degenerate (4x), spin or valley degenerate (2x) or fully polarized (1x) are labeled and separated by dashed lined. Insulating phases are highlighted in red. The measurement was conducted at a temperature of T = 10 mK using Stack 99.

The band structure of Bernal bilayer graphene is electron-hole asymmetric. At large electric displacement fields, this leads to the emergence of different sets of correlated phases that are compared in the following.

At non-zero electric displacement fields, changes in the Fermi surface topology of bilayer graphene start to appear at low electric displacement fields in the valence band but only at large electric displacement fields in the conduction band. Since these Lifshitz transitions come along with an increase in the DOS that is needed to fulfill the Stoner criterion, spin and valley polarized phases emerge at different electric displacement fields in both bands (see Figure 8.5).

Insulating phases consistent with charge density waves or Wigner crystals are revealed on both sides of the phase diagram and are highlighted in red in Figure 8.5. On both sides, these phases appear near the regime in which the Fermi surface is annular and the DOS is largest. In hole-doped bilayer graphene, trigonal warping is more pronounced and the van Hove singularities appear at finite energies. Thus, the correlated insulators (phase II and phase III) do not emerge at the band edge but in the middle of the band. In electron-doped bilayer graphene, however, transitions in the Fermi surface appear in a much smaller density regime near the band edge where the bands are almost flat. Consequently, the correlated insulators (the svi and si phases) appear at the band edge and persist within the entire polarized density regime.

Even though the correlated insulators in hole- and electron-doped bilayer graphene appear in the vicinity of Lifshitz transitions where the DOS is high, there are some fundamental differences between the phases:

In hole-doped bilayer graphene, phase II exhibits a slope in the magnetic field that is consistent with a Chern number of -2 while the svi and si phases in electron-doped bilayer graphene do not have a slope in the out-of-plane magnetic field that can be related to a finite Chern number. Furthermore, phase II exhibits a conductance of approximately 2 e^2/h (at least in Stack 99 where this phase is most pronounced). We consequently assume this phase to be fully gapped and to only exhibit edge states. Thus, phase II is consistent with a Wigner Hall crystal phase.

The svi and si phases in the conduction band (and also phase III in the valence band) are likely not fully gapped. These phases can either be Wigner crystals that are not fully gapped due to disorder, or charge density waves in which the Fermi surface is only partially gapped. These states are, however, difficult to disentangle and can transform into each other via second order phase transitions [208, 209].

Further theoretical and experimental investigation of these phases is needed to find out why the different phases emerge. Measurements on four-terminal devices as well as complementary measurement techniques that are discussed in the previous sections would help in this regard.

8.3.2. Comparing the correlated phases in Bernal bilayer graphene and rhombohedral-stacked trilayer graphene

Stoner half and quarter metals have recently been investigated in electron-doped rhombohedral-stacked trilayer graphene at zero and finite magnetic fields but no insulating states similar to our **svi** and **si** phases have been reported [24, 25]. Since the band structure of rhombohedral-stacked trilayer and Bernal bilayer graphene is very similar, it is well worth to examine these phases in rhombohedral-stacked trilayer graphene or other rhombohedral-stacked multilayer graphene systems, too, despite the increased experimental effort needed to fabricate these samples [25]. In fact, spin and valley polarized phases at $B = 0$ T have been observed at even smaller electric displacement fields below 0.1 Vnm^{-1} but no temperature or current bias dependence in these phases has been shown which could potentially reveal insulating behavior. The low electric displacement field onset of these phases might even allow to observe the phases in freestanding rhombohedral-stacked multilayer graphene samples that are easier to fabricate.

Lastly, it is worth mentioning that also superconductivity has recently been observed in electron-doped rhombohedral-stacked trilayer graphene at ≈ 0.1 Vnm^{-1} in a density regime in which the spin polarized phase emerges [166]. Potentially, this superconducting phase can be reproduced in electron-doped bilayer graphene at even lower temperatures and in cleaner samples or when spin-orbit coupling is enhanced [98, 196].

9 Conclusions

In this thesis, investigations into the complex band structure and the intriguing correlated phase diagram of Bernal bilayer graphene are presented. An essential requirement for gaining insight into these topics is the fabrication of high-quality encapsulated bilayer graphene heterostructures that can be electrically contacted and measured at millikelvin temperatures. The key results of the electrical transport measurements that have been performed throughout this thesis can be divided into three parts and are summarized below.

Firstly, the low-energy band structure of unbiased bilayer graphene is uncovered. By analyzing the Landau level spectrum of bilayer graphene at zero electric displacement field, it is experimentally revealed for the first time that the band structure of bilayer graphene consists of four electron-hole asymmetric mini Dirac cones. This experimental result is shown to be consistent with theoretical predictions and makes Bernal bilayer graphene the first massless Dirac material with a truly linear energy dispersion that can be tuned electrostatically. A reordering of quantum Hall states is observed at finite electric displacement fields when Lifshitz transitions in the band structure occur and the topology of the Fermi surface changes.

Next, transport measurements that were conducted at large applied electric displacement fields. Here, Lifshitz transitions and concomitant van Hove singularities in the low-energy band structure give rise to electron-electron interaction-induced states. In hole-doped bilayer graphene, several magnetic phases consistent with Stoner ferromagnetic phases are revealed. Furthermore, experimental signatures of competing insulating states are found. Two insulating states are consistent with a topologically trivial Wigner crystal state and a topologically non-trivial Wigner Hall crystal state. In addition, two correlated metal phases of non-Stoner type are observed in the vicinity of the insulating phases and are concluded to be consistent with strange metal phases.

Lastly, correlated phases at large electric displacement fields are found in electron-doped bilayer graphene. In the conduction band, trigonal warping is less pronounced and interaction effects appear in the vicinity of the band edge where the conduction band is flatter compared to the valence band. Similar to hole-doped bilayer graphene, Stoner ferromagnetic phases with different spin and valley polarization are observed. At low magnetic fields, phase transitions to an insulating spin- and valley-polarized phase and an insulating spin-polarized phase occur. Both phases are consistent with electron-electron interaction-induced charge density waves or again Wigner crystals.

In summary, it is clearly shown that the complex low-energy band structure of Bernal bilayer graphene hosts several correlated phases when the Fermi energy lies in the vicinity of Lifshitz transitions and the density of states diverges. While some of the observed phases, including Stoner ferromagnetic phases and correlated metal phases of non-Stoner type, were previously identified in much more complicated systems, like in magic-angle twisted bilayer graphene, the topologically non-trivial Wigner-Hall crystal state has only been revealed in Bernal bilayer graphene during the course of this thesis.

These investigations have greatly elucidated the complex correlation physics present in bilayer graphene. However, the correlated phase diagram is still far from being fully understood and demands further investigation. In particular, more-ideal devices with four-terminal graphite contacts are needed to investigate how experimental parameters such as the thickness of the hBN flakes influence the appearance of interaction-induced phenomena. Furthermore, it would be interesting to analyze the phases using a set of different measurement techniques, such as scanning tunneling microscopy. Thereby, information on the spatial ordering of electrons that cannot be gained by conventional transport measurements would possibly be obtained (see Section 8.2.3).

Finally, it is worth highlighting that correlated electronic states in Bernal bilayer graphene are currently only stable at temperatures up to 1 K. Thus, possible applications, such as in topological quantum computing [210–212], that demand stability at higher temperatures are still far off. Nevertheless, the tunability and simplicity of Bernal bilayer graphene already provides an attractive platform for exploring intricate many-body phases in further experiments.

Appendix

A. Supplementary material for ’Mapping out the tunable multi-cone band structure in Bernal bilayer graphene’ (Chapter 5)

In this supplementary material we give more details on the tight-binding and inverse compressibility calculations described in the main text. Furthermore, we give a characterization of the device discussed in the main text and present data conducted in a second device.

Tight-binding calculations

The Landau level calculations were based on a realistic tight binding model for the π-electrons as described in Ref. [26].

The model includes different hopping processes which are described by different parameters: γ_0 describes the tunneling for neighboring sites within a single graphene sheet. γ_1 accounts for hopping processes between the aligned lattice sites of the two sheets, the so-called dimer sites. Finally, γ_3 and γ_4 are the hopping parameters between non-dimer sites. γ_3 causes the trigonal warping of the Fermi sea at low carrier densities. Further parameters are Δ', an energy difference between dimer and non-dimer sites, and the interlayer potential U accounting for an out-of-plane displacement field. The magnitudes of these parameters were taken from Ref. [85].

We used a two-band model which is reduced to the non-dimer sites and includes direct hoppings via $\gamma_3$and γ_4, as well as hoppings via dimer sites. It is expected to capture the correct low-energy physics if γ_0 and γ_1 are the relevant energy scales of the problems.

Writing

$\pi = \xi p_x + ip_y$ and $\pi^+ = \xi p_x - ip_y$ with denoting the valley index and p_x and p_y denoting the x and y components of the momentum vector, one may decompose the Hamiltonian into as $h = h_0 + h_w + h_{as} + h_U$ with

$$h_0 = -\frac{1}{2m}\begin{pmatrix} 0 & (\pi^+)^2 \\ \pi^2 & 0 \end{pmatrix},$$

$$h_w = v_3\begin{pmatrix} 0 & \pi \\ \pi^+ & 0 \end{pmatrix} - \frac{v_3 a}{4\sqrt{3}\hbar}\begin{pmatrix} 0 & (\pi^+)^2 \\ \pi^2 & 0 \end{pmatrix},$$

$$h_{as} = \left(\frac{2vv_4}{\gamma_1} + \frac{\Delta' v^2}{\gamma_1^2}\right)\begin{pmatrix} \pi^+\pi & 0 \\ 0 & \pi\pi^+ \end{pmatrix},$$

$$h_U = -\frac{U}{2}\left[\begin{pmatrix} 1 & 0 \\ 0 & -1 \end{pmatrix} - \frac{2v^2}{\gamma_1^2}\begin{pmatrix} \pi^+\pi & 0 \\ 0 & -\pi\pi^+ \end{pmatrix}\right],$$

where we have introduced the velocities $v = \frac{\sqrt{3}a\gamma_0}{2\hbar}$, $v_3 = \frac{\sqrt{3}a\gamma_3}{2\hbar}$, $v_4 = \frac{\sqrt{3}a\gamma_4}{2\hbar}$ with the lattice constant a and the band mass $m = \frac{\gamma_1}{2v^2}$. A diagonalization yields momentum space representations of two component wave functions $\Psi = \frac{1}{\sqrt{2}}(\psi_1, \psi_2)$, with the components $\psi_{1(2)}$specifying the wave functions projections on the non-dimer sites.

The first term (h_0) describes the simple parabolic two band model with the dominant hopping processes between non-dimer sites, the second (h_w) accounts for trigonal warping, the third one (h_{as}) introduces an intrinsic electron-hole asymmetry and the fourth one (h_U) the influence of external fields.

The effect of the latter may be understood by realizing that a displacement field results in a potential difference U between the two graphene sheets. A rigorous estimation of the magnitude of the potential requires a self-consistent computation that includes the screening effects due to the redistribution of charge carriers between the two sheets in the presence of a displacement field [26].

Without aiming for an exact quantitative description, we estimate the rough magnitude of U via a simple plate-capacitor calculation as $U = cD$ where $c = 3.35$ Å is the interlayer spacing. This estimate assumes minor importance of screening effects at small displacement fields.

The out-of-plane magnetic field of magnitude B is introduced by adding a contribution from the vector potential to canonical momenta. In the Landau gauge this modifies the momentum operator according to $\pi = -i\xi\hbar\partial_x +$

$\hbar\partial_y - ieBx$ and $\pi^+ = -i\xi\hbar\partial_x - \hbar\partial_y + ieBx$. The operators satisfy the same algebraic relation as the ladder operators of the harmonic oscillator up to prefactors, namely $[\pi, \pi^+] = -2Be\xi$. One may use this fact to define the operators $a = -\frac{i}{\sqrt{2eB}}\pi$ and $a^+ = \frac{i}{\sqrt{2e}}\pi^+$ for the K_+ -valley or $a^+ = -\frac{i}{\sqrt{2eB}}\pi$ and $a = -\frac{i}{\sqrt{2e}}\pi^+$ for the K_--valley. These operators act like raising and lowering operators for an oscillator with the cyclotron frequency $\omega_c = \frac{eB}{m}$. Their action on the oscillator wave functions reads $a\Phi_l = \sqrt{l}\Phi_{l-1}$and $a^+\Phi_l = \sqrt{l+1}\Phi_{l+1}$

The Hamiltonian in the K_+-valley may then be rewritten as

$$\hat{h} = \begin{bmatrix} -\frac{U}{2} + C_+ a^+ a & A(a^+)^2 - iRa \\ Aa^2 + iRa^+ & \frac{U}{2} + C_- aa^+ \end{bmatrix}$$

with

$$A = \hbar\omega_c\left(1 + \frac{\gamma_1\gamma_3}{6\gamma_0^2}\right),$$

$$R = \frac{\gamma_3}{\gamma_0}\sqrt{\gamma_1\hbar\omega_c}$$

and

$$C_\pm = \hbar\omega_c\left(\frac{2\gamma_4}{\gamma_0} + \frac{\Delta' \pm U}{\gamma_1}\right).$$

In the opposite valley the roles of creators and annihilators are switched.

In the presence of trigonal the eigenvalue problem has no analytic solution. In order to get a numerical solution, we used a matrix representation the Hamiltonian in a truncated basis. This method is expected to give good results for the low-energy spectrum, as the discarded high-energy states do not hybridize with those at low energy.

In the K_+-valley, using

$$\left\{\begin{bmatrix}\phi_0\\ 0\end{bmatrix},\ \begin{bmatrix}\phi_1\\ 0\end{bmatrix},\ \frac{1}{\sqrt{2}}\begin{bmatrix}\phi_n\\ \sigma\phi_{n-2}\end{bmatrix}\middle|(n \geq 2)\ \sigma =\ \pm\right\},$$

the matrix elements evaluate to

$$\langle 0|h|0\rangle = \frac{-U}{2} \ \langle 3,\sigma|h|0\rangle = \frac{\sigma i R}{\sqrt{2}}$$

$$\langle 1|h|1\rangle = \frac{-U}{2} + C_+ \ \langle 4,\sigma|h|1\rangle = \sigma i R$$

$$\begin{aligned}\langle n,\sigma|h|n,\sigma'\rangle &= \sigma\delta_{\sigma\sigma'} A\sqrt{n(n-1)} + D(1-\delta_{\sigma\sigma'})\\ &+\frac{1}{2}\Big(C_+ n + \sigma\sigma' C_-(n-1)\Big)\end{aligned}$$

$$\langle n+3,\sigma|h|n,\sigma'\rangle = \frac{\sigma i R\sqrt{n+1}}{2}.$$

All remaining matrix elements follow from the requirement of Hermitian adjointness.

Analogously, for the K_-- valley we used

$$\left\{\begin{bmatrix}0\\ \phi_0\end{bmatrix},\ \begin{bmatrix}0\\ \phi_1\end{bmatrix},\ \frac{1}{\sqrt{2}}\begin{bmatrix}\phi_{n-2}\\ \sigma\phi_n\end{bmatrix}\middle|(n\geq 2)\ \sigma = \ \pm\right\}$$

to obtain

$$\langle 0|h|0\rangle = \frac{U}{2} \ \langle 3,\sigma|h|0\rangle = \frac{-iR}{\sqrt{2}},$$

$$\langle 1|h|1\rangle = \frac{U}{2} + C_- \ \langle 4,\sigma|h|1\rangle = -iR,$$

$$\begin{aligned}\langle n,\sigma|h|n,\sigma'\rangle &= \sigma\delta_{\sigma\sigma'} A\sqrt{n(n-1)} + D(1-\delta_{\sigma\sigma'})\\ &+\frac{1}{2}(C_+(n-1) + \sigma\sigma' C_- n),\end{aligned}$$

and

$$\langle n+3,\sigma|h|n,\sigma'\rangle = \frac{-\sigma' i R\sqrt{n+1}}{2}.$$

For the calculation an upper cutoff for the Landau level index of $n_{max} = 300$ was set by observing the convergence behavior of the low-lying energy levels.

To illustrate the impact of γ_3, γ_4, and Δ' the band structure, calculated inverse compressibility as a function of charge carrier density and magnetic field and the evolution of Landau levels as a function of the magnetic field is shown in Fig. S1 and Fig. S2 when γ_3, γ_4, and $\Delta'$are not included (a), when only γ_3 is included (b) and when γ_3, γ_4, and Δ' are all included (c).

Calculation of the inverse compressibility

The inverse compressibility is defined by $\frac{\partial\mu}{\partial n}$. In contrast to the conductance G , it can be extracted from the Landau level spectrum only, which makes it a suitable quantity for theoretical considerations. It is related to the conductance: Divergences in the inverse compressibility indicate filled Landau levels where the conductance exhibits a plateau.

By fixing the temperature T , it is straightforward to calculate the charge carrier density n as a function of μ by populating the energy levels $\{\epsilon_i\}$ according to the Fermi function. Each level comes with a degeneracy of $g = \frac{ABe}{2\pi\hbar}$, leading to a charge carrier density of

$n(\mu) = 2\sum_i \frac{Be}{2\pi\hbar}\,\frac{1}{1+\exp\left(\frac{\epsilon_i-\mu}{k_B T}\right)}$ with another prefactor of 2 due to spin degeneracy.

$\mu(n)$ and the inverse compressibility were obtained by a numerical inversion of this function. To this end, we defined a reservoir M of 10^5 equispaced values of μ in a range that was roughly adjusted to the lowest and highest Landau level energies accessible the considered charge carrier densities. For these values of μ, the carrier densities were computed. The contribution from the lower half of the spectrum, (the hole Landau levels) had to be subtracted as an offset.

Fixing the carrier density to n^*, the corresponding chemical potential could then be determined as

$\mu(n^*) = \min(\mu \in M \mid n(\mu) > n^*)$. This so-defined inverse function may attain all values from the reservoir from the bottom to the top when n is increased. The numerical error of this procedure is controlled by the spacing within the reservoir. For the practical implementation the temperature entering in the Fermi distribution was chosen to be 0.1 K. This is higher than the usual cryogenic temperatures of the actual experimental realization. However, the resulting broadening may also mimic the finite width of Landau levels due to sample impurities.

Device characterization

We performed quantum Hall measurements in two different devices. Measurements conducted in one device are shown in the main text. This device and its fabrication is described in detail in Ref. [1] where the same device is denoted as Device A. Measurements conducted in a second device are discussed in Section C.

In our dually gated bilayer graphene samples the charge carrier density n as well as the electric displacement field D can be tuned individually via the use of graphite top and bottom gates. They are defined as

$$n = \varepsilon_0 \ \varepsilon_{hBN} \ (V_t/d_t + V_b/d_b)/e$$

and $D = \varepsilon_{hBN} \ (V_t/d_t \ - V_b/d_b \ )/2$

where V_t (V_b) is the gate voltage applied to the top (bottom) gate, d_t (d_b) the thickness of the upper (lower) hBN flake serving as a dielectric, e the charge of an electron, ε_{hBN} the dielectric constant of hBN and ε_0 the vacuum permittivity.

In order to determine ε_{hBN} and to thereby assign n and D, integer quantum Hall plateaus at finite magnetic fields were aligned with their corresponding slopes in the fan diagram. All observed LL crossings show excellent agreement with those observed previously (see Ref. [1] where data from the same device is shown). For example, at $B = 0.4$ T (Fig. 3b) one can see the known LL crossings of the $\nu = \pm 1$ and $\nu = 0$ quantum Hall states at $D \approx 15$ mV/nm as well as crossings at $\nu = \pm 2$ and $D \approx 0$ mV/nm.

Having aligned the sample by using the slopes of the quantum Hall states would in principle allow to determine the contact resistance by comparing the measured resistance with the expected quantum Hall resistance. However, due to the use of graphite contacts in a two-terminal device configuration the contact resistance increases linearly with increasing magnetic field (see for example Fig. S3, more details are given in Ref. [1]). Furthermore, there is a line of decreased conductance across zero displacement field (Fig. S3). This region is only bottom- but not top-gate dependent and stems from the region of the BLG that is located below the graphite contacts where the top graphite contacts screen the field of the top gate but not of the bottom gate. Thus, the contact resistance is additionally dependent on the top gate voltage (therefore also on n and D). To not confuse the reader with the line of decreased conductance we only show the derivative of the conductance in the main text. Another advantage of showing the derivative of the conductance is that it allows to track quantum Hall states at lower magnetic fields where the conductance is not fully quantized yet as traceable fluctuations near incompressible quantum Hall states can appear [33, 213, 214]. Exemplary, the conductance including a subtracted contact resistance is shown in Fig. S4 for D = 0 mV/nm and in Fig. S5 for D = 50 mV/nm. Here a contact resistance was subtracted that linearly increases with B. However, we did not account for the dependence on the charge carrier density. Therefore, the resistance values are only valid in a small density regime (negative densities close to the band edge). In Fig. S4, we included data taken at larger magnetic fields up to $B = 1.5$ T which we did not show in the main text. At $B > 0.6$ T and D = 0 V/nm the quantum Hall states are fully polarized due to additional valley imbalances implying a small residual displacement field. In agreement with previous studies [28, 33, 109, 111], the even integer quantum Hall states still show wider plateaus compared to the odd integer quantum Hall states.

Measurements conducted in a second Device

Electrical measurements conducted in a second device are shown in Fig. S6. This device was fabricated the same way as the device described in the main text [1] but it exhibits four graphite contacts instead of two. The corresponding measurement configuration is shown in Fig. S6a. The measurements show agreement with the theoretical simulations and the electrical measurements discussed in the main text.

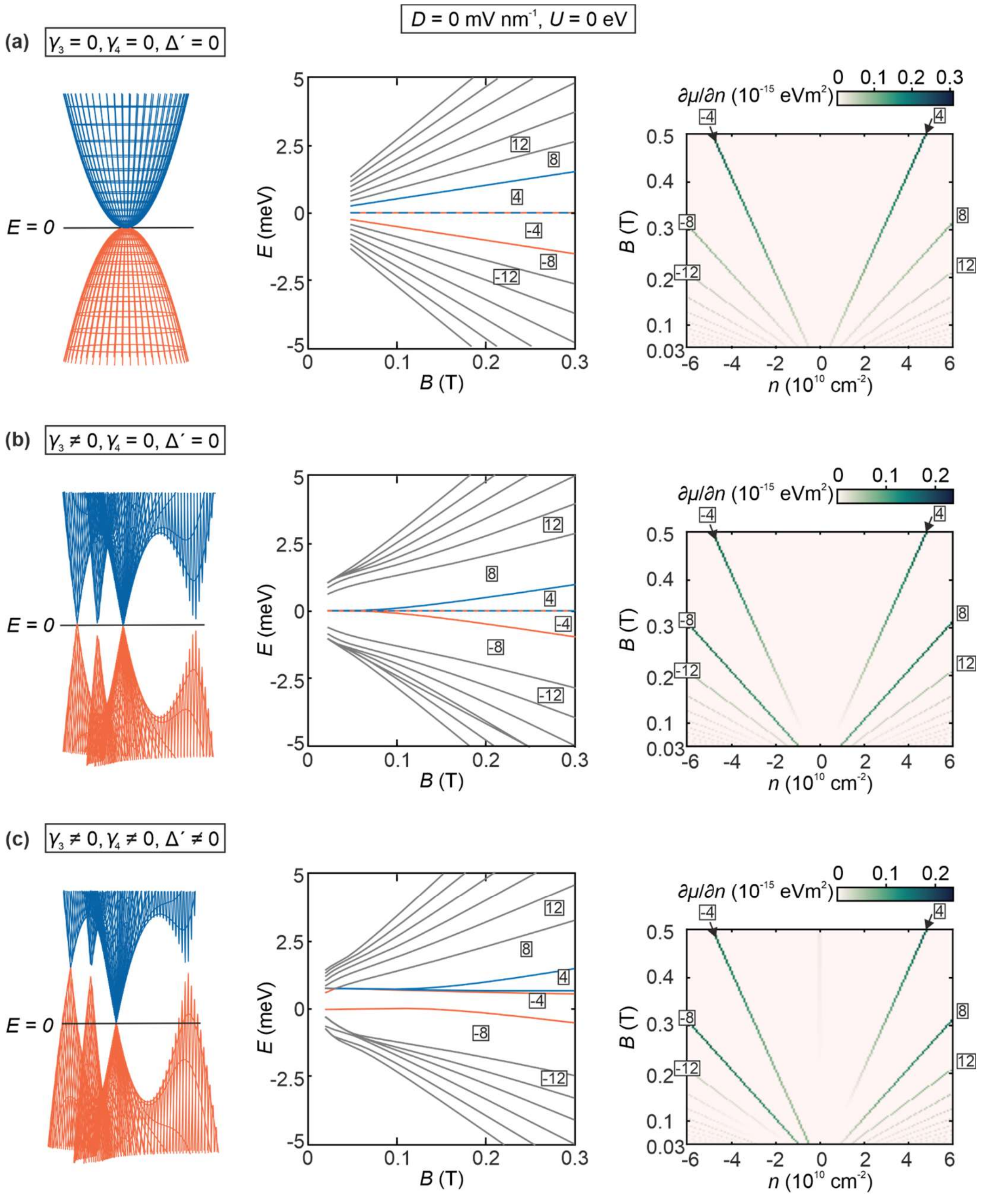

FIG S1. Impact of Coupling parameters γ_3, γ_4, and Δ' on the band structure shown in an energy range from -2 meV to + 2 meV (left panel), the evolution of Landau levels as a function of the magnetic field (middle panel), and the calculated inverse compressibility as a function of charge carrier density and magnetic field (right panel) at $U = 0$. (a) γ_3, γ_4, and $\Delta'$are not included into the calculations. The parabolic band structure results in four-fold degenerate Landau level and an eight-fold degenerate lowest Landau level. This results in the appearance of quantum Hall states with ν = -12, -8, -4, +4, +8, +12,

… at very low magnetic fields. (b) γ_3 is included into the calculations, γ_4, and $\Delta'$are not included. At low energies, the band structure consists of four mini Dirac cones resulting in a 16-fold degenerate lowest Landau level and in the appearance of quantum Hall states with ν = -12, -8, +8, +12, … at very low magnetic fields. Quantum Hall states with ν = -4, +4 appear at B > 0.1 T after the magnetic breakdown has occurred. (c) γ_3, γ_4, and $\Delta'$are all included into the calculations. This case is discussed in detail in the main text.

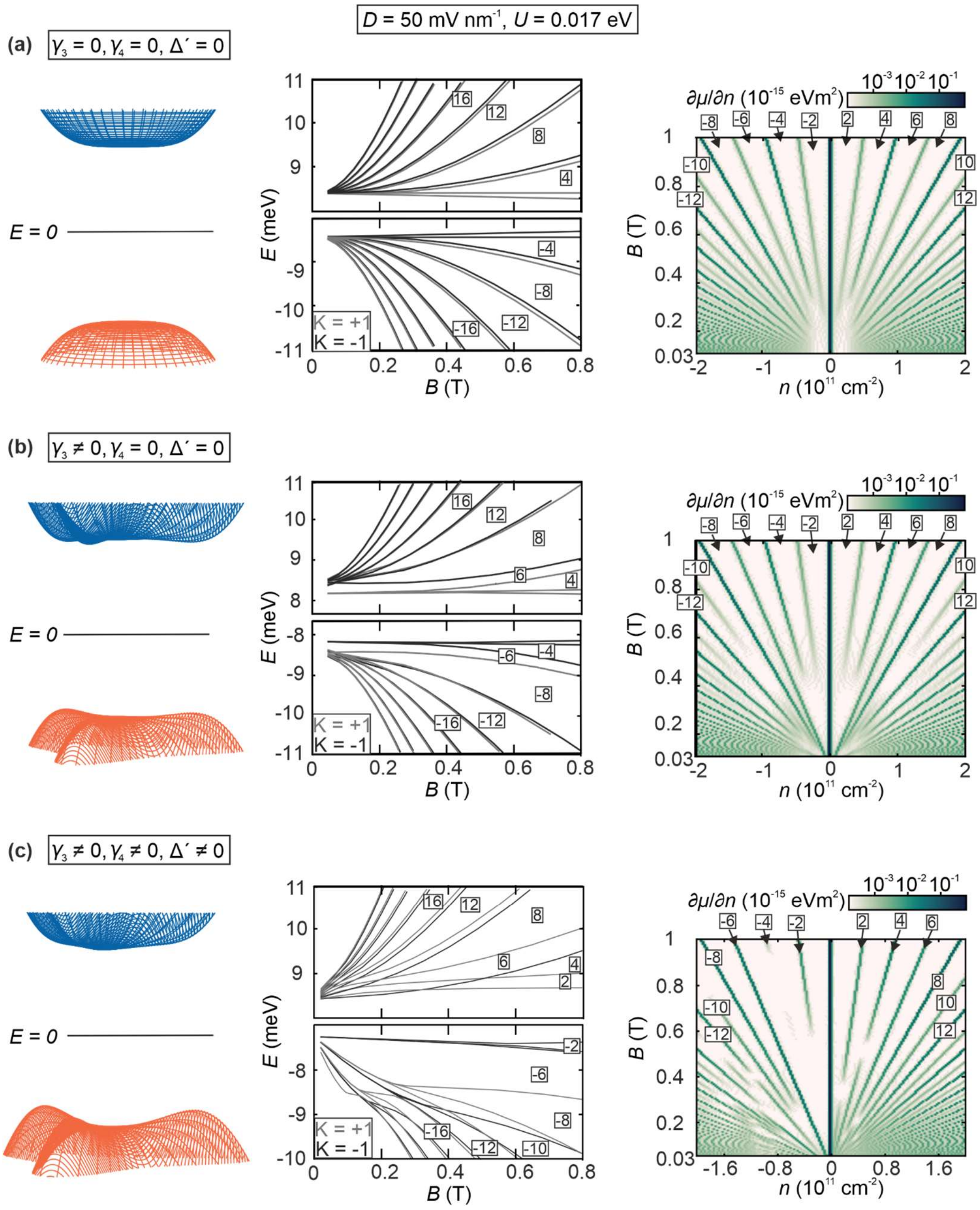

FIG S2. Impact of Coupling parameters γ_3, γ_4, and Δ' on the band structure shown in an energy range from -12 meV to + 12 meV (left panel), the evolution of Landau levels as a function of the magnetic field (middle panel), and the calculated inverse compressibility as a function of charge carrier density and magnetic field (right panel) at $U = 0.017$ eV. (a) γ_3, γ_4, and $\Delta'$are not included into the calculations. The almost parabolic band structure results in four-fold degenerate Landau level that split up into two-fold degenerate Landau level with increasing magnetic field. This results in the appearance of quantum Hall states with ν = -4, -2, 0, +2, +4, …. (b) γ_3 is included into the calculations, γ_4, and $\Delta'$are not included. At low energies, the band structure consists of three pockets resulting in a 12-fold degenerate lowest Landau level at low magnetic field and in the appearance of quantum Hall states with ν = -6 and +6 at very low magnetic fields. Quantum Hall states with ν = -4, -2, 0, +2, +4, … appear at B > 0.1 T after the magnetic breakdown has occurred. (c) γ_3 , γ_4 , and Δ' are all included into the calculations. This case is discussed in detail in the main text.

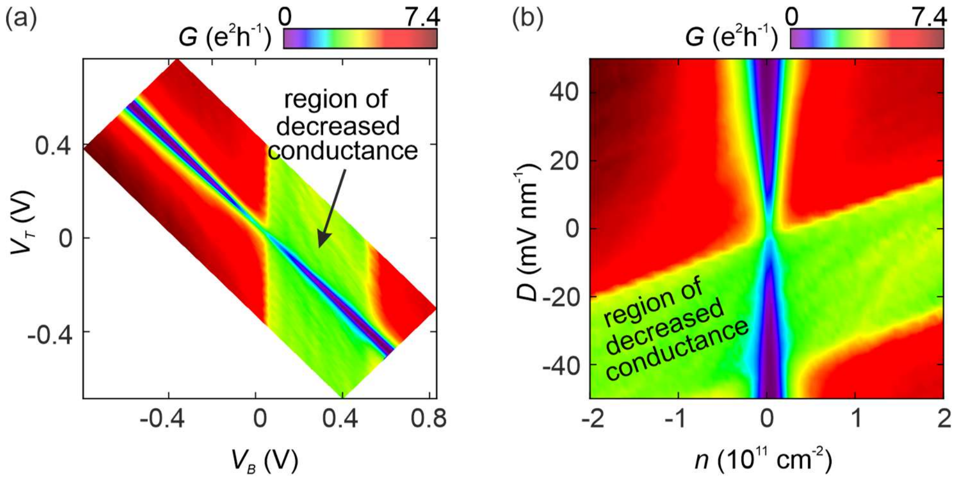

FIG S3. (a) Measured conductance as a function of bottom and top gate. There is a region of decreased conductance that only depends on V_B but not on V_T. There is no contact resistance subtracted. b) Measured conductance as a function of density and electric displacement field in the same regime that is shown in (a).

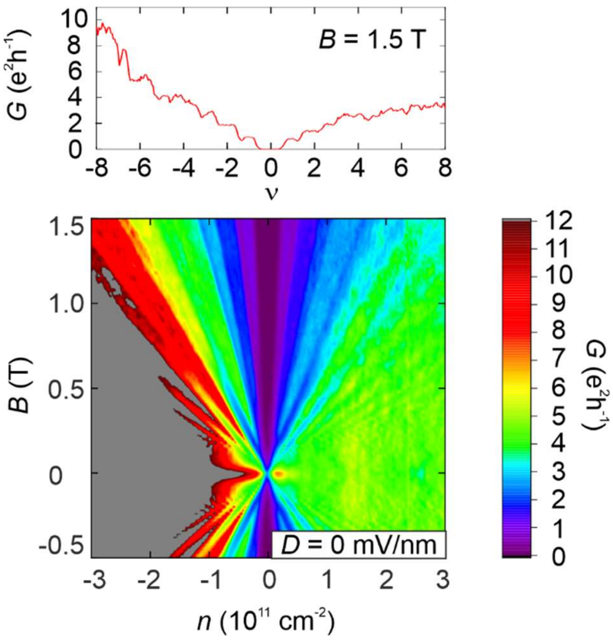

FIG. S4. Conductance G as a function of charge carrier density n and magnetic field B in the same n- and B- space at $D = 0$ mV nm^{-1} as shown in Fig. 1g. A contact resistance of $R_C = 3300\ \Omega$ - $4600\ \Omega\ \mathrm{T} \cdot B^{1}$ was subtracted from the measured resistance. Using this value of R_C the quantum Hall states with $\nu < 0$ show a quantized conductance where $G =$ IνI e^2h^1 while the conductance values for $\nu > 0$ are lower due to a higher contact resistance (see Fig. S3). A line-cut at B = 1.5 T is shown in the top. Here the density n is converted into filling factor ν.

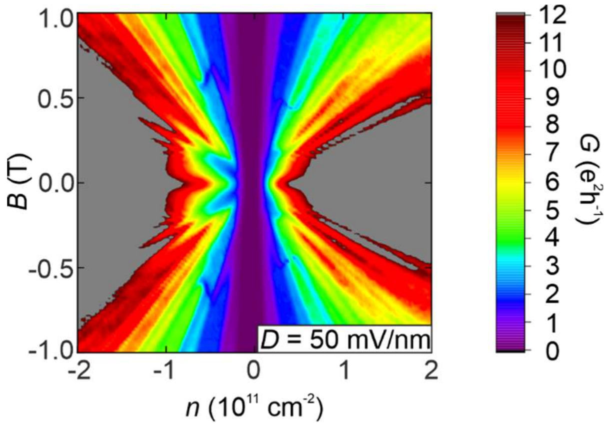

FIG. S5. Conductance G as a function of charge carrier density n and magnetic field B at $D = 50$mV/nm in the same n- and B- space as shown in Fig. 2e. A contact resistance of $R_C = 3000\ \Omega$ - $3500\ \Omega$ T / B was subtracted from the measured resistance. Using this value of R_C the quantum Hall states with $\nu < 0$ show a quantized conductance where $G =$ IνI e^2/h while the conductance values for $\nu > 0$ are lower due to a higher contact resistance (see Fig. S3).

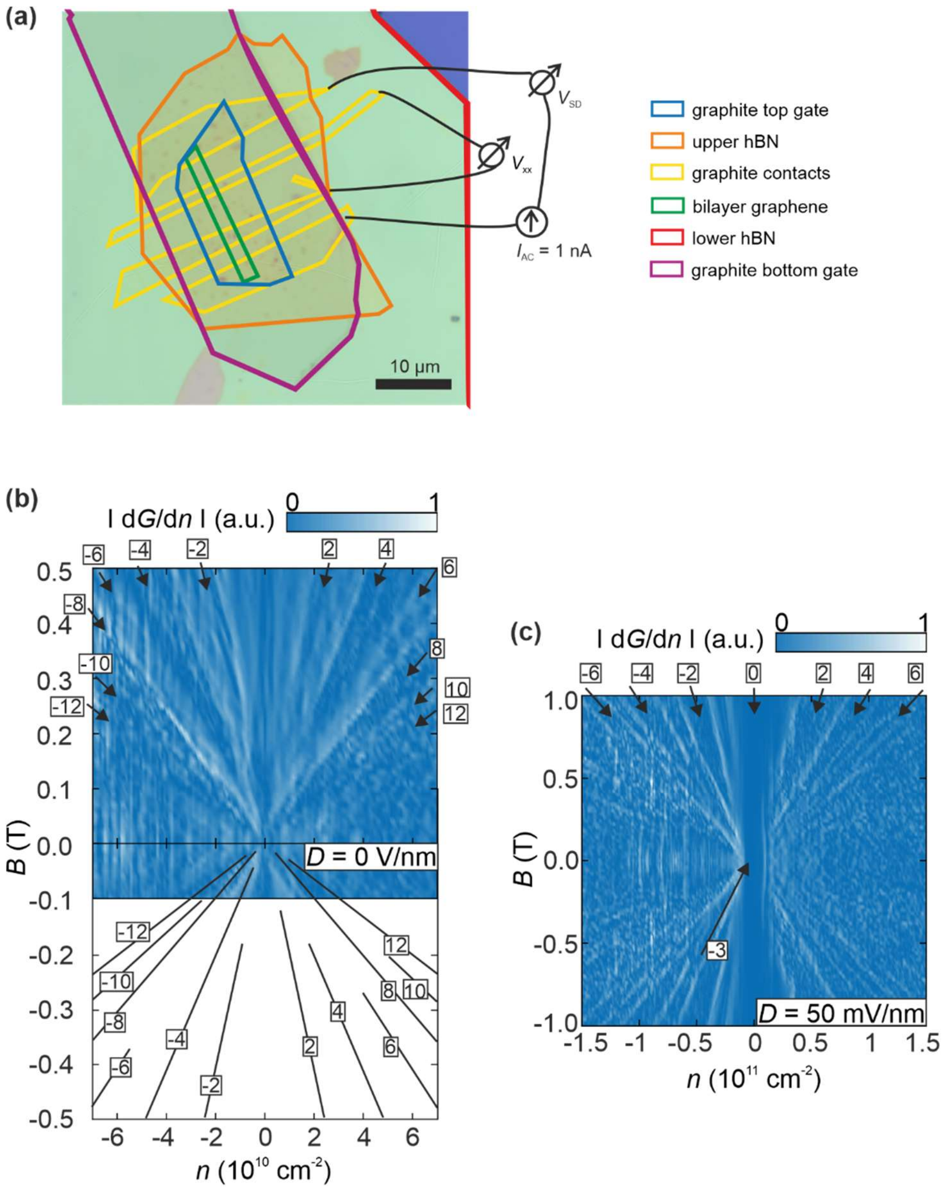

FIG. S6. Electrical Measurements conducted in a second device. (a) Optical microscope image of the second device and corresponding configuration of transport measurements. The different flakes are outlined. (b, c) Normalized derivative of the conductance as a function of n and B for $D = 0$ V/nm (b) and $D = 50$ mV/nm (c). Quantum Hall states with $\nu = \pm 8$ and $\nu = -4$ are the most prominent at $D = 0$ V/nm. At $D = 50$ mV/nm quantum Hall states with $\nu = -6$ and $\nu = -3$ are the most prominent for hole doping while the quantum Hall state with $\nu = +4$ is the most prominent for electron doping.

10 References

[1] A. M. Seiler *et al.,* “Quantum cascade of correlated phases in trigonally warped bilayer graphene,” *Nature*, vol. 608, no. 7922, pp. 298–302, 2022, doi: 10.1038/s41586-022-04937-1.

[2] T. Ihn, *Electronic Quantum Transport in Mesoscopic Semiconductor Structures*. New York, NY: Springer New York, 2004. [Online]. Available: https://ebookcentral.proquest.com/lib/kxp/detail.action?docID=6823498

[3] R. Gross and A. Marx, *Festkörperphysik*: De Gruyter, 2014.

[4] E. Pavarini, E. Koch, R. Scalettar, and R. Martin, Eds., *The physics of correlated insulators, metals, and superconductors: Lecture notes of the Autumn School on Correlated Electrons 2017 : at Forschungszentrum Jülich 25-29 September 2017*. Jülich: Forschungszentrum Jülich Zentralbibliothek Verlag, 2017. [Online]. Available: http://nbn-resolving.de/urn:nbn:de:hbz:5:2-139089

[5] G. Giuliani and G. Vignale, *Quantum Theory of the Electron Liquid*. Cambridge: Cambridge University Press, 2005. [Online]. Available: https://www.cambridge.org/core/books/quantum-theory-of-the-electron-liquid/EA75F41350A1C41D5E1BD202D539BB9E

[6] E. C. Stoner, “Collective electron ferromagnetism,” *Proceedings of the Royal Society of London. Series A. Mathematical and Physical Sciences*, vol. 165, no. 922, pp. 372–414, 1938, doi: 10.1098/rspa.1938.0066.

[7] W. Kohn and J. M. Luttinger, “Ground-State Energy of a Many-Fermion System,” *Phys. Rev.*, vol. 118, no. 1, pp. 41–45, 1960, doi: 10.1103/PhysRev.118.41.

[8] D. C. Tsui, H. L. Stormer, and A. C. Gossard, “Two-Dimensional Magnetotransport in the Extreme Quantum Limit,” *Phys. Rev. Lett.*, vol. 48, no. 22, pp. 1559–1562, 1982, doi: 10.1103/PhysRevLett.48.1559.

[9] B. Spivak, S. V. Kravchenko, S. A. Kivelson, and X. P. A. Gao, “Colloquium: Transport in strongly correlated two dimensional electron fluids,” *Rev. Mod. Phys.*, vol. 82, no. 2, pp. 1743–1766, 2010, doi: 10.1103/RevModPhys.82.1743.

[10] T. N. Zavaritskaya and É. I. Zavaritskaya, “Metal-insulator transition in inversion channels of cilicon MOS structures,” *JETP Lett.*, 1987, p. 609, 1987.

[11] M. D'Iorio, V. M. Pudalov, and S. G. Semenchinsky, “Magnetic field induced transitions between quantized hall and insulator states in a dilute 2D electron gas,” *Physics Letters A*, vol. 150, 8-9, pp. 422–426, 1990, doi: 10.1016/0375-9601(90)90244-I.

[12] D. C. Tsui, “Nobel Lecture: Interplay of disorder and interaction in two-dimensional electron gas in intense magnetic fields,” *Rev. Mod. Phys.*, vol. 71, no. 4, pp. 891–895, 1999, doi: 10.1103/RevModPhys.71.891.

[13] H. L. Stormer, “Nobel Lecture: The fractional quantum Hall effect,” *Rev. Mod. Phys.*, vol. 71, no. 4, pp. 875–889, 1999, doi: 10.1103/RevModPhys.71.875.

[14] K. I. Bolotin, F. Ghahari, M. D. Shulman, H. L. Stormer, and P. Kim, “Observation of the fractional quantum Hall effect in graphene,” *Nature*, vol. 462, no. 7270, pp. 196–199, 2009, doi: 10.1038/nature08582.

[15] K. S. Novoselov *et al.,* “Two-dimensional gas of massless Dirac fermions in graphene,” *Nature*, vol. 438, no. 7065, pp. 197–200, 2005, doi: 10.1038/nature04233.

[16] Y. Cao *et al.,* “Correlated insulator behaviour at half-filling in magic-angle graphene superlattices,” *Nature*, vol. 556, no. 7699, pp. 80–84, 2018, doi: 10.1038/nature26154.

[17] Y. Cao *et al.,* “Unconventional superconductivity in magic-angle graphene superlattices,” *Nature*, vol. 556, no. 7699, pp. 43–50, 2018, doi: 10.1038/nature26160.

[18] Y. Cao *et al.,* “Strange Metal in Magic-Angle Graphene with near Planckian Dissipation,” *Phys. Rev. Lett.*, vol. 124, no. 7, p. 76801, 2020, doi: 10.1103/PhysRevLett.124.076801.

[19] Sharpe Aaron L. *et al.,* “Emergent ferromagnetism near three-quarters filling in twisted bilayer graphene,” *Science*, vol. 365, no. 6453, pp. 605–608, 2019, doi: 10.1126/science.aaw3780.

[20] Serlin M. *et al.,* “Intrinsic quantized anomalous Hall effect in a moiré heterostructure,” *Science*, vol. 367, no. 6480, pp. 900–903, 2020, doi: 10.1126/science.aay5533.

[21] G. Chen *et al.,* “Signatures of tunable superconductivity in a trilayer graphene moiré superlattice,” *Nature*, vol. 572, no. 7768, pp. 215–219, 2019, doi: 10.1038/s41586-019-1393-y.

[22] A. Uri *et al.,* “Mapping the twist-angle disorder and Landau levels in magic-angle graphene,” *Nature*, vol. 581, no. 7806, pp. 47–52, 2020, doi: 10.1038/s41586-020-2255-3.

[23] C. N. Lau, M. W. Bockrath, K. F. Mak, and F. Zhang, “Reproducibility in the fabrication and physics of moiré materials,” *Nature*, vol. 602, no. 7895, pp. 41–50, 2022, doi: 10.1038/s41586-021-04173-z.

[24] H. Zhou, T. Xie, T. Taniguchi, K. Watanabe, and A. F. Young, “Superconductivity in rhombohedral trilayer graphene,” *Nature*, vol. 598, pp. 434–438, 2021, doi: 10.1038/s41586-021-03926-0.

[25] H. Zhou *et al.,* “Half and quarter metals in rhombohedral trilayer graphene,” *Nature*, vol. 598, pp. 429–433, 2021, doi: 10.1038/s41586-021-03938-w.

[26] E. McCann and M. Koshino, “The electronic properties of bilayer graphene,” *Reports on Progress in Physics*, vol. 76, no. 5, p. 56503, 2013, doi: 10.1088/0034-4885/76/5/056503.

[27] F. Zhang, B. Sahu, H. Min, and A. H. MacDonald, “Band structure of ABC-stacked graphene trilayers,” *Phys. Rev. B*, vol. 82, no. 3, p. 35409, 2010, doi: 10.1103/PhysRevB.82.035409.

[28] R. T. Weitz, M. T. Allen, B. E. Feldman, J. Martin, and A. Yacoby, “Broken-Symmetry States in Doubly Gated Suspended Bilayer Graphene,” *Science*, vol. 330, no. 6005, pp. 812–816, 2010, doi: 10.1126/science.1194988.

[29] B. E. Feldman, J. Martin, and A. Yacoby, “Broken-symmetry states and divergent resistance in suspended bilayer graphene,” *Nature Physics*, vol. 5, no. 12, pp. 889–893, 2009, doi: 10.1038/nphys1406.

[30] J. I. A. Li *et al.,* “Even-denominator fractional quantum Hall states in bilayer graphene,” *Science*, vol. 358, no. 6363, pp. 648–652, 2017, doi: 10.1126/science.aao2521.

[31] A. Kou *et al.,* “Electron-hole asymmetric integer and fractional quantum Hall effect in bilayer graphene,” *Science*, vol. 345, no. 6192, pp. 55–57, 2014, doi: 10.1126/science.1250270.

[32] P. Maher *et al.,* “Tunable fractional quantum Hall phases in bilayer graphene,” *Science*, vol. 345, no. 6192, pp. 61–64, 2014, doi: 10.1126/science.1252875.

[33] F. R. Geisenhof *et al.,* “Quantum anomalous Hall octet driven by orbital magnetism in bilayer graphene,” *Nature*, vol. 598, pp. 53–58, 2021, doi: 10.1038/s41586-021-03849-w.

[34] J. Velasco *et al.,* “Transport spectroscopy of symmetry-broken insulating states in bilayer graphene,” *Nature Nanotechnology*, vol. 7, no. 3, pp. 156–160, 2012, doi: 10.1038/nnano.2011.251.

[35] H. Zhou *et al.,* “Isospin magnetism and spin-polarized superconductivity in Bernal bilayer graphene,” *Science*, 2022, pp. 774–778, 2022. doi://10.1126/science.abm8386

[36] S. C. de La Barrera *et al.,* “Cascade of isospin phase transitions in Bernal-stacked bilayer graphene at zero magnetic field,” *Nature Physics*, vol. 18, no. 7, pp. 771–775, 2022.

[37] E. McCann and V. I. Fal’ko, “Landau-Level Degeneracy and Quantum Hall Effect in a Graphite Bilayer,” *Phys. Rev. Lett.*, vol. 96, no. 8, p. 86805, 2006, doi: 10.1103/PhysRevLett.96.086805.

[38] Novoselov K. S. *et al.,* “Electric Field Effect in Atomically Thin Carbon Films,” *Science*, vol. 306, no. 5696, pp. 666–669, 2004, doi: 10.1126/science.1102896.

[39] C. Lee, X. Wei, J. W. Kysar, and J. Hone, “Measurement of the Elastic Properties and Intrinsic Strength of Monolayer Graphene,” *Science*, vol. 321, no. 5887, pp. 385–388, 2008, doi: 10.1126/science.1157996.

[40] A. A. Balandin *et al.,* “Superior Thermal Conductivity of Single-Layer Graphene,” *Nano Letters*, vol. 8, no. 3, pp. 902–907, 2008, doi: 10.1021/nl0731872.

[41] K. I. Bolotin *et al.,* “Ultrahigh electron mobility in suspended graphene,” *Solid State Communications*, vol. 146, no. 9, pp. 351–355, 2008, doi: 10.1016/j.ssc.2008.02.024.

[42] A. K. Geim and K. S. Novoselov, “The rise of graphene,” *Nature Materials*, vol. 6, no. 3, pp. 183–191, 2007, doi: 10.1038/nmat1849.

[43] R. R. Nair *et al.,* “Fine Structure Constant Defines Visual Transparency of Graphene,” *Science*, vol. 320, no. 5881, p. 1308, 2008, doi: 10.1126/science.1156965.

[44] A. K. Geim and I. V. Grigorieva, “Van der Waals heterostructures,” *Nature*, vol. 499, no. 7459, pp. 419–425, 2013, doi: 10.1038/nature12385.

[45] K. S. Novoselov *et al.,* “Two-dimensional atomic crystals,” *Proceedings of the National Academy of Sciences*, vol. 102, no. 30, pp. 10451–10453, 2005, doi: 10.1073/pnas.0502848102.

[46] M. M. Benameur, B. Radisavljevic, J. S. Héron, S. Sahoo, H. Berger, and A. Kis, “Visibility of dichalcogenide nanolayers,” *Nanotechnology*, vol. 22, no. 12, p. 125706, 2011, doi: 10.1088/0957-4484/22/12/125706.

[47] Y. Li, B. Yang, S. Xu, B. Huang, and W. Duan, “Emergent Phenomena in Magnetic Two-Dimensional Materials and van der Waals Heterostructures,” *ACS Applied Electronic Materials*, vol. 4, no. 7, pp. 3278–3302, 2022, doi: 10.1021/acsaelm.2c00419.

[48] M. I. Katsnelson, “Graphene: carbon in two dimensions,” *Materials Today*, vol. 10, no. 1, pp. 20–27, 2007, doi: 10.1016/S1369-7021(06)71788-6.

[49] A. H. Castro Neto, F. Guinea, N. M. R. Peres, K. S. Novoselov, and A. K. Geim, “The electronic properties of graphene,” *Rev. Mod. Phys.*, vol. 81, no. 1, pp. 109–162, 2009, doi: 10.1103/RevModPhys.81.109.

[50] B. Partoens and F. M. Peeters, “From graphene to graphite: Electronic structure around the K point,” *Phys. Rev. B*, vol. 74, no. 7, p. 75404, 2006, doi: 10.1103/PhysRevB.74.075404.

[51] P. R. Wallace, “The Band Theory of Graphite,” *Phys. Rev.*, vol. 71, no. 9, pp. 622–634, 1947, doi: 10.1103/PhysRev.71.622.

[52] S. Das Sarma, S. Adam, E. H. Hwang, and E. Rossi, “Electronic transport in two-dimensional graphene,” *Rev. Mod. Phys.*, vol. 83, no. 2, pp. 407–470, 2011, doi: 10.1103/RevModPhys.83.407.

[53] G. W. Semenoff, “Condensed-Matter Simulation of a Three-Dimensional Anomaly,” *Phys. Rev. Lett.*, vol. 53, no. 26, pp. 2449–2452, 1984, doi: 10.1103/PhysRevLett.53.2449.

[54] M. Goerbig and G. Montambaux, “Dirac Fermions in Condensed Matter and Beyond,” in *Dirac Matter*, B. Duplantier, V. Rivasseau, and J.-N. Fuchs, Eds., Cham: Springer International Publishing, 2017, pp. 25–53.

[55] S. Sahu and G. C. Rout, “Band gap opening in graphene: a short theoretical study,” *International Nano Letters*, vol. 7, no. 2, pp. 81–89, 2017, doi: 10.1007/s40089-017-0203-5.

[56] D. D. L. Chung, “Review Graphite,” *Journal of Materials Science*, vol. 37, no. 8, pp. 1475–1489, 2002, doi: 10.1023/A:1014915307738.

[57] F. R. Geisenhof *et al.,* “Anisotropic Strain-Induced Soliton Movement Changes Stacking Order and Band Structure of Graphene Multilayers: Implications for Charge Transport,” *ACS Applied Nano Materials*, vol. 2, no. 9, pp. 6067–6075, 2019, doi: 10.1021/acsanm.9b01603.

[58] W. Bao *et al.,* “Stacking-dependent band gap and quantum transport in trilayer graphene,” *Nature Physics*, vol. 7, no. 12, pp. 948–952, 2011, doi: 10.1038/nphys2103.

[59] T. Latychevskaia *et al.,* “Stacking transition in rhombohedral graphite,” *Frontiers of Physics*, vol. 14, no. 1, p. 13608, 2018, doi: 10.1007/s11467-018-0867-y.

[60] M. Koshino, “Interlayer screening effect in graphene multilayers with ABA and ABC stacking,” *Phys. Rev. B*, vol. 81, no. 12, p. 125304, 2010, doi: 10.1103/PhysRevB.81.125304.

[61] M. Topsakal, E. Aktürk, and S. Ciraci, “First-principles study of two- and one-dimensional honeycomb structures of boron nitride,” *Phys. Rev. B*, vol. 79, no. 11, p. 115442, 2009, doi: 10.1103/PhysRevB.79.115442.

[62] R. S. PEASE, “Crystal Structure of Boron Nitride,” *Nature*, vol. 165, no. 4201, pp. 722–723, 1950, doi: 10.1038/165722b0.

[63] G. Constantinescu, A. Kuc, and T. Heine, “Stacking in Bulk and Bilayer Hexagonal Boron Nitride,” *Phys. Rev. Lett.*, vol. 111, no. 3, p. 36104, 2013, doi: 10.1103/PhysRevLett.111.036104.

[64] J. Wang, F. Ma, and M. Sun, “Graphene, hexagonal boron nitride, and their heterostructures: properties and applications,” *RSC Advances*, vol. 7, no. 27, pp. 16801–16822, 2017, doi: 10.1039/C7RA00260B.

[65] N. Ooi, A. Rairkar, L. Lindsley, and J. B. Adams, “Electronic structure and bonding in hexagonal boron nitride,” *Journal of Physics: Condensed Matter*, vol. 18, no. 1, p. 97, 2006, doi: 10.1088/0953-8984/18/1/007.

[66] K. Watanabe, T. Taniguchi, and H. Kanda, “Direct-bandgap properties and evidence for ultraviolet lasing of hexagonal boron

nitride single crystal," *Nature Mater*, vol. 3, no. 6, pp. 404–409, 2004, doi: 10.1038/nmat1134.

[67] A. Avsar *et al.,* "Optospintronics in Graphene via Proximity Coupling," *ACS Nano*, vol. 11, no. 11, pp. 11678–11686, 2017, doi: 10.1021/acsnano.7b06800.

[68] W. Han, R. K. Kawakami, M. Gmitra, and J. Fabian, "Graphene spintronics," *Nature Nanotechnology*, vol. 9, no. 10, pp. 794–807, 2014, doi: 10.1038/nnano.2014.214.

[69] J. O. Island *et al.,* "Spin-orbit-driven band inversion in bilayer graphene by the van der Waals proximity effect," *Nature*, vol. 571, no. 7763, pp. 85–89, 2019, doi: 10.1038/s41586-019-1304-2.

[70] D. Schmitt *et al.,* "Formation of moiré interlayer excitons in space and time," *Nature*, vol. 608, no. 7923, pp. 499–503, 2022, doi: 10.1038/s41586-022-04977-7.

[71] C. R. Dean *et al.,* "Hofstadter's butterfly and the fractal quantum Hall effect in moiré superlattices," *Nature*, vol. 497, no. 7451, pp. 598–602, 2013, doi: 10.1038/nature12186.

[72] C. Dean *et al.,* "Graphene based heterostructures," *Solid State Communications*, vol. 152, no. 15, pp. 1275–1282, 2012, doi: 10.1016/j.ssc.2012.04.021.

[73] C. R. Dean *et al.,* "Boron nitride substrates for high-quality graphene electronics," *Nature Nanotechnology*, vol. 5, no. 10, pp. 722–726, 2010, doi: 10.1038/nnano.2010.172.

[74] M. Yankowitz, Q. Ma, P. Jarillo-Herrero, and B. J. LeRoy, "van der Waals heterostructures combining graphene and hexagonal boron nitride," *Nature Reviews Physics*, vol. 1, no. 2, pp. 112–125, 2019, doi: 10.1038/s42254-018-0016-0.

[75] G. Giovannetti, P. A. Khomyakov, G. Brocks, P. J. Kelly, and J. van den Brink, "Substrate-induced band gap in graphene on hexagonal boron nitride: Ab initio density functional calculations," *Phys. Rev. B*, vol. 76, no. 7, p. 73103, 2007, doi: 10.1103/PhysRevB.76.073103.

[76] L. A. Ponomarenko *et al.,* "Tunable metal–insulator transition in double-layer graphene heterostructures," *Nature Physics*, vol. 7, no. 12, pp. 958–961, 2011, doi: 10.1038/nphys2114.

[77] Q. Cai *et al.,* "High thermal conductivity of high-quality monolayer boron nitride and its thermal expansion," *Science advances*, vol. 5, no. 6, eaav0129, 2019, doi: 10.1126/sciadv.aav0129.

[78] J. Xue *et al.,* “Scanning tunnelling microscopy and spectroscopy of ultra-flat graphene on hexagonal boron nitride,” *Nature Mater*, vol. 10, no. 4, pp. 282–285, 2011, doi: 10.1038/nmat2968.

[79] A. F. Young *et al.,* “Electronic compressibility of layer-polarized bilayer graphene,” *Phys. Rev. B*, vol. 85, no. 23, p. 235458, 2012, doi: 10.1103/PhysRevB.85.235458.

[80] G.-H. Lee *et al.,* “Electron tunneling through atomically flat and ultrathin hexagonal boron nitride,” *Appl. Phys. Lett.*, vol. 99, no. 24, p. 243114, 2011, doi: 10.1063/1.3662043.

[81] Y. Hattori, T. Taniguchi, K. Watanabe, and K. Nagashio, “Layer-by-Layer Dielectric Breakdown of Hexagonal Boron Nitride,” *ACS Nano*, vol. 9, no. 1, pp. 916–921, 2015, doi: 10.1021/nn506645q.

[82] F. Jovell and X. Cartoixà, “Electrical contact resistance in graphite–graphene contacts from ab initio methods,” *Journal of Physics: Condensed Matter*, vol. 30, no. 32, p. 325302, 2018, doi: 10.1088/1361-648X/aacd83.

[83] T. Chari, R. Ribeiro-Palau, C. R. Dean, and K. Shepard, “Resistivity of Rotated Graphite–Graphene Contacts,” *Nano Letters*, vol. 16, no. 7, pp. 4477–4482, 2016, doi: 10.1021/acs.nanolett.6b01657.

[84] Y. Sata, R. Moriya, S. Masubuchi, K. Watanabe, T. Taniguchi, and T. Machida, “N- and p-type carrier injections into WSe2 with van der Waals contacts of two-dimensional materials,” *Japanese Journal of Applied Physics*, vol. 56, 4S, 04CK09, 2017, doi: 10.7567/JJAP.56.04CK09.

[85] J. Jung and A. H. MacDonald, “Accurate tight-binding models for the π bands of bilayer graphene,” *Phys. Rev. B*, vol. 89, no. 3, p. 35405, 2014, doi: 10.1103/PhysRevB.89.035405.

[86] L. M. Malard *et al.,* “Probing the electronic structure of bilayer graphene by Raman scattering,” *Phys. Rev. B*, vol. 76, no. 20, p. 201401, 2007, doi: 10.1103/PhysRevB.76.201401.

[87] L. M. Zhang, Z. Q. Li, D. N. Basov, M. M. Fogler, Z. Hao, and M. C. Martin, “Determination of the electronic structure of bilayer graphene from infrared spectroscopy,” *Phys. Rev. B*, vol. 78, no. 23, p. 235408, 2008, doi: 10.1103/PhysRevB.78.235408.

[88] A. B. Kuzmenko, I. Crassee, D. van der Marel, P. Blake, and K. S. Novoselov, “Determination of the gate-tunable band gap and tight-binding parameters in bilayer graphene using infrared spectroscopy,”

Phys. Rev. B, vol. 80, no. 16, p. 165406, 2009, doi: 10.1103/PhysRevB.80.165406.

[89] N. M. R. Peres, F. Guinea, and A. H. Castro Neto, “Electronic properties of disordered two-dimensional carbon,” *Phys. Rev. B*, vol. 73, no. 12, p. 125411, 2006, doi: 10.1103/PhysRevB.73.125411.

[90] M. Koshino and E. McCann, “Trigonal warping and Berry's phase N π in ABC-stacked multilayer graphene,” *Phys. Rev. B*, vol. 80, no. 16, p. 165409, 2009, doi: 10.1103/PhysRevB.80.165409.

[91] S. B. Dugdale, “Life on the edge: a beginner’s guide to the Fermi surface,” *Phys. Scr.*, vol. 91, no. 5, p. 53009, 2016, doi: 10.1088/0031-8949/91/5/053009.

[92] J. B. Oostinga, H. B. Heersche, X. Liu, A. F. Morpurgo, and L. M. K. Vandersypen, “Gate-induced insulating state in bilayer graphene devices,” *Nature Mater*, vol. 7, no. 2, pp. 151–157, 2008, doi: 10.1038/nmat2082.

[93] T. Ohta, A. Bostwick, T. Seyller, K. Horn, and E. Rotenberg, “Controlling the Electronic Structure of Bilayer Graphene,” *Science*, vol. 313, no. 5789, pp. 951–954, 2006, doi: 10.1126/science.1130681.

[94] Y. Zhang *et al.,* “Direct observation of a widely tunable bandgap in bilayer graphene,” *Nature*, vol. 459, no. 7248, pp. 820–823, 2009, doi: 10.1038/nature08105.

[95] M. Mucha-Kruczyński, E. McCann, and V. I. Fal'ko, “Electron–hole asymmetry and energy gaps in bilayer graphene,” *Semiconductor Science and Technology*, vol. 25, no. 3, p. 33001, 2010, doi: 10.1088/0268-1242/25/3/033001.

[96] I. M. Lifshitz, *Anomalies of electron characteristics of a metal in the high pressure region*, 1960. [Online]. Available: http://www.jetp.ras.ru/cgi-bin/dn/e_011_05_1130.pdf

[97] E. McCann, “Asymmetry gap in the electronic band structure of bilayer graphene,” *Phys. Rev. B*, vol. 74, no. 16, p. 161403, 2006, doi: 10.1103/PhysRevB.74.161403.

[98] Y. Zhang *et al.,* “Enhanced superconductivity in spin–orbit proximitized bilayer graphene,” *Nature*, vol. 613, no. 7943, pp. 268–273, 2023, doi: 10.1038/s41586-022-05446-x.

[99] D. Tong, “Lectures on the Quantum Hall Effect,” Jun. 2016. [Online]. Available: https://arxiv.org/pdf/1606.06687

[100] K. von Klitzing, “The quantized Hall effect,” *Rev. Mod. Phys.*, vol. 58, no. 3, pp. 519–531, 1986, doi: 10.1103/RevModPhys.58.519.

[101] K. v. Klitzing, G. Dorda, and M. Pepper, “New Method for High-Accuracy Determination of the Fine-Structure Constant Based on Quantized Hall Resistance,” *Phys. Rev. Lett.*, vol. 45, no. 6, pp. 494–497, 1980, doi: 10.1103/PhysRevLett.45.494.

[102] M. E. Suddards, A. Baumgartner, M. Henini, and C. J. Mellor, “Scanning capacitance imaging of compressible and incompressible quantum Hall effect edge strips,” *New J. Phys.*, vol. 14, no. 8, p. 83015, 2012, doi: 10.1088/1367-2630/14/8/083015.

[103] D. A. Abanin and L. S. Levitov, “Conformal invariance and shape-dependent conductance of graphene samples,” *Phys. Rev. B*, vol. 78, no. 3, p. 35416, 2008, doi: 10.1103/PhysRevB.78.035416.

[104] K. S. Novoselov *et al.,* “Unconventional quantum Hall effect and Berry’s phase of 2π in bilayer graphene,” *Nature Physics*, vol. 2, no. 3, pp. 177–180, 2006, doi: 10.1038/nphys245.

[105] A. Varlet *et al.,* “Anomalous Sequence of Quantum Hall Liquids Revealing a Tunable Lifshitz Transition in Bilayer Graphene,” *Phys. Rev. Lett.*, vol. 113, no. 11, p. 116602, 2014, doi: 10.1103/PhysRevLett.113.116602.

[106] A. Varlet *et al.,* “Tunable Fermi surface topology and Lifshitz transition in bilayer graphene,” *Synthetic Metals*, vol. 210, pp. 19–31, 2015, doi: 10.1016/j.synthmet.2015.07.006.

[107] V. N. Kotov, B. Uchoa, V. M. Pereira, F. Guinea, and A. H. Castro Neto, “Electron-Electron Interactions in Graphene: Current Status and Perspectives,” *Rev. Mod. Phys.*, vol. 84, no. 3, pp. 1067–1125, 2012, doi: 10.1103/RevModPhys.84.1067.

[108] K. Nomura and A. H. MacDonald, “Quantum Hall Ferromagnetism in Graphene,” *Phys. Rev. Lett.*, vol. 96, no. 25, p. 256602, 2006, doi: 10.1103/PhysRevLett.96.256602.

[109] J. Li, Y. Tupikov, K. Watanabe, T. Taniguchi, and J. Zhu, “Effective Landau Level Diagram of Bilayer Graphene,” *Phys. Rev. Lett.*, vol. 120, no. 4, p. 47701, 2018, doi: 10.1103/PhysRevLett.120.047701.

[110] Y. Zhao, P. Cadden-Zimansky, Z. Jiang, and P. Kim, “Symmetry Breaking in the Zero-Energy Landau Level in Bilayer Graphene,”

Phys. Rev. Lett., vol. 104, no. 6, p. 66801, 2010, doi: 10.1103/PhysRevLett.104.066801.

[111] K. Lee *et al.,* “Chemical potential and quantum Hall ferromagnetism in bilayer graphene,” *Science*, vol. 345, no. 6192, pp. 58–61, 2014, doi: 10.1126/science.1251003.

[112] M. S. Colclough *et al.,* “Radio-frequency SQUID operation using a ceramic high-temperature superconductor,” *Nature*, vol. 328, no. 6125, pp. 47–48, 1987, doi: 10.1038/328047a0.

[113] P. W. Phillips, N. E. Hussey, and P. Abbamonte, “Stranger than metals,” *Science (New York, N.Y.)*, vol. 377, no. 6602, eabh4273, 2022, doi: 10.1126/science.abh4273.

[114] A. Pustogow *et al.,* “Rise and fall of Landau's quasiparticles while approaching the Mott transition,” *Nat Commun*, vol. 12, no. 1, p. 1571, 2021, doi: 10.1038/s41467-021-21741-z.

[115] A. C. Jacko, J. O. Fjærestad, and B. J. Powell, “A unified explanation of the Kadowaki–Woods ratio in strongly correlated metals,” (in En;en), *Nat. Phys.*, vol. 5, no. 6, pp. 422–425, 2009, doi: 10.1038/nphys1249.

[116] G. Mirarchi, G. Seibold, C. Di Castro, M. Grilli, and S. Caprara, “The Strange-Metal Behavior of Cuprates,” *Condensed Matter*, vol. 7, no. 1, p. 29, 2022, doi: 10.3390/condmat7010029.

[117] A. Jaoui *et al.,* “Quantum critical behaviour in magic-angle twisted bilayer graphene,” (in En;en), *Nat. Phys.*, vol. 18, no. 6, pp. 633–638, 2022, doi: 10.1038/s41567-022-01556-5.

[118] M. Gurvitch and A. T. Fiory, “Resistivity of La1.825Sr0.175CuO4 and YBa2Cu3O7 to 1100 K: Absence of saturation and its implications,” *Phys. Rev. Lett.*, vol. 59, no. 12, pp. 1337–1340, 1987, doi: 10.1103/PhysRevLett.59.1337.

[119] N. F. MOTT, “The Basis of the Electron Theory of Metals, with Special Reference to the Transition Metals,” *Proc. Phys. Soc. A*, vol. 62, no. 7, pp. 416–422, 1949, doi: 10.1088/0370-1298/62/7/303.

[120] M. Greiner, O. Mandel, T. Esslinger, T. W. Hänsch, and I. Bloch, “Quantum phase transition from a superfluid to a Mott insulator in a gas of ultracold atoms,” *Nature*, vol. 415, no. 6867, pp. 39–44, 2002, doi: 10.1038/415039a.

[121] N. F. MOTT, “Metal-Insulator Transition,” *Rev. Mod. Phys.*, vol. 40, no. 4, pp. 677–683, 1968, doi: 10.1103/RevModPhys.40.677.

[122] S. B. Roy, *Mott Insulators*: IOP Publishing, 2019.

[123] J. González, A. H. Vozmediano, G. Sierra, and M. A. Martín-Delgado, *Quantum Electron Liquids and High-TcSuperconductivity*. Berlin, Heidelberg: Springer Berlin Heidelberg; Springer e-books, 1995. [Online]. Available: https://ebookcentral.proquest.com/lib/kxp/detail.action?docID=6485920

[124] G. Grüner, "The dynamics of charge-density waves," *Rev. Mod. Phys.*, vol. 60, no. 4, pp. 1129–1181, 1988, doi: 10.1103/RevModPhys.60.1129.

[125] K. Rossnagel, "On the origin of charge-density waves in select layered transition-metal dichalcogenides," *Journal of physics. Condensed matter : an Institute of Physics journal*, vol. 23, no. 21, p. 213001, 2011, doi: 10.1088/0953-8984/23/21/213001.

[126] W. L. McMillan, "Landau theory of charge-density waves in transition-metal dichalcogenides," *Phys. Rev. B*, vol. 12, no. 4, pp. 1187–1196, 1975, doi: 10.1103/PhysRevB.12.1187.

[127] Z. Xu *et al.,* "Topical review: recent progress of charge density waves in 2D transition metal dichalcogenide-based heterojunctions and their applications," *Nanotechnology*, vol. 32, no. 49, p. 492001, 2021, doi: 10.1088/1361-6528/ac21ed.

[128] M. Shayegan, "Wigner crystals in flat band 2D electron systems," (in En;en), *Nat Rev Phys*, vol. 4, no. 4, pp. 212–213, 2022, doi: 10.1038/s42254-022-00444-4.

[129] V. J. Goldman, M. Santos, M. Shayegan, and J. E. Cunningham, "Evidence for two-dimentional quantum Wigner crystal," *Phys. Rev. Lett.*, vol. 65, no. 17, pp. 2189–2192, 1990, doi: 10.1103/PhysRevLett.65.2189.

[130] H. Li *et al.,* "Imaging two-dimensional generalized Wigner crystals," *Nature*, vol. 597, no. 7878, pp. 650–654, 2021, doi: 10.1038/s41586-021-03874-9.

[131] V. T. Dolgopolov, "Quantum melting of a two-dimensional Wigner crystal," *Phys.-Usp.*, vol. 60, no. 7, pp. 731–742, 2017, doi: 10.3367/UFNe.2017.01.038051.

[132] E. Abrahams, S. V. Kravchenko, and M. P. Sarachik, "Metallic behavior and related phenomena in two dimensions," *Rev. Mod. Phys.*, vol. 73, no. 2, pp. 251–266, 2001, doi: 10.1103/RevModPhys.73.251.

[133] R. T. Clay, R. P. Hardikar, and S. Mazumdar, “Temperature-driven transition from the Wigner crystal to the bond-charge-density wave in the quasi-one-dimensional quarter-filled band,” *Phys. Rev. B*, vol. 76, no. 20, p. 205118, 2007, doi: 10.1103/PhysRevB.76.205118.

[134] Private Communication with Fan Zhang (University of Texas at Dallas).

[135] B.-B. Chen *et al.,* “Realization of topological Mott insulator in a twisted bilayer graphene lattice model,” *Nature Communications*, vol. 12, no. 1, p. 5480, 2021, doi: 10.1038/s41467-021-25438-1.

[136] S. Raghu, X.-L. Qi, C. Honerkamp, and S.-C. Zhang, “Topological Mott Insulators,” *Phys. Rev. Lett.*, vol. 100, no. 15, p. 156401, 2008, doi: 10.1103/PhysRevLett.100.156401.

[137] Z. Tešanović, F. Axel, and B. I. Halperin, “"Hall crystal" versus Wigner crystal,” *Phys. Rev. B*, vol. 39, no. 12, pp. 8525–8551, 1989, doi: 10.1103/PhysRevB.39.8525.

[138] H. Polshyn *et al.,* “Topological charge density waves at half-integer filling of a moiré superlattice,” (in En;en), *Nat. Phys.*, vol. 18, no. 1, pp. 42–47, 2022, doi: 10.1038/s41567-021-01418-6.

[139] C.-X. Liu, S.-C. Zhang, and X.-L. Qi, “The Quantum Anomalous Hall Effect: Theory and Experiment,” *Annu. Rev. Condens. Matter Phys.*, vol. 7, no. 1, pp. 301–321, 2016, doi: 10.1146/annurev-conmatphys-031115-011417.

[140] K. S. Novoselov *et al.,* “Electric field effect in atomically thin carbon films,” *Science (New York, N.Y.)*, vol. 306, no. 5696, pp. 666–669, 2004, doi: 10.1126/science.1102896.

[141] G. Fiori and G. Iannaccone, “On the Possibility of Tunable-Gap Bilayer Graphene FET,” *IEEE Electron Device Letters*, vol. 30, no. 3, pp. 261–264, 2009, doi: 10.1109/LED.2008.2010629.

[142] A. S. Mayorov *et al.,* “Interaction-driven spectrum reconstruction in bilayer graphene,” *Science (New York, N.Y.)*, vol. 333, no. 6044, pp. 860–863, 2011, doi: 10.1126/science.1208683.

[143] M. S. A. Bhuyan, M. N. Uddin, M. M. Islam, F. A. Bipasha, and S. S. Hossain, “Synthesis of graphene,” (in En;en), *Int Nano Lett*, vol. 6, no. 2, pp. 65–83, 2016, doi: 10.1007/s40089-015-0176-1.

[144] Y. Huang *et al.,* “Reliable Exfoliation of Large-Area High-Quality Flakes of Graphene and Other Two-Dimensional Materials,” *ACS*

Nano, vol. 9, no. 11, pp. 10612–10620, 2015, doi: 10.1021/acsnano.5b04258.

[145] T. Taniguchi and K. Watanabe, “Synthesis of high-purity boron nitride single crystals under high pressure by using Ba–BN solvent,” *Journal of Crystal Growth*, vol. 303, no. 2, pp. 525–529, 2007, doi: 10.1016/j.jcrysgro.2006.12.061.

[146] F. Winterer *et al.,* “Spontaneous Gully-Polarized Quantum Hall States in ABA Trilayer Graphene,” *Nano Letters*, vol. 22, no. 8, pp. 3317–3322, 2022, doi: 10.1021/acs.nanolett.2c00435.

[147] H. Li *et al.,* “Rapid and reliable thickness identification of two-dimensional nanosheets using optical microscopy,” *ACS Nano*, vol. 7, no. 11, pp. 10344–10353, 2013, doi: 10.1021/nn4047474.

[148] D. Golla, K. Chattrakun, K. Watanabe, T. Taniguchi, B. J. LeRoy, and A. Sandhu, “Optical thickness determination of hexagonal boron nitride flakes,” *Appl. Phys. Lett.*, vol. 102, no. 16, p. 161906, 2013, doi: 10.1063/1.4803041.

[149] R. V. Gorbachev *et al.,* “Hunting for monolayer boron nitride: optical and Raman signatures,” *Small*, vol. 7, no. 4, pp. 465–468, 2011, doi: 10.1002/smll.201001628.

[150] A. C. Ferrari and D. M. Basko, “Raman spectroscopy as a versatile tool for studying the properties of graphene,” *Nature Nanotech*, vol. 8, no. 4, pp. 235–246, 2013, doi: 10.1038/nnano.2013.46.

[151] D. Graf *et al.,* “Spatially resolved Raman spectroscopy of single- and few-layer graphene,” *Nano Letters*, vol. 7, no. 2, pp. 238–242, 2007, doi: 10.1021/nl061702a.

[152] A. C. Ferrari *et al.,* “Raman Spectrum of Graphene and Graphene Layers,” *Phys. Rev. Lett.*, vol. 97, no. 18, p. 187401, 2006, doi: 10.1103/PhysRevLett.97.187401.

[153] R. A. Oliver, “Advances in AFM for the electrical characterization of semiconductors,” *Reports on Progress in Physics*, vol. 71, no. 7, p. 76501, 2008, doi: 10.1088/0034-4885/71/7/076501.

[154] C. J. Shearer, A. D. Slattery, A. J. Stapleton, J. G. Shapter, and C. T. Gibson, “Accurate thickness measurement of graphene,” *Nanotechnology*, vol. 27, no. 12, p. 125704, 2016, doi: 10.1088/0957-4484/27/12/125704.

[155] D. G. Purdie, N. M. Pugno, T. Taniguchi, K. Watanabe, A. C. Ferrari, and A. Lombardo, “Cleaning interfaces in layered materials

heterostructures," *Nature Communications*, vol. 9, no. 1, p. 5387, 2018, doi: 10.1038/s41467-018-07558-3.

[156] L. Wang *et al.,* "One-dimensional electrical contact to a two-dimensional material," *Science (New York, N.Y.)*, vol. 342, no. 6158, pp. 614–617, 2013, doi: 10.1126/science.1244358.

[157] A. M. Seiler, "Towards Electric Field Control of Fractional Quantum Hall States in Encapsulated Bilayer Graphene," Master's thesis, Ludwig-Maximilians-Universität München, 2019.

[158] P. J. Zomer, M. H. D. Guimarães, J. C. Brant, N. Tombros, and B. J. van Wees, "Fast pick up technique for high quality heterostructures of bilayer graphene and hexagonal boron nitride," *Appl. Phys. Lett.*, vol. 105, no. 1, p. 13101, 2014, doi: 10.1063/1.4886096.

[159] C. F. Fan, T. Çagin, W. Shi, and K. A. Smith, "Local chain dynamics of a model polycarbonate near glass transition temperature: A molecular dynamics simulation," *Macromol. Theory Simul.*, vol. 6, no. 1, pp. 83–102, 1997, doi: 10.1002/mats.1997.040060107.

[160] N. Almtireen, J. J. Brandner, and J. G. Korvink, "Pulse Tube Cryocooler: Phasor Analysis and One-Dimensional Numerical Simulation," (in En;en), *J Low Temp Phys*, vol. 199, 5-6, pp. 1179–1197, 2020, doi: 10.1007/s10909-020-02378-6.

[161] Cryomech, "Cryogenic Refrigerator - Installation and operation manual," Jul. 2018.

[162] F. Pobell, *Matter and Methods at Low Temperatures,* 3rd ed. Berlin, Heidelberg: Springer-Verlag Berlin Heidelberg, 2007. [Online]. Available: http://nbn-resolving.org/urn:nbn:de:bsz:31-epflicht-1579240

[163] BlueFors Cryogenics, "BF-LD-Series Cryogen - Free Dilution Refrigerator System - User manual," Jan. 2016.

[164] F. Freitag, J. Trbovic, M. Weiss, and C. Schönenberger, "Spontaneously Gapped Ground State in Suspended Bilayer Graphene," *Phys. Rev. Lett.*, vol. 108, no. 7, p. 76602, 2012, doi: 10.1103/PhysRevLett.108.076602.

[165] E. Icking *et al.,* "Transport Spectroscopy of Ultraclean Tunable Band Gaps in Bilayer Graphene," *Adv Elect Materials*, vol. 8, no. 11, p. 2200510, 2022, doi: 10.1002/aelm.202200510.

[166] H. Zhou, *Ferromagnetism and Superconductivity in Rhombohedral Trilayer Graphene*: University of California, Santa Barbara, 2021.

[167] P. P. Shinde and V. Kumar, “Direct band gap opening in graphene by BN doping: Ab initio calculations,” *Phys. Rev. B*, vol. 84, no. 12, p. 125401, 2011, doi: 10.1103/PhysRevB.84.125401.

[168] X. Wang *et al.,* “N-doping of graphene through electrothermal reactions with ammonia,” *Science (New York, N.Y.)*, vol. 324, no. 5928, pp. 768–771, 2009, doi: 10.1126/science.1170335.

[169] P. Rani and V. K. Jindal, “Designing band gap of graphene by B and N dopant atoms,” *RSC Adv*, vol. 3, no. 3, pp. 802–812, 2013, doi: 10.1039/C2RA22664B.

[170] F. Guinea, M. I. Katsnelson, and A. K. Geim, “Energy gaps and a zero-field quantum Hall effect in graphene by strain engineering,” (in En;en), *Nature Physics*, vol. 6, no. 1, pp. 30–33, 2010, doi: 10.1038/nphys1420.

[171] Z. Peng, X. Chen, Y. Fan, D. J. Srolovitz, and D. Lei, “Strain engineering of 2D semiconductors and graphene: from strain fields to band-structure tuning and photonic applications,” *Light Sci Appl*, vol. 9, no. 1, p. 190, 2020, doi: 10.1038/s41377-020-00421-5.

[172] Z. H. Ni, T. Yu, Y. H. Lu, Y. Y. Wang, Y. P. Feng, and Z. X. Shen, “Uniaxial strain on graphene: Raman spectroscopy study and band-gap opening,” *ACS Nano*, vol. 2, no. 11, pp. 2301–2305, 2008, doi: 10.1021/nn800459e.

[173] G. Gui, J. Li, and J. Zhong, “Band structure engineering of graphene by strain: First-principles calculations,” *Phys. Rev. B*, vol. 78, no. 7, p. 75435, 2008, doi: 10.1103/PhysRevB.78.075435.

[174] E. McCann, D. S. Abergel, and V. I. Fal'ko, “The low energy electronic band structure of bilayer graphene,” *The European Physical Journal Special Topics*, vol. 148, no. 1, pp. 91–103, 2007, doi: 10.1140/epjst/e2007-00229-1.

[175] F. R. Geisenhof, F. Winterer, A. M. Seiler, J. Lenz, F. Zhang, and R. T. Weitz, “Impact of Electric Field Disorder on Broken-Symmetry States in Ultraclean Bilayer Graphene,” *Nano Letters*, vol. 22, no. 18, pp. 7378–7385, 2022, doi: 10.1021/acs.nanolett.2c02119.

[176] A. A. Zibrov *et al.,* “Emergent Dirac Gullies and Gully-Symmetry-Breaking Quantum Hall States in ABA Trilayer Graphene,” *Phys. Rev. Lett.*, vol. 121, no. 16, p. 167601, 2018, doi: 10.1103/PhysRevLett.121.167601.

[177] Y. Shi *et al.,* “Tunable Lifshitz Transitions and Multiband Transport in Tetralayer Graphene,” *Phys. Rev. Lett.*, vol. 120, no. 9, p. 96802, 2018, doi: 10.1103/PhysRevLett.120.096802.

[178] J. Nilsson, A. H. Castro Neto, F. Guinea, and N. M. R. Peres, “Electronic properties of bilayer and multilayer graphene,” *Phys. Rev. B*, vol. 78, no. 4, p. 45405, 2008, doi: 10.1103/PhysRevB.78.045405.

[179] J. L. Collins *et al.,* “Electric-field-tuned topological phase transition in ultrathin Na3Bi,” *Nature*, vol. 564, no. 7736, pp. 390–394, 2018, doi: 10.1038/s41586-018-0788-5.

[180] F. Winterer, F. R. Geisenhof, N. Fernandez, A. M. Seiler, F. Zhang, and R. T. Weitz, “Ferroelectric and anomalous quantum Hall states in bare rhombohedral trilayer graphene: Preprint at https://arxiv.org/pdf/2305.04950 (2023),” Preprint at https://arxiv.org/pdf/2305.04950 (2023). [Online]. Available: https://arxiv.org/pdf/2305.04950

[181] A. Shtyk, G. Goldstein, and C. Chamon, “Electrons at the monkey saddle: A multicritical Lifshitz point,” *Phys. Rev. B*, vol. 95, no. 3, p. 35137, 2017, doi: 10.1103/PhysRevB.95.035137.

[182] Z. Dong, P. A. Lee, and L. S. Levitov, “(in preparation, 2023),”

[183] S. Chatterjee, T. Wang, E. Berg, and M. P. Zaletel, “Inter-valley coherent order and isospin fluctuation mediated superconductivity in rhombohedral trilayer graphene,” *Nature Communications*, vol. 13, no. 1, p. 6013, 2022, doi: 10.1038/s41467-022-33561-w.

[184] R. M. Fleming and C. C. Grimes, “Sliding-Mode Conductivity in NbSe3: Observation of a Threshold Electric Field and Conduction Noise,” *Phys. Rev. Lett.*, vol. 42, no. 21, pp. 1423–1426, 1979, doi: 10.1103/PhysRevLett.42.1423.

[185] V. Lukic and E. J. Nicol, “Conductance characteristics between a normal metal and a two-band superconductor carrying a supercurrent,” *Phys. Rev. B*, vol. 76, no. 14, p. 144508, 2007, doi: 10.1103/PhysRevB.76.144508.

[186] L. Landau, “Diamagnetismus der Metalle,” *Zeitschrift für Physik*, vol. 64, no. 9, pp. 629–637, 1930, doi: 10.1007/BF01397213.

[187] J. Velasco *et al.,* “Competing ordered states with filling factor two in bilayer graphene,” *Nat Commun*, vol. 5, no. 1, p. 4550, 2014, doi: 10.1038/ncomms5550.

[188] K. S. Novoselov, V. I. Fal'ko, L. Colombo, P. R. Gellert, M. G. Schwab, and K. Kim, “A roadmap for graphene,” *Nature*, vol. 490, no. 7419, pp. 192–200, 2012, doi: 10.1038/nature11458.

[189] F. Schwierz, “Graphene transistors,” *Nature Nanotech*, vol. 5, no. 7, pp. 487–496, 2010, doi: 10.1038/nnano.2010.89.

[190] C. Tan, D. Adinehloo, J. Hone, and V. Perebeinos, “Phonon-Limited Mobility in h-BN Encapsulated AB-Stacked Bilayer Graphene,” *Phys. Rev. Lett.*, vol. 128, no. 20, p. 206602, 2022, doi: 10.1103/PhysRevLett.128.206602.

[191] Private Communication with Vladimir Falko (University of Manchester).

[192] F. R. Geisenhof, F. Winterer, A. M. Seiler, J. Lenz, I. Martin, and R. T. Weitz, “Interplay between topological valley and quantum Hall edge transport,” *Nat Commun*, vol. 13, no. 1, p. 4187, 2022, doi: 10.1038/s41467-022-31680-y.

[193] F. Zhang, “Spontaneous chiral symmetry breaking in bilayer graphene,” *Synthetic Metals*, vol. 210, pp. 9–18, 2015, doi: 10.1016/j.synthmet.2015.07.028.

[194] D. C. Elias *et al.,* “Dirac cones reshaped by interaction effects in suspended graphene,” *Nat. Phys.*, vol. 7, no. 9, pp. 701–704, 2011, doi: 10.1038/nphys2049.

[195] F. Guinea, “Superconductivity and other phases in graphene multilayers, without twists,” *Journal Club for Condensed Matter Physics*, 2021, doi: 10.36471/JCCM_November_2021_01.

[196] L. Holleis *et al.,* “Ising Superconductivity and Nematicity in Bernal Bilayer Graphene with Strong Spin Orbit Coupling,” Mar. 2023. [Online]. Available: https://arxiv.org/pdf/2303.00742

[197] T. Wang, M. Vila, M. P. Zaletel, and S. Chatterjee, “Electrical control of magnetism in spin-orbit coupled graphene multilayers,” Mar. 2023. [Online]. Available: http://arxiv.org/pdf/2303.04855v1

[198] A. Jimeno-Pozo, H. Sainz-Cruz, T. Cea, P. A. Pantaleón, and F. Guinea, “Superconductivity from electronic interactions and spin-orbit enhancement in bilayer and trilayer graphene,” Oct. 2022. [Online]. Available: https://arxiv.org/pdf/2210.02915

[199] Y.-Z. Chou, F. Wu, and S. Das Sarma, “Enhanced superconductivity through virtual tunneling in Bernal bilayer

graphene coupled to WSe2," *Phys. Rev. B*, vol. 106, no. 18, L180502, 2022, doi: 10.1103/PhysRevB.106.L180502.

[200] Y.-Z. Chou, F. Wu, J. D. Sau, and S. Das Sarma, "Acoustic-phonon-mediated superconductivity in Bernal bilayer graphene," *Phys. Rev. B*, vol. 105, no. 10, L100503, 2022, doi: 10.1103/PhysRevB.105.L100503.

[201] M. Xie and S. D. Sarma, "Flavor symmetry breaking in spin-orbit coupled bilayer graphene," Feb. 2023. [Online]. Available: https://arxiv.org/pdf/2302.12284

[202] P. A. Pantaleon, A. Jimeno-Pozo, H. Sainz-Cruz, T. Cea, V. T. Phong, and F. Guinea, "Superconductivity and correlated phases in bilayer, trilayer graphene and related structures," Nov. 2022. [Online]. Available: https://arxiv.org/pdf/2211.02880

[203] Z. Dong, A. V. Chubukov, and L. Levitov, "Spin-triplet superconductivity at the onset of isospin order in biased bilayer graphene," May. 2022. [Online]. Available: http://arxiv.org/pdf/2205.13353v1

[204] A. L. Szabó and B. Roy, "Competing orders and cascade of degeneracy lifting in doped Bernal bilayer graphene," *Phys. Rev. B*, vol. 105, no. 20, L201107, 2022, doi: 10.1103/PhysRevB.105.L201107.

[205] T. Cea, "Superconductivity induced by the intervalley Coulomb scattering in a few layers of graphene," *Phys. Rev. B*, vol. 107, no. 4, L041111, 2023, doi: 10.1103/PhysRevB.107.L041111.

[206] H. Li *et al.,* "Electrode-Free Anodic Oxidation Nanolithography of Low-Dimensional Materials," *Nano Letters*, vol. 18, no. 12, pp. 8011–8015, 2018, doi: 10.1021/acs.nanolett.8b04166.

[207] W. Ruan *et al.,* "Evidence for quantum spin liquid behaviour in single-layer 1T-TaSe2 from scanning tunnelling microscopy," *Nat. Phys.*, vol. 17, no. 10, pp. 1154–1161, 2021, doi: 10.1038/s41567-021-01321-0.

[208] Y. Kuramoto, "Wigner Crystal, Electron Chain, and Charge Density Wave in Strong Magnetic Fields," *J. Phys. Soc. Jpn.*, vol. 44, no. 5, pp. 1572–1582, 1978, doi: 10.1143/JPSJ.44.1572.

[209] Y. He, K. Yang, M. O. Goerbig, and R. S. K. Mong, "Charge density waves and their transitions in anisotropic quantum Hall systems," (in En;en), *Commun Phys*, vol. 4, no. 1, pp. 1–12, 2021, doi: 10.1038/s42005-021-00613-4.

[210] S. Dzsaber *et al.,* “Control of electronic topology in a strongly correlated electron system,” *Nat Commun*, vol. 13, no. 1, p. 5729, 2022, doi: 10.1038/s41467-022-33369-8.

[211] D. M. Kennes *et al.,* “Moiré heterostructures as a condensed-matter quantum simulator,” (in En;en), *Nat. Phys.*, vol. 17, no. 2, pp. 155–163, 2021, doi: 10.1038/s41567-020-01154-3.

[212] N. P. de Leon *et al.,* “Materials challenges and opportunities for quantum computing hardware,” *Science (New York, N.Y.)*, vol. 372, no. 6539, 2021, doi: 10.1126/science.abb2823.

[213] D. S. Lee, V. Skákalová, R. T. Weitz, K. von Klitzing, and J. H. Smet, “Transconductance Fluctuations as a Probe for Interaction-Induced Quantum Hall States in Graphene,” *Phys. Rev. Lett.*, vol. 109, no. 5, p. 56602, 2012, doi: 10.1103/PhysRevLett.109.056602.

[214] M. Kumar, A. Laitinen, and P. Hakonen, “Unconventional fractional quantum Hall states and Wigner crystallization in suspended Corbino graphene,” *Nature Communications*, vol. 9, no. 1, p. 2776, 2018, doi: 10.1038/s41467-018-05094-8.

Acknowledgements

I would like to take the chance to thank everyone who has worked with me and supported me during the last four years.

First and foremost, I want to thank my supervisor **Thomas Weitz** for granting me the opportunity to work in his group during my master's and Ph.D. studies. Thank you, Thomas, for all the discussions and ideas, for giving me the freedom to try out new things, for providing advice and listening to concerns, and for always being approachable.

I am grateful for all members of the examination board, consisting of **Thomas Weitz**, **Claus Ropers**, **Fabian Heidrich-Meisner**, **Stefan Mathias**, **Jasnamol Palakkal**, and **Martin Wenderoth**. Thank you, Thomas, Fabian, and Claus, also for being on my thesis advisory committee, and you, Thomas and Claus, for reviewing my thesis.

I am very thankful for my great colleagues in the AG Weitz, without whom this work would not have been possible. I enjoyed the supportive, easy-going, and joyful atmosphere in our group as well as the coffee breaks, cakes, and after-work beers.

In particular, I would like to mention some of my former colleagues in Munich. First, I thank **Felix Winterer** for being a great supervisor during my master's thesis and a great mentor in the subsequent years. Thank you, **Fabian Geisenhof**, for your advice, support, and many discussions on graphene as well as on "the good old times", **Jakob Lenz** for sharing your knowledge on how to move around AFMs and benches, and **Lisa Walter** for managing the move to Göttingen, for taking care of everything and everyone in the group and for being a really good friend. Furthermore, I am happy to have worked with **Lucca Kühner**, **Jonas Biechteler**, **Xin Huang**, **Gilles Rodway-Gant**, **Marco Dembecki**, **Maximilian Kögl**, **Lucas Hille**, **Maurice Larsson**, **Rayner Schelwald**, **Daniela Priesack**, and **Stefan Wakolbinger**.

I am grateful for **Noelia Fernandez**, **Francesca Falorsi**, **Lukas Renn**, and **Christian Eckel**, who also moved from Munich to Göttingen. Thank you, Noelia, for sharing the frustration and joy about performing measurements at the cryostat, Francesca, for always providing support and encouragement, for your constant interest and for bringing the Italian spirit to our group. Thank you, Lukas and

Christian, for some fun beach volleyball matches and your faith in my chess skills. Unfortunately, I need to apologize for not standing up to the high expectations you set for me.

Thank you, **Jonas Pöhls**, for joining the group as the first “Göttinger” Ph.D. student, for always being reliable and helpful, for being a great office mate, and for ordering the new coffee machine that saved me while writing this thesis. It was a fun time when the group in Göttingen only consisted of you, **Monica Kolek Martinez de Azagra**, and me. I really enjoyed building up the labs in Göttingen with both of you; thanks a lot! **James Borchert**, thank you for joining us as the first postdoc in Göttingen and sharing your knowledge and experiences with me.

I am very grateful for being part of the Bernal bilayer graphene team consisting of **Martin Statz**, **Isabell Weimer**, **Nils Jacobsen**, and **Moritz Knaak.** Thank you for many insightful discussions and theoretical inputs and for carrying on the projects. Thanks to **David Urbaniak**, who always finds the perfect flakes for building a stack.

I am also happy to have worked with all other former and current members of the AG Weitz. Especially, I would like to mention **Bernd Damaschke**, **Jonas Schröder**, **Adrian Paulus**, **Daniel Vitroler**, **Philipp Kaiser** and **Batuhan Kalkan**.

I am deeply indebted to Batu, Christian, Flo, Francesca, Jim, Jonas, Martin and Rudi for careful proof reading of my thesis and to Nils, who answered all theory questions that came up while writing.

A big thank you goes to the **AG Mathias**, the **AG Moshnyaga**, and the **AG Ulrichs** for welcoming us to the I. Institute and for fun nights in the institute’s kitchen. I also enjoyed a large number of research collaborations. Explicitly, I would like to thank **Stefan Mathias**, **Marcel Reutzel**, **David Schmitt**, **Jan Philipp Bange**, **Wiebke Bennecke**, and **Paul Werner** for great discussions and joint projects.

I could not have undertaken this journey without the continuous technical support from **Philipp Altpeter**, **Christian Obermayer**, **Heribert Lorenz**, **Reinhold Rath**, **Stefan Manus**, and **Anton Heindl** in Munich and from **Carsten Mahn**, **Uta Filippich** (who is also a great office mate), **Kai Dörner**, **Simon Stoldt**, **Katrin Gehrke**, **Hartmut Eichenberg**, **Bastian Beyland**, **Florian Fellner**, the **Team of the Central Workshop** and the **Team of the Electrical Workshop** in Göttingen. Thank you all very, very much not only for keeping the labs running every day but also for helping to move all our instruments from Munich to Göttingen, which was a real challenge.

I enjoyed setting up the “old” cryostat with Carsten and am grateful for **Prof. Winzer**’s help. I am also very happy that Isabell will take care of it from now on.

Thanks also to **Martina Edenhofer**, **Michaela Mecke**, **Finn Krummacker**, and **Miriam Müller-Reimann** , who I could always approach with any administrational problem and who kept the group/ the institute running.

This thesis greatly benefits from collaborations with **Fan Zhang**, **Tianyi Xu**, **Leonid Levitov**, and **Zhiyu Dong**. Thank you all for the many discussions and your ideas and input. Thank you, **Takashi Taniguchi**, and **Kenji Watanabe**, for providing us continuously with hBN. I am also grateful for the discussions with **Vladimir Falko**, **Aitor Garcia-Ruiz Fuentes** , **Chunli Huang**, and **Tobias Wolf**. Thank you, **Jurgen Smet**, and **Dong Zhao**, for letting us perform measurements at your cryostat in Stuttgart.

Finally, I would like to thank **my parents** for their unconditional support and care, and **Rudolf Haindl** for letting me share my emotional highs and lows, for always supporting me, for giving me confidence, for long-night discussions on how to phrase sentences, improve figures or how to present data, for leaving behind Bavaria and moving to Göttingen and for always being there for me.